Springer Proceedings in Mathematics & Statistics

Amina Eladdadi
Peter Kim
Dann Mallet *Editors*

Mathematical Models of Tumor-Immune System Dynamics

Springer

Springer Proceedings in Mathematics & Statistics

Volume 107

More information about this series at http://www.springer.com/series/10533

Springer Proceedings in Mathematics & Statistics

This book series features volumes composed of select contributions from workshops and conferences in all areas of current research in mathematics and statistics, including OR and optimization. In addition to an overall evaluation of the interest, scientific quality, and timeliness of each proposal at the hands of the publisher, individual contributions are all refereed to the high quality standards of leading journals in the field. Thus, this series provides the research community with well-edited, authoritative reports on developments in the most exciting areas of mathematical and statistical research today.

Amina Eladdadi • Peter Kim • Dann Mallet
Editors

Mathematical Models of Tumor-Immune System Dynamics

Springer

Editors
Amina Eladdadi
Mathematics Department
The College of Saint Rose
Albany, NY, USA

Peter Kim
School of Mathematics and Statistics
University of Sydney
Sydney, NSW, Australia

Dann Mallet
Mathematical Sciences School
Queensland University of Technology
Brisbane, QLD, Australia

ISSN 2194-1009 ISSN 2194-1017 (electronic)
ISBN 978-1-4939-1792-1 ISBN 978-1-4939-1793-8 (eBook)
DOI 10.1007/978-1-4939-1793-8
Springer New York Heidelberg Dordrecht London

Library of Congress Control Number: 2014953926

Mathematics Subject Classification (2010): 92B05, 92C50, 92C17, 92C45, 34D20, 34H20, 35Q92, 68Q80

Printed on acid-free paper

Springer is part of Springer Science+Business Media (www.springer.com)

Preface

Mathematical models are not only practical but also crucial for understanding biological systems, and the cancer-immune system is no exception. This book on *"Mathematical Models of Tumor-Immune System Dynamics"* highlights current advances in mathematical models (e.g., deterministic, stochastic, and agent-based models) and demonstrates their applicability in problems arising from cancer immunology. This book can serve as a reference for researchers working in the field of cancer immunology and those who might consider entering it.

Recent progress in cancer immunology and advances in immunotherapy suggest that the immune system plays a fundamental role in combatting tumors, and hence can be used as a vehicle to prevent or cure cancer. Although theoretical and experimental studies of tumor-immune dynamics date back to the early 1890s, fundamental questions concerning complex interactions between the immune system and the growing tumor remain. For example, contemporary research programs are driven by questions concerning how components of the immune system synergize to limit cancer development, how tumors escape immune recognition and control, and why some immunotherapies inhibit growth of certain tumors while stimulating the growth of others.

Indeed, the multidimensional nature of these complex interactions requires cross-disciplinary approaches to capture more realistic dynamics of the essential biology. One such approach combines cancer immunology with mathematics to model the interactions. In particular, mathematical modeling has been used to understand immune surveillance of developing tumors, the role of the immune system's response in maintaining tumor dormancy, and the potential impact of enhancing anti-tumor immune responses through cancer vaccination. Other novel uses of mathematical modeling involve optimizing preventative vaccination strategies against tumor cells and studying the feasibility of virotherapy, which involves infecting patients with viruses engineered to favor the infection of tumor cells, rendering the cancer a target of the patient's immune response. Understanding these intricate interactions between cancer and the immune system offers scientists and clinicians

powerful insights into stimulating and modulating immune responses to prevent or treat cancer and advance the development of cancer-immunotherapies.

This volume brings together a range of topics on mathematical models of tumor-immune system dynamics by applied mathematicians and scientists. The mathematical methods used to study the dynamics of the tumor-immune system in this book range from ordinary differential equations, to nonlinear partial differential equations representing complex time- and space-dependent discrete and continuous processes, to discrete and probabilistic cellular automata. A total of ten chapters are contributed to this book as follows:

Geoffrey Clapp and Doron Levy, *"Incorporating Asymmetric Stem Cell Division into the Roeder Model for Chronic Myeloid Leukemia."* The authors develop a system of difference equations to modify Roeder's agent-based model (ABM) of chronic myeloid leukemia (CML). Specifically, they incorporate asymmetric division of stem cells and precursors, allow precursors to live a variable amount of time before maturing, and introduce feedback inhibition from mature cells to stem cells and precursors. These modifications result in more accurate simulations of CML genesis and treatment.

Andrea K. Cooper and Peter S. Kim, *"A Cellular Automata and a Partial Differential Equation Model of Tumor-Immune Dynamics and Chemotaxis."* The authors present mathematical models of an anti-tumor immune response using a cellular automaton (CA) and a system of partial differential equations (PDEs) to account for stochasticity and spatiotemporal heterogeneity. Their models exhibit three types of behavior: tumor elimination, oscillation, and uncontrolled tumor growth that depend substantially on the strength of immune cell chemotaxis, or recruitment, to the tumor site.

Marcello Delitala, Tommaso Lorenzi, and Matteo Melensi, *"A Structured Population Model of Competition Between Cancer Cells and T Cells Under Immunotherapy."* The authors present a structured population model of cancer-immune competition under immunotherapy. The model consists of a system of structured equations for the dynamics of cancer cells and activated T cells. Simulations highlight the ability of the model to reproduce the emergence of cancer immuno-editing, that is, the well-documented process by which the immune system guides the somatic evolution of tumors by eliminating highly immunogenic cancer cells.

Lisette G. dePillis and Ami E. Radunskaya, *"Modeling Tumor-Immune Dynamics."* The goal of this chapter is to understand the dynamics of immune-mediated tumor rejection, in addition to exploring results of applying combination immune, vaccine, and chemotherapy treatments. The authors develop and analyze a mathematical model formulated as a system of ordinary differential equations (ODEs) that governs cancer growth on a cell population level. The model includes populations of cancer cells, natural killer (NK) cells, and CD8+ T cells.

Peter Hinow and Ami E. Radunskaya, *"The Mathematics of Drug Delivery."* The authors review a discrete and a continuous mathematical model for drug delivery by matrix tablets and liposomes. The discrete model begins with the construction of a graph as the contact graph of a random dense sphere packing. The continuous

model is based on a system of reaction-diffusion partial differential equations for the concentrations of dissolved and undissolved drug and excipient, respectively. Their cellular automaton (CA) model has shown the best results and is ready for more concrete applications.

Yangjin Kim, Hyunji Kang, and Sean Lawler, *"The Role of the miR-451-AMPK Signaling Pathway in Regulation of Cell Migration and Proliferation in Glioblastoma."* The authors present a hybrid model (ODEs and PDEs) of glioblastoma that identifies a key mechanism behind the molecular switches between proliferative and migratory phases in response to metabolic stress and biophysical interaction between cells. They then examine a hybrid model for the biomechanical interaction between invasive and proliferative cells, in which all cells are modeled individually, and show how biophysical properties of cells and the core miR-451- AMPK control system affect the growth and invasion patterns of glioma spheroids in response to various glucose levels in the microenvironment.

Urszula Ledzewicz and Heinz Schättler, *"An Optimal Control Approach to Cancer Chemotherapy with Tumor-Immune System Interactions."* The authors review some results about the structure of optimal chemotherapy protocols in the presence of tumor immune system interactions that can be derived from population-based mathematical models using optimal control.

Ignacio A. Rodriguez-Brenes, Natalia L. Komarova, and Dominik Wodarz, *"Negative Feedback Regulation in Hierarchically Organized Tissues: Exploring the Dynamics of Tissue Regeneration and the Role of Feedback Escape in Tumor Development."* The authors present a mathematical model that includes feedback regulation in both the division rate and the self-renewal probability of stem cells. They find a trade-off between requiring a small equilibrium fraction of stem cells while avoiding oscillations and the speed at which the system is able to recover from a perturbation. Spatial interactions and the addition of feedback inhibition on the cell division rate reduce the amplitude of oscillations and contribute to the robustness of the system. In addition, feedback inhibition on the division rate also increases the speed of regeneration.

Trisilowati, Scott W. McCue, and Dann G. Mallet, *"A Cellular Automata Model to Investigate Immune Cell–Tumor Cell Interactions in Growing Tumors in Two Spatial Dimensions."* The authors develop a hybrid cellular automata (CA) model to describe the interaction between a growing tumor and the immune system of the host, including chemokines. The model is able to describe the effect of the immune system and chemokines on a growing tumor. Increasing the number of immature dendritic cells (DCs) in the domain causes a decrease in the number of tumor cells. This result strongly supports the hypothesis that DCs can be used as a cancer treatment.

Joanna R. Wares, Joseph J. Crivelli, and Peter S. Kim, *"Differential Equation Techniques for Modeling a Cycle-Specific Oncolytic Virotherapeutic."* The authors present a mathematical model of oncolytic vesticular stomatitis virus (VSV) in stages. They start by discussing standard mathematical tools along with the development and analysis of the model. Then they develop the model to incorporate

the property that oncolytic VSV only tends to affect tumor cells in the active phases of the cell cycle. The authors show that this mathematical model can be used to investigate the dynamics of the tumor-virus system.

We thank all of the contributing authors for their hard work that made this Springer Book a reality. We also thank the reviewers for their dedicated effort and valuable comments. We sincerely thank the excellent Springer editorial team for their professional help, patience, and guidance throughout the production process of this book. The idea for this book was conceived during the US-Sydney International Workshop on *"Mathematical Modeling of Tumor-Immune Dynamics,"* held in Sydney on January 7–10, 2013. This workshop could not have happened without the help of many dedicated people and generous financial support from various sponsors. We gratefully acknowledge all of the funding organizations, particularly the National Science Foundation (Award # DMS-1249258), the Australian Mathematical Sciences Institute, the Australian Research Council (Award # DE120101113), and the Society for Mathematical Biology for their generous support that made the US-Sydney workshop a remarkable success.

Albany, NY, USA — Amina Eladdadi
Sydney, NSW, Australia — Peter Kim
Brisbane, QLD, Australia — Dann Mallet

Contents

Incorporating Asymmetric Stem Cell Division into the Roeder Model for Chronic Myeloid Leukemia

Geoffrey Clapp and Doron Levy

Abstract In this chapter we propose several modifications to the Roeder model of chronic myeloid leukemia (Roeder et al.: Nat. Med. **12**(10), 1181–1184 2006). Specifically, we incorporate asymmetric division of stem cells and precursors, allow precursors to live a variable amount of time before maturing, and introduce feedback inhibition from mature cells to stem cells and precursors. These modifications result in more accurate simulations of cancer genesis and treatment. In comparison with the original model, our results indicate lower transition rates of stem cells between their quiescent and cycling states, which are supported by the rates suggested by experimental data. Decreased transition rates of stem cells translate into quiescent cancer stem cells that are better protected from imatinib, resulting in a large residual cancer burden, even after many years of therapy. Our modeling results suggest that the efficacy of imatinib would increase if it is combined with a drug that induces cancer stem cells to cycle.

1 Introduction

Chronic myeloid leukemia (CML) is a myeloproliferative disorder that represents about 20 % of leukemias in adults [1]. A majority of cases of CML is initiated by the formation of the Philadelphia chromosome (Ph), which results in the production of the BCR-ABL gene, coding for a constitutively active tyrosine kinase. The tyrosine kinase inhibitor imatinib (IM) has significantly improved CML patient outlook. Treatment with IM results in complete hematological remission in most patients [16] and cytogenetic remission in 75 % of patients [4]. Moreover, in many patients, IM induces a major molecular response (MMR), or a 3-log decrease in BCR-ABL

G. Clapp
Department of Mathematics, University of Maryland, College Park, MD 20742, USA
e-mail: clappge1@umd.edu

D. Levy (✉)
Department of Mathematics and Center for Scientific Computation and Mathematical Modeling (CSCAMM), University of Maryland, College Park, MD 20742, USA
e-mail: dlevy@math.umd.edu

A. Eladdadi et al. (eds.), *Mathematical Models of Tumor-Immune System Dynamics*, Springer Proceedings in Mathematics & Statistics 107,
DOI 10.1007/978-1-4939-1793-8_1

ratio [9]. Still, in most cases, even after several years of therapy, a small population of Ph+ cells persists, and cessation of treatment will generally lead to a rapid relapse [4].

Several mathematical models have been developed and applied to CML and its treatment. Modeling approaches include ordinary differential equations (ODEs) [19, 21,22,27], delay differential equations (DDEs) [3,10], branching processes [15,28], and birth–death processes [13,14]. These tools have been applied to studying cancer genesis, therapy, combination therapy, and drug resistance. Additionally, in [10,22], the immune system is incorporated, and in [10], a combination therapy is proposed that combines IM with cancer vaccines, whose dose and timing are adjusted to the profile of the immune response in individual patients.

Roeder et al. [24] develop a stochastic agent-based model (ABM) for the interaction between IM and CML. This model considers the differentiation of cells through three stages: stem cells, proliferating precursor cells, and non-proliferating precursor and mature cells. The stem cells are divided into two compartments: proliferating and non-proliferating stem cells. Individual stem cells circulate continually between the two compartments and are affected by IM only while proliferating.

Applications of the Roeder et al. ABM can be found in several papers. In [7], interferon-α (IFN-α) is considered in combination with IM, in order to stimulate quiescent cancer cells to enter the cell cycle, where they are more likely to be affected by IM. In considering drug schedules, it is shown in [24] that pulsed IFN-α with continuous IM leads to the greatest clinical benefits while still limiting side effects. Using patient-specific data, the Roeder model is used in [8] to predict which patients can be safely taken off IM without relapsing.

Although ABMs are able to capture cell dynamics and interactions, simulations with a large number of agents can be computationally prohibitive. To address this difficulty, Kim et al. reformulate the Roeder model as a system of difference equations [12] and as a system of partial differential equations (PDEs) [11]. A simplified version of the PDE model is later studied in [5]. An alternative approach to obtaining a continuum limit of the ABM is proposed by Roeder et al. in [25]. By using these reduced systems, computation time no longer depends on cell population sizes, and simulations with realistic numbers of cells are made possible.

In this chapter, we propose several modifications to the Roeder model [24], constructing a model that more closely represents hematopoiesis. Specifically, we incorporate asymmetric division of stem cells and precursors, allow precursors to live a variable amount of time before maturing, and introduce feedback inhibition from mature cells to stem cells and precursors. These modifications result in more accurate simulations of cancer genesis and treatment.

The rest of the chapter is organized as follows. In Sect. 2, we provide a brief overview of the Roeder model. The derivation of the corresponding system of difference equations is given in Sect. 3. We present our modifications to the Roeder model in Sect. 4. Parametrization of the model and numerical simulations are discussed in Sect. 5. The final section "Conclusion" concludes with a discussion and insight about how CML therapy can be potentially improved.

2 The Roeder Model

In this section we provide a brief overview of the Roeder model [24]. This model is an ABM that considers hematopoietic cells in three compartments: stem cells (STC), proliferating precursor cells (P), and mature cells (M). Stem cells are either quiescent, denoted by A, or cycling, denoted by Ω. Let $A(t)$ and $\Omega(t)$ represent the total number of quiescent and cycling stem cells at time t. Each individual stem cell is characterized by an affinity variable $a(t) \in [a_{min}, a_{max}]$ which determines the probability that the cell will be quiescent or cycling. At each time step, which represents 1 h, a quiescent stem cell will enter the cell cycle with probability ω, and a cycling stem cell will become quiescent with probability α, where

$$\omega(\Omega(t), a(t)) = \frac{a_{min}}{a(t)} f_\omega(\Omega(t)), \tag{1}$$

$$\alpha(A(t), a(t)) = \frac{a(t)}{a_{max}} f_\alpha(A(t)). \tag{2}$$

Thus, cells with affinity $a(t)$ close to a_{max} tend to remain or become quiescent, while cells with $a(t)$ close to a_{min} tend to remain or become cycling. The functions f_ω and f_α are defined by

$$f_\omega(\Omega(t)) = \frac{1}{\nu_1 + \nu_2 \exp\left(\nu_3 \frac{\Omega(t)}{N_\omega}\right)} + \nu_4, \tag{3}$$

$$f_\alpha(A(t)) = \frac{1}{\mu_1 + \mu_2 \exp\left(\mu_3 \frac{A(t)}{N_\alpha}\right)} + \mu_4. \tag{4}$$

Both functions, f_ω and f_α, are decreasing sigmoidal functions whose shapes depend on the parameters ν_i and μ_i. The parameters N_ω and N_α are scaling factors for $\Omega(t)$ and $A(t)$. Given the values of f_ω at $\Omega(t) = 0$, $N_\omega/2$, N_ω, and ∞, we can compute the coefficients ν_i as follows:

$$\begin{aligned}
\nu_1 &= (h_1 h_3 - h_2^2)/(h_1 + h_3 - 2h_2), \\
\nu_2 &= h_1 - \nu_1, \\
\nu_3 &= \log((h_3 - \nu_1)/\nu_2), \\
\nu_4 &= f_\omega(\infty),
\end{aligned}$$

where

$$\begin{aligned}
h_1 &= 1/(f_\omega(0) - f_\omega(\infty)), \\
h_2 &= 1/(f_\omega(N_\omega/2) - f_\omega(\infty)), \\
h_3 &= 1/(f_\omega(N_\omega) - f_\omega(\infty)).
\end{aligned}$$

A similar set of formulas can be used to determine the parameters μ_i of f_α. These functions are constructed so that the cells that are in the less-populated compartment are less likely to move.

Quiescent cells that remain quiescent during a time step increase their affinity by a factor of r, until they reach the maximum affinity a_{max}. Cycling cells that continue to cycle during a time step decrease their affinity by a factor of d, until they reach the minimum affinity a_{min}. In other words, cells that remain in A or Ω become more likely to stay in A or Ω in the future.

Cycling cells are also characterized by a cell cycle counter $c(t)$, which represents their place in the cell cycle. In [24], the cell cycle lasts 49 h, so $c(t) \in \{0, 1, \ldots, 48\}$. The first 32 h represent the G1 phase, where cells grow and can transition to quiescence. Cells that reach $c(t) = 32$ commit to division and must go through the S, G2, and M stages of the cell cycle. After the cell divides ($c(t) = 48$), each daughter cell reenters G1 ($c(t) = 0$) and becomes an uncommitted cycling cell that may transition to quiescence. Quiescent cells that enter the cell cycle have their cell cycle counter initialized to $c(t) = 32$, which means that they commit to at least one division.

Stem cells that reach affinity $a(t) = a_{min}$ differentiate into precursor cells. Precursors (P) live for a fixed amount of time and undergo a fixed number of divisions. They then differentiate into mature cells (M), which do not divide and die after a fixed amount of time. Figure 1 summarizes the Roeder model.

Both healthy (Ph−) and cancer (Ph+) cells differentiate through the maturity stages discussed above. Ph− cells and Ph+ cells compete at the stem cell level through the functions f_ω and f_α, whose inputs are the total number of cycling cells and quiescent cells, respectively. Ph+ cells differ from Ph− cells in their transition functions f_ω and f_α. It is assumed that Ph+ stem cells are more likely to transition between quiescence and cycling and that the probability of a quiescent Ph+ stem cell transitioning to cycling is only slightly affected by the current number of cycling stem cells. Cancer genesis is characterized by a long latency period of 5–7 years, in which Ph+ and Ph− populations coexist. Without treatment, Ph+ cells are eventually able to out-compete Ph− cells and take over the system.

Treatment with IM is assumed to have two effects on Ph+ stem cells while not directly affecting Ph− cells. First, all cycling Ph+ stem cells are killed at a rate r_{deg}. In addition, all cycling Ph+ stem cells become IM-affected with probability r_{inh}. Once a Ph+ stem cell becomes IM-affected, its transition function f_ω is decreased significantly, making it much less likely for quiescent Ph+ stem cells to enter the cell cycle. Note that there is no direct action of IM on quiescent Ph+ stem cells.

The effect of the treatment is evaluated by monitoring levels of BCR-ABL fusion transcript in the blood. These levels are reported relative to an endogenous control transcript, BCR or ABL, in order to normalize the BCR-ABL measurements. This relative value, known as the BCR-ABL ratio, is estimated in [24] by

$$\text{BCR-ABL ratio} = \frac{100 \times (\#\text{ of mature Ph+ cells})}{2 \times (\#\text{ of mature Ph− cells}) + (\#\text{ of mature Ph+ cells})}. \quad (5)$$

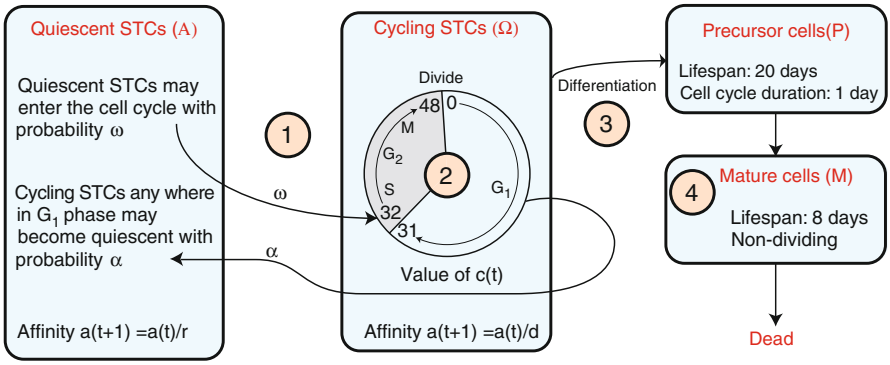

Fig. 1 A diagram for the Roeder model. (*1*) At each time step, quiescent stem cells enter the cell cycle with probability ω, while cycling cells in G1 become quiescent with probability α. Quiescent stem cells that remain quiescent during a time step increase their affinity by a factor of r, up to a maximum value of a_{max}. Cycling stem cells that continue to cycle decrease their affinity by a factor of d. (*2*) Cycling stem cells progress through G_1, S, G_2, and M. The cell cycle counter $c(t) \in \{0, 1, \ldots, 48\}$ indicates the cell's phase in the cell cycle. Stem cells enter the cell cycle at hour $c(t) = 32$. At hour $c(t) = 48$, the cell divides, and its daughter cells reset their cell cycle counters to $c(t) = 0$. (*3*) A cycling stem cell whose affinity reaches a_{min} differentiates into a precursor cell, which lives for 20 days and divides once per day. (*4*) In the last division, precursor cells differentiate into mature cells, which do not divide and die after 8 days

The contributions of stem cells and precursors to this ratio are negligible because these populations are small relative to the mature cells, and the mature cells are the dominant population in the blood. In each healthy Ph− cell, there are two copies of the control gene, while Ph+ cells are assumed to possess one copy of the BCR-ABL fusion gene and one copy of the control gene. Thus, BCR-ABL transcript levels should be proportional to the number of mature Ph+ cells, while the control transcript levels should be proportional to twice the number of mature Ph− cells plus the number of mature Ph+ cells. This quantity is multiplied by 100 so that it represents a percentage.

In simulations, long-term treatment leads to a biphasic decline in BCR-ABL levels, with a rapid first decline followed by a slower second decline. However, small populations of Ph+ cells persist over many years of treatment, and cessation of treatment generally leads to a rapid relapse.

3 Reducing the Agent-Based Model to a System of Difference Equations

Although the Roeder model has the advantage of being able to capture the dynamics of cell–cell interactions, simulations with a realistic number of agents is computationally very expensive. In the simulations in [24], the number of cells is

down-scaled to $1/10$ of normal patient values, resulting in approximately 10^5 stem cells. Even with this reduction in the number of agents, a simulation of 20 years requires approximately 175,000 steps for each of the 10^5 agents. (Precursors and mature cells can be represented as populations, so the total number of agents is the total number of stem cells.) To address this limitation, the Roeder model is reduced to a system of PDEs in [11, 25] and a system of difference equations in [12]. In this section we follow [12] and provide a brief summary of the system of difference equations. A modified version of this system is what we later use for the numerical simulations of our modified version of the Roeder model.

In order to decrease the number of variables, Kim et al. [12] discretize the affinity state space. In [24], $d = 1.05$ and $r = 1.1$, so $\log(d) = \rho = 0.0488 \approx \log(r)/2$. By setting $d = e^{\rho}$ and $r = e^{2\rho}$, any cell whose initial affinity is of the form $a(t) = e^{-k\rho}$ for an integer k will continue to have this form. Since $0.002 \leq a(t) \leq 1$, k is restricted to $0 \leq k \leq 127$. Because of the negative in the exponent, the maximum affinity corresponds to the minimum k value, and the minimum affinity corresponds to the maximum k value. More importantly, though, with these new values of r and d, it is no longer necessary to track individual agents. Rather, for each of the various k values, we can group stem cells into populations whose affinity $a(t) = e^{-k\rho}$, for each of the finitely many k values.

Define $A_k(t)$ and $\Omega_{k,c}(t)$ as follows:

$$A_k(t) = \text{Number of cells in } A \text{ at time } t \text{ with } \log a(t) = -k\rho, \tag{6}$$

$$G_{k,c}(t) = \text{Number of cells in } \Omega \text{ at time } t \text{ with } \log a(t) = -k\rho \text{ and } c(t) = c. \tag{7}$$

As mentioned earlier, $k \in \{0, \ldots, 127\}$, and $c \in \{0, \ldots, 48\}$. Given this discretization, the Roeder model is represented by the following system of difference equations:

$$A_k(t+1) = \begin{cases} (A_0(t) - B_0(t)) + (A_1(t) - B_1(t)) + (A_2(t) - B_2(t)), & k = 0, \\ (A_{k+2}(t) - B_{k+2}(t)) + \sum_{c=0}^{31} \Psi_{k,c}(t), & k = 1 \ldots 125, \\ \sum_{c=0}^{31} \Psi_{k,c}(t), & k = 126, 127, \end{cases} \tag{8}$$

$$\Omega_{k,c}(t+1) = \begin{cases} B_0(t), & k = 0,\ c = 32, \\ 2\Omega_{k-1,48}(t), & k > 0,\ c = 0, \\ \Omega_{k-1,c-1}(t) - \Psi_{k-1,c-1}(t), & k > 0,\ c = 1, \ldots, 31, \\ (\Omega_{k-1,31}(t) - \Psi_{k-1,31}(t)) + B_k(t), & k > 0,\ c = 32, \\ \Omega_{k-1,c-1}(t), & k > 0,\ c = 33, \ldots, 48, \\ 0, & \text{otherwise.} \end{cases} \tag{9}$$

The terms B_k represent the number of cells that leave A_k and enter the cycling compartment $\Omega_{k,32}$. $\Psi_{k,c}$ is the number of cells that leave $\Omega_{k,c}$ and enter the quiescent compartment A_k. These terms are defined by

$$B_k(t) \sim \text{Bin}\left(A_k(t), \omega(\Omega(t), e^{-k\rho})\right), \tag{10}$$

$$\Psi_{k,c}(t) \sim \text{Bin}\left(\Omega_{k,c}(t), \alpha(A(t), e^{-k\rho})\right), \qquad c = 0, \ldots, 31, \tag{11}$$

where $\Omega(t) = \sum_{k,c} \Omega_{k,c}(t)$ and $A(t) = \sum_k A_k(t)$ are the total number of cycling and quiescent stem cells, and the functions ω and α are defined in Eqs. (1) and (2). In our simulations, we replace these stochastic variables with their expected value and allow populations to be continuous variables.

At each time step, a quiescent cell may remain quiescent or enter the cell cycle. Cells that remain quiescent increase their affinity by a factor of r, which translates to a decrease in k by two. Equation (8) describes the number of quiescent cells in each compartment, at time $t + 1$. The first line ($k = 0$) represents the number of cells entering A_0, namely those cells previously in A_0, A_1, or A_2 that remain quiescent. In the second line ($k = 1, \ldots, 125$), cells previously in A_{k+2} that remain quiescent enter A_k. The summation term is the number of cycling cells in $\Omega_{k,c}$ that become quiescent. The sum is over $c \in \{0, \ldots, 31\}$ because only cells in G1 can become quiescent. Lastly, when $k = 126$ or $k = 127$, there are no quiescent cells with $k > 127$ to feed these compartments. Therefore, the only cells entering these compartment are cycling cells that become quiescent.

On the other hand, cycling cells that continue to cycle decrease their affinity by a factor of d, which translates to an increase in k by one. At each step, the cell cycle counter also increases by one. The cycling cells are described by Eq. (9). The first line ($k = 0, c = 32$) represents cells that have maximum affinity who are entering the S phase of the cell cycle. Since there are no cycling cells with greater affinity, the only cells entering this compartment are quiescent cells that have just entered the cell cycle. The second line ($k > 0, c = 0$) represents cells that have just completed the cell cycle. The constant 2 represents division into two daughter cells, whose cell cycle counters are reset to $c(t) = 0$. The third line ($k > 0, c = 1, \ldots, 31$) represents cycling cells in the G1 phase. The right-hand side is the number of cycling cells in the $(k-1)^{st}$ compartment that continue to cycle. The beginning of the S phase, marked by $c(t) = 32$, is where transitioning quiescent cells enter the cell cycle. The fourth line ($k > 0, c = 32$) is similar to the third, with an additional term for the quiescent cells that begin cycling. The fifth line ($k > 0, c = 33, \ldots, 48$) represents cells in S, G2, and M. Because these cells have committed to division, they all progress to the next step in the cell cycle and increase their k value by one, until division. All other cycling cell compartments are zero at all times.

When a cycling cell's affinity reaches its minimum, corresponding to k taking its maximum value of 127, the cell differentiates into a precursor cell. The precursor cell divides once per day for 20 days (480 h). Upon the last division, both daughter cells differentiate into mature cells, which live for another 8 days without dividing, and then die. The equations for these compartments are

$$P_j(t+1) = \begin{cases} \sum_{c=0}^{48} \Omega_{127,c}(t) - \sum_{c=0}^{31} \Psi_{127,c}(t), & j = 0, \\ 2P_{j-1}(t), & j = 24, 48, 72, \ldots, 456, \\ P_{j-1}(t), & \text{otherwise}, \end{cases} \tag{12}$$

$$M_j(t+1) = \begin{cases} 2P_{479}(t), & j = 0, \\ M_{j-1}(t), & \text{otherwise}. \end{cases} \tag{13}$$

Here, $P_j(t)$ is the number of cells that have been precursors for j hours, where $j \in \{0, \ldots, 479\}$. $M_j(t)$ is the number of cells that have been mature for j hours, where $j \in \{0, \ldots, 191\}$. In Eq. (12), the first line on the right-hand side represents cycling stem cells that reach minimum affinity ($k = 127$), continue to cycle, and become precursors. The second line accounts for the division of precursor cells, which occurs every 24 h. For all other values of j, cells increase their age j by one per time step. In Eq. (13), precursor cells completing their final division become mature, which is the first line. The second line represents the fact that mature cells continue to age without dividing.

As in the Roeder model, cancer genesis is simulated by initializing a single Ph+ stem cell into the Ph− cell steady state. Both populations are described by the system of difference equations (Eqs. 8, 9, 12, 13). The two populations compete at the stem cell level and differ in their transition functions f_ω and f_α.

In simulating treatment, we divide the Ph+ population into two categories: those that are not affected by IM, which we denote Ph+/R, and those that are, which we denote Ph+/I. These two Ph+ populations differ in their transition function f_ω, with the Ph+/I stem cells being much less likely to transition from quiescence to cycling. At the beginning of treatment, all Ph+ cells are not IM-affected. The effects of treatment are assumed to occur at the beginning of every time step. For each k and c, let $\Omega_{k,c}^{+/R}(t)$ be the number of cycling Ph+/R cells, and let $\Omega_{k,c}^{+/I}(t)$ be the number of Ph+/I cells. Each cell in $\Omega_{k,c}^{+/R}$ will become IM-affected with probability r_{inh}. The number of cells in $\Omega_{k,c}^{+/R}$ that becomes IM-affected at that time step is given by $\Omega_{k,c}^{+/I,new}(t) \sim \text{Bin}(\Omega_{k,c}^{+/R}(t), r_{inh})$. We set

$$\Omega_{k,c}^{+/R}(t) := \Omega_{k,c}^{+/R}(t) - \Omega_{k,c}^{+/I,new}(t), \tag{14}$$

$$\Omega_{k,c}^{+/I}(t) := \Omega_{k,c}^{+/I}(t) + \Omega_{k,c}^{+/I,new}(t). \tag{15}$$

We additionally assume that all cycling Ph+ cells will apoptose with probability r_{deg}. We therefore remove these cells from the Ph+ populations at the beginning of each time step, by subtracting them from Eqs. (14) and (15). In our simulations, we choose to make the effects of IM deterministic by setting the number of cells that become IM-affected and apoptose to the expected values rather than taking them from their binomial distributions. Once the values of $\Omega_{k,c}(t)$ are updated, all three populations (Ph−, Ph+/R, Ph−/I) evolve following Eqs. (8), (9), (12), and (13).

4 Modifications to the Roeder Model

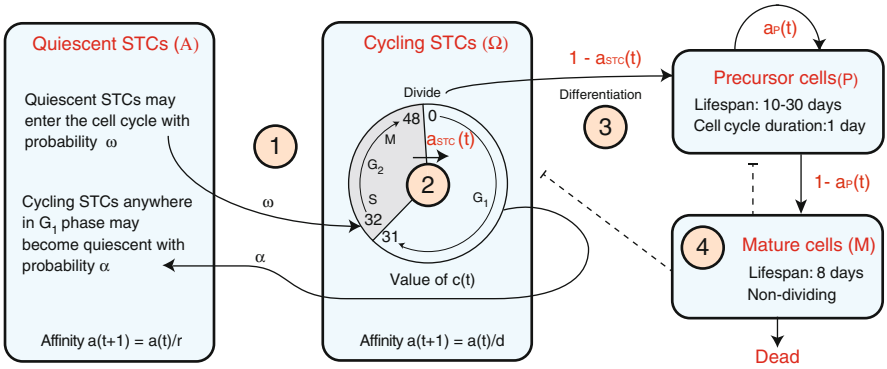

Fig. 2 A diagram of the modified Roeder model. (*1*) Stem cell transitions between quiescence and the cell cycle are unchanged. The affinity variable is updated in the same way as in the original model. (*2*) Cycling stem cells progress through G_1, S, G_2, and M. Stem cells enter the cell cycle at hour $c(t) = 32$. (*3*) At hour $c(t) = 48$, the cell divides, and each daughter cell will remain a stem cell with probability $a_{STC}(t)$ and will differentiate into a precursor with probability $1 - a_{STC}(t)$. Precursor cells symmetrically renew ten times. For all subsequent divisions, up to a total of thirty divisions, the daughter cells will remain precursors with probability $a_P(t)$ and will differentiate into mature cells with probability $1 - a_P(t)$. (*4*) On the last division, both precursor cells differentiate into mature cells. Mature cells provide feedback, marked by *dashed lines*, that affects the renewal fractions $a_{STC}(t)$ and $a_P(t)$ of the stem and precursor cells. After 8 days, mature cells die

In this section we propose several modifications to the Roeder model [24]. Our model is summarized in Fig. 2. First, we consider three types of stem cell division:

1. Asymmetric division, in which one daughter cell remains a stem cell and the other differentiates into a precursor cell
2. Symmetric differentiation, in which both daughter cells differentiate into precursors
3. Symmetric renewal, in which both daughter cells remain stem cells.

In the Roeder model, all dividing stem cells symmetrically renew. Differentiation into precursor cells is not tied to a division event, and stem cells whose affinity reaches a_{min} instantaneously transform into precursor cells. Thus, the affinity variable controls both cell cycle transitions and differentiation.

By incorporating these three types of cell division, each with probability a', b', and c', where $a' + b' + c' = 1$, we provide a mechanism for differentiation that is independent of affinity, while still allowing a cell's affinity to control transitions between quiescence and cycling. Several other modeling groups have represented differentiation in this way, including [19, 28]. Moreover, in [28], it is suggested that cancer stem cells tend to symmetrically renew, while healthy stem cells tend to divide asymmetrically. By associating differentiation with a cell division, it becomes possible to implement this hypothesis in the model.

Secondly, we allow precursor cells to divide a variable number of times before they differentiate into mature cells. To implement this, we allow precursors to go through the same three types of divisions as stem cells. Precursors can divide between 10 and 30 times before differentiating into mature cells. This range is centered around 20 divisions, which is assumed for all precursor cells in [24]. The lower bound to the number of divisions enforces a minimum number of divisions before maturation, and the upper bound prevents any precursor cells from living forever.

Lastly, it is known that hematopoiesis is a very closely regulated process that is affected by many different signals and cytokines [20]. For instance, granulocyte colony-stimulating factor (G-CSF) is known to play a significant role in granulopoiesis [20, 23]. Motivated by [19], we implement feedback inhibition from mature cells that affects less mature cells (precursors and stem cells). Consider a cytokine $S(t)$ that is produced at a constant rate α, degraded at a constant rate d, and is consumed by mature cells at a rate β. Then

$$\frac{dS}{dt} = \alpha - dS - \beta SM, \tag{16}$$

where $M(t)$ is the number of mature cells. Since the cytokine dynamics occur on a faster time scale than cell division, we may assume that the cytokine exists at its quasi-steady state, which when scaled to $s(t) \in [0, 1]$, is

$$s(t) = \frac{1}{1 + kM(t)}, \tag{17}$$

where $s = dS/\alpha$ and $k = \beta/d$. We define the renewal fraction a of the stem cell population as

$$a = \frac{a'}{2} + c'. \tag{18}$$

This quantity represents the probability that a daughter cell of a stem cell will also be a stem cell. In [19], feedback inhibition affects proliferation rates, renewal fractions, or both, in the less mature compartments. It is found that regulation of self-renewal fractions is essential for the system to be able to recover from events such as chemotherapy that deplete the mature blood cell population. Therefore, we choose to focus on feedback inhibition that affects renewal fractions a_{STC} and a_P of stem cells and precursors by defining

$$a_{STC}(t) = \frac{a_{STC,max}}{1 + kM(t)}, \tag{19}$$

$$a_P(t) = \frac{a_{P,max}}{1 + kM(t)}. \tag{20}$$

Here, $a_{STC,max}$ and $a_{P,max}$ define the maximum renewal fractions of the stem cell and precursors, respectively. As $M(t)$ becomes smaller, the renewal fractions of both stem cells and precursors increases, in order to expand both pools, which ultimately leads to an increase in mature cells.

We incorporate these changes into the system of difference equations defined by Eqs. (8), (9), (12), and (13). These changes do not change the form of Eq. (8). Line 2 in Eq. (9) is replaced by

$$\Omega_{k,c}(t+1) = 2a_{STC}(t)\Omega_{k-1,48}(t), \qquad 0 < k < 127,\ c = 0, \tag{21}$$

to incorporate asymmetric division of stem cells. Each of the two daughter cells of the dividing stem cell will remain a stem cell with probability $a_{STC}(t)$. Note that instead of choosing the number of daughter stem cells from a binomial distribution, we use the expected value. All other lines in Eq. (9) are unchanged, for $0 \leq k < 127$. However, when $k = 127$, we must account for the fact that cycling cells with minimum affinity are no longer differentiating into precursors but instead remain stem cells. Thus, when $k = 127$, we replace Eq. (9) with

$$\Omega_{127,c}(t+1) = \begin{cases} 2a_{STC}(t)(\Omega_{126,48}(t) + \Omega_{127,48}(t)), & c = 0, \\ \sum_{k=126}^{127} \Omega_{k,c-1}(t) - \Psi_{k,c-1}(t), & c = 1 \ldots 31, \\ \sum_{k=126}^{127} (\Omega_{k,31}(t) - \Psi_{k,31}(t)) + B_k(t), & c = 32, \\ \Omega_{126,c-1}(t) + \Omega_{127,c-1}(t), & c = 33, \ldots, 48. \end{cases} \tag{22}$$

The precursor cells are described by

$$P_j(t+1) = \begin{cases} 2(1 - a_{STC}(t)) \sum_k \Omega_{k,48}(t), & j = 0, \\ 2P_{j-1}(t), & j = 24, 48, 72, \ldots, 240, \\ 2a_P(t)P_{j-1}(t), & j = 264, 288, 312, \ldots, 696, \\ P_{j-1}(t), & \text{otherwise.} \end{cases} \tag{23}$$

Since the precursors can now live for up to 30 days, $j = 0, \ldots, 719$. Line 1 in Eq. (23) represents new precursor cells. Stem cells differentiate into precursors during cell divisions, each of which produces two daughter cells. Each daughter cell will become a precursor with probability $1 - a_{STC}(t)$. All progenitor cells divide every 24 h. The first 10 divisions are symmetric renewals, which is represented by line 2 in Eq. (23). For each subsequent division, up to a total of 30 divisions, daughter cells will remain precursors with probability $a_P(t)$. For all other times, precursor cells age by 1 h.

The mature cells are described by

$$M_j(t+1) = \begin{cases} 2P_{719}(t) + 2(1 - a_P(t)) \sum_{d=11}^{29} P_{24d-1}(t), & j = 0, \\ M_{j-1}(t), & \text{otherwise.} \end{cases} \tag{24}$$

The only difference from Eq. (13) is when $j = 0$. This line represents the source of mature cells. The first term of line 1 of Eq. (24) represents precursors who are completing their 30th division and must undergo symmetric differentiation. The second term represents the contributions of all precursors who are completing their d^{th} division, where $d = 11, \ldots, 29$. For these divisions, each of the two daughter cells differentiates with probability $1 - a_P(t)$. We use this modified system of difference equations to produce the simulations that are discussed in Sect. 5.

5 Numerical Results

For our simulations, we use the system of difference equations in [12], modified to incorporate the changes discussed in Sect. 4. For all parameters that are present in the original Roeder model, we choose the same values given in [24]. In order to allow the stem cell compartment to grow or shrink, we must set $a_{STC,max} > 0.5$. We choose $a_{STC,max} = 0.52$ and $a_{P,max} = 0.51$. In determining the value of k, we observe that at steady state, the total number of stem cells should be constant. In this model, this occurs when the renewal fraction of the stem cells $a_{STC}(t) = 0.5$. Thus, if we want a steady-state solution with $M(t) = M'$, then we should choose

$$k = \frac{2a_{STC,max} - 1}{M'}. \tag{25}$$

We set $M' = 6.8246(10)^{10}$ cells, which is the mature healthy cell steady-state value in [12] and apply Eq. (25) to determine k.

Using these parameters, numerical simulations of healthy cells produce a shift in the stem cell population toward their cycling state, when compared to the simulations in [12,24]. This shift had to be addressed since it is known that the stem cells tend to be quiescent [2]. In order to restore the quiescent stem cell population, we reduce the function f_ω by a factor of 10, in comparison to the function used in the original Roeder model. In other words, we reduce the probability that a quiescent stem cell will enter the cell cycle. This modification restores the balance of stem cells, with 91 % in quiescence at steady state. The parameters, including this modification of f_ω, are given in Table 1.

In implementing carcinogenesis, as in [24], we introduce a single Ph+ stem cell into the healthy cell population at its steady state. As mentioned previously, in [24], Ph− and Ph+ cells compete at the stem cell level. They differ in their transition functions f_ω and f_α. We decrease f_ω for both populations by a factor of 10, in order to maintain the same relative difference between these functions for the Ph− and Ph+ cells. We additionally assume that Ph− and Ph+ stem cells compete for cytokine, which is consumed by the mature cells of both populations. We choose a smaller value of k for the Ph+ population, which represents cancer's decreased sensitivity to environmental signals. Specifically, we set $k_{cancer} = k_{healthy}/2$.

Table 1 Parameters for the simulations in Sect. 5

Parameter	Description	Ph−	Ph+/R, Ph+/I
a_{min}	Minimum value of affinity a	0.002	0.002
a_{max}	Maximum value of affinity a	1.0	1.0
ρ	Affinity factor	0.0488	0.0488
d	Differentiation coefficient	e^{ρ}	e^{ρ}
r	Regeneration coefficient	$e^{2\rho}$	$e^{2\rho}$
τ_c	Cell cycle duration	49 h	49 h
τ_S	Duration of S phase	8 h	8 h
$\tau_{G_2/M}$	Duration of G_2 and M phases	8 h	8 h
λ_p	Lifespan of proliferating precursor cells	10–30 days	10–30 days
λ_m	Lifespan of mature cells	8 days	8 days
$\tilde{\tau}_c$	Cell cycle of proliferating precursors	24 h	24 h
$f_\alpha(0)$	Transition characteristic for f_α	0.5	1.0
$f_\alpha(N_\alpha/2)$	Transition characteristic for f_α	0.45	0.9
$f_\alpha(N_\alpha)$	Transition characteristic for f_α	0.05	0.058
$f_\alpha(\infty)$	Transition characteristic for f_α	0.0	0.0
N_α	Scaling factor	10^5	10^5
$f_\omega(0)$	Transition characteristic for f_ω	0.05	0.1, 0.00500
$f_\omega(N_\omega/2)$	Transition characteristic for f_ω	0.03	0.099, 0.00499
$f_\omega(N_\omega)$	Transition characteristic for f_ω	0.01	0.098, 0.00498
$f_\omega(\infty)$	Transition characteristic for f_ω	0.0	0.096, 0.00496
N_ω	Scaling factor	10^5	10^5
$a_{STC,max}$	The maximum renewal fraction of stem cells	0.52	0.52
$a_{P,max}$	The maximum renewal fraction of precursors	0.51	0.51
M'	The steady-state number of mature cells	$6.8246(10)^{10}$	$1.36492(10)^{11}$

We replace the constant lifespan $\lambda_p = 20$ days of precursors with a range of 10–30 days. Additionally, all parameters related to f_ω are decreased by a factor of 10 compared with the values in [12], to restore the population of quiescent stem cells. For all other parameters included in the original Roeder model, we choose the same values given in [12]. The last three parameters arise because of our modifications to the model. The parameter M' is used in Eq. (25) to determine the value of k

Figure 3 shows a simulation of cancer genesis for the parameter values described above. The simulation shows a long latency time during which Ph− (solid) and Ph+ (dashed) cells coexist. The Ph+ population becomes greater than the Ph− population between years 5 and 6. These simulations show similar behavior to the simulations of cancer genesis in [12, 24].

A simulation of a treatment is shown in Fig. 4. The initial conditions are taken from the end of the cancer simulation in Fig. 3. The number of quiescent stem cells, number of mature cells, and BCR-ABL ratio are displayed as functions of time. In comparison with results from [12, 24], we observe a much slower decline in the BCR-ABL ratio and the number of cancer cells during treatment. This difference can be understood by considering the Ph+ stem cells. First, recall that quiescent

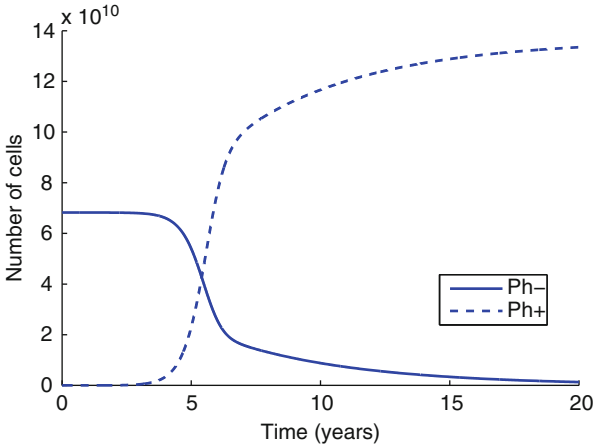

Fig. 3 A simulation of cancer genesis. The *solid line* represents mature Ph− cells, and the *dashed line* represents mature Ph+ cells

Ph+ stem cells are assumed to be unaffected by IM. These cells are only affected by IM if they enter the cell cycle. Thus, a decrease in the transition rate of stem cells from quiescence to cycling results in quiescent Ph+ stem cells that will remain quiescent for longer periods of time, during which they will remain protected from IM. Figure 4a illustrates this phenomenon, as the number of quiescent Ph+ stem cells decreases by less than one order and remains above 10^4, after 20 years of treatment. As a result, the number of mature Ph+ cells, shown in Fig. 4b, remains above 10^7. The BCR-ABL ratio, shown in Fig. 4c, decreases by about 3.5 orders. The simulated patient achieves a MMR, or a 3-log decrease in BCR-ABL ratio, at year 4. However, MMR^4 (a 4-log decrease in BCR-ABL ratio) and MMR^5 (a 5-log decrease) are not achieved.

We consider varying the two treatment parameters, r_{deg} and r_{inh}, in order to simulate patients that achieve MMR^4 and MMR^5. We find that increasing r_{deg}, the rate at which IM kills cycling Ph+ stem cells, results in an increase in the rate at which cancer is cleared, as illustrated in Fig. 5. By increasing r_{deg}, our simulated patient achieves MMR^4 ($r_{deg} = 0.066\,\text{h}^{-1}$) and MMR^5 ($r_{deg} = 0.132\,\text{h}^{-1}$).

On the other hand, r_{inh} has a non-monotonic relationship with the rate of cancer clearance. The parameter r_{inh} describes the rate at which cycling Ph+ stem cells become IM-affected, meaning they become less likely to enter the cell cycle. Decreasing the transitions of quiescent Ph+ stem cells to cycling has two contrasting effects. On one hand, Ph+ stem cells are prevented from cycling, limiting the number of mature Ph+ cells. On the other hand, these quiescent Ph+ stem cells cannot be eliminated from the stem cell population, as IM does not kill non-cycling Ph+ stem cells.

For large r_{inh}, the Ph+ population rapidly shifts toward these decreased transition rates. As a result, initially the simulations show a sharper decline in mature Ph+

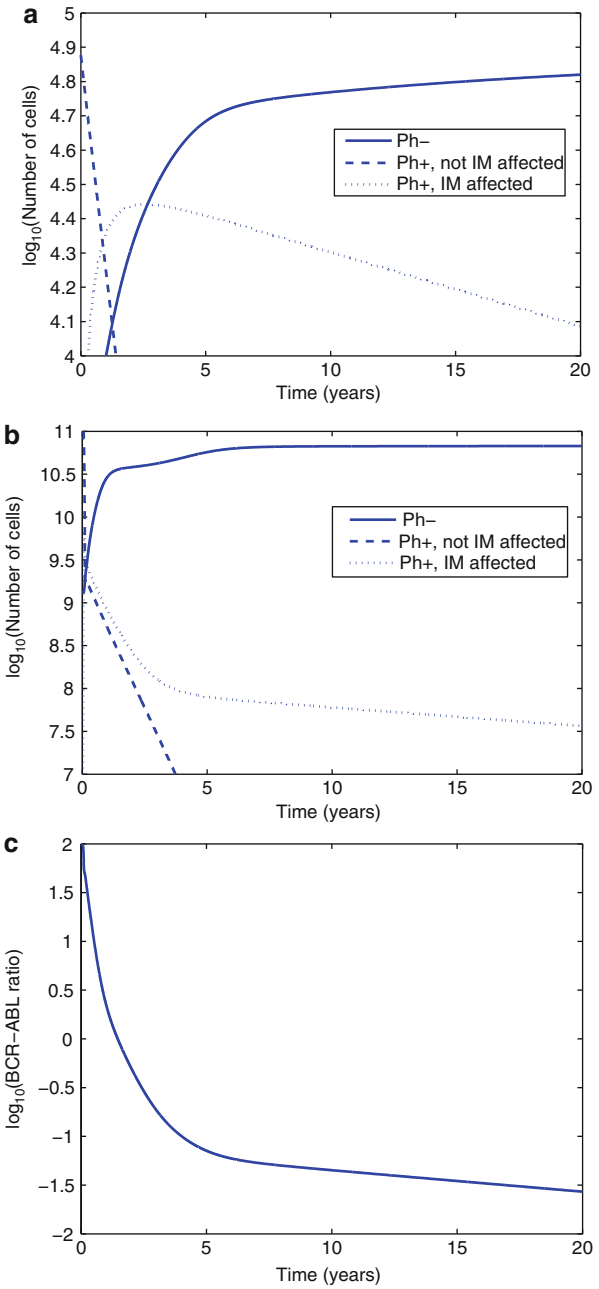

Fig. 4 A simulation of treatment. (**a**) Quiescent stem cells. (**b**) Mature cells. (**c**) BCR-ABL ratio. In (**a**, **b**), Ph− cells are represented by a *solid line*, Ph+ cells that are not affected by IM are represented by a *dashed line*, and Ph+ cells that are affected by IM are represented by a *dotted line*

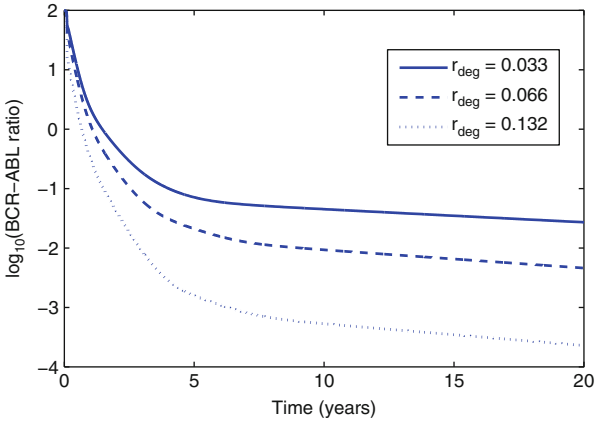

Fig. 5 BCR-ABL ratio is plotted during treatment, for three different values of r_{deg}: 0.033 h^{-1} (*solid*), 0.066 h^{-1} (*dashed*), and 0.132 h^{-1} (*dotted*). As r_{deg} increases, the BCR-ABL ratio declines more rapidly. For all three simulations, $r_{inh} = 0.05\ h^{-1}$

cells, compared to simulations with smaller r_{inh} values. However, Ph+ stem cells with IM-affected transition rates remain quiescent for longer periods of time and are protected from the degradation effect of IM. Eventually, the number of mature Ph+ cells for r_{inh} large becomes greater than the number of mature Ph+ cells for r_{inh} smaller. Figure 6b shows the effects of treatment on mature Ph+ cells over time, for different values of r_{inh}.

Figure 6a shows the number of quiescent Ph+ stem cells over time for different values of r_{inh}. Here, the relationship is more straightforward. As r_{inh} increases, Ph+ stem cells become IM-affected more rapidly, and as a result, the number of quiescent Ph+ stem cells increases.

Conclusion

In this chapter we modify the Roeder model [24] by adding more biological detail. Specifically, we incorporate asymmetric division of stem cells and precursors, allow precursors to live for a variable amount of time before maturing, and add feedback inhibition from mature cells that affects stem cells and precursors. A more accurate representation of hematopoiesis can lead to more realistic simulations of CML genesis and treatment.

Parametrization of our model suggests that healthy stem cells transition between the quiescent and proliferating compartments at rates that are lower than the rates obtained in the original Roeder model. In the Roeder model, at healthy steady state, approximately 1 quiescent stem cell enters the cell cycle per 1,000 quiescent stem cells per time step. Thus, quiescent cells enter the

(continued)

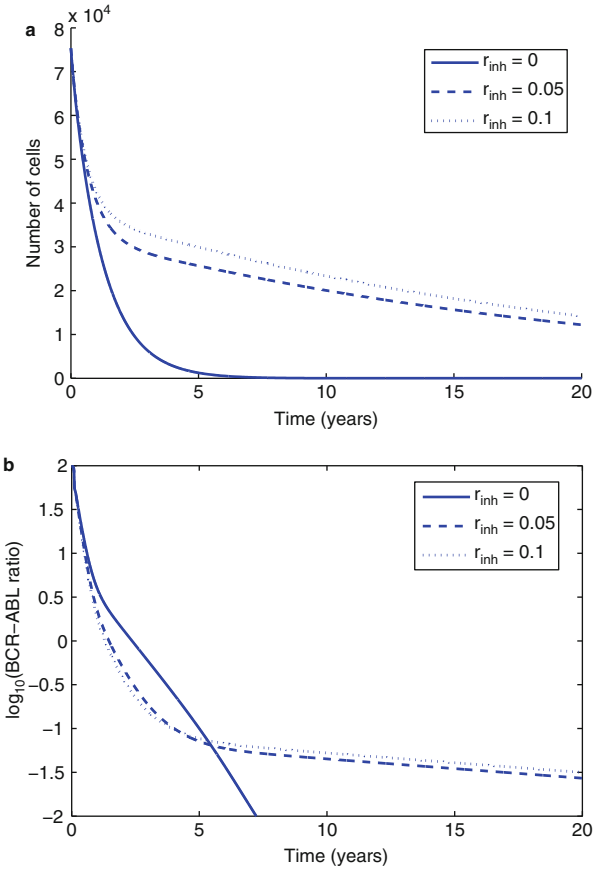

Fig. 6 Number of quiescent Ph+ stem cells and BCR-ABL ratio during treatment, for three different values of r_{inh}: 0 h^{-1} (*solid*), 0.05 h^{-1} (*dashed*), 0.1 h^{-1} (*dotted*). (**a**) Quiescent Ph+ stem cells. (**b**) BCR-ABL ratio. Initially, a higher value of r_{inh} leads to faster cancer clearance, but later the lower values of r_{inh} become more favorable. For all three simulations, $r_{deg} = 0.033$ h^{-1}

cell cycle, on average, once per 1.4 months. In contrast, in our simulations, 1 quiescent stem cell enters the cell cycle per 10,000 cells, which translates to quiescent cells entering the cell cycle, on average, once every 14 months. This lower rate of entry into the cell cycle by stem cells is supported by [17, 26].

Lower stem cell transition rates have a significant effect on the results of IM therapy. In our model, we assume that IM only affects cycling Ph+ cells. By decreasing the transition rates of Ph+ stem cells, quiescent Ph+ stem cells can never mind evade the effects of IM during treatment. During 20 years of

(continued)

simulated treatment, we see an initial phase of a few months when IM kills most cycling Ph+ stem cells. Once the cycling Ph+ population is depleted, the majority of the remaining Ph+ stem cell population is quiescent and is therefore protected from IM. What follows is a very slow decline in the number of quiescent Ph+ cells over time, since only a few of these cells enter the cell cycle every hour. Our treatment simulations indicate a much larger residual cancer population than those in [24]. These results suggest that IM alone, acting through the implemented mechanisms, can never fully eradicate the cancer population.

The Stop Imatinib trial [18] sought to determine whether patients who responded well to IM therapy could be safely taken off treatment without relapsing. They found that while 61 % of patients relapsed, 39 % remained in remission for the duration of the 2-year study. It is possible that some of the patients in sustained remission had no Ph+ cells remaining when they stopped IM. If this is the case, it may imply that there is an additional action of IM that is not included in the model. Alternatively, patients that remain in sustained remission after stopping IM may still harbor small populations of Ph+ cells. Remaining in remission after stopping IM would then require some other mechanism (e.g., the immune response) to control the Ph+ population and prevent it from expanding.

Still, the fact that many patients do relapse after being taken off IM motivates studying methods by which IM therapy can be improved. Our results suggest that IM therapy may greatly benefit from quiescent Ph+ stem cell activation. IFN-α has been shown to activate quiescent stem cells [6] and is therefore a strong candidate for combination therapy. A detailed analysis of immunotherapy in this context is left for a future study.

Acknowledgements The work of GC was supported by the National Science Foundation Graduate Research Fellowship under Grant No. DGE1322106. The work of DL was supported in part by the John Simon Guggenheim Memorial Foundation and by the joint National Science Foundation/National Institute of General Medical Sciences program under Grant No. DMS-0758374. Any opinions, findings, and conclusions or recommendations expressed in this material are those of the authors and do not necessarily reflect the views of the National Science Foundation, the National Cancer Institute, or the National Institutes of Health.

References

1. An, X., Tiwari, A., Sun, Y., Ding, P., Ashby Jr., C., Chen, Z.: BCR-ABL tyrosine kinase inhibitors in the treatment of Philadelphia chromosome positive chronic myeloid leukemia: a review. Leuk. Res. **34**, 1255–1268 (2010)
2. Arai, F., Hirao, A., Ohmura, M., Sato, H., Matsuoka, S., Takubo, K., Ito, K., Koh, G., Suda, T.: Tie_2/Angiopoietin-1 signaling regulates hematopoietic stem cell quiescence in the bone marrow niche. Cell **118**, 149–161 (2004)

3. Colijn, C., Mackey, M.: A mathematical model of hematopoiesis—I. Periodic chronic myelogenous leukemia. J. Theor. Biol. **237**, 117–132 (2005)
4. Cortes, J., Talpaz, M., O'Brien, S., Jones, D., Luthra, R., Shan, J., Giles, F., Faderl, S., Verstovsek, S., Garcia-Manero, G., Rios, M.B., Kantarjian, H.: Molecular responses in patients with chronic myelogenous leukemia in chronic phase treated with imatinib mesylate. Clin. Cancer Res. **11**, 3425–3432 (2005)
5. Doumic-Jauffret, M., Kim, P., Perthame, B.: Stability analysis of simplified yet complete model for chronic myelogenous leukemia. Bull. Math. Biol. **72**, 1732–1759 (2010)
6. Essers, M., Offner, S., Blanco-Bose, W., Waibler, Z., Kalinke, U., Duchosal, M., Trumpp, A.: IFNα activates dormant haematopoietic stem cells in vivo. Nature **458**, 904–909 (2009)
7. Glauche, I., Horn, K., Horn, M., Thielecke, L., Essers, M., Trumpp, A., Roeder, I.: Therapy of chronic myeloid leukemia can benefit from the activation of stem cells: simulation studies of different treatment combinations. Br. J. Cancer **106**(11), 1742–1752 (2012)
8. Horn, M., Glauche, I., Muller, M., Hehlmann, R., Hochhaus, A., Loeffler, M., Roeder, I.: Model-based decision rules reduce the risk of molecular relapse after cessation of tyrosine kinase inhibitor therapy in chronic myeloid leukemia. Blood **121**, 378–384 (2013)
9. Hughes, T., Kaeda, J., Branford, S., Rudzki, Z., Hochhaus, A., Hensley, M., Gathmann, I., Bolton, A., van Hoomissen, I., Goldman, J., Radich, J.: International randomised study of interferon versus STI571 (IRIS) Study Group. Frequency of major molecular responses to imatinib or interferon alfa plus cytarabine in newly diagnosed chronic myeloid leukemia. N. Engl. J. Med. **349**(15), 1423–1432 (2003)
10. Kim, P., Lee, P., Levy, D.: Dynamics and potential impact of the immune response to chronic myelogenous leukemia. PLoS Comput. Biol. **4**(6), e1000095 (2008)
11. Kim, P., Lee, P., Levy, D.: A PDE model for imatinib-treated chronic myelogenous leukemia. Bull. Math. Biol. **70**, 1994–2016 (2008)
12. Kim, P., Lee, P., Levy, D.: Modeling imatinib-treated chronic myelogenous leukemia: reducing the complexity of agent-based models. Bull. Math. Biol. **70**, 728–744 (2008)
13. Komarova, N., Katouli, A., Wodarz, D.: Combination of two but no three current targeted drugs can improve therapy of chronic myeloid leukemia. PLoS One **4**(2), e4423 (2009)
14. Komarova, N., Wodarz, D.: Drug resistance in cancer: Principles of emergence and prevention. PNAS **102**(27), 9714–9719 (2005)
15. Leder, K., Foo, J., Skaggs, B., Gorre, M., Sawyers, C., Michor, F.: Fitness conferred by BCR-ABL kinase domain mutations determines the risk of pre-existing resistance in chronic myeloid leukemia. PLoS One **6**(11), e27682 (2011)
16. Lee, S.J.: Chronic myelogenous leukaemia. Br. J. Haematol. **111**, 993–1009 (2000)
17. Mahmud, N., Devine, S., Weller, K., Parmar, S., Sturgeon, C., Nelson, M., Hewett, T., Hoffman, R.: The relative quiescence of hematopoietic stem cells in nonhuman primates. Blood **97**, 3061–3068 (2001)
18. Mahon, F.X., Rea, D., Guilhot, J., Guilhot, F., Huguet, F., Nicolini, F., Legros, L., Charbonnier, A., Guerci, A., Varet, B., Etienne, G., Reiffers, J., Rousselot, P.: Discontinuation of imatinib in patients with chronic myeloid leukaemia who have maintained complete molecular remission for at least 2 years: the prospective, multicentre Stop Imatinib (STIM) trial. Lancet. Oncol. **11**, 1029–1035 (2010)
19. Marciniak-Czochra, A., Stiehl, T., Ho, A., Jager, W., Wagner, W.: Modeling of asymmetric cell division in hematopoietic stem cells: regulation of self renewal is essential for efficient repopulation. Stem Cells Dev. **18**, 377–385 (2009)
20. Metcalf, D.: Hematopoietic cytokines. Blood **111**(2), 485–491 (2008)
21. Michor, F., Hughes, T., Iwasa, Y., Branford, S., Neil, P., Sawyers, C., Nowak, M.: Dynamics of chronic myeloid leukemia. Nature **435**(7046), 1267–1270 (2005)
22. Moore, H. and N. Li: A mathematical model for chronic myelogenous leukemia (CML) and T cell interaction. J. Theoret. Biol. **227**, 513–523 (2004)
23. Price, T., Chatta, G., Dale, D.: Effect of recombinant granulocyte colony-stimulating factor on neutrophil kinetics in normal young and elderly humans. Blood **88**(1) 335–340 (1996)

24. Roeder, I., Horn, M., Glauche, I., Hochhaus, A., Mueller, M., Loeffler, M.: Dynamic modeling of imatinib-treated chronic myeloid leukemia: functional insights and clinical implications. Nat. Med. **12**(10) 1181–1184 (2006)
25. Roeder, I., Herberg, M., Horn, M.: An age-structured model of hematopoietic stem cell organization with application to chronic myeloid leukemia. Bull. Math. Biol. **71**, 602–626 (2009)
26. Rufer, N., Brummendorf, T., Kolvraa, S., Bischoff, C., Christensen, K., Wadsworth, L., Schulzer, M.: Telomere fluorescence measurements in granulocytes and T lymphocyte subsets point to a high turnover of hematopoietic stem cells and memory T cells in early childhood. J. Exp. Med. **190**(2), 157–167 (1999)
27. Stiehl, T., Marciniak-Czochra, A.: Mathematical modeling of leukemogenesis and cancer stem cell dynamics. Math. Model. Nat. Phenom. **7**(1), 166–202 (2012)
28. Tomasetti, C., Levy, D.: Role of symmetric and asymmetric division of stem cells in developing drug resistance. PNAS **107**(39), 16766–16771 (2010)

A Cellular Automata and a Partial Differential Equation Model of Tumor–Immune Dynamics and Chemotaxis

Andrea K. Cooper and Peter S. Kim

Abstract Immunotherapy is a newly emerging approach to cancer treatment that seeks to stimulate a body's immune defenses, especially T cells, to combat and potentially eliminate tumors. Relevant tumor–immune interactions depend on stochasticity, since the dynamics involve a small and decreasing number of cells, and spatiotemporal heterogeneity, since the dynamics occur in a localized tumor environment. To account for these two aspects of the system, we develop mathematical models of an anti-tumor immune response using a cellular automaton and a system of partial differential equations. We explicitly model immune cell recruitment to the tumor via cytokine secretion and chemotaxis of immune cells. Our models exhibit three types of behavior: tumor elimination, oscillation, and uncontrolled tumor growth that depend substantially on the strength of immune cell chemotaxis, or recruitment, to the tumor site.

1 Introduction

The early stages of tumor growth are important to understand in medicine. It is the time when the tumor is most vulnerable, but also the least likely to be detected. A modern approach to combat tumor development is cancer vaccination [42]. Vaccination takes advantage of the immune system's natural capacity to fight pathogens and is seen as an effective means of controlling infectious diseases. Now, researchers are attempting to use a similar technique in the treatment of cancer, and experimental evidence has repeatedly shown that the immune system is capable of selectively targeting tumor cells [21, 52, 53, 56]. However, the dynamics of the anti-tumor immune response remain poorly understood making it difficult to translate these results into effective clinical treatments [17, 49].

By developing mathematical and computational models, we can gain a better understanding of the dynamics of the system and help us determine which

A.K. Cooper • P.S. Kim (✉)
School of Mathematics and Statistics, University of Sydney, Camperdown, NSW 2006, Australia
e-mail: acoo9460@uni.sydney.edu.au; pkim@maths.usyd.edu.au

A. Eladdadi et al. (eds.), *Mathematical Models of Tumor-Immune System Dynamics*, Springer Proceedings in Mathematics & Statistics 107,
DOI 10.1007/978-1-4939-1793-8_2

parameters most strongly influence the success or failure of an anti-tumor immune response. In this study, we are most interested in cytotoxic T lymphocytes, or effector T cells, since these are the immune agents that are most commonly stimulated by cancer vaccines and other immunotherapies [42]. Effector T cells interact with cells via a T cell receptor that binds to specific protein sequences, called antigens, and when an effector T cell interacts strongly enough, it kills the target cell [22]. Effector T cells that react to unique and specific antigens on tumor cells are called tumor-specific or anti-tumor effector T cells.

A variety of mathematical models have applied a range of modeling approaches to study tumor–immune interactions. Tumor–immune models have been formulated using ordinary differential equations (ODE) [1, 8, 23, 27, 29–32, 38, 40, 47], delay differential equations (DDE) [3, 4, 6, 11, 12, 26, 45, 55], partial differential equations (PDE) [14, 35, 36], impulsive differential equations [5], and fractional differential equations [15]. A recent review of tumor immune models using ODE systems can be found in [13]. Other papers develop agent-based models (ABM), cellular automata (CA), and hybrid formulations [25, 34, 46, 48].

In this chapter, we focus particularly on the hybrid CA-PDE model in Mallet and De Pillis [34] and the hybrid ABM-DDE model of Kim and Lee [25]. Inspired by these models, we formulate a simplified CA to model tumor cell and effector T cell interactions. Extending these two models, we add a chemoattractant population and incorporate the chemotaxis of effector cells up the gradient. During an immune response, effector cells recruit other effectors to the target site by secreting several immunostimulatory cytokines, such as IL-2 and IL-15, and chemokines, such as MIP-1α [7, 33, 37, 61]. Experiments have also demonstrated that the same type of effector recruitment occurs during an effector response against a tumor [52, 53].

Neither [34] or [25] explicitly model effector recruitment via chemotaxis, both opting for a simplified, phenomenological approach. An important extension to these two models is to incorporate effector recruitment by chemotaxis, so that we can understand if chemotactic recruitment influences the effectiveness of an anti-tumor immune response. In this chapter, we discuss how we can develop a CA model and derive an analogous PDE model of tumor–effector interactions with chemotaxis.

The chapter is organized as follows: In Sect. 2, we present a probabilistic CA, in which tumor and effector cell motion and interactions are modeled probabilistically, while cytokine diffusion is modeled deterministically, and we show numerical simulations of the CA and discuss how chemotaxis influences the success or failure of the anti-tumor immune response. In Sect. 3, we show how to derive an analogous PDE model as a mean field approximation of the probabilistic CA, and we show numerical simulations of the PDE model and compare them to simulations of the CA. In Sect. 4, we discuss similarities and differences between the CA and PDE approaches and suggest possible directions for future work.

2 Individual Cell-Based Model

In this section, we develop a probabilistic CA model of tumor–immune interactions. For simplicity, we model the tumor–effector system on a two-dimensional plane as in [34], although it is straightforward to extend the system to three-dimensions as in [25]. As in [34], we consider a square domain $[-L, L] \times [-L, L]$, partitioned into square elements of width and height Δx.

We consider four populations: (1) tumor cells, (2) effector cells, (3) tumor–effector complexes, and (4) cytokines. At each time step of length Δt, these populations are updated according to probabilistic and deterministic rules described below.

Tumor Cells At each time step, each tumor cell attempts to divide with probability $1 - e^{-\Delta t/\tau_{\text{div}}}$, where τ_{div} is the average time between tumor cell divisions. When a tumor cell attempts to divide, it randomly chooses one of the four squares (up, down, left, or right) adjacent to its position with equal probability 1/4. If that square does not already contain a tumor cell or a tumor–effector complex, a new tumor cell is placed there, representing a newly divided tumor cell. If a new tumor cell is placed in a square only occupied by an effector cell, they form a tumor–effector complex. We ignore any newly divided tumor cells that get placed outside the domain $[-L, L] \times [-L, L]$.

Effector Cells Effector cells migrate according to a random walk. At each time step of duration Δt, each effector cell tries to move one step of length Δx to one of the four adjacent squares, up, down, left, and right, with probabilities p_{up}, p_{down}, p_{left}, and p_{right}, respectively. The probabilities are functions of the cytokine concentrations at the effector's location and four adjacent squares.

We devise our chemotaxis model using a weighted random walk. An effector at point (x, y) chooses to try to move one step up, down, left, or right with relative weightings

$$\begin{aligned} w_{\text{up}} &= 1 + \lambda C(x, y + \Delta x, t) \,, \\ w_{\text{down}} &= 1 + \lambda C(x, y - \Delta x, t) \,, \\ w_{\text{left}} &= 1 + \lambda C(x - \Delta x, y, t) \,, \\ w_{\text{right}} &= 1 + \lambda C(x + \Delta x, y, t) \,, \end{aligned} \tag{1}$$

for some nonnegative constant λ. See Fig. 1a.

As we see in (1), the relative weighting in each direction grows linearly with respect to the cytokine concentration in the corresponding square. The probabilities of moving in each direction are given by

$$p_{\text{up}} = \frac{w_{\text{up}}}{w_{\text{total}}}, \qquad p_{\text{down}} = \frac{w_{\text{down}}}{w_{\text{total}}}, \qquad p_{\text{left}} = \frac{w_{\text{left}}}{w_{\text{total}}}, \qquad p_{\text{right}} = \frac{w_{\text{right}}}{w_{\text{total}}},$$

where $w_{\text{total}} = w_{\text{up}} + w_{\text{down}} + w_{\text{left}} + w_{\text{right}}$.

If an effector tries to move into a square already containing an effector cell or tumor–effector complex, it does not move, but stays still. On the other hand, if an effector cell tries to move into a square occupied by a tumor cell, it moves and the tumor and effector cells form a tumor–effector complex. See Fig. 1b,c.

We assume that effector cells exist at a constant average concentration E_0 (in terms of cells per area) outside the domain of the model. We calculate the probability that a single effector migrates into the domain during one time step in the following manner. Consider the rim of adjacent squares shown in Fig. 2 just beyond the domain. The total area of the rim is $4(2L\Delta x)$, so the expected number of effectors on the rim at any given time is $8E_0L\Delta x$. If we assume that the presence of effectors in the rim is governed by a Poisson process, the probability that there is at least one effector on the rim at the start of a time step is $1 - e^{-8E_0L\Delta x}$. (For simplicity, let us assume that $8E_0L\Delta x \ll 1$ and make the approximation that at most one effector is on the rim at any time.)

If an effector is on the rim, we assume it is not affected by the cytokine gradient in the domain, so it has an equal probability of 1/4 of moving in any direction, including into the domain. If an effector tries to enter the domain during the next time step, we randomly choose the entry location among the internal squares along the edge of the domain. All edge squares are chosen with equal probability, except corner squares, which are counted twice, since they can be entered from two directions. If an effector tries to enter a square that is already occupied by an effector or tumor–effector complex, it is blocked and does not enter.

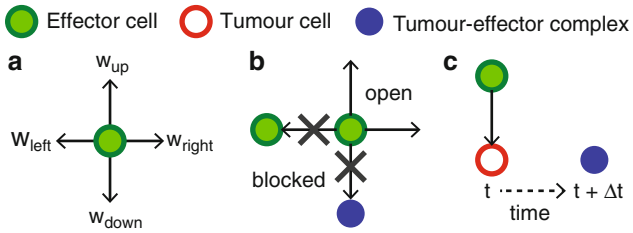

Fig. 1 Diagrams of rules of effector motion. (**a**) At each time step, an effector tries to move one step up, down, left, or right with relative weightings w_{up}, w_{down}, w_{left}, and w_{right} that depend on the cytokine concentrations in adjacent squares. (**b**) Effector cell motion is blocked if the space is occupied by an effector or tumor–effector complex. (**c**) If an effector tries to enter a space occupied by a tumor cell, the two cells form a tumor–effector complex

At each time step, effectors die with probability $1 - e^{-\Delta t/\tau_{\text{death}}}$, where τ_{death} is the average lifespan of effectors. As with tumor cells, if an effector migrates outside the domain $[-L, L] \times [-L, L]$, we eliminate it from the system.

Tumor–Effector Complexes Tumor–effector complexes form when tumor and effector cells end up in the same square. These complexes represent effectors engaging tumor cells. At each time step, we assume that the tumor cell in a complex dies with probability $1 - e^{-\Delta t/\tau_{\text{kill}}}$, where τ_{kill} is the average time for an effector to kill a tumor cell. In this case, the complex is replaced by only the effector.

Effectors in complexes can still die with probability $1 - e^{-\Delta t/\tau_{\text{death}}}$ at each time step. In this case, the complex is replaced by only the tumor cell. It is possible that both cells in a complex could die during the same time step, in which case the square is left empty.

Cytokine We assume that cytokine attracts effectors through chemotaxis and is secreted by effectors that are engaging tumor cells as tumor–effector complexes. This formulation is similar to the one in [34], which assumes that effectors interacting with tumor cells can induce, or recruit, other effectors into the region. Since our cytokines represent a huge number of molecules, we model the cytokine level in each square deterministically and continuously, rather than as a probabilistic collection of individual particles. The cytokine level at each square can be any nonnegative real number.

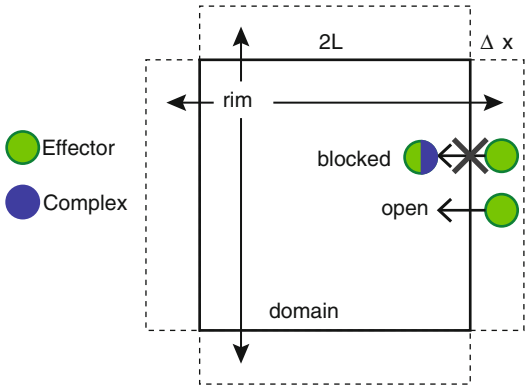

Fig. 2 Effector immigration into the domain. At each time step, an effector tries to enter the domain with probability $\frac{1}{4}(1 - e^{-8E_0 L\Delta x})$. An entering effector has an equal chance of entering from any of the squares on the rim outside the domain. An effector cannot enter a square already occupied by an effector or tumor–effector complex

We assume cytokine levels decay exponentially at rate $1/\tau_{\text{ck}}$, are secreted by each tumor–effector complex at a constant rate σ, and diffuse with coefficient D_C. We estimate that cytokines diffuse approximately 20 times as fast as effectors [20], and we model cytokine diffusion deterministically, rather than as a random walk. Since the time scale of cytokine diffusion is much faster than other dynamics in the system, we assume that cytokine levels exist at quasi-steady state with respect to the locations of the tumor–effector complexes.

To calculate the quasi-steady state, we suppose a tumor–effector complex secretes cytokine as a point source centered at (x_0, y_0). Then, using the fundamental solution of the diffusion equation [16], the steady-state cytokine level at (x, y) is given by

$$C(x,y) = \sigma \int_0^\infty \frac{1}{4\pi D_C t} \exp\left(-\frac{t}{\tau_{ck}}\right) \exp\left(-\frac{(x-x_0)^2 + (y-y_0)^2}{4D_C t}\right) dt \ . \quad (2)$$

We say that the cytokine level in a square of the CA grid is given by the expression $C(x, y)$ at the center of the square, so if a complex occupies a square centered at $(i\Delta x, j\Delta y)$, then the cytokine level at a square centered at $(k\Delta x, l\Delta y)$ is given by (2) for $x_0 = i\Delta x$, $y_0 = j\Delta x$, $x = k\Delta x$, and $y = l\Delta x$.

At every time step, we determine the quasi-steady state cytokine distribution of the entire system by determining the locations $(i_n\Delta x, j_n\Delta x)$ for $n = 1, \ldots, N_X$ of all N_X complexes. Then, we evaluate (2) for each complex and sum the results to obtain the overall cytokine level in the CA.

Initial Conditions To initialize the simulation, we begin with one tumor cell at the center of the domain at $(0, 0)$ and iterate the system over several tumor cell divisions to obtain a starting tumor mass of between 150 and 250 cells around the center of the domain. As in [25, 34], we assume that the surrounding tissue plays a passive role, so we do not explicitly model it. All other populations begin at 0.

2.1 Parameter Estimates

We draw many of our parameter estimates from [25], which obtains its estimates from a variety of sources. Parameters, descriptions, and estimates are shown in Table 1.

Table 1 Parameters used in simulations of the cellular automaton

Parameter	Description	Estimate
Δt	Time step	1 min
Δx	Space step	12 μm
L	Half width of domain	606 μm
τ_{div}	Avg. time for tumor cell division	7 days = 10,080 min
τ_{death}	Avg. effector lifespan	2.5 day = 3,600 min
τ_{kill}	Avg. time for effector to kill tumor cell	1 day = 1,440 min
τ_{ck}	Avg. cytokine lifespan	1/2 day = 720 min
λ	Chemotaxis parameter in (1)	0, 60, or 120
σ	Secretion rate of cytokine by complexes	1/cell/min
E_0	Surrounding concentration of effectors	1×10^{-6} cells/μm^2

Based on experimental results of Friedl and Gunzer and an estimate from Catron et al. we estimate that effectors migrate at velocity 12 μm/min [9, 18], so for our time step, we set $\Delta t = 1$ min, and for the space step, we set $\Delta x = 12$ μm. This space step is convenient, because it is also approximately the diameter of a single cell [2, 9, 32, 34]. We assume that the domain of the CA is a grid with 101 squares on each side, so that the center square is located at $(0, 0)$. This means that the halfwidth of the grid is $L = 101\Delta x/2 = 606$ μm.

For consistency, we draw all of our experimental estimates of tumor growth rates from breast cancer data. Various experimental studies estimate tumor doubling times of approximately 1 month to a decade [28, 39, 54, 59]. Some mathematical models consider the possibility of aggressive early-stage tumors with division times of less than 10 days [27, 34]. In this chapter, we also model a fast-growing tumor with an average division time of $\tau_{\text{div}} = 7$ days as in [25]. This rate gives simulations that produce varied behavior more quickly.

During immune contraction, experiments have measured an effector halflife of 41 h [10], which corresponds to an average lifespan of $\tau_{\text{death}} = 41/\log(2)$ h $= 2.5$ days. We do not have clear estimates of the average times for effector killing of tumor cells, but experimental studies show that anti-tumor effectors can sometimes rapidly kill target cells and even kill multiple target cells simultaneously [60]. However, since the action of killing a target cell may require a long recovery period between consecutive killings, we use the conservative estimate of $\tau_{\text{kill}} = 1$ day, or an average of one per cell per day, as used in [25].

We do not have good estimates of cytokine decay rates, but we assume these molecules decay faster than the death rate of effector cells, so we estimate $\tau_{\text{ck}} = 1/2$ day. We also do not have good estimates of cytokine secretion rate, σ, by effector cells, but we observe that this parameter scales inversely with respect to λ. Indeed, if we multiply σ by a factor f, then we end up scaling the cytokine population, C, by a factor f, so if we scale λ by a factor $1/f$, the effectors act exactly the same. So, we only vary λ and keep σ fixed at 1 unit of cytokine per cell per minute. Based on experimentation, we choose the values 0, 60, and 120 for the chemotaxis parameter λ, because these values produce the three main dynamic behaviors of the system: uncontrolled tumor growth, oscillation, and rapid tumor elimination.

Since we are dealing with a two-dimensional CA, it is difficult to directly translate immune cell concentrations in units of cells per volume as used in [25] to units of cells per area. For our simulations, we choose an effector concentration of $E_0 = 1 \times 10^{-6}$ cells/μm^2, or 1 cell/mm^2.

2.2 *Simulations of the Cellular Automata Model*

We used Matlab R2011b to code and simulate the CA described in Sect. 2. Results of an example simulation are shown in Fig. 3. In this example, we use the parameters in Table 1 with chemotaxis parameter $\lambda = 120$.

Figure 3 shows the distribution of cells and cytokine levels for one simulation of the CA at time $t = 10$ days. There are 155 tumor cells, 5 effectors, and 15 tumor–effector complexes. The complexes secrete cytokine, causing a higher cytokine level in the vicinity of the tumor mass. Diffusion of cytokine produces a gradient that attracts circulating effectors towards the cluster of complexes surrounding the tumor mass.

Since the model is probabilistic, we run ten simulations to explore a range of probable behaviors. Effector cells eliminate the tumor population in all simulations. Figure 4 shows time evolutions of the fastest and slowest times to tumor elimination.

In Fig. 4a, effector cells find the tumor mass quickly, form tumor–effector complexes, and begin secreting cytokine, which attracts additional effectors, leading to rapid tumor elimination on day 31. The main difference in Fig. 4b is that effectors take longer to find the tumor, so the tumor grows to 421 cells before being eliminated on day 103. In all ten simulations, the ability of tumor–effector complexes to recruit additional effectors to the tumor site enables the immune response to eliminate the tumor population quickly.

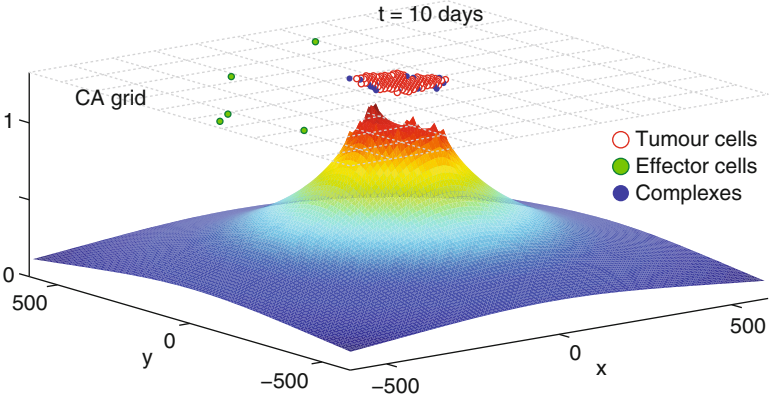

Fig. 3 Example CA simulation for chemotaxis parameter $\lambda = 120$ at time $t = 10$ days. Locations of tumor cells, effector cells, and tumor–effector complexes on the 2-D grid are shown at a height 10 % higher than the maximum cytokine level. Cytokine levels are shown by the surface plot. Other parameter values are taken from Table 1

To determine whether chemotaxis plays a role in the outcome of the anti-tumor immune response, we simulate the CA with chemotaxis parameter $\lambda = 0$, i.e., no chemotaxis. Figure 5 shows the state of the CA at time $t = 400$ days for one simulation.

In Fig. 5, the tumor has grown to 4,485 tumor cells on day 400. There are also 6 tumor–effector complexes and 1 effector. In contrast to the simulation shown in Fig. 3, tumor–effector complexes cannot recruit additional effectors, since effectors do not respond to the cytokine gradient. Without chemotaxis, the tumor–effector complexes are scattered around the tumor mass with hardly any clustering or aggregation of effectors or complexes (see Fig. 5). As a result, the effector response fails to control tumor growth. Figure 6 shows the time evolution of the cell populations for one simulation.

As we see in Fig. 6, the tumor population continues to grow at a steady rate without any surge in the effector response. All ten simulations that we ran using $\lambda = 0$ exhibit quantitatively similar behavior with the tumor population growing to between 3,980 and 4,634 cells by day 400. This result shows that chemotaxis of effectors plays a significant role in tumor elimination.

To see what happens for intermediate levels of chemotaxis, we run ten simulations of the CA with $\lambda = 60$. Results of an example simulation at time $t = 4{,}000$ days are shown in Fig. 7.

In Fig. 7, there are 1,154 tumor cells, 5 effectors, and 13 tumor–effector complexes on day 2,600. Unlike the case when $\lambda = 0$, the effector response has kept the tumor population under control even up to day 2,600. On the other hand, unlike the case when $\lambda = 120$, the effector response has not managed to eliminate the tumor by then. Nonetheless, as in the case when $\lambda = 120$, the effector response eventually succeeds in eliminating the tumor for all ten simulations, but the variability in time to elimination is much higher. Figure 8 shows time evolutions of the fastest and slowest times to tumor elimination.

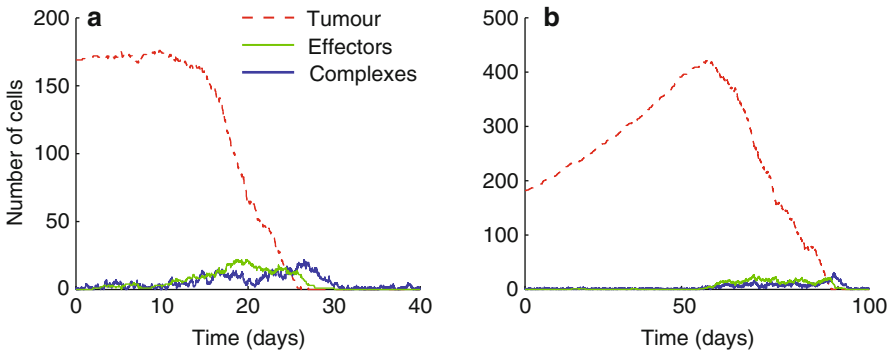

Fig. 4 Time evolution of tumor cells, effectors, and tumor–effector complexes when $\lambda = 120$. Other parameters values are taken from Table 1. (**a**) Fastest tumor elimination among ten simulations. Tumor is eliminated on day 31. (**b**) Slowest tumor elimination among ten simulations. Tumor is eliminated on day 103

Figure 8a shows that in the case when $\lambda = 60$, it is possible for effectors to eliminate the tumor without much of a relapse, but as shown in Fig. 8b, it is far more likely that the system oscillates. Oscillations occur because chemotaxis is strong enough to recruit a strong effector response against a large tumor; however, as the tumor shrinks to a smaller size, the number of tumor–effector complexes surrounding the tumor mass also declines, which reduces the amount of cytokine secreted at the tumor site. At this point the effector recruitment rate becomes too low to sustain the response against the tumor, and the tumor relapses.

The highly oscillatory scenario in Fig. 8b is most likely an undesirable outcome. The tumor reaches high peaks and does not get eliminated for a long time, so it is quite possible that tumor cells would have had time to mutate or metastasize, making it more difficult to treat.

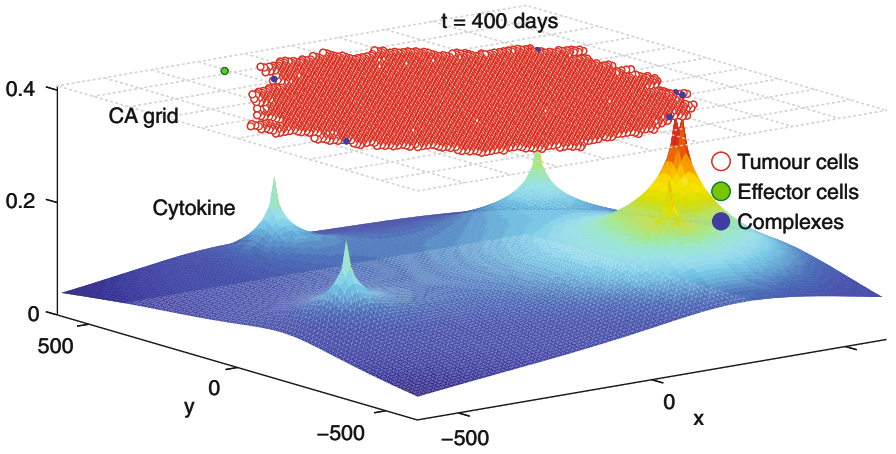

Fig. 5 Example CA simulation for chemotaxis parameter $\lambda = 0$, i.e., no chemotaxis, at time $t = 400$ days. Locations of tumor cells, effector cells, and tumor–effector complexes on the 2-D grid are shown at a height 10 % higher than the maximum cytokine level. Cytokine levels are shown by the surface plot. Other parameter values are taken from Table 1

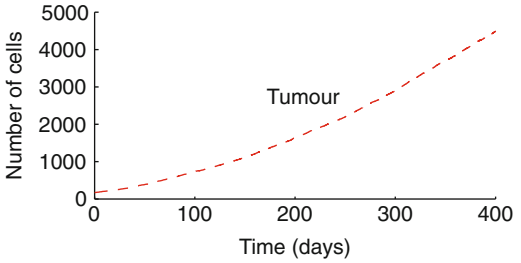

Fig. 6 Time evolution of tumor cells. The effector response fails to control tumor growth, which reaches 4,485 cells on day 400. Numbers of effectors and complexes never exceed 6 and 7, respectively. Parameters values are taken from Table 1 with $\lambda = 0$

We have seen that the CA model exhibits a variety of behaviors and that chemotaxis of effectors plays a significant role in the final outcome. In the next section, we develop an analogous PDE model to see how a continuous, deterministic formulation of the system compares with the CA model.

3 Population Model

To investigate the system from the perspective of a deterministic dynamical system, we take a mean field approximation of the CA in Sect. 2 to obtain an analogous PDE model. The approach that we follow is similar to those of [44,50,51,57,58]. In fact, we directly use a result from Wang and Hillen [57], which we derive again here.

For simplicity, we show how we derive a mean field approximation in one space dimension. The generalization to higher dimensions is straightforward. Let us consider the following rules of cell motion (see Fig. 9):

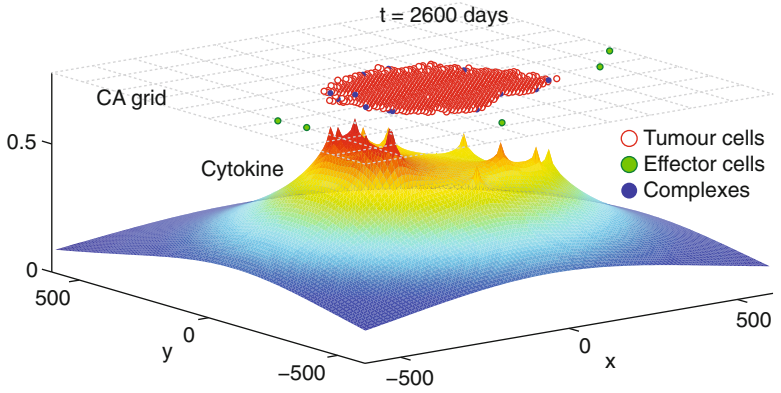

Fig. 7 Example CA simulation for chemotaxis parameter $\lambda = 60$ at time $t = 2{,}600$ days. Locations of tumor cells, effector cells, and tumor–effector complexes on the 2-D grid are shown at a height 10 % higher than the maximum cytokine level. Cytokine levels are shown by the surface plot. Other parameter values are taken from Table 1

1. At each time step Δt, a cell at point x tries to move left with probability $1/2 - \varepsilon(x,t)$ and right with probability $1/2 + \varepsilon(x,t)$.
2. A cell trying to enter point x succeeds in moving there with probability $q(x,t)$, called the *squeezing probability* in [57].

To derive our mean field model, we make the assumption that the number of individuals observed within any interval of space at any given time is independent of the number observed in any nonoverlapping interval [44, 50, 51, 57]. It is a standard assumption for mean field approximations and is sometimes called the *Poisson-point assumption* [43, p. 232].

Let $u(x,t)$ denote the density of cells at point (x,t). To clean up notation, if $f = f(x,t)$ is a function of x and t, let us define $f_- = f(x - \Delta x, t)$ and $f_+ = f(x + \Delta x, t)$. Later on, when we take the limit to the continuum model, we also use f_x, f_{xx}, and f_t to denote the first and second partial derivatives of f with respect to x and the partial derivative of f with respect to t, respectively. From the rules of cell motion, also diagrammed in Fig. 9, we obtain the recursion

$$\begin{aligned} u(t+\Delta t) = u &- \left(\frac{1}{2} - \varepsilon\right) q_- u - \left(\frac{1}{2} + \varepsilon\right) q_+ u \\ &+ \left(\frac{1}{2} + \varepsilon_-\right) q u_- + \left(\frac{1}{2} - \varepsilon_+\right) q u_+ \,. \end{aligned} \tag{3}$$

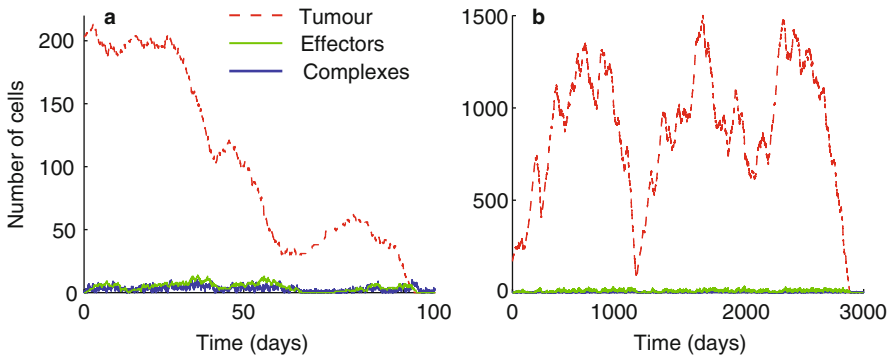

Fig. 8 Time evolution of tumor cells, effectors, and tumor–effector complexes when $\lambda = 60$. Other parameters values are taken from Table 1. (**a**) Fastest tumor elimination among ten simulations. Tumor is eliminated on day 105. (**b**) Slowest tumor elimination among ten simulations. The system is characterized by irregular, stochastic oscillations, and the tumor is eliminated on day 2,884

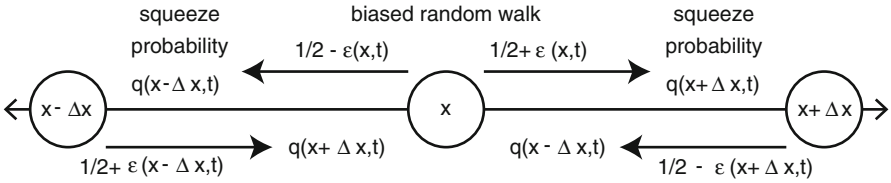

Fig. 9 Cell motion out of and into the point x. A cell at point x tries to move in a biased random walk with a right bias of $\varepsilon(x,t)$. If a cell tries to move to a point x, it successfully moves with squeeze probability $q(x,t)$

Simplifying (3), we obtain

$$\begin{aligned} u(t+\Delta t) - u &= \frac{1}{2}\left(-q_- u - q_+ u + q u_- + q u_+\right) + q_- \varepsilon u - q_+ \varepsilon u + q\varepsilon_- u_- - q\varepsilon_+ u_+ \\ &= -\frac{q_- - 2q + q_+}{2} \cdot u + q \cdot \frac{u_- - 2u + u_+}{2} \\ &\quad - (q_+ - q_-)\varepsilon u - q(\varepsilon_+ u_+ - \varepsilon_- u_-). \end{aligned}$$

After further rearrangement, we obtain

$$\begin{aligned} \frac{u(t+\Delta t) - u}{\Delta t} &= \left(\frac{\Delta x^2}{2\Delta t}\right)\left[-\frac{q_- - 2q + q_+}{\Delta x^2} \cdot u + q \cdot \frac{u_- - 2u + u_+}{\Delta x^2}\right. \\ &\quad \left. - \frac{4}{\Delta x}\left(\frac{q_+ - q_-}{2\Delta x} \cdot \varepsilon u + q \cdot \frac{\varepsilon_+ u_+ - \varepsilon_- u_-}{2\Delta x}\right)\right]. \end{aligned}$$

Taylor expanding this expression, taking the limit as Δx and Δt go to zero, assuming that the random walk bias ε is of order Δx, so that the limit

$$E(x,t) = \lim_{\Delta x \to 0} \frac{\varepsilon(x,t)}{\Delta x}$$

exists, and assuming that the limit

$$D = \lim_{\substack{\Delta x \to 0 \\ \Delta t \to 0}} \frac{\Delta x^2}{2\Delta t}$$

exists, we arrive at the PDE

$$\begin{aligned} u_t &= D[-q_{xx}u + qu_{xx} - 4(q_x(Eu) + q(Eu)_x)] \\ &= D(qu_x - q_x u - 4qEu)_x \ . \end{aligned}$$

This derivation readily generalizes to the higher dimensional form

$$u_t = D\nabla \cdot (q\nabla u - u\nabla q - 4qEu) \ , \tag{4}$$

except that

$$D = \lim_{\substack{\Delta x \to 0 \\ \Delta t \to 0}} \frac{\Delta x^2}{4\Delta t} \quad \text{and} \quad D = \lim_{\substack{\Delta x \to 0 \\ \Delta t \to 0}} \frac{\Delta x^2}{6\Delta t} \tag{5}$$

for the 2-D and 3-D cases, respectively [41,43].

For our particular model, consider the case of effectors, and for simplicity, let us consider 1-D random walks as before. The 1-D version of the random walk weightings (1) is given by

$$\begin{aligned} w_{\text{left}} &= 1 + \lambda C(x - \Delta x, y, t) \ , \\ w_{\text{right}} &= 1 + \lambda C(x + \Delta x, y, t) \ , \end{aligned}$$

and an effector moves right with probability

$$p_{\text{right}} = \frac{1 + \lambda C(x + \Delta x, y, t)}{2 + \lambda C(x - \Delta x, y, t) + \lambda C(x + \Delta x, y, t)} \ .$$

Taylor expanding this expression, we obtain

$$p_{\text{right}} = \frac{1}{2} + \frac{\lambda \Delta x}{2(1 + \lambda C)} C_x + o(\Delta x^3) \ ,$$

so the random walk bias is

$$\varepsilon(x,t) = \frac{\lambda \Delta x}{2(1+\lambda C)} C_x + o(\Delta x^3) \,,$$

which means that

$$E(x,t) = \lim_{\Delta x \to 0} \frac{\varepsilon(x,t)}{\Delta x} = \frac{\lambda \Delta x}{2(1+\lambda C)} C_x.$$

Hence, we can rewrite (4) as

$$u_t = D\nabla \cdot (q\nabla u - u\nabla q - q\chi u \nabla v) \,,$$

where

$$\chi(x,t) = \frac{2\lambda}{1+\lambda C} \,, \qquad v = C \,, \tag{6}$$

and it is straightforward to generalize this equation to higher dimensions. In general, our PDEs will be of the form

$$u_t = D\nabla \cdot (q\nabla u - u\nabla q - q\chi u \nabla v) + g(x,t) \tag{7}$$

for some growth function $g(x,t)$, which is also the form obtained in [57].

To obtain a PDE system based on the CA presented in Sect. 2, let the variables $T(\mathbf{r},t)$, $E(\mathbf{r},t)$, $X(\mathbf{r},t)$, and $C(\mathbf{r},t)$ denote the population densities at point $\mathbf{r}$ and time t of tumor cells, effectors, complexes, and cytokine, respectively. A diagram of interactions is shown in Fig. 10.

Tumor Cells For the tumor population $T(\mathbf{r},t)$, let us assume that tumor cells diffuse at some slow rate $D = D_T$ and grows logistically at rate $\rho T(1-(T+X)/K)$, where ρ is the maximum growth rate and K is the maximum possible density of cells of the same type. Note that in the CA, tumor cells do not actually diffuse. Instead, dividing cells sprout off new cells in adjacent squares as long as empty squares are available. This process is tricky to capture using a reaction-diffusion equation, and it would probably require a free boundary formulation as in [19], so for simplicity, we model tumor growth as a diffusion and logistic growth process.

We assume that the rate of tumor–effector interactions follows the law of mass action, so that the interaction rate is of the form αET, where α is the mass-action coefficient. In the CA of Sect. 2, the formation of complexes happens immediately when tumors and effectors came into contact, so we set α to be relatively high. Also, effector cells in complexes die with mortality rate μ, causing the complex to return to a tumor-cell state at rate μX. Combining all the rates of growth and interactions, we obtain the reaction term $g = \rho T(1-(T+X)/K) - \alpha ET + \mu X$.

For tumor diffusion, we assume that the squeeze probability is $q = 1 - (T + X)/K$, so that the probability of entering a space is the fraction of space remaining unoccupied by tumor cells and complexes. Tumor cells do not respond to the cytokine gradient, so for tumors, the chemotaxis factor $\chi = 0$. Substituting these values of D, q, χ, and g into (7), we have the equation

$$T_t = D_T \nabla \cdot \left(\left(1 - \frac{X}{K} \right) \nabla T + \frac{T}{K} \nabla X \right) + \rho T \left(1 - \frac{T + X}{K} \right) - \alpha E T + \mu X \quad (8)$$

for tumor cells.

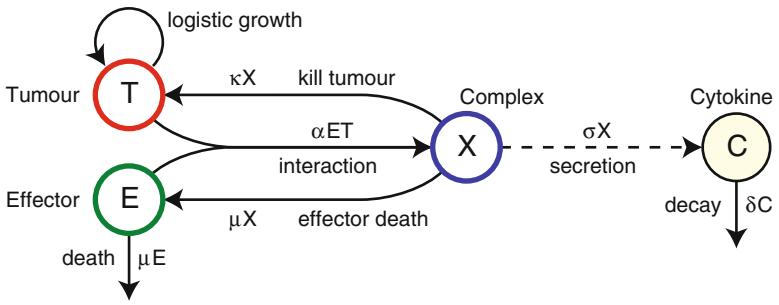

Fig. 10 Diagram of interactions for the PDE model. Tumor cells grow at a logistic rate $(1 - (T + X)/K)$. Effectors die at rate μE. Interacting tumors and effectors form complexes at rate αET. A complex reverts to a tumor cell or effector when the effector in the complex dies at rate μX or kills the tumor cell at rate κX, respectively. Complexes secrete cytokine at rate σX, and cytokine decays at rate δC. All cells diffuse and effector cells exist at a constant concentration at the boundary

Effector Cells For the effector population $E(\mathbf{r}, t)$, we have a diffusion rate $D = D_E$. Because effectors cannot move into spaces occupied by other effectors or complexes, the squeeze probability is $q = 1 - (E + X)/K)$, where K is again the maximum density of cells of the same type. Effectors form complexes with tumor cells at rate αET, die at rate μE, and return from being part of a complex by killing the attached tumor cell at rate κX. We have the chemotaxis term χ from (6), so from (7), we obtain

$$\begin{aligned} E_t = {} & D_E \nabla \cdot \left(\left(1 - \frac{X}{K} \right) \nabla E + \frac{E}{K} \nabla X - \left(1 - \frac{E + X}{K} \right) \frac{2\lambda E \nabla C}{1 + \lambda C} \right) \\ & - \alpha E T - \mu E + \kappa X \ . \end{aligned} \quad (9)$$

Note that the chemotaxis term has a form that saturates as the cytokine concentration C grows. This form results from our rules of biased random motion of effectors in Sect. 2. As an alternative, if we replaced the relative weightings in (1) for motion in each direction by

$$
\begin{aligned}
w_{\text{up}} &= 1 + \lambda(C(x, y + \Delta x, t) - C(x, y - \Delta x, t)) \,, \\
w_{\text{down}} &= 1 + \lambda(C(x, y - \Delta x, t) - C(x, y + \Delta x, t)) \,, \\
w_{\text{left}} &= 1 + \lambda(C(x - \Delta x, y, t) - C(x + \Delta x, y, t)) \,, \\
w_{\text{right}} &= 1 + \lambda(C(x + \Delta x, y, t) - C(x - \Delta x, y, t)) \,,
\end{aligned}
$$

and followed a similar derivation that we used to obtain (6), we would obtain a constant χ, which apart from the squeeze probability would correspond to the classical Keller–Segel model of chemotaxis [24].

Tumor–Effector Complexes We assume tumor–effector complexes $X(\mathbf{r}, t)$ diffuse at rate $D = D_T$, like tumor cells. Complexes cannot move into spaces occupied by either tumor cells or effectors, so their squeeze probability is $q = 1 - (T + E + X)/K$. Complexes form when tumor cells and effectors interact at rates αET, and they revert to single cells at rate $(\kappa + \mu)X$ when effectors kill the tumor cell or die. We assume that complexes do not respond chemotactically to the cytokine gradient. From (7), we obtain

$$
X_t = D_T \nabla \cdot \left(\left(1 - \frac{E + T}{K} \right) \nabla X + \frac{X}{K} \nabla (E + T) \right) + \alpha ET - (\kappa + \mu) X. \quad (10)
$$

Cytokine We assume cytokine $C(\mathbf{r}, t)$ diffuses at some rate $D = D_C$ without any volume exclusion, so that $q = 1$. Cytokine is secreted by complexes at rate σX and decays at rate δC, so from (7), we have

$$
C_t = D_C \nabla^2 C + \sigma X - \delta C \,. \quad (11)
$$

Boundary and Initial Conditions On the boundary of the domain, we assume that all populations have a constant value of 0, except the effector population, which has a constant density E_0. For a simple initial condition, we assume that all populations start at 0 at time $t = 0$, except for the tumor population, which has value K on a disk of radius R, i.e., $T(\mathbf{r}, t) = \mathbf{1}_{\{||\mathbf{r}||^2 \le R^2\}}$.

PDE System Combining (8)–(11), we have the system

$$
\begin{aligned}
T_t &= D_T \nabla \cdot \left(\left(1 - \frac{X}{K} \right) \nabla T + \frac{T}{K} \nabla X \right) + \rho T \left(1 - \frac{T + X}{K} \right) - \alpha ET + \mu X \,, \\
E_t &= D_E \nabla \cdot \left(\left(1 - \frac{X}{K} \right) \nabla E + \frac{E}{K} \nabla X - \left(1 - \frac{E + X}{K} \right) \frac{2\lambda E \nabla C}{1 + \lambda C} \right) \\
&\quad - \alpha ET - \mu E + \kappa X \,, \\
X_t &= D_T \nabla \cdot \left(\left(1 - \frac{E + T}{K} \right) \nabla X + \frac{X}{K} \nabla (E + T) \right) + \alpha ET - (\kappa + \mu) X \,, \\
C_t &= D_C \nabla^2 C + \sigma X - \delta C \,.
\end{aligned}
$$

This system can apply in any number of dimensions, but to keep in line with CA, we consider the system in two dimensions. However, since our model does not imply a favored spatial direction, we can reasonably assume that the system is radially symmetric and simplify the PDE system to one spatial dimension. If we assume radial symmetry and transform the system to polar coordinates, we obtain

$$\begin{aligned}
\frac{\partial T}{\partial t} &= D_T \frac{1}{r}\frac{\partial}{\partial r}\left[r\left(\left(1-\frac{X}{K}\right)\frac{\partial T}{\partial r}+\frac{T}{K}\frac{\partial X}{\partial r}\right)\right]+\rho T\left(1-\frac{T+X}{K}\right)-\alpha E T+\mu X\ ,\\
\frac{\partial E}{\partial t} &= D_E \frac{1}{r}\frac{\partial}{\partial r}\left[r\left(\left(1-\frac{X}{K}\right)\frac{\partial E}{\partial r}+\frac{E}{K}\frac{\partial X}{\partial r}-\left(1-\frac{E+X}{K}\right)\frac{2\lambda E(\partial C/\partial r)}{1+\lambda C}\right)\right]\\
&\quad -\alpha E T-\mu E+\kappa X\ ,\\
\frac{\partial X}{\partial t} &= D_T \frac{1}{r}\frac{\partial}{\partial r}\left[r\left(\left(1-\frac{E+T}{K}\right)\frac{\partial X}{\partial r}+\frac{X}{K}\frac{\partial (E+T)}{\partial r}\right)\right]+\alpha E T-(\kappa+\mu)X\ ,\\
\frac{\partial C}{\partial t} &= D_C \frac{1}{r}\frac{\partial}{\partial r}\left[r\frac{\partial C}{\partial r}\right]+\sigma X-\delta C\ .
\end{aligned} \tag{12}$$

on domain $r \in (0, L)$ with boundary conditions $T(L,t) = 0$, $E(L,t) = E_0$, $X(L,t) = 0$, and $C(L,t) = 0$ with no-flux boundary conditions at r = 0. We also have the initial condition $T(r,t) = K$ for $r \le R$ for some $R < L$ and $T(r,t) = 0$, otherwise. All other populations start at 0.

With the radially symmetric formulation (12), total populations are given by

$$P_{\text{tot}}(t) = 2\pi \int_0^L rP(r,t)dr$$

for all populations $P = T, E, X$, and C.

3.1 Parameter Estimates

We translate our parameters from values in Table 1 that we used for the CA in Sect. 2. A table of parameters, descriptions, and estimates are shown in Table 2.

We consider a domain of approximately the same size as with the CA, so we set the radius of the PDE domain to be $L = 600$ μm. In the CA, we allowed one cell to occupy a square of width 12 μm, so our maximum density of cells of the same type is $K = 1$ cell/(12 μm)^2 = 0.0069 cells/μm^2.

If we set the initial radius of the tumor to be $R = 100$ μm, this corresponds to an initial tumor population of $\pi R^2 K = 218$ cells, which is close to our initial condition for the CA of starting at around 200 cells.

In our past derivations, for simplicity, we obtained our PDEs from 1-D random walks, and so we used the relation that the diffusion rate of randomly walking cells is $\Delta x^2/(2\Delta t)$. These derivations generalize readily to higher dimensions, but in 2-D, the diffusion rate is given by $\Delta x^2/(4\Delta t)$ as in (5). Since our CA is built on a 2-D lattice, the effector diffusion rate that corresponds to a 2-D random walk of step size Δx and time step Δt is given by $D_E = \Delta x^2/(4\Delta t) = (12\ \mu\text{m})^2/(2 \times 1\ \text{min}) = 36\ \mu\text{m}^2/\text{min}$. We assume that the diffusion rate of tumor cells is very slow at $D_T = 0.0001 D_E$ and that the cytokine diffusion rate is twenty times the effector diffusion rate at $D_C = 20 D_E$, which agrees with the CA rules for cytokine diffusion in Sect. 2.

Table 2 Parameters used in simulations of the partial differential equation model

Parameter	Description	Unscaled estimate	Rescaled
L	Radius of domain	600 μm	0.6 mm
R	Radius of initial tumor	100 μm	0.1 mm
K	Maximum cell density	0.0069 cells/μm^2	1 cell/Δx^2
D_E	Diffusion rate of effector cells	36 μm^2/min	0.05 mm^2/day
D_T	Diffusion rate of tumor cells	$0.0001 D_E$	$0.0001 D_E$
D_C	Diffusion rate of cytokine cells	$20 D_E$	$20 D_E$
ρ	Logistic tumor growth rate	9.9×10^{-5}/min	0.14/day
κ	Rate effectors kill tumor	6.9×10^{-4}/min	1/day
μ	Mortality rate of effectors	2.8×10^{-4}/min	0.4/day
σ	Secretion rate of cytokine	1/cell/min	1440 (cells/Δx^2)$^{-1}$day^{-1}
δ	Decay rate of cytokine	0.0014/min	2/day
α	Tumor–effector interaction rate	0.017/cell/min	24 (cells/Δx^2)$^{-1}$day^{-1}
λ	Chemotaxis parameter	0, 60, or 120	0, 60, or 120
E_0	Ambient effector concentration	1×10^{-6} cells/μm^2	1.4×10^{-4} cells/Δx^2

The tumor growth rate, effector killing rate, effector mortality rate, and cytokine decay rate are given by $\rho = 1/\tau_{\text{div}}$, $\kappa = 1/\tau_{\text{kill}}$, $\mu = 1/\tau_{\text{death}}$, and $\delta = 1/\tau_{\text{ck}}$, where parameters of the form τ are from Table 1. Values of the cytokine secretion rate σ, the cytokine parameter λ, and the ambient effector concentration rate E_0 can be used as is from Table 1.

We assume that the interaction rate between tumor cells and effectors in the same space is fast, so we set $\alpha = 24$/cell/day, which corresponds to an average interaction time of 1 h per cell. In column 3 of Table 2, we list all parameters in units of μm and minutes for consistency with the CA.

3.2 Rescaling of Parameters

Because the units in the third column of Table 2 have very disparate orders of magnitude, we rescale the system to time units of days and length units of millimeters and normalize the population such that the maximum density K scales to 1. As we will see, this rescaling will result in reasonable parameter values.

It is straightforward to rescale units of time and length to days and millimeters. Let K_0 denote the unscaled value of K, so that $K_0 = 6.9 \times 10^3$ cells/mm^2. The only other value that is affected by rescaling population densities is the ambient effector concentration, E_0. The rescaled value of E_0 is E_0/K_0. The rescaling puts all population densities in units of fraction of maximum cell density, or cells/Δx^2, where Δx is as in Table 1. Note that population units of cells^{-1} in the CA translate without a conversion factor to population density units of (cells/Δx^2)$^{-1}$ in the PDE, since one cell in the CA occupies an area of Δx^2.

To calculate an unscaled value of a total population, we use

$$P_{\text{tot}}(t) = 2\pi K_0 \int_0^L rP(r,t)dr \ , \tag{13}$$

for populations $P = T$, E, X, and C, where the variable on the left-hand side is unscaled and the variable on the right-hand side is scaled.

3.3 Results of the Partial Differential Equation Model

We numerically simulate the PDE model (12) using the solver "pdepe" in Matlab R2011b. Figure 11 shows results of a numerical simulation using parameters in Table 2 with chemotaxis parameter $\lambda = 120$.

Figure 11a shows that the effector response causes a fast drop of the initial tumor population, resulting in a decline to 5.8 cells on day 41.8, which is comparable to the fastest time to tumor elimination for the CA shown in Fig. 4a. On the other hand, the effector response fades after the tumor reaches low levels, and the tumor relapses, leading to another effector response followed by a tumor decline in what appears to be an unstable oscillation. (Note that since we are dealing with a finite domain $r \in (0, L)$, the system will eventually approach an equilibrium in which the tumor population occupies nearly all of the domain, but we consider size of the domain somewhat arbitrary, since many tumors can expand to diameters of well beyond 1 mm before running into physical limitations.)

Figure 11b shows the profile of the tumor density, $T(r,t)$, at the six tumor peaks in Fig. 11a. As time progresses, each subsequent peak of tumor cells broadens and propagates farther from the origin. Since we are considering a radially symmetric system, the bulges in Fig. 11b correspond to rings of tumor cells around the origin. In contrast, in our simulations of the CA, we never saw a ring of tumor cells

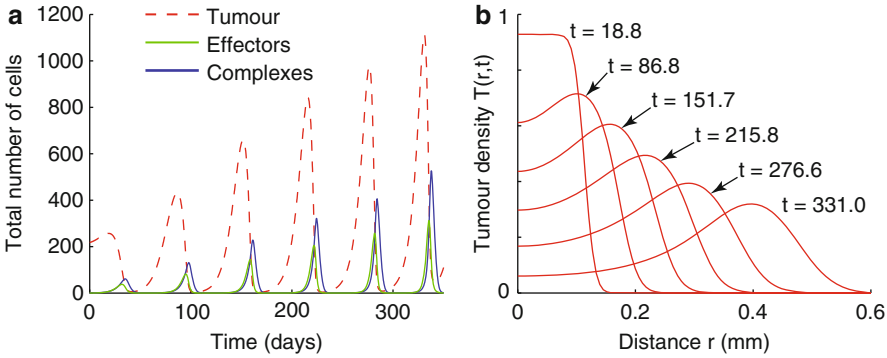

Fig. 11 Numerical solution of the PDE system (12) with chemotaxis parameter $\lambda = 120$. Other parameter values are taken from Table 2. (**a**) Time evolution of the total tumor, effector, and complex populations, calculated using (13). All three populations oscillate with six peaks between time 0 and 350. (**b**) Profile of tumor cell densities, $T(r, t)$, as a function of distance r from the origin at the times of the five tumor peaks at $t = 18.8, 86.8, 151.7, 215.8, 276.6$, and 331.0

propagating away from the origin even up to time 2,600 (see Fig. 7). Perhaps, this difference is due to the continuous nature of the PDE model versus the discrete nature of the CA. Incorporating a slow rate of tumor diffusion in the CA does not lead to a widening ring of relapsing tumor cells (data not shown), so slow tumor cell motion by itself is not enough to create a dispersing tumor. In any case, metastatic tumors are common, so it would be an interesting future direction to determine what dynamic characteristics of tumors would make tumor dispersal more likely. Examples of tumors that migrate away from a pursuing immune response occur in the model of Mallet and De Pillis [34].

To explore the system without chemotaxis, we consider the system when $\lambda = 0$ and plot the results in Fig. 12. As we found in the CA, the effector response in the PDE model without chemotaxis also cannot stop tumor growth (see Fig. 12a). Furthermore, the leading edge of the tumor population propagates with constant speed (see Fig. 12b). In fact, if we assume that the effector population remains so low as to be negligible, the equation for tumor growth simply reduces to Fisher's Equation.

We also consider the PDE model with $\lambda = 60$. Results of the numerical simulation are shown in Fig. 13. In this scenario, the effector response only manages to bring the tumor population down to 225.7 and 127.1 cells on days 213.1 and 287.6, respectively, and the magnitudes of the relapses increase more rapidly than in the case when $\lambda = 120$ (see Fig. 13a). As before, each successive relapse results in a ring of tumor cells that broadens and propagates away from the origin (see Fig. 13b).

As in Fig. 11a, the oscillations when $\lambda = 60$ also appear unstable. In contrast, none of the oscillations that we observed in simulations of the CA consistently grew in magnitude. Instead, the peak heights remained roughly the same until the effector response probabilistically eliminated the tumor (see Fig. 8b.)

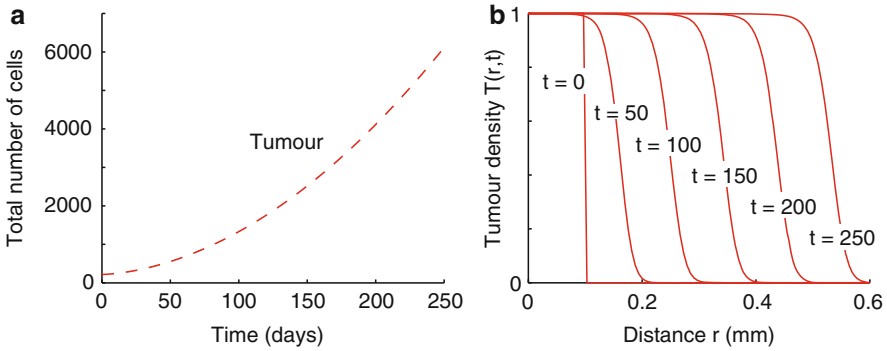

Fig. 12 Numerical solution of the PDE system (12) with chemotaxis parameter $\lambda = 0$. Other parameter values are taken from Table 2. (**a**) Time evolution of the total tumor population, calculated using (13). (**b**) Profile of tumor cell densities, $T(r, t)$ at $t = 0, 50, 100, 150$, and 200

Like the CA, the PDE model is sensitive to the chemotaxis parameter λ, and higher λ leads to a stronger effector response against the tumor, while the absence of chemotaxis when $\lambda = 0$ leads to uncontrolled tumor growth. On the other hand, the PDE model behaves fundamentally differently from the CA model, because the PDE system does not result in complete elimination of the tumor population, and the unstable oscillations result in a widening ring of relapsing tumor cells traveling away from the origin, a phenomenon that we did not observe in our simulations of the CA. An interesting problem for future investigation would be to determine when the CA would exhibit fragmentation of a primary tumor mass into propagating secondary tumors.

4 Discussion

We develop a CA model of tumor and effector T cell interactions that is based on the hybrid CA-PDE model of Mallet and De Pillis [34] and agent-based model of Kim and Lee [25]; however, we explicitly add secretion of cytokines and chemotaxis to model immune recruitment. We then develop an analogous mean-field approximation of the CA as a system of PDEs and compare the PDE model to the CA.

For the CA, we see the three types of behavior also obtained in [25, 34]: rapid elimination of tumor, uncontrolled tumor growth, and a long period of oscillation before probabilistic tumor elimination. We obtained the three behaviors by only varying the chemotaxis parameter λ from relatively high sensitivity to chemoattractant at $\lambda = 120$ to no chemotaxis at $\lambda = 0$ and found that chemotaxis strongly influences the ability of the immune response to control or eliminate the tumor. These simulations corroborate the results of [25, 34], in which the authors find that T cell recruitment rates strongly influence the effectiveness of anti-tumor immune responses in both models.

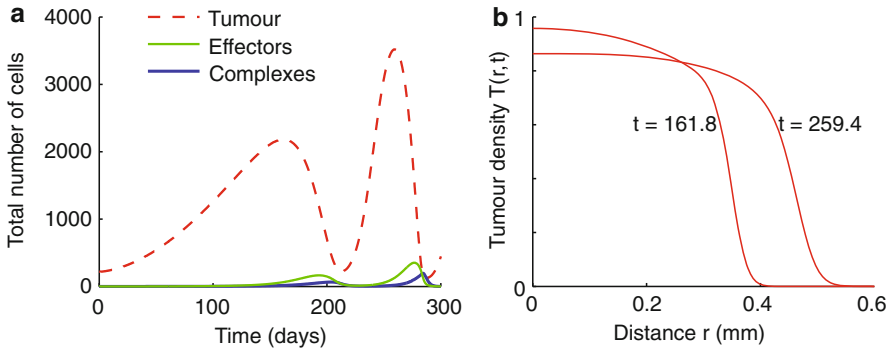

Fig. 13 Numerical solution of the PDE system (12) with chemotaxis parameter $\lambda = 60$. Other parameter values are taken from Table 2. (**a**) Time evolution of the total tumor, effector, and complex populations, calculated using (13). All three populations oscillate with two peaks between time 0 and 300. (**b**) Profile of tumor cell densities, $T(r, t)$, at the times of the tumor peaks at $t = 161.8$, and 259.4

Numerical simulations of the PDE model also show that dynamics are highly influenced by the chemotaxis parameter. For the parameter values in Table 2, which were chosen to be comparable to those of the CA, we do not see a stable solution corresponding to complete tumor elimination. In fact, it is possible that the underlying dynamics of the CA with strong chemotaxis is not stable either; it is just that effector recruitment is strong enough to ensure a high, but not guaranteed, chance of rapid tumor elimination (see Fig. 4a,b).

A direction for future work would be to determine under what conditions the PDE model is stable at the tumor-free equilibrium, produces oscillations, or leads to monotonic tumor growth. Both the PDE model and CA exhibit different characteristics making them useful to study independently and in comparison. The CA allows us to more realistically investigate stochasticity and variability of tumor growth, immune cell migration, and resulting outcomes. On the other hand, the PDE system can be numerically evaluated much faster than the CA and does not need to be evaluated multiple times to obtain the average behavior. Studying CA and PDE models in conjunction will also increase our understanding of the similarities and differences of modeling systems using discrete, probabilistic frameworks and continuous, deterministic models.

One could also conduct a more thorough parameter sensitivity analysis of the CA and PDE models of the same style done in [25]. As in [25], parameters that could be varied include the tumor growth rate, effector kill rate, sensitivity to cytokine gradients, and the ambient effector concentration. Such a parameter sensitivity analysis is relatively straightforward, but for the length and scope of this chapter, we do not delve into such a study here. In addition, it is also straightforward to convert the CA and PDE models to three dimensions as considered in [25].

Finally, the CA and PDE models in this chapter can be readily extended to devise even larger systems of tumor–immune dynamics that could include additional

populations, such as a heterogenous tumor population, additional immune cells, multiple cytokines, and chemotaxis of multiple cells to multiple signals. The role of CA and PDE models in cancer modeling will only grow in the coming years, and having an understanding of both modeling frameworks and connections between the two will become increasingly important in mathematical biology.

Acknowledgements AKC was supported by the KE Bullen Scholarship III awarded to honours students in the School of Mathematics and Statistics at the University of Sydney, and PSK was supported by the Australian Research Council Discovery Early Career Research Award (DE120101113).

References

1. Aguda, B.D., Marsh, C.B., Thacker, M., Crouser, E.D.: An in silico modeling approach to understanding the dynamics of sarcoidosis. PLoS One **6**(5), e19,544 (2011)
2. Alarcón, T., Byrne, H.M., Maini, P.K.: A cellular automaton model for tumour growth in inhomogeneous environment. J. Theor. Biol. **225**, 257–274 (2003)
3. Banerjee, S., Sarkar, R.R.: Delay-induced model for tumor-immune interaction and control of malignant tumor growth. BioSystems **91**(1), 268–288 (2008)
4. Barbarossa, M.V., Kuttler, C., Zinsl, J.: Delay equations modeling the effects of phase-specific drugs and immunotherapy on proliferating tumor cells. Math. Biosci. Eng. **9**(2), 241–257 (2012)
5. Bunimovich-Mendrazitsky, S., Byrne, H., Stone, L.: Mathematical model of pulsed immunotherapy for superficial bladder cancer. Bull. Math. Biol. **70**(7), 2055–2076 (2008)
6. Buzea, C.G., Agop, M., Moraru, E., Stana, B.A., Gir?u, M., Iancu, D.: Some implications of Scale Relativity theory in avascular stages of growth of solid tumors in the presence of an immune system response. J. Theor. Biol. **282**(1), 52–64 (2011)
7. Cabrero, J.R., Serrador, J.M., Barreiro, O., Mittelbrunn, M., Naranjo-Suarez, S., Martin-Cofreces, N., Vicente-Manzanares, M., Mazitschek, R., Bradner, J.E., Avila, J., Valenzuela-Fernandez, A., Sanchez-Madrid, F.: Lymphocyte chemotaxis is regulated by histone deacetylase 6, independently of its deacetylase activity. Mol. Biol. Cell **17**(8), 3435–3445 (2006)
8. Castiglione, F., Piccoli, B.: Cancer immunotherapy, mathematical modeling and optimal control. J. Theor. Biol. **247**(4), 723–732 (2007)
9. Catron, D.M., Itano, A.A., Pape, K.A., Mueller, D.L., Jenkins, M.K.: Visualizing the first 50 h of the primary immune response to a soluble antigen. Immunity **21**(3), 341–347 (2004)
10. De Boer, R.J., Homann, D., Perelson, A.S.: Different dynamics of CD4+ and CD8+ T cell responses during and after acute lymphocytic choriomeningitis virus infection. J Immunol. **171**(8), 3928–3935 (2003)
11. DeConde, R., Kim, P.S., Levy, D., Lee, P.P.: Post-transplantation dynamics of the immune response to chronic myelogenous leukemia. J. Theor. Biol. **236**(1), 39–59 (2005)
12. Depillis, L., Gallegos, A., Radunskaya, A.: A model of dendritic cell therapy for melanoma. Front. Oncol. **3**, 56 (2013)
13. Eftimie, R., Bramson, J.L., Earn, D.J.: Interactions between the immune system and cancer: a brief review of non-spatial mathematical models. Bull. Math. Biol. **73**(1), 2–32 (2011)
14. Eikenberry, S., Thalhauser, C., Kuang, Y.: Tumor-immune interaction, surgical treatment, and cancer recurrence in a mathematical model of melanoma. PLoS Comput. Biol. **5**, e1000,362 (2009)

15. Erjaee, G.H., Ostadzad, M.H., Amanpour, S., Lankarani, K.B.: Dynamical analysis of the interaction between effector immune and cancer cells and optimal control of chemotherapy. Nonlinear Dyn. Psychol. Life Sci. **17**(4), 449–463 (2013)
16. Evans, L.C.: Partial Differential Equations, 2ndedn. American Mathematical Society, Providence (2010)
17. Finn, O.J.: Cancer vaccines: between the idea and the reality. Nat. Rev. Immunol. **3**, 630–641 (2003)
18. Friedl, P., Gunzer, M.: Interaction of T cells with APCs: the serial encounter model. Trends Immunol. **22**(2), 187–191 (2001)
19. Friedman, A., Tian, J.P., Fulci, G., Chiocca, E.A., Wang, J.: Glioma virotherapy: effects of innate immune suppression and increased viral replication capacity. Cancer Res. **66**(4), 2314–2319 (2006)
20. Goodhill, G.J.: Diffusion in axon guidance. Eur. J. Neurosci. **9**(7), 1414–1421 (1997)
21. Jaini, R., Kesaraju, P., Johnson, J.M., Altuntas, C.Z., Jane-Wit, D., Tuohy, V.K.: An autoimmune-mediated strategy for prophylactic breast cancer vaccination. Nat. Med. **16**, 799–803 (2010)
22. Janeway Jr., C.A., Travers, P., Walport, M., Shlomchik, M.J.: Immunobiology : The Immune System in Health and Disease, 6th edn. Garland Science Publishing, New York (2005)
23. Kareva, I., Berezovskaya, F., Castillo-Chavez, C.: Myeloid cells in tumour-immune interactions. J. Biol. Dyn. **4**(4), 315–327 (2010)
24. Keller, E.F., Segel, L.A.: Initiation of slime mold aggregation viewed as an instability. J. Theor. Biol. **26**, 399–415 (1970)
25. Kim, P.S., Lee, P.P.: Modeling protective anti-tumor immunity via preventative cancer vaccines using a hybrid agent-based and delay differential equation approach. PLoS Comput. Biol. **8**(10), e1002,742 (2012)
26. Kim, P.S., Lee, P.P., Levy, D.: Dynamics and potential impact of the immune response to chronic myelogenous leukemia. PLoS Comput. Biol. **4**(6), e1000,095 (2008)
27. Kirschner, D., Panetta, J.C.: Modeling immunotherapy of the tumor-immune interaction. J. Math. Biol. **37**, 235–252 (1998)
28. Kuroishi, T., Tominaga, S., Morimoto, T., Tashiro, H., Itoh, S., Watanabe, H., Fukuda, M., Ota, J., Horino, T., Ishida, T.: Tumor growth rate and prognosis of breast cancer mainly detected by mass screening. Jpn. J. Cancer Res. **81**(5), 454–462 (1990)
29. Kuznetsov, V.A., Makalkin, I.A., Taylor, M.A., Perelson, A.S.: Nonlinear dynamics of immunogenic tumors: parameter estimation and global bifurcation analysis. Bull. Math. Biol. **56**(2), 295–321 (1994)
30. León, K., Lage, A., Carneiro, J.: How regulatory CD25+CD4+ T cells impinge on tumor immunobiology? on the existence of two alternative dynamical classes of tumors. J. Theor. Biol. **247**(1), 122–137 (2007)
31. León, K., Lage, A., Carneiro, J.: How regulatory CD25+CD4+ T cells impinge on tumor immunobiology: the differential response of tumors to therapies. J. Immunol. **179**(9), 5659–5668 (2007)
32. Lin, A.: A model of tumor and lymphocyte interactions. Discrete and Continuous Dynamical Systems B **4**(1), 241–266 (2004)
33. Mackay, C.R.: Chemokine receptors and T cell chemotaxis. J. Exp. Med. **184**(3), 799–802 (1996)
34. Mallet, D.G., De Pillis, L.G.: A cellular automata model of tumor-immune system interactions. J. Theor. Biol. **239**, 334–350 (2006)
35. Matzavinos, A., Chaplain, M.A.: Travelling-wave analysis of a model of the immune response to cancer. C. R. Biol. **327**(11), 995–1008 (2004)
36. Matzavinos, A., Chaplain, M.A., Kuznetsov, V.A.: Mathematical modelling of the spatio-temporal response of cytotoxic T-lymphocytes to a solid tumour. Math. Med. Biol. **21**(1), 1–34 (2004)
37. Maurer, M., von Stebut, E.: Macrophage inflammatory protein-1. Int. J. Biochem. Cell Biol. **36**(10), 1882–1886 (2004)

38. Merrill, S.J.: A model of the role of natural killer cells in immune surveillance I. J. Math. Biol. **12**, 363–373 (1981)
39. Michaelson, J., Satija, S., Moore, R., Weber, G., Halpern, E., Garland, A., Kopans, D.B.: Estimates of breast cancer growth rate and sojourn time from screening database information. J. Women Imaging **5**(1), 11–19 (2003)
40. Moore, H., Li, N.K.: A mathematical model for chronic myelogenous leukemia (CML) and T cell interaction. J. Theor. Biol. **225**(4), 513–523 (2004)
41. Murray, J.D.: Mathematical Biology: I. An Introduction, 3rd edn. Springer, New York (2002)
42. Nestle, F.O., Tonel, G., Farkas, A.: Cancer vaccines: the next generation of tools to monitor the anticancer immune response. PLoS Med. **2**, e339 (2005)
43. Okubo, A., Levin, S.A.: Diffusion and Ecological Problems: Modern Perspectives, 2rd edn. Springer, New York (2010)
44. Penington, C.J., Hughes, B.D., Landman, K.A.: Building macroscale models from microscale probabilistic models: a general probabilistic approach for nonlinear diffusion and multispecies phenomena. Phys. Rev. E **84**(4 Pt 1), 041,120 (2011)
45. Pennisi, M.: A mathematical model of immune-system-melanoma competition. Comput. Math. Methods Med. **2012**, 850,754 (2012)
46. de Pillis, L.G., Mallet, D.G., Radunskaya, A.E.: Spatial tumor-immune modeling. Comput. Math. Methods Med. **7**(2–3), 159–176 (2006)
47. de Pillis, L.G., Radunskaya, A.E., Wiseman, C.L.: A validated mathematical model of cell-mediated immune response to tumor growth. Cancer Res. **65**(17), 7950–7958 (2005)
48. Qi, A.S., Zheng, X., Du, C.Y., An, B.S.: A cellular automaton model of cancerous growth. J. Theor. Biol. **161**(1), 1–12 (1993)
49. Robert-Tissot, C., Nguyen, L.T., Ohashi, P.S., Speiser, D.E.: Mobilizing and evaluating anticancer T cells: pitfalls and solutions. Expert Rev. Vaccines **12**(11), 1325–1340 (2013)
50. Simpson, M.J., Baker, R.E.: Corrected mean-field models for spatially dependent advection-diffusion-reaction phenomena. Phys. Rev. E **83**(5 Pt 1), 051,922 (2011)
51. Simpson, M.J., Landman, K.A., Hughes, B.D.: Multi-species simple exclusion processes. Phys. A **388**(4), 399–406 (2009)
52. Soiffer, R., Hodi, F.S., Haluska, F., Jung, K., Gillessen, S., Singer, S., Tanabe, K., Duda, R., Mentzer, S., Jaklitsch, M., Bueno, R., Clift, S., Hardy, S., Neuberg, D., Mulligan, R., Webb, I., Mihm, M., Dranoff, G.: Vaccination with irradiated, autologous melanoma cells engineered to secrete granulocyte-macrophage colony-stimulating factor by adenoviral-mediated gene transfer augments antitumor immunity in patients with metastatic melanoma. J. Clin. Oncol. **21**, 3343–3350 (2003)
53. Soiffer, R., Lynch, T., Mihm, M., Jung, K., Rhuda, C., Schmollinger, J.C., Hodi, F.S., Liebster, L., Lam, P., Mentzer, S., Singer, S., Tanabe, K.K., Cosimi, A.B., Duda, R., Sober, A., Bhan, A., Daley, J., Neuberg, D., Parry, G., Rokovich, J., Richards, L., Drayer, J., Berns, A., Clift, S., Cohen, L.K., Mulligan, R.C., Dranoff, G.: Vaccination with irradiated autologous melanoma cells engineered to secrete human granulocyte-macrophage colony-stimulating factor generates potent antitumor immunity in patients with metastatic melanoma. Proc. Natl. Acad. Sci. USA **95**, 13,141–13,146 (1998)
54. Spratt, J.A., von Fournier, D., Spratt, J.S., Weber, E.E.: Decelerating growth and human breast cancer. Cancer **71**, 2013–2019 (1993)
55. Villasana, M., Radunskaya, A.: A delay differential equation model for tumor growth. J. Math. Biol. **47**(3), 270–294 (2003)
56. Wang, W., Epler, J., Salazar, L.G., Riddell, S.R.: Recognition of breast cancer cells by CD8+ cytotoxic T-cell clones specific for NY-BR-1. Cancer Res. **66**, 6826–6833 (2006)
57. Wang, Z., Hillen, T.: Classical solutions and pattern formation for a volume filling chemotaxis model. Chaos **17**(3), 037,108 (2007)
58. Wang, Z.A.: On chemotaxis models with cell population interactions. Math. Model Nat. Phenom. **5**(3), 173–190 (2010)
59. Weedon-Fekjaer, H., Lindqvist, B.H., Vatten, L.J., Aalen, O.O., Tretli, S.: Breast cancer tumor growth estimated through mammography screening data. Breast Cancer Res. **10**, R41 (2008)

60. Wiedemann, A., Depoil, D., Faroudi, M., Valitutti, S.: Cytotoxic T lymphocytes kill multiple targets simultaneously via spatiotemporal uncoupling of lytic and stimulatory synapses. Proc. Natl. Acad. Sci. USA **103**, 10,985–10,990 (2006)
61. Wilkinson, P.C., Komai-Koma, M., Newman, I.: Locomotion and chemotaxis of lymphocytes. Autoimmunity **26**(1), 55–72 (1997)

A Structured Population Model of Competition Between Cancer Cells and T Cells Under Immunotherapy

Marcello Delitala, Tommaso Lorenzi, and Matteo Melensi

Abstract How does immunotherapy affect the evolutionary dynamics of cancer cells? Can we enhance the anti-cancer efficacy of T cells by using different types of immune boosters in combination? Bearing these questions in mind, we present a mathematical model of cancer–immune competition under immunotherapy. The model consists of a system of structured equations for the dynamics of cancer cells and activated T cells. Simulations highlight the ability of the model to reproduce the emergence of cancer immunoediting, that is, the well-documented process by which the immune system guides the somatic evolution of tumors by eliminating highly immunogenic cancer cells. Furthermore, numerical results suggest that more effective immunotherapy protocols can be designed by using therapeutic agents that boost T cell proliferation in combination with boosters of immune memory.

M. Delitala (✉)
Department of Mathematical Sciences, Politecnico di Torino, Corso Duca degli Abruzzi 24, 10129 Torino, Italy
e-mail: marcello.delitala@polito.it

T. Lorenzi
Sorbonne Universités, UPMC Univ Paris 06, UMR 7598, Laboratoire Jacques-Louis Lions, F-75005, Paris, France

CNRS, UMR 7598, Laboratoire Jacques-Louis Lions, F-75005, Paris, France

INRIA-Paris-Rocquencourt, EPC MAMBA, Domaine de Voluceau, BP105, 78153 Le Chesnay Cedex, France
e-mail: tommaso.lorenzi@upmc.fr

M. Melensi
Department of Health Sciences, A. Avogadro Università del Piemonte Orientale, Via Solaroli 17, 28100 Novara, Italy
e-mail: matteo.melensi@med.unipmn.it

A. Eladdadi et al. (eds.), *Mathematical Models of Tumor-Immune System Dynamics*, Springer Proceedings in Mathematics & Statistics 107,
DOI 10.1007/978-1-4939-1793-8_3

1 Introduction

Immunotherapy is a type of treatment that can be used to boost or restore the ability of the immune system to fight cancer, infections or other form of disease. The molecular identification of human cancer antigens has allowed the development of different antigen-specific immunotherapy protocols. These include in vitro activation of autologous tumor T cells which are re-infused into patients after expansion, ex vivo expansion of autologous antigen-specific T cells which are then re-infused into patients, and vaccination with an antigen and an adjuvant to elicit therapeutic T cells [24, 28].

While T-cell-based therapies have been shown to boost the body's ability to fight cancers such as leukemia, lymphoma and breast cancer, they have not improve the survival rates of patients with melanoma or lung cancer [29, 30]. However, current immunotherapy protocols have not resulted in durable clinical improvements, except in single patients [2, 13]. A possible reason for the limited ability of cytotoxic T cells to kill or to contain tumor growth is that they die quickly. In this scenario, the immune response is not sustained and cancer eventually returns. For this reason, current research trends include engineering cancer vaccines that induce both tumor-specific effector T cells, which can reduce the tumor mass, and tumor-specific memory T cells, which can control tumor relapse by providing the immune system with "memory" (i.e., they quickly expand becoming activated T cells upon re-exposure to their cognate antigen).

How does immunotherapy affect the evolutionary dynamics of cancer cells? Can we enhance the anti-cancer efficacy of T cells by using different types of immune boosters in combination? Bearing these questions in mind, we propose a structured population model that describes the dynamics of a well-mixed sample (i.e., space effects are, *prima facie*, kept aside) of cancer cells and activated T cells under immunotherapy. The immunotherapy we consider is based on the delivery of agents that boost the proliferation of T cells and immune memory. The model includes proliferation and death processes of both cancer cells and activated T cells. The mesoscopic formalism of the present model allows us to take into account microscopic features of cancer–immune competition, which is not possible in macroscopic models.

In spite of more complex mathematical models of cancer–immune competition [1–12, 14–20, 23, 25, 26], the one we present here relies on just a few parameters. In fact, as a first step of a long term project, this model is conceived as a tool to test different hypothetical scenarios, rather than to perform quantitative forecasts.

The reminder of the chapter is organized as follows. In Sect. 2, we describe the mathematical model and the related underlying assumptions. Section 3 introduces the general setup for numerical simulations and presents the results obtained under different parameter settings, which mimic different biological scenarios. We study the adaptation of the antigenic profile of cancer cells in response to the action exerted by activated T cells. We also analyze the evolution of the cancer cell density in the

presence of T cell proliferation boosters and immune memory boosters. Finally, Sect. 4 contains the conclusions of this chapter and provides also ideas about future research perspectives.

2 The Model

As a reference system, we consider a population of cancer cells, structured by a non-negative real variable $u \in U \subset \mathbb{R}_+$ that represents the antigenic expression, and a population of activated T cells, structured by a non-negative real variable $v \in V \subseteq U$ that represents those antigens that T cells can effectively attack. For brevity, we refer to the variables u and v as traits of the cancer cells and T cells, respectively. Both cell populations are exposed to the action of two types of immunotherapies: one aimed at boosting the proliferation of activated T cells, and the other aimed at boosting immune memory. The local densities of cancer cells and T cells are modeled by the functions $f_C(t,u) \geq 0$ and $f_I(t,v) \geq 0$. The related total densities are computed as

$$\rho_C(t) = \int_U f_C(t,u)du, \qquad \rho_I(t) = \int_V f_I(t,v)dv. \tag{1}$$

We represent the infusion rates of therapeutic agents boosting proliferation and immune memory at time $t \in [0,T]$ by the functions $c_P(t) \geq 0$ and $c_M(t) \geq 0$, respectively.

The biological phenomena of interest are modeled according to the assumptions and the strategies summarized below. Mathematical details are similar to those previously introduced in [6], apart from those which concern the modeling of immunotherapies:

Cancer Cell Proliferation and Competition for Resources In order to mimic cancer growth, we introduce a parameter $\kappa_C > 0$, which models the average rate of cell proliferation net of apoptosis. Furthermore, since cellular proliferation is hampered by the competition for resources, we assume that interactions can lead cancer cells to die at an average rate $\mu_C > 0$.

Clonal Expansion of T Cells and Homeostatic Regulation In order to enhance the efficacy of immune response, T cells undergo a rapid *in situ* clonal expansion. We account for this process by including binary interactions between cancer cells with trait u and activated T cells with trait v, that occur at a rate described by the function

$$\eta_{\theta_E}(|u-v|) > 0, \qquad \eta'_{\theta_E}(\cdot) \leq 0, \tag{2}$$

and lead to the proliferation of T cells. In order to model the selectivity of clonal expansion, the interaction rate is defined as a symmetric and decreasing function of the distance between the traits of the interacting cells. Parameter $\theta_E > 0$

measures, on average, the selectivity of the interactions. Moreover, due to the limited availability of nutrients, and homeostatic regulation mechanisms as well, T cells cannot proliferate in an unbounded way. As a consequence, we assume that they can die at an average rate $\mu_I > 0$ due to interactions with other cells of the same population.

Action of T Cells Against Cancer Cells T cells are able to target and kill cancer cells that express their cognate antigen. Therefore, we also include binary interactions between cancer cells with trait u and activated T cells with trait v, that occur at a rate described by function

$$\eta_{\theta_I}(|u-v|) > 0, \qquad \eta'_{\theta_I}(\cdot) \leq 0 \tag{3}$$

and lead to the destruction of cancer cells. Considerations analogous to those drawn about function η_{θ_E} hold. It is worth noting that $\eta_{\theta_I}(\cdot)$ may be different from $\eta_{\theta_E}(\cdot)$, namely because clonal expansion and immune competition can be characterized by different levels of selectively.

Boosting of T Cell Proliferation and Immune Memory The effect of therapeutic agents that enhance the proliferation of T cells are modeled through an increase in the proliferation rate of T cells by parameter $\kappa_P > 0$. On the other hand, the action of therapeutic agents that boost immune memory is modeled through a reduction in the death rate related to homeostatic regulation by parameter $\mu_M > 0$.

Therefore, we describe the dynamics of the two cell populations through the following system of structured equations

$$\begin{cases} \dfrac{\partial}{\partial t} f_C(t,u) = R_C(t,u) f_C(t,u), \\ \dfrac{\partial}{\partial t} f_I(t,v) = R_I(t,v) f_I(t,v), \end{cases} \tag{4}$$

where R_C and R_I model the net proliferation rates of cancer cells and T cells, respectively,

$$R_C(t,u) := \underbrace{(\kappa_C - \mu_C \rho_C(t))}_{\text{cancer cell proliferation and competition for resources}} \underbrace{- \int_V \eta_{\theta_I}(|u-v|) f_I(t,v) dv}_{\text{action of T cells against cancer cells}}, \tag{5}$$

$$R_I(t,v) := \underbrace{\left[\int_U \eta_{\theta_E}(|u-v|) f_C(t,u) du + \kappa_P c_P(t) \right]}_{\text{clonal expansion and boosting of T cell proliferation}} - \underbrace{\frac{\mu_I}{1+\mu_M c_M(t)} \rho_I(t)}_{\substack{\text{homeostatic regulation and} \\ \text{boosting of immune memory}}}.$$

Remark 1. Since we assume a well-mixed cell sample, the current model does not account for any spatial dynamics. However, we note that the formalism at hand

would allow us to incorporate spatial effects of the two cell populations. This could be namely done by integrating the modeling strategies presented in [22] with the considerations made in [8].

3 Numerical Results

In this section, we study the evolution of cancer cells under the effects of immunotherapy in the framework of the model presented in the previous section. In particular, our simulations

1. analyze how cancer cells adapt to the immune response exerted by activated T cells, in the presence of therapeutic agents that boost the proliferation of activated T cells and immune memory;
2. verify the existence of suitable infusion schemes that enhance the efficacy of immunotherapy protocols.

We assume $U = V := [0, 1]$, while as a time domain we select the interval $[0, T = 120]$. Time is in units of the average cell cycle. We choose the initial conditions

$$f_C(t = 0, u) = C_C e^{-\frac{(u-0.5)^2}{0.001}}, \qquad f_I(t = 0, v) = C_I \chi_V(v),$$

where χ_V is the characteristic function of the set V and the factors $C_{C,I} \in \mathbb{R}_+$ are such that

$$\rho_{C,I}(t = 0) \approx 1.$$

These conditions mimic a biological scenario where, at the beginning of observations, the cancer cell population is almost monomorphic (i.e., most of the cancer cells are characterized by the same antigenic expression). Concurrently, the distribution of activated T cells over the possible antigenic expressions is assumed to be uniform.

In order to perform numerical simulations, we select a uniform grid with $N = 400$ points on the segment $[0, 1]$. We denote by $f_C(t_k, u_n) \geq 0$ and $f_I(t_k, v_n) \geq 0$ the numerical solutions at grid points $u_n = n\Delta u$ and $v_n = n\Delta v$ (space steps $\Delta u = \Delta v = 1/N$) and time $t_k = k\Delta t$ (time step $\Delta t = 0.1$). Therefore,

$$f_C(t, u) \approx f_C(t_k, u_n), \qquad f_I(t, v) \approx f_I(t_k, v_n).$$

We implement in MATLAB the following implicit–explicit finite difference scheme, see e.g. [21],

$$\begin{cases} f_C(t_{k+1}, u_n) = f_C(t_k, u_n) + \Delta t \left[R_C^+(t_k, u_n) f_C(t_k, u_n) - R_C^-(t_k, u_n) f_C(t_{k+1}, u_n) \right], \\ \\ f_I(t_{k+1}, v_n) = f_I(t_k, v_n) + \Delta t \left[R_I^+(t_k, v_n) f_I(t_k, v_n) - R_I^-(t_k, v_n) f_I(t_{k+1}, v_n) \right], \end{cases}$$

where $R^{+}_{C,I}(t_k, u_n)$ and $R^{-}_{C,I}(t_k, v_n)$ denote, respectively, the positive and negative parts of the numerical approximations for $R_C(t, u)$ and $R_I(t, v)$.

For all simulations, the functions η_{θ_E} and η_{θ_I} are defined as

$$\eta_{\theta_E}(|u-v|) := e^{-\theta_E |u-v|^2}, \qquad \eta_{\theta_I}(|u-v|) := e^{-\theta_I |u-v|^2},$$

and the other parameters of the model are set as

$$\kappa_{C,P} := 1, \quad \mu_{C,I} := 0.5, \quad \theta_{E,I} := 1{,}000, \quad \mu_M := 1. \tag{6}$$

The above functions and the related parameters are chosen to be simple and offering clear illustrations of the generic properties (2) and (3).

Definitions of functions c_P and c_M are selected case by case to mimic different infusion schedules. At first, we study the dynamics of cancer cells without immunotherapies, that is, when

$$c_{P,M}(t) := 0, \qquad \forall t \in [0, T].$$

Figure 1 shows the "chase-and-escape" dynamics of activated T cells and cancer cells, i.e.,

1. clonal expansion leads to a rapid proliferation of those T cells that can effectively attack the antigens mostly expressed by the cancer cell population;
2. the selective pressure exerted by activated T cells causes the selection of the cancer cells that are actually able to evade immune predation.

This cause the emergence of oscillations in the total densities of cancer cells and T cells (see the right panel of Fig. 1).

From the evolutionary perspective, let us note that immune competition pushes the monomorphic cancer cell population to become, in succession, dimorphic, trimorphic and then tetramorphic (i.e., most of the cells are characterized by two, three or four given antigenic expressions, respectively). In turn, the same pattern of evolution is followed by activated T cells with a certain delay, which is due to the time required to adapt to the antigenic distribution of cancer cells (see the left and center panels of Fig. 1). In the framework of our model, these evolutionary patterns can be seen as the result of cancer immunoediting, that is, the well-documented process by which the immune system guides the somatic evolution of tumors by eliminating highly immunogenic cancer cells [4,9].

Next we analyze the evolution of cancer cells under three different immunotherapy regimes:

1. T cell proliferation boosters only, i.e.,

$$c_P(t) := C\ \mathrm{sgn}(\sin(\omega t))^{+}, \qquad c_M(t) := 0; \tag{7}$$

2. immune memory boosters only, i.e.,

$$c_P(t) := 0, \qquad c_M(t) := C\ \mathrm{sgn}(\sin(\omega t))^{+}; \tag{8}$$

3. simultaneous delivery of both boosters, i.e.,

$$c_P(t) := \frac{C}{2}\,\mathrm{sgn}(\sin(\omega t))^+, \qquad c_M(t) := \frac{C}{2}\,\mathrm{sgn}(\sin(\omega t))^+. \tag{9}$$

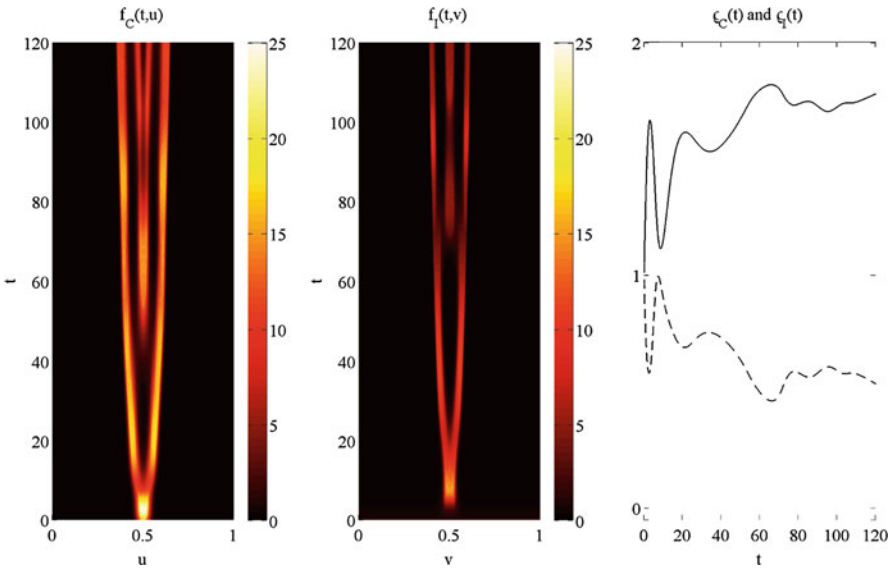

Fig. 1 Cell dynamics without immune boosters. Evolution of $f_C(t,u)$ (*left panel*), $f_I(t,v)$ (*center panel*), $\rho_C(t)$ (*right panel, solid line*) and $\rho_I(t)$ (*right panel, dashed line*). Clonal expansion leads to a rapid proliferation of the T cells that can effectively attack the antigens mostly expressed by the cancer cell population. The selective pressure exerted by activated T cells causes, in turn, the selection of those cancer cells that are able to evade immune predation

During simulations, we choose $\omega = 10\pi/T$ and we test three different instances of infusion, which are characterized by picks of different height (see the center panels of Figs. 2, 3, 4), i.e., we set alternatively $C = 4$, $C = 6$ or $C = 8$. Provided that the same value of parameter C is selected, the integral

$$\int_0^T [c_P(t) + c_M(t)]\,dt$$

does not change under definitions (7)–(9), that is, the total delivered dose is kept the same in the three cases at hand. This is actually of primary importance to make a consistent comparison between the protocols under study.

At first, we study the effects of immunotherapy protocols that rely on the delivery of T cell proliferation boosters only, i.e., we perform simulations under definitions (7). The results presented in the left panels of Fig. 2 support the idea that boosters of T cell proliferation may only allow a temporary reduction in the total density of cancer cells, which is then followed by a relapse.

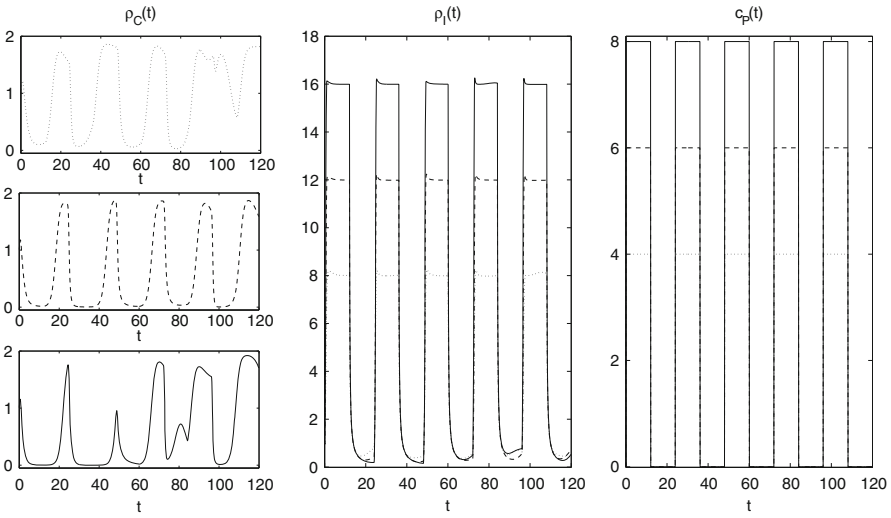

Fig. 2 Cell dynamics with boosters of T cell proliferation. Evolution of $\rho_C(t)$, $\rho_I(t)$ and $c_P(t)$ for $C = 4$ (*dotted lines*), $C = 6$ (*dashed lines*) and $C = 8$ (*solid lines*). Boosters of T cell proliferation allow only a temporary reduction of the concentration of cancer cells

Next, we analyze the efficacy of immunotherapy protocols that make use of immune memory boosters only, i.e., we perform simulations under definitions (8). After a comparison between the results shown by the left panels of Fig. 3 and those presented in the right panel of Fig. 1, we are led to conclude that the dynamics of the cancer cell density is left almost unaltered with respect to the case without therapies. The addition of oscillations seems to be the only significant effect.

Finally, we consider the case where the two types of immune boosters are used in combination, i.e., we perform simulations under definitions (9). The results shown by the lower left panel of Fig. 4 support the idea that if the two types of immune boosters considered are used in combination, then there exists certain doses that make it possible to push the cancer cell population toward extinction, and effectively control tumor relapse. This may be due to the fact that the simultaneous delivery of T cell proliferation boosters and boosters of immune memory at sufficiently high doses allows the total density of immune cells to attain higher values (compare the center panel of Fig. 4 with the center panels of Figs. 2 and 3).

The qualitative properties of the results presented in Figs. 2, 3, 4 are left unaltered by variations of the parameter values (6), within reasonable ranges. Furthermore, let us note that we have developed additional simulations (data not shown) under the following definitions of functions c_P and c_M

$$c_P(t) := \frac{C}{2}\,\mathrm{sgn}(\sin(\omega t))^+, \quad c_M(t) := \frac{C}{2}\,\mathrm{sgn}(\sin(\omega t + \pi))^+, \quad C \in \{4, 6, 8\},$$

$$c_P(t) := \frac{C}{2}\,\mathrm{sgn}(\sin(\omega t + \pi))^+, \quad c_M(t) := \frac{C}{2}\,\mathrm{sgn}(\sin(\omega t))^+, \quad C \in \{4, 6, 8\},$$

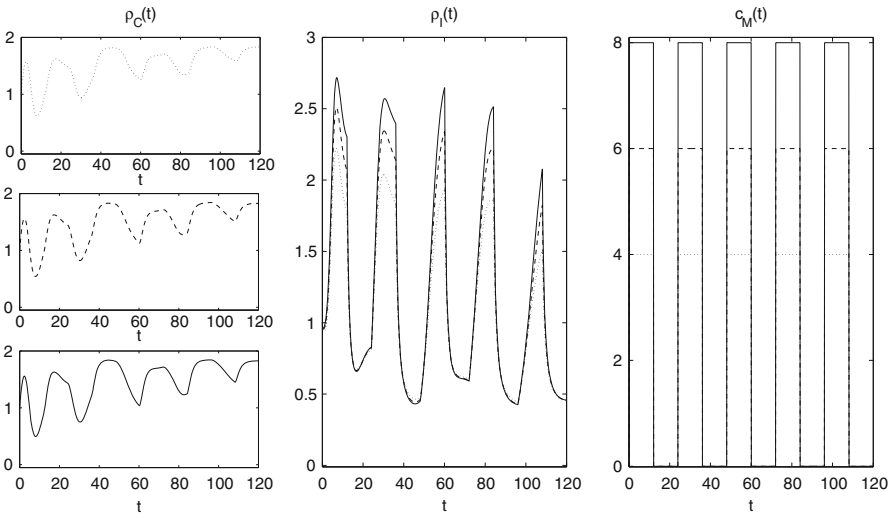

Fig. 3 Cell dynamics with boosters of immune memory. Evolution of $\rho_C(t)$, $\rho_I(t)$ and $c_M(t)$ for $C = 4$ (*dotted lines*), $C = 6$ (*dashed lines*) and $C = 8$ (*solid lines*). Immune memory boosters leave the qualitative dynamics of the cancer cell density almost unaltered with respect to the case without therapies (to be compared with the right panel of Fig. 1), apart from the addition of oscillations in the total density of cancer cells

with $\omega = 10\pi/T$. The obtained results highlight how protocols that rely on the alternate delivery of T cell proliferation boosters and boosters of immune memory do not allow to eradicate the cancer cell population.

These results lead us to conclude that, with the doses used in our tests, more effective immunotherapy protocols can be designed by using combinations of therapeutic agents that boost T cell proliferation and immune memory. This is in agreement with the ideas presented in [11, 27].

4 Conclusions and Perspectives

In this chapter, we have presented a structured population model that describes the dynamics of a well-mixed sample of cancer cells and activated T cells under immunotherapy. The immunotherapy we consider is based on the delivery of agents that boost the proliferation of T cells and immune memory. The model includes proliferation and death processes of both cancer cells and activated T cells, as well as clonal expansion of T cells and their action against cancer cells.

In spite of more complex mathematical models of cancer–immune competition, the one we have presented here relies on just a few parameters and it is conceived as a tool to test different hypothetical scenarios, rather than to perform quantitative

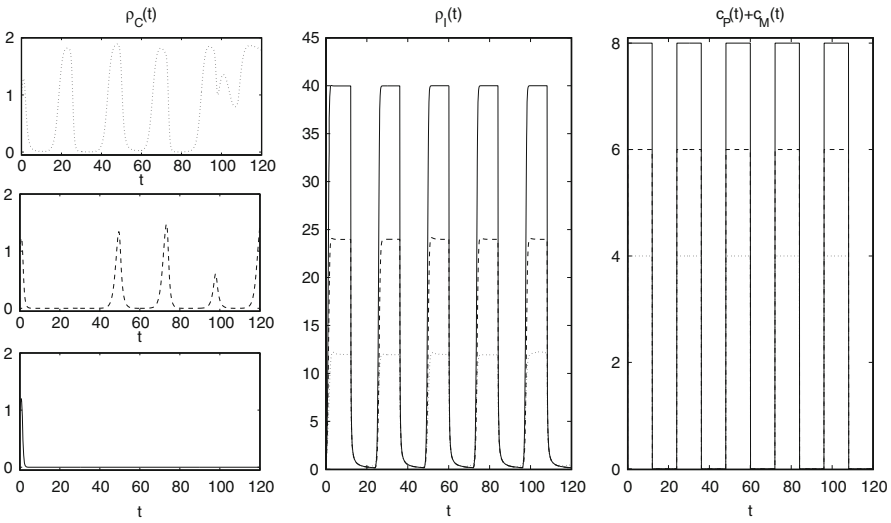

Fig. 4 Cell dynamics with boosters of T cell proliferation in combination with boosters of immune memory. Evolution of $\rho_C(t)$, $\rho_I(t)$ and $c_P(t) + c_M(t)$ for $C = 4$ (*dotted lines*), $C = 6$ (*dashed lines*) and $C = 8$ (*solid lines*). If the two types of immune boosters considered are used in combination, then there exists certain doses that allow to achieve the complete eradication of cancer cells

forecasts. In the framework of this model, we have studied, through numerical simulations, the adaptation of the antigenic profile of cancer cells in response to the action exerted by activated T cells. We have also analyzed the evolution of cancer cell density in the presence of T cell proliferation boosters only, immune memory boosters only, and combination of them.

Despite its simplicity, the model seems able reproduce the emergence of the "chase-and-escape" dynamics involving activated T cells and cancer cells. Furthermore, the results presented here support the idea that, *ceteris paribus*, more effective immunotherapy protocols can be designed by using suitable combinations of therapeutic agents that boost both T cell proliferation and immune memory.

Future research will be focussing on refining the modeling strategies of the evolutionary dynamics of cancer cells. For instance, a natural improvement of the model would be to include an additional structuring variable, let us say w, related to the proliferative potential of cancer cells, and replace the parameter κ_C with an increasing function of this variable. Furthermore, since cell proliferation implies resource reallocation (i.e., redistribution of energetic resources from competition-oriented tasks toward development and maintenance of proliferative potential), it might also be worth replacing parameter μ_C and function η_{θ_I} with some functions $\mu_C(w)$ and $\eta_{\theta_I}(|u - v|, w)$.

From a mathematical standpoint, it could be interesting to provide a detailed characterization of the oscillations that arise in the total densities of the two cell populations. Namely the techniques applied in [21] may prove to be useful to show

that the evolution equations for $\rho_{C,I}(t)$ can resemble a kind of Lotka–Volterra system, under a proper time rescaling together with suitable assumptions on the functions and parameters of the model.

Acknowledgements This work has been partially supported by the FIRB project—RBID08PP3J, the Fondation Sciences Mathématiques de Paris (FSMP) and by a public grant overseen by the French National Research Agency (ANR) as part of the "Investissements d'Avenir" program (reference: ANR-10-LABX-0098).

References

1. Agliari, E., Barra, A., Guerra, F., Moauro, F.: A thermodynamical perspective of immune capabilities. J. Theor. Biol. **287**, 48–63 (2010)
2. Brichard, V., Dréno, B., Tessier, M.H., Rankin, E., Parmiani, G., Arienti, F., Humblet, Y., Bourlond, A., Vanwijck, R., Liénard, D., Beauduin, M., Dietrich, P.Y., Russo, V., Kerger, J., Masucci, G., Jäger, E., De Greve, J., Atzpodien, J., Brasseur, F., Coulie, P.G., van der Bruggen, P., Boon, T.: Tumor regressions observed in patients with metastatic melanoma treated with an antigenic peptide encoded by gene MAGE-3 and presented by HLA-A1. Int. J. Cancer **80**, 219–230 (1999)
3. Bunimovich-Mendrazitsky, S., Byrne, H., Stone, L.: Mathematical model of pulsed immunotherapy for superficial bladder cancer. Bull. Math. Biol. **70**, 2055–2076 (2008)
4. Burgess, D.J.: Tumour immunogenicity: editorial selection demystified. Nat. Rev. Cancer **12**, 227 (2012)
5. Calvez, V., Korobeinikov, A., Maini, P.K.: Cluster formation for multi-strain infections with cross-immunity. J. Theor. Biol. **233**, 75–83 (2005)
6. Delitala, M., Lorenzi, T.: Recognition and learning in a mathematical model for immune response against cancer. Discrete Contin. Dyn. Syst. Ser. B **18**, 891–914 (2013)
7. De Pillis, L.G., Radunskaya, A.E., Wiseman, C.L.: A validated mathematical model of cell-mediated immune response to tumor growth. Cancer Res. **65**, 7950–7958 (2005)
8. De Pillis, L.G., Mallet, D.G., Radunskaya, A.E.: Spatial tumor-immune modeling. Comput. Math. Meth. Med. **7**, 159–176 (2006)
9. DuPage, M., Mazumdar, C., Schmidt, L.M., Cheung, A.F., Jacks, T.: Expression of tumour-specific antigens underlies cancer immunoediting. Nature **482**, 405–409 (2012)
10. Eftimie, R., Bramson, J.L., Earn, D.J.: Interactions between the immune system and cancer: a brief review of non-spatial mathematical models. Bull. Math. Biol. **73**, 2–32 (2011)
11. Guloglu, F.B., Ellis, J.S., Wan, X., Dhakal, M., Hoeman, C.M., Cascio, J.A., Zaghouani, H.: Antigen-free adjuvant assists late effector CD4 T cells to transit to memory in lymphopenic hosts. J. Immunol. **191**, 1126–1135 (2013)
12. Hillen, T., Enderling, H., Hahnfeld, P.: The tumor growth paradox and immune system-mediated selection for cancer stem cells. Bull. Math. Biol. **75**, 161–184 (2013)
13. Jäeger, E., Bernhard, H., Romero, P., Ringhoffer, M., Arand, M., Karbach, J., Ilsemann, C., Hagedorn, M., Knuth, A.: Generation of cytotoxic T-cell responses with synthetic melanoma-associated peptides in vivo: implications for tumor vaccines with melanoma-associated antigens. Int. J. Cancer **66**, 162–169 (1996)
14. Kim, P., Lee, P., Peter, P.: Dynamics and potential impact of the immune response to chronic myelogenous leukemia. PLoS Comput. Biol. **4**, e1000095 (2008)
15. Kim, P., Lee, P., Levy, D.: A theory of immunodominance and adaptive regulation. Bull. Math. Biol. **73**, 1645–1665 (2011)
16. Komarova, N., Barnes, E., Klenerman, P., Wodarz, D.: Boosting immunity by anti-viral drug therapy: a simple relationship between timing, efficacy and success. Proc. Natl. Acad. Sci. **100**, 1855–1860 (2008)

17. Kolev, M., Kozlowska, E., Lachowicz, M.: A mathematical model for single cell cancer-immune system dynamics. Math. Comput. Model. **41**, 1083–1095 (2005)
18. Kzhyshkowska, J., Marciniak-Czochra, A., Gratchev, A.: Perspectives of mathematical modelling for understanding of macrophage function. Immunobiology **212**, 813–825 (2007)
19. Ledzewicz, U., d'Onofrio, A., Schattler, H.: Tumor development under combination treatments with anti-angiogenic therapies. Mathematical methods and models in biomedicine. Lecture Notes on Mathematical Modelling in the Life Sciences, pp. 311–337. Springer, New York (2013)
20. Lollini, P.L., Palladini, A., Pappalardo, F., Motta, S.: Predictive models in tumor immunology. In: Bellomo, N., De Angelis, E. (eds.) Selected Topics in Cancer Modeling, vol. 4, pp. 363–384. Birkhäuser, Boston (2008)
21. Lorenzi, T., Lorz, A., Restori, G.: Asymptotic dynamics in populations structured by sensitivity to global warming and habitat shrinking. Acta Appl. Math. (2013). doi:10.1007/s10440-013-9849-9
22. Lorz, A., Lorenzi, T., Clairambault, J., Escargueil, A., Perthame, B.: Effects of space structure and combination therapies on phenotypic heterogeneity and drug resistance in solid tumors (2013, preprint)
23. Matzavinos, A., Chaplain, M.A.J., Kuznetsov, V.A.: Mathematical modelling of the spatio-temporal response of cytotoxic T-lymphocytes to a solid tumor. Math. Med. Biol. **21**, 1–34 (2004)
24. Palucka, K., Banchereau, J.: Cancer immunotherapy via dendritic cells. Nat. Rev. Cancer **12**, 265–277 (2012)
25. Perelson, A., Weisbuch, G.: Immunology for physicists. Rev. Mod. Phys. **69**, 1219–1268 (1997)
26. Plesa, A., Ciuperca, G., Genieys, S., Louvet, V., Pujo-Menjouet, L., Dumontet, C., Volpert, V.: Diagnostics of the AML with immunophenotypical data. Math. Mod. Nat. Phen. **2**, 104–123 (2006)
27. Ravkov, E.V., Williams, M.A.: The magnitude of CD4+ T cell recall responses is controlled by the duration of the secondary stimulus. J. Immunol. **183**, 2382–2389 (2009)
28. Ricupito, A., Grioni, M., Calcinotto, A., Hess Michelini, R., Longhi, R., Mondino, A., Bellone, M.: Booster vaccinations against cancer are critical in prophylactic but detrimental in therapeutic settings. Cancer Res. **73**, 3545–3554 (2013)
29. Rosenberg, S.A., Yannelli, J.R., Yang, J.C., Topalian, S.L., Schwartzentruber, D.J., Weber, S.J., Parkinson, D.R., Seipp, C.A., Einhorn, J.H., White, D.E.: Treatment of patients with metastatic melanoma with autologous tumorinfiltrating lymphocytes and interleukin 2. J. Natl. Cancer Inst. **86**, 1159–1166 (1994)
30. Semino, C., Martini, L., Queirolo, P., Cangemi, G., Costa, R., Alloisio, A., Ferlazzo, G., Sertoli, M.R., Reali, U.M., Ratto, G.B., Melioli, G.: Adoptive immunotherapy of advanced solid tumors: an eight year clinical experience. Anticancer Res. **19**, 5645–5649 (1999)

Modeling Tumor–Immune Dynamics

Lisette G. de Pillis and Ami E. Radunskaya

Abstract Mathematical models of tumor–immune interactions provide an analytical framework in which to address specific questions regarding tumor–immune dynamics and tumor treatment options. We present a mathematical model, in the form of a system of ordinary differential equations (ODEs), that governs cancer growth on a cell population level. In addition to a cancer cell population, the model includes a population of Natural Killer (NK) and $CD8^+$ T immune cells. Our goal is to understand the dynamics of immune-mediated tumor rejection, in addition to exploring results of applying combination immune, vaccine and chemotherapy treatments. We characterize the ODE system dynamics by locating equilibrium points, determining stability properties, performing a bifurcation analysis, and identifying basins of attraction. These system characteristics are useful, not only for gaining a broad understanding of the specific system dynamics, but also for helping to guide the development of combination therapies. Additionally, a parameter sensitivity analysis suggests that the model can predict which patients may respond positively to treatment. Numerical simulations of mixed chemo-immuno and vaccine therapy using both mouse and human parameters are presented. Simulations of tumor growth using different levels of immune stimulating ligands, effector cells, and tumor challenge, are able to reproduce data from published studies. We illustrate situations for which neither chemotherapy nor immunotherapy alone are sufficient to control tumor growth, but in combination the therapies are able to eliminate the entire tumor.

L.G. de Pillis (✉)
Department of Mathematics, Harvey Mudd College, Claremont, CA, USA
e-mail: depillis@hmc.edu

A.E. Radunskaya
Department of Mathematics, Pomona College, Claremont, CA, USA
e-mail: aradunskaya@pomona.edu

A. Eladdadi et al. (eds.), *Mathematical Models of Tumor-Immune System Dynamics*, Springer Proceedings in Mathematics & Statistics 107,
DOI 10.1007/978-1-4939-1793-8_4

1 Introduction

There are many unanswered and important questions as to how the immune system interacts with a growing tumor, and which components of the immune system play significant roles in responding to immunotherapy. For example, does the varying strength of an individual's immune response play a significant role in affecting tumor growth during treatment, and if so, is it possible to predict which individuals will respond well, and which will not? Mathematical models provide an analytical framework in which to address such questions, and these models can be used both descriptively and predictively. It is important to develop models of tumor growth that include a representation of an immune response. The ultimate goal is to create models that can reflect a system's response to emerging biological therapies, such as vaccine therapy. Mathematical modeling of tumor growth and treatment has been approached by a number of researchers using a variety of models over the past decades. (For overviews, see for example [4, 9, 27, 55, 68].)

The Importance of the Immune System and Immunotherapy Immunotherapies are quickly becoming an important component in the multi-pronged approaches being developed to treat certain forms of cancer. The goal of immunotherapy is to strengthen the body's own natural ability to combat cancer by enhancing the effectiveness of the immune system. The importance of the immune system in fighting cancer has been verified in the laboratory as well as with clinical experiments. See, for example, [28, 52, 53, 57, 69]. Additionally, it is known that those with weakened immune systems, such as those suffering from AIDS, are more likely to contract certain rare forms of cancer. This phenomenon can be interpreted as providing further evidence that the role played by the immune response in battling cancer is critical. See, for example, [12, 38].

The clear importance of the immune system in controlling cancer growth, both clinically and mathematically, indicates that models incorporating tumor growth and treatment would do well to include an immune system component. Once this component is in place, it is then possible to model how various immunotherapies may affect the system, either singly or in combination with one another. Recent clinical data have shown there is potential benefit in harnessing the power of the immune system in combination with traditional chemotherapy. For example, in Wheeler et al. [72], it is demonstrated that vaccine therapy in combination with chemotherapy more effectively extends patient survival times than either chemotherapy or vaccine therapy alone.

Immunotherapy The clinical evidence for the potential of immune system control of certain malignancies has motivated new research into the development of immunotherapies and vaccine therapies for cancers. Some examples are described in [5, 11, 25, 59, 65, 72]. Immunotherapy falls into three main categories: immune response modifiers, monoclonal antibodies, and vaccines (see, for example, [64]). The first category contains substances that affect the immune response, such as interleukins (including IL-2), interferons, tumor necrosis factors (TNF), colony-stimulating factors (CSF), and B-cell growth factors. In the next category,

monoclonal antibodies are currently being developed to target specific cancer antigens. These monoclonals can distinguish between normal and cancer cells, and they can then be used to diagnose cancer, as well as to treat tumors by "guiding" anticancer drugs toward the malignant cells (see, e.g., [34, 48, 62]). In the third category are vaccines, which are generally used therapeutically, and are created from tumor cells. These work by helping the immune system to recognize and attack specific cancer cells. In this work, we implement treatment from the first category in the form of mathematical terms that represent IL-2 and tumor infiltrating lymphocyte (TIL) injections, and additionally incorporate treatment from the third category: new mathematical forms that distinguish between specific and nonspecific immune responses, allowing for the incorporation of a vaccine component into the model. Although monoclonal antibody treatments are considered promising, they are currently not considered in this work.

Cancer Vaccines There are fundamental differences between the use and effects of antiviral vaccines and anticancer vaccines. While many vaccines for infectious diseases are preventative, cancer vaccines are designed to be used therapeutically, treating the disease after it has begun, and preventing the disease from recurring. Cancer vaccines are still considered to be highly experimental as compared with other forms of cancer immunotherapy, but in early clinical trials are showing increasing promise in their ability to improve the immune response to certain forms of cancer (see, e.g., [64, 72]).

Since cancer vaccines and antiviral vaccines differ in their application, mathematical models of these vaccines should exhibit different dynamics. The goal of this chapter is to build on existing models of tumor growth, incorporating an immune system response and expanding these models to include the effect of anti-tumor vaccination and immunotherapies in conjunction with chemotherapies. In another work, the authors will extend this model into a larger framework that incorporates spatial and geometric components.

The outline of this chapter is as follows. In Sect. 2 we describe four cell population growth models that are commonly used to represent cancer growth, and outline a parameter fitting approach that can extract growth parameters from laboratory data. In Sect. 3, we discuss growth and interaction dynamics governing an immune response to tumor, assuming a single population representing effector-killer cells of the immune system. In Sect. 4 we further expand our description of the immune response to include both the innate and the specific responses, and in Sect. 5, we formulate the mathematical forms that govern the different dynamics of the innate and specific immune responses. In Sect. 6, we construct a three population mathematical model that describes the interactions of a tumor cell population with both the innate and specific immune cell populations. We also carry out a parameter sensitivity analysis, as well as a bifurcation analysis of the system. In Sect. 7, we build upon our three population model to allow for simulation of treatments. Treatment modalities include both cytotoxic chemotherapy and immune-stimulating therapies. We present numerical simulations that represent both mouse and human scenarios, using parameters extracted from published literature. Finally, in Sect. 8, we provide a discussion and summary of this work.

2 Growth Models

An important step in building a tumor–immune model is to capture the dynamics of tumor cell population growth alone, before considering growth-limiting interference from, for example, immune cells or from competition by normal cells for nutrients and space. There is, so far, no universal consensus as to which fundamental growth models best reflect tumor cell growth. Among the most commonly used models, however, are exponential growth (and its generalization, power law growth), logistic growth, Von Bertalanffy growth, and Gompertz growth. The forms of these growth laws are in Table 1. All but von Bertalanffy growth require two parameter values be determined. The Von Bertalanffy model requires three parameter values.

Table 1 Commonly used cell population growth laws

Growth law	Equation	Number of parameters
Power	$\frac{dT}{dt} = aT^b$	Two: a, b.
Logistic	$\frac{dT}{dt} = aT(1 - bT)$	Two: a, b.
Gompertz	$\frac{dT}{dt} = aT \ln(1/bT)$	Two: a, b.
von Bertalanffy	$\frac{dT}{dt} = aT\left((bT)^c - 1\right)$	Three: a, b, c.

T represents the number of tumor cells, t is time, a, b and c are parameters

The choice of growth law depends, among other things, on the cancer cell type, whether the cancer is early or late stage, and the location of the tumor. In the case of tumor stage, consider, for example, a comparison of exponential and logistic growth models. As can be seen in Fig. 1, in which we compare exponential to logistic growth, if the tumor is small (early stage), there is no significant distinction between the two growth models. The distinction becomes apparent, however, in the later stages. As opposed to exponential growth, logistic growth is self-limiting. Even though there are no external growth-limiting factors, a self-limiting growth model, such as a logistic model, accounts for self-competition within the tumor cell population for resources like space and nutrients. An exponential growth model is reasonable to use for early stage growth, but a self-limiting growth model is often more appropriate for later stage growth. Therefore, even in the absence of tumor growth data, a modeler can consider tumor size and make a qualitative decision about whether to the model should reflect self-limiting growth.

Ideally, a modeler will be able to acquire some tumor growth data, and should use the model that provides the best fit to those data. The process of fitting a model to the data also yields the appropriate model parameters. There are a number of approaches to data fitting that are possible. One approach to fitting a model to data is numerical, and makes use of packaged computational routines. In Matlab [70], for example, the simplest way to fit a curve to a data set is to plot the data points and make use of Matlab's `Basic Fitting` tool from the pull-down menu of the figure window. However, the choice of curves that can be fit to the data is limited to splines and polynomials. If we want to determine how well the solutions to our growth laws of

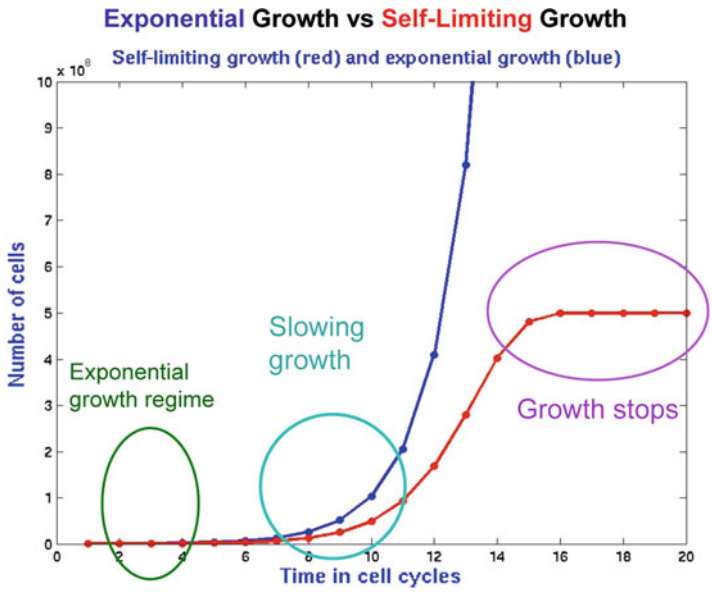

Fig. 1 Exponential versus logistic versus growth. In early stage growth, cycle zero through about cycle 6, both models are similar, and appear to overlap. After cycle 6, the two graphs begin to diverge, and by cycle 14, the growth curves have diverged significantly. By cycle 15, the logistic growth curve has leveled off, but the exponential growth curve continues to increase

interest could fit a data set, our numerical approach requires a different approach. The steps in the process are as follows.

1. Choose a tumor growth data set. Many tumor growth data sets are given in units of approximate volume, surface area, cross sectional area, or relative volume. Since the growth laws we are considering represent numbers or concentrations of cells, then if the data are not already given in cell counts, convert the measures to approximate cell counts. A useful conversion metric assumes that there are generally between 1.0×10^6 cellls/mm^3 and 2.0×10^6 cells/mm^3, [51]. Suppose we have n data points. Let us call the time-data pairs (t_i, d_i), where $i = 1, \cdots, n$.
2. Assume the tumor cell population, $T(t)$, obeys a particular growth law, which in our case will be chosen from Table 1.
3. Solve for $T(t_i)$, that is, determine the model's predicted population values at the same time points, t_i, as are used in the data set. For relatively simple ODE laws, like the ones in Table 1, it is actually possible to find explicit solution formulas. Solutions to the four growth law ODEs are given in Table 2. However, it is also acceptable to solve these ODEs numerically. There are many options for how to do this in Matlab. For example, Matlab's `ode45` routine uses an adaptive fourth and fifth order Runge–Kutta scheme, and the numerical solutions are highly accurate in most cases. Many ODEs are not easily solved analytically, but are fairly straightforward to solve numerically. Thus, a numerical approach is generally more universally applicable.

4. Choose a metric, or distance. If you are working in Matlab, you can write a function in an m-file that Matlab can minimize. The function should return the sum of the squares of the distances of the solution (analytic or numerical) to the data points. Suppose we are fitting the logistic curve. Then the distance D depends on the two parameters a and b, and is given by

$$D(a,b) = \sum_{i=1}^{n} (T_{(a,b)}(t_i) - d_i)^2$$

where $T_{(a,b)}(t_i)$ is the chosen model output at time point t_i using parameters a and b. The input to the distance function includes a vector of the unknown parameters $[\,a \quad b\,]$, in addition to the known values of the data points $\{(t_i, d_i)\}$, and the solution to the ODE, $T(t)$. In some cases, the uncertainty in the data should be taken into account when defining the distance function. For example, in many cases the data at later time points have more variability, since small differences in initial conditions can grow over time. We have often found it fruitful to use a *weighted distance function*, where the distance to each data point is normalized by the standard error at that time point.
5. Call a function minimization routine to minimize the distance function $D(a,b)$. Here, again, there is a variety of possible approaches. Routines that look for function minima can be classified broadly as either "local" or "global" search algorithms. A "local" minimization routine will attempt to move closer to the function minimum with every step. In our case, this is done by ensuring that the distance function $D(a,b)$ can only decrease or stay the same with every iteration of the search, but $D(a,b)$ will never be allowed to increase. The result is that if we start our search near to a local function minimum, the local algorithm will converge fairly rapidly to that close minimum point, even if there is a "better" minimum point somewhere else in the function. Global search algorithms, on the other hand, try to broaden the search for the "best" (or "global") minimum by occasionally allowing the distance function to increase before decreasing it again. One can think of this temporary increase in $D(a,b)$ as the search function allowing us to climb a hill that will move us to a different, deeper, valley, in which a better minimum can be found. Local algorithms that can search for a function's minimum include Newton's method, the Conjugate Gradients method, and the Nelder–Mead Simplex algorithm. These approaches depend on choosing initial guesses for the values of the parameters a and b, and the accuracy of the initial guess affects the outcome of the minimization. Matlab has a built-in routine `fminsearch` that minimizes an input function using the Nelder–Mead algorithm. Matlab also has the routine `lsqnonlin`, that specifically solves nonlinear least squares problems. As opposed to local algorithms, global parameter estimation algorithms are able to test a broader range of parameters, and are therefore less likely to get "stuck" in a local minimum, but they also may not yield values as accurate as local methods can. Global approaches include algorithms such as simulated annealing [37],

and Markov Chain Monte Carlo [32, 67]. Whether a local or global approach is employed, this step will return values for the model parameters (a and b in the case of logistic growth), as well as the distance measure that indicates how good the model fit is (the smaller the distance, the better the fit).

Table 2 Solutions to the four commonly used cell population growth laws

Growth law	Equation	Solution
Power	$\frac{dT}{dt} = aT^b$	$T(t) = ((1-b)(at+C))^{1/(1-b)}$, where $C = \frac{T_0^{1-b}}{(1-b)}$
Logistic	$\frac{dT}{dt} = aT(1-bT)$	$T(t) = \frac{1}{Ce^{-at}+b}$, where $C = \frac{1}{T_0} + b$
Gompertz	$\frac{dT}{dt} = aT\ln(1/bT)$	$T(t) = b\left(\frac{T_0}{b}\right)^{e^{(-at)}}$
von Bertalanffy	$\frac{dT}{dt} = aT\left((bT)^c - 1\right)$	$T(t) = \frac{1}{b}\frac{T_0^c}{\left(T_0^c(1-e^{-act}) + e^{\frac{-act}{b^c}}\right)^{1/c}}$

T represents the number of tumor cells, t is time, a, b and c are parameters. In each case, the given initial condition is $T(0) = T_0$

As an example, we took a published tumor growth data set from Diefenbach et al. [24], and fit each of the four growth curves to the data. This example can also be found in [19,20]. Combining Matlab's `ode45` adaptive Runge–Kutta ODE solver to get predicted solutions for $T(t)$ with `fminsearch` to find the parameter values that minimized the distance between the data points and the model prediction, yielded the fits seen in Fig. 2. The data we show are from Diefenbach[24] experiments in which groups of immuno-compromised mice were challenged with increasing levels of B16-BL6 (a melanoma cell line). Data set 1 represents the mean tumor cell count in five mice over 33 days after an initial inoculation with 10^4 melanoma cells. Data set 2 tracks over 23 days the mean tumor growth data in five mice after an inoculation of 10^5 cells, and Data set 3 tracks the mean growth in five mice after an inoculation of 10^6 melanoma cells, also over 23 days. With each growth curve, we also plot the "residual:" the distance between each data point and the predicted value given by the growth curve. The best fits are those with the smallest residuals. We can see from Fig. 2 that the smallest residuals and thus the best fits appear to come from the logistic model and the von Bertalanffy model. However, the principle of "parameter parsimony" says that the model with the fewest parameters that still yields a good fit is preferable. Therefore, we should choose to use the logistic model over the von Bertalanffy model, since the logistic model requires fitting one less parameter.

The interested reader can find in [66] a larger catalog of fits of these four growth laws to ten separate tumor cell types: bladder cancer, breast cancer, colon cancer, head and neck squamous cell carcinoma, hepatocellular carcinoma, lung cancer, melanoma, ovarian cancer, pancreatic cancer, and renal cell carcinoma. In that work, tumor growth information for each cell line came from collecting published peer-reviewed data from at least five separate sources. Similar to the results of [35], the authors found that the power growth law often yielded a good fit in the sense of minimizing the residual.

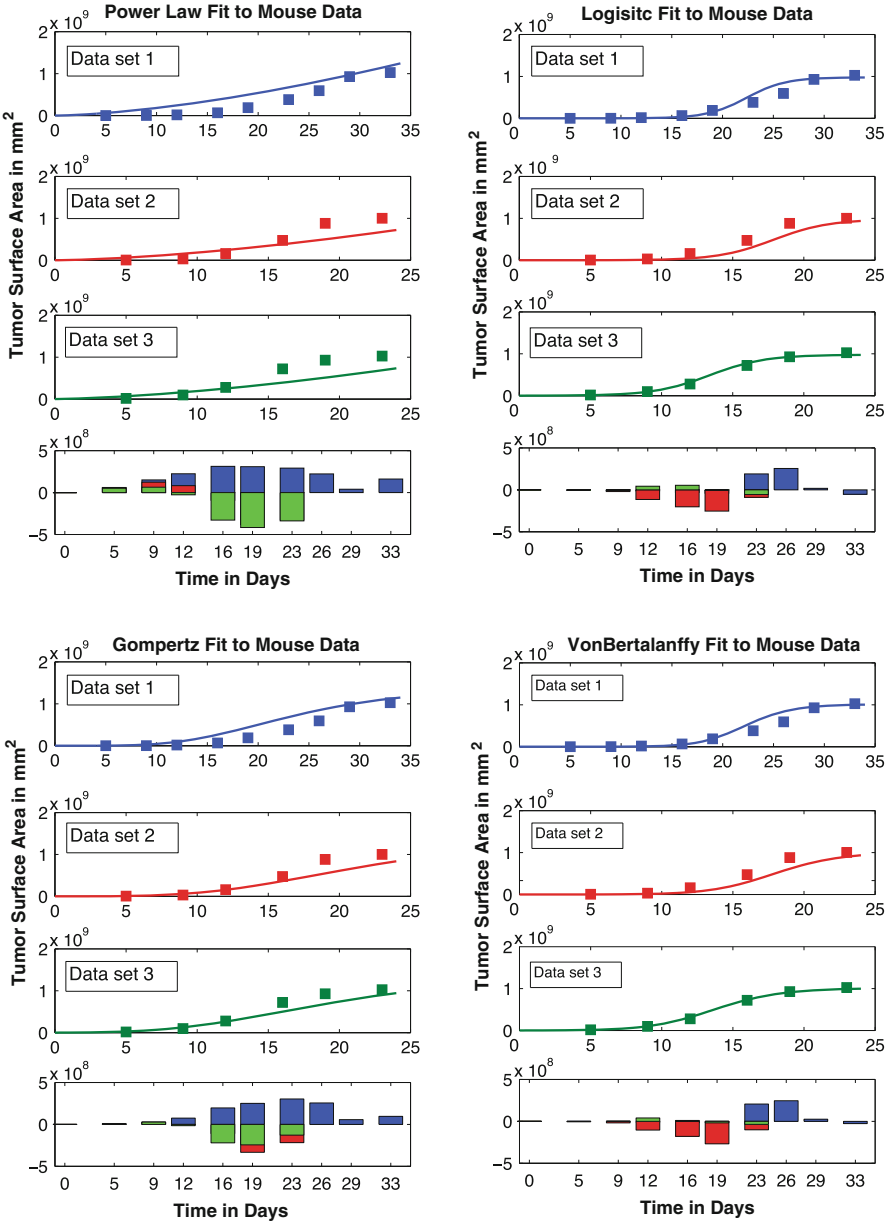

Fig. 2 A comparison of four growth laws. Data from [24], which describes three different mouse experiments (marked as "Data set 1," "Data set 2," and "Data set 3," respectively), are used to fit four different growth laws. Data set 1 represents the mean tumor growth values in a group of five

3 Competition Models: Adding the Immune System

An individual's immune system is created to help defend the body from invading pathogens such as bacteria, fungi, viruses, parasites, and in some cases, cells in the body that have become cancerous. The immune system is made up of a wide variety of cells with different functions, ranging from antigen uptake and presentation to killing of infected or mutated cells. The immune cells are created in the bone marrow and can be found in the blood and tissue of an individual. The immune cells in the blood are commonly known as the "white blood cells," and the average human body makes about 10^9 new white blood cells each day.

The immune response to the presence of a foreign substance is a complex cascade of events, including self-regulating feedback loops. Although there is much we have learned about the dynamics of the immune response, there is still much we do not fully understand. Details about some of the known complex workings of the immune system can be found in [54].

One goal of the immune response is to attack and destroy harmful cells. Immune cells with the ability to kill are called *effector* cells. In this section we introduce effector cells into the model of tumor growth. In the simplest realization, we use a competition model consisting of a system of two differential equations: one equation describing the growth of the tumor population, and one equation describing the growth of the effector cell population.

Early tumor–immune models used the "predator–prey" relationship developed by Lotka in 1910, and then used by Kolmogorov and subsequently by Volterra in 1925 to describe the fate of fish populations in the Adriatic [1,43,71]. In the context of tumor growth, effector cells play the role of the predators, and tumor cells are the prey. Let T denote the population of tumor cells, and E the population of effector cells. The classical predator–prey relationship assumes:

1. the prey will grow in the absence of the predator;
2. interactions between predator and prey are harmful to the prey but beneficial to the predator;

Fig. 2 (continued) mice after an initial challenge of 10^4 melanoma cells. Data set 2 shows growth after a challenge with 10^5 melanoma cells, and Data set 3 shows growth after a challenge with 10^6 cells. The solution to each growth model is shown in *solid curves*, while the data points are shown by *filled squares*. In each case, the parameters of the models are chosen to minimize the least squares distance from the model's predicted values to the data. Residuals showing the difference between the predicted values and the data are shown as *bars* below the graphs in each case. Note that the first data set has more time points than the other two, so that the last three residuals are due to differences coming only from the first data set. The two models shown in the *left column*, the power law and the Gompertz models, have larger residuals than do the two models depicted on the *right*, the logistic and the von Bertalanffy models. Since the logistic model uses fewer parameters than does von Bertalanffy, we consider logistic growth to yield the best fit to these data

3. the predators will die in the absence of prey;
4. the number of interactions between predators and prey is proportional to the product of the two populations.

If we describe the growth of the tumor population using a logistic function, these assumptions yield the following system of differential equations.

Simplest predator–prey model of tumor (prey) and effector–immune (predator) interactions:

$$\text{Tumor:} \quad \frac{dT}{dt} = rT(1 - bT) - c_1 TE \tag{1}$$

$$\textit{Effector}: \quad \frac{dE}{dt} = -dE + c_2 TE \tag{2}$$

where c_1, c_2, d and r are constants.

The interaction terms in Eqs. (1)–(2) have a "mass-action" form, reflecting Assumption 4, that the total number of encounters between predators and prey are proportional to the product of the two populations. This follows from a well-mixed condition, i.e. we assume that each predator is equally likely to encounter each prey. The discerning reader might note that this will not be the case in the context of the immune response to solid tumors in vivo, since immune cells won't have equal access to all of the tumor cells. We discuss this further in Sect. 5.

Another problem with this simple model is that Assumptions 2 and 3 are not biologically realistic in the context of tumor–immune interactions. Effector cells can kill tumor cells in one of two ways: by damaging the tumor cell's membrane using a protein called *perforin*, or by initiating *apoptosis* (programmed cell death) via another protein called *FasL*. Since effector cells produce these proteins in a limited amount, each interaction decreases their ability to kill in the future. We therefore introduce a negative *inactivation* term into Eq. (2). Counteracting this negative effect is the fact that the presence of the tumor cells stimulates the production of new immune cells, and the recruitment of these immune cells to the site of the tumor However, there is some limit to the rate at which the body can produce these cells. We therefore introduce a positive *rate-limiting recruitment* term in the Effector cell equation shown in Fig. 3.

Effector immune cells are present in the body even in the absence of a specific threat. This "standing army" of cells is created in the bone marrow, and distributes itself in the tissues, blood and organs in search of harmful cells. We therefore include in the simple effector–tumor model a constant source rate of effector cells, σ, noting that in reality this rate will change with the overall condition of the host, as well in response to complex regulatory signals from the immune system. Putting these terms together gives a two-population model of the tumor–immune response:

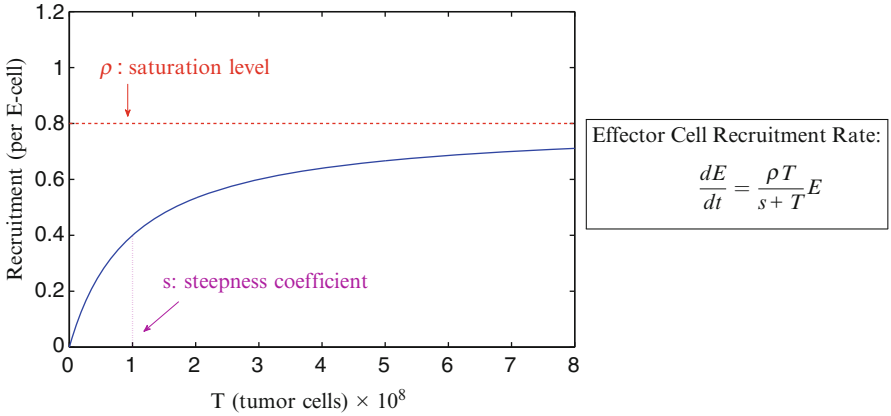

Fig. 3 Saturating recruitment term. This type of term occurs frequently in biological and physical models where rates cannot be infinite

Two-population model of tumor and effector–immune interactions:

$$\text{Tumor:} \quad \frac{dT}{dt} = rT(1 - bT) - c_1 TE \tag{3}$$

$$\text{Effector:} \quad \frac{dE}{dt} = \sigma + \frac{\rho T}{s + T} - c_2 TE - dE \tag{4}$$

where $c_1, c_2, d, \sigma, \rho, s$ and r are constants.

This two-population model has been useful in describing observed behavior that was mysterious to clinicians. For example, in the work of Kuznetsov et al. [45, 46], in which the nonlinear dynamics of immunogenic tumors are examined, this tumor–effector model is shown to exhibit oscillatory growth patterns in tumors, as well as dormancy and "creeping through": when the tumor stays very small for a relatively long period of time, and subsequently grows to be dangerously large (Fig. 4). This model also demonstrates that two simulated patients could begin with almost identical characteristics (IC1 and IC2 in Fig. 4), but one has a progressive disease (IC2) while the immune response of the other patient is able to keep the tumor relatively small (IC1). Note that, in this case, it is only the initial number of immune cells that makes the difference, and that the results are non-intuitive: a slightly *lower* initial immune response (IC1) results in a smaller tumor. This non-intuitive behavior can be understood by knowing the geometry of the phase space of the dynamical system: a *separatrix*, the stable manifold of the unstable, saddle equilibrium separates the basins of attraction of the two stable equilibria. Initial conditions close to the basin boundaries, but on opposite sides of the separatrix, give rise to trajectories with drastically different long-term behavior.

In this and other mathematical models, the cyclical behavior of the tumor is directly attributable to the interaction of the tumor with the immune system. In [16], the authors also use a single effector population to represent the immune response, and are able to demonstrate the critical role this effector response plays in the process of tumor elimination, even when chemotherapy treatments are given. We discuss models with treatments in Sect. 7.

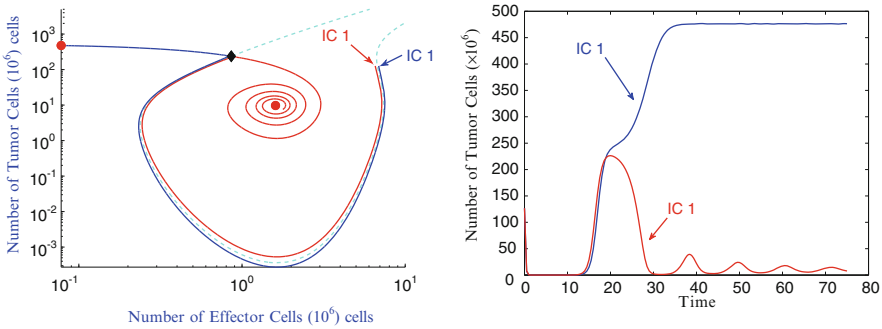

Fig. 4 Simulations of the two-population model (Eqs. 3–4) showing sensitivity to initial conditions and the "creeping through" effect. The separatrix or stable manifold of the saddle equilibrium is shown as a *dashed line* in the *left panel*. Two simulations are shown: one with initial conditions $E(0) = 6.5558$ (labeled "IC 1" in *red*) and one with $E(0) = 6.8777$ (labeled "IC 2" in *blue*). Both simulations have initial tumor values at $T(0) = 126.6807$. *Left panel* The two trajectories are shown in the sate space: in both trajectories, the tumor values initially get very small and remain there for a while. The first trajectory (IC1) is in the basin of attraction of the low tumor equilibrium, and it spirals towards it. The second trajectory (IC2) is in the basin of attraction of the large tumor equilibrium, which it approaches quickly after the initial "dormant" period. Note the logarithmic scale in the *left panel*. *Right panel* The same two trajectories are shown over time. Only the tumor populations are plotted in the *right panel*. Units are 10^6 cells. The parameter values used in these simulations are $a = 1.636, b = 0.002, d = 0.3743, s = 20.19, c_1 = 1, c_2 = 0.00311, \rho = 1.131$ and $\sigma = 0.06$

4 The Innate and Adaptive Immune Response

As we build a mathematical model, our goal is to keep the model as simple as possible while still addressing the question of interest. If the model is found to be too simple, we then add complexity in steps. The simple model given in Eqs. (3) and (4) assumes that the response of the immune system can be represented by a single "effector" cell population. This simplification of the immune system works well when modeling clinically observed tumor–immune behaviors such as tumor dormancy, oscillations in tumor size, and spontaneous tumor regression.

This simplified single-population representation of the immune system is obviously not sufficient, however, to address questions specific to the roles different components of the immune response play in the evolution of a tumor. The next question we will address, as we continue to build and refine our model, is driven

by the results of a set of experiments by Diefenbach et al. In these experiments, mouse tumor cell lines are modified to express higher levels of immune stimulating NKG2D ligands, and the responses of both the "innate" and "specific" components of the immune system are observed.

Immune cells called NK "Natural Killer" cells, are part of the innate, or non-specific, immune response. Killer T "Thymus" cells are part of the specific, or adaptive, immune response, and are activated differently from NK cells. The Killer T cells are also referred to as CTL "Cytotoxic T Lymphocyte" cells, or $CD8^+$ T cells (which distinguishes them from $CD4^+$ T helper cells). Both NK cells and Killer T cells come from a common lymphoid progenitor, and once activated, are both called "effector" cells. We next briefly discuss the differences between the innate and specific responses and discuss their behaviors in very general terms before introducing the model in Sect. 6 that includes these as separate populations.

The innate immune response, which includes NK cells, is an early defense against pathogens. The NK cells patrol the body, searching for and killing cells that they do not recognize as "self" cells (belonging to the body). NK cells are large granular lymphocytes which do not express markers of either T or B-cell lineage. NK cells recognize and destroy tumor cells, among others, independent of prior exposure. Natural killer cells are thought to play a key role in preventing the development of clinical cancer by killing abnormal cells before they multiply and grow. One way NK cells recognize that a potential target cell is a "self" cell is when the target cell presents self antigens through MHC class I receptors on its surface. When an NK cell comes in contact with a potential target cell, kill-activating receptors attach to common glycoproteins on the potential target cell, and the NK cell is primed to kill. However, if the target cell is expressing self antigens in the MHC-I receptor, when the NK cell binds to the MHC-I-self-antigen complex, the kill signal is interrupted and neutralized, and the potential target cell remains unharmed. In the case that the target cell is not expressing a self antigen in the MHC-I receptor, the activated NK cell will continue in kill mode, releasing perforin and granzymes, leading to the destruction of the target cell. The NK cell will also continue in kill mode if the target cell is simply not expressing MHC-I receptors on its surface. Downregulated MHC-I receptor expression means that the NK cell cannot bind to that receptor, and there therefore is nothing to inhibit the NK cell's kill signal. In some cancer cells, MHC-I receptors are down-regulated on the cell surface, and are therefore susceptible to NK cell attack. In a sense, when a potential target cell expresses the self-antigen-MHC-I receptor complex, this can be thought of as the cell knowing the "secret handshake," which allows it to escape NK cell patrols unharmed.

Killer T cells are unlike NK cells in that they must first be primed to recognize a particular antigen, and in the case of cancer, to recognize a tumor-specific antigen. The killer T cells, which carry the $CD3^+$ marker, are morphologically small lymphocytes in the peripheral blood. They develop in the thymus and mediate the immune system's response to infected or malignant cells. These $CD3^+CD8^+$ T cells (or just "$CD8^+$" T cells) are a critical subpopulation of T-lymphocytes that can be cytotoxic to tumor cells provided previous sensitization has occurred.

$CD8^+$ T cells are able to kill tumor cells through recognition of the tumor-specific antigen presented on MHC-I receptors on the surface of the tumor cell. The tumor-antigen specific T cell binds to the MHC-I-tumor-antigen complex. Once bound, the $CD8^+$ T cell is triggered to release perforin and granzymes, leading to the destruction of the target tumor cell. The $CD8^+$ T cell can be thought of as a "police dog trained in scent discrimination"—it first has to be taught what its target is, and only then, can it seek out that specific target.

In summary, both NK cells and CTL cells must come in contact with target tumor cells in order to be able to kill them. The NK cells need no priming, are constantly on patrol, and kill tumor cells when they do not recognized them as "self." The CTL cells, on the other hand, must first be primed to recognize antigen specific to the tumor cells, and only then will be able to destroy the target tumor cells.

5 Estimating Kill Rates from Data: The de Pillis–Radunskaya Law

In this section we explore how the differences between the innate and adaptive immune response manifest themselves in a mathematical model of tumor–immune interactions. In particular, we want to look more closely at the "kill rate" term given as c_1TE in Eq. (3). If we divide this term by the number of tumor cells, T, we get the "fractional cell kill rate", which in this simplest mass-action setting is proportional to the number of effector cells. In the context of predator–prey dynamics, the mass-action form is not always appropriate, and the ecological literature discusses alternative forms, (see [2] and the references therein). As we mentioned in Sect. 3, a mass-action kill rate assumes that all immune cells are equally likely to interact with any tumor cell: it assumes *spatial homogeneity*. In reality, however, this is not necessarily the case. In the case of the adaptive immune response, CTLs are recruited to the tumor site by the presence of specific chemicals—not all tumor cells will be equally accessible to this type of attack. A mass-action form of cell kill also precludes "resource sharing": the notion that the number of predators per prey affects the probability of a kill, and hence the benefit to the predator. Resource-sharing suggests that the fractional cell kill will be a function of the *ratio* of predator to prey.

To determine the fractional cell kill dynamics, data from chromium release assays published in [24, 26] were used. Chromium release assays determine the ability of $CD8^+$ T cells to lyse target cells expressing specific ligands. The assays in both [24, 26] were standard 4 h ^{51}Cr release assays. Standard techniques exist for collecting, storing, and co-culturing patients' immune cells with tumor cells, a procedure which can be implemented before the onset of treatment, or anytime thereafter. The lytic activity of these cells can then be analyzed with the assay (see, e.g., approaches referenced in [26]).

We rewrite Eq. (3) in the general form:

$$\frac{dT}{dt} = rT(1 - bT) - g(E, T)T. \tag{5}$$

The function $g(E, T)$ is the fractional cell kill rate, sometimes called the "functional response". In order to determine which fractional cell kill term best fit the data, we performed data fitting experiments with two different functional responses: one that depends only on the number of effector cells, and the other that depends on the ratio of effector to tumor cells.

$$\text{Power Form} \quad g(E, T) = cE^{\lambda}; \tag{6}$$

$$\text{Rational Form} \quad g(E, T) = d\frac{(E/T)^{\lambda}}{s + (E/T)^{\lambda}}. \tag{7}$$

We note that the Power Form has fewer parameters than the Rational Form. Therefore, if we get good fits using both the Power Form and the Rational Form, we should select the Power Form, following the Principle of Parsimony.

Using cell lysis data from [24], we employed an iterative process to find the parameters c and λ in the Power Form that minimized the distance between the data points and the predicted percent lysis curves generated by the model over a range of c and λ values. For each $[c, \lambda]$ pair, a prediction was made by solving a system of differential equations up to time $T_{final} = 4$ h, with initial values from the effector:target ratio data in [24]. When using data from assays using only NK cells, the Power Form provided a good fit, with the best-fit exponent begin $\lambda \approx 1$. Since a good mathematical model will be one in which the desired behaviors of the system are captured using the simplest mathematics possible, we chose to keep the mass-action form, $g(E, T) = -cE$, to describe the effect of the NK cells on tumor cells. In fact, the optimal value of c determined using our algorithm reproduced the lysis rate data extremely well (see Fig. 5, top row).

However, when fitting for parameters c and λ for the $CD8^+$ T cell kill term, we found that the power form produced growth curves for T that were not particularly good fits to the data provided in [24]. Instead, we found that we could produce curves that better fit the data by allowing this term to have the rational form given in Eq. (7), for which we also had to determine parameter s. In (7), the exponent λ represents how the lysis rate depends on the effector:target ratio, the parameter s affects the steepness of the curve, and parameter d gives the maximum lysis rate.

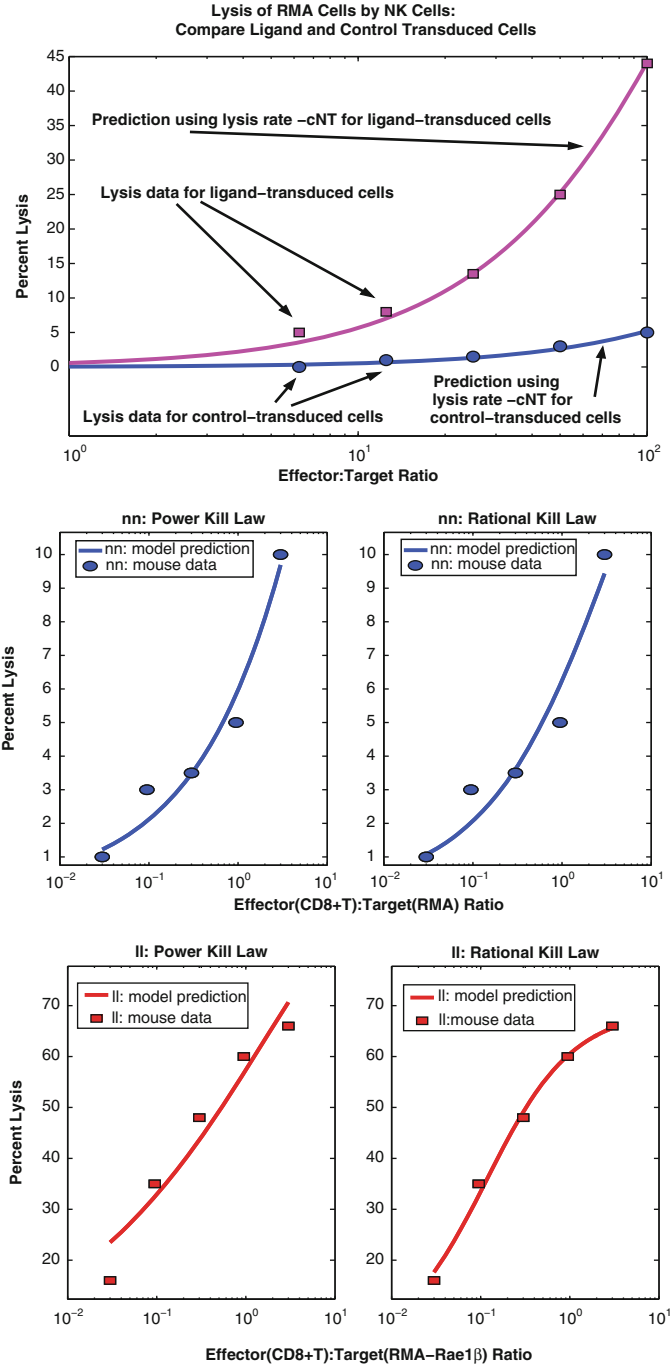
Lysis of RMA Cells by NK Cells:
Compare Ligand and Control Transduced Cells
Percent Lysis
Prediction using lysis rate –cNT for ligand–transduced cells
Lysis data for ligand–transduced cells
Lysis data for control–transduced cells
Prediction using
lysis rate –cNT for
control–transduced cells
Effector:Target Ratio
nn: Power Kill Law
nn: Rational Kill Law
nn: model prediction
nn: mouse data
Percent Lysis
Effector(CD8+T):Target(RMA) Ratio
ll: Power Kill Law
ll: Rational Kill Law
ll: model prediction
ll: mouse data
ll:mouse data
Percent Lysis
Effector(CD8+T):Target(RMA–Rae1β) Ratio

We note that the additional parameter in Eq. (7) gives three degrees of freedom, so that a better fit to the data *should* be expected using the rational form. However, since the observations in [24] give five data points for each cell-type considered, the closeness of fit to the data supports the idea that the form of this term is correct. In particular, both in vitro and in vivo experiments indicate that percent lysis appears to be a function of the *ratio* of $CD8^+$ T cells to tumor cells, explaining the dependence on the ratio (E/T). Furthermore, the data indicate that the percent of cells lysed never exceeds a maximum, a saturation effect that is reflected by the rational form given in Eq. (7).

This saturation effect highlights the fact that the NK cells and $CD8^+$ T cells are interacting with tumor cells in a qualitatively different way, since there is no saturation level for the NK cell competition term. It may be that the NK cell-kill rate could achieve saturation as well in theory, but in practice this does not occur. On the other hand, it may be that the antigen-specific T-cells follow this curve to saturation because they are targeting a specific tumor type, and are therefore more effective in terms of cell–cell interactions.

For conciseness, we will represent the rational form for the fractional cell kill rate with the letter D, and refer to the fact that cell lysis rates by activated $CD8^+$ T-cells agree with this form as the *de Pillis–Radunskaya Law*.

The de Pillis–Radunskaya Law:

For tumor-specific effector cells such as $CD8^+$ T-cells, the fractional kill rate is given by:

$$g(E,T) = D = d\frac{(E/T)^\lambda}{s + (E/T)^\lambda} = d\frac{E^\lambda}{sT^\lambda + E^\lambda} \tag{8}$$

The ratio-dependent form for the fractional cell kill term is mainly phenomenological, in the sense that it models observable outcomes, not direct underlying mechanisms. It is not immediately clear what the individual components of this term

Fig. 5 Comparison of mathematical cell lysis laws. *Top row* NK-Cell Lysis. The *top graph* shows model predictions *smooth curves*) plotted with experimental data (*squares and circles*) from [24] on RMA cells. The *shallow curve* predicts lysis percentages for the control cells, while the steep curve predicts lysis percentages for the ligand-transduced cells. *Center and bottom row* $CD8^+$ T-Tumor Cell Lysis. The *second row* of graphs plots experimental data points (*circles and squares*) taken from [24] against model cell lysis predictions (*solid lines*). The *center graphs* show the power law prediction and the rational law prediction against lysis data for tumor cells whose primary and secondary challenges were with control-transduced tumor cells (RMA cells). The *bottom row* shows the same comparison for tumor cells whose primary and secondary challenges were with ligand-transduced cells (RMA cells transduced with Rae1β ligand)

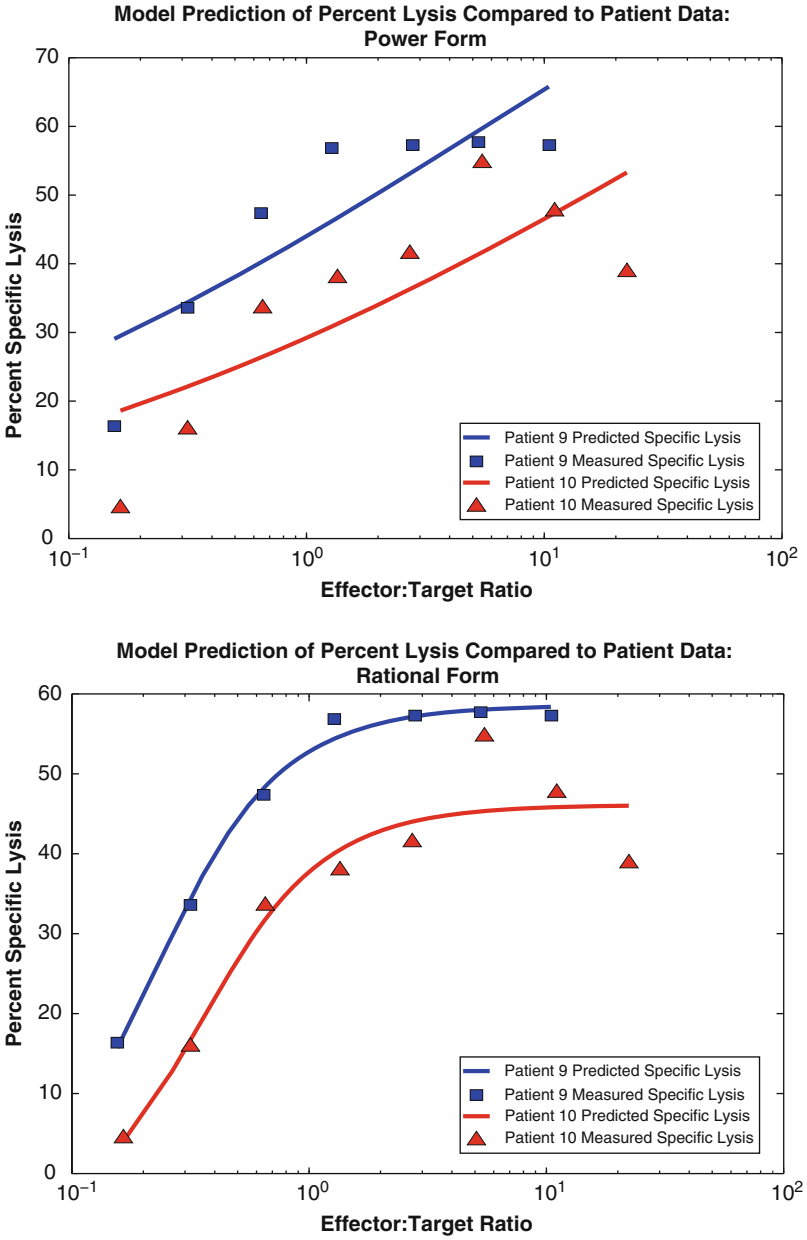

Fig. 6 Model validation using human data from [26]. Presented here is a comparison between the power form and the rational form in describing human ($CD8^+$) T-tumor lysis, as was done in Fig. 5 for mouse data. In *each graph*, two separate simulations are plotted along with data from two different patients who experienced regression of melanoma after receiving TIL treatment.

represent biologically. The use of phenomenological dynamics in modeling biological processes is quite common and can serve to provide predictive capabilities in the model. Such descriptive (as opposed to explanatory) dynamics are frequently used as a foundation on which to build models of tumor development. For example, see the comparison of several phenomenological tumor growth models presented in [7], p. 239. Perhaps future investigations may elucidate the the underlying mechanisms that give rise to the rational form of the fractional cell kill rate in the context of tumor–immune interactions.

5.1 Validation of the de Pillis–Radunskaya Law with Human Data

In order to validate the fundamental model dynamics with respect to the new rational form of the tumor-specific cell lysis term, we performed another comparison of the power form versus rational form predictions, this time using human ($CD8^+$) T-tumor lysis data from [26]. Figure 6 shows the results of this comparison. The top graph shows the power–law predictions plotted against ($CD8^+$) T-tumor lysis data for two separate patients. It is clear that the power–law prediction does not fit the data particularly well. On the other hand, the bottom graph shows the prediction using our newly introduced rational law. In this case, the model can predict cell lysis quite accurately, even when applied to this human data set.

For this particular set of data, effector cells are fairly efficient at lysing tumor cells, with a maximum lysis rate around 60 %. Note that, as with the ligand-transduced mouse data, the difference between the power form and the rational form fractional cell kill rates is quite pronounced, once again indicating that the rational form is particularly well suited to simulating cases in which effector cell lysis rates are relatively strong.

It is necessary in each case to find the parameters which will describe the particular type of tumor–immune interaction under study. The two data sets pictured here underline a feature inherent in the modeling process: there is a wide variety of cell behavior between any two different patients. Care must therefore be taken in making sweeping statements regarding specific responses to treatments, and any quantitative information must be interpreted as one *possibility*, and not as a firm predictor in any given case. However, a large set of simulations, along with

Fig. 6 (continued) The data show results of cytotoxicity assays with TILs taken 7 days after cell transfer. The model predictions are represented by the smooth curves, while the experimental data are represented by *squares* for patient nine and *triangles* for patient 10. Note, once again, that the rational form for predicting ($CD8^+$) T-tumor lysis rates as a function of the effector:target ratio (as depicted in the *lower graph*) provides a much better fit to the experimental data than does the power form (as depicted in the *top graph*)

some analysis of the sensitivity of the model to parameter fluctuations can certainly provide a general picture of possible behaviors under certain conditions. Further comparisons may lead to new insights in the nature of the differences between different tumor types, as well as different immuno-therapeutic protocols.

6 Three Population Model: Tumor, NK, CTL

In this section, we introduce the three population tumor–immune model developed in [23]. Most of the material in this chapter can also be found in [23]. This mathematical model of tumor–immune interactions sheds light on the differing roles of the Natural Killer (NK) and $CD8^+$ T cells in suppressing various tumor cell lines

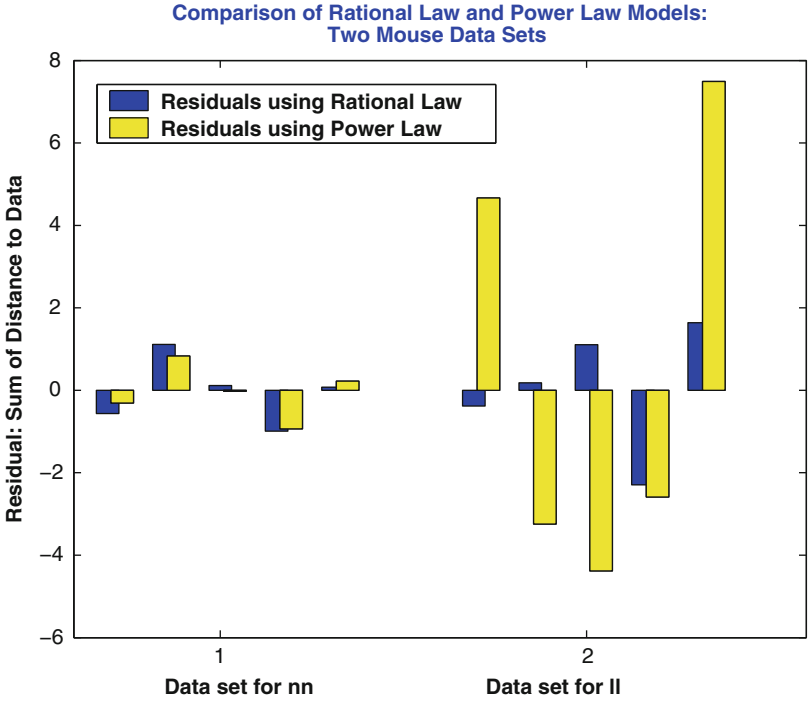

Fig. 7 The *bars* show the residuals (*errors*) for the same two data sets shown in Fig. 5 ($CD8^+$ T cell lysis of control-transduced and ligand-transduced tumor cells). The height of each *bar* shows the value predicted by the power and rational laws, minus the experimental data values at each effector:target ratio point. The difference between the power law and rational law models is most pronounced in the ligand-transduced case, in which the effector cells are far more efficient at lysing tumor cells

in mice and humans. The model is driven by the results of experiments carried out by Diefenbach et al. [24], in which mice were challenged with tumor cells that were modified to be more recognizable by NK cells and $CD8^+$ T cells. The responses of these two branches of the immune system to the tumor challenge were observed both separately and in conjunction with each other. After developing the model, using the methods outlined in Sect. 5 to fit the parameters both to the murine (mouse) data from [24], and also to human data provided in Dudley et al. [26]. In the human study, subjects with metastatic melanoma were treated with highly selected tumor-reactive T cells, and results were observed. Both the mouse and the human studies provide experimental information about tumor growth rates and effector to tumor cell kill (or lysis) rates. We use the model to explore the dynamics of tumor rejection, the specific role of the NK and $CD8^+$ T cells, and the development of protective immunity to subsequent tumor rechallenge.

6.1 Model Development

The specific biological assumptions we took into account when developing our model equations are based on both accepted knowledge of immune system function and conclusions stated in [24, 26]. The assumptions include:

1. A tumor grows logistically in the absence of an immune response. This is one accepted growth model for tumors [7], and is also based on fittings of the data in [24].
2. Both NK and $CD8^+$ T cells are capable of killing tumor cells. (See, for example, [24, 31, 40].)
3. Both NK and $CD8^+$ T cells respond to tumor cells by expanding and increasing cytolytic activity. (See, for example, [41, 58].) Note that the level of effector cell "effectiveness" depends on both the number of cells present, as well as the individual cell's cytotoxicity. In the model, we do not separate the measures of high-effectiveness per cell from an increase in cell population, but measure the combined overall increase in effectiveness in response to tumor.
4. NK cells are normally present in the body, even when no tumor cells are present, since they are part of the innate immune response. See, for example, [63].
5. As part of the specific immune response, active tumor-specific $CD8^+$ T cells are only present in large numbers when tumor cells are present. (See, for example, [42, 63])
6. NK and $CD8^+$ T cells become inactive after some number of encounters with tumor cells. (See, for example, [44].)

In the equations, we denote the three cell populations by:

- $T(t)$, tumor cell population at time t
- $N(t)$, total level of natural killer cell effectiveness at time t
- $L(t)$, total level of tumor specific $CD8^+$ T cell effectiveness at time t

6.2 Model Equations

Using the list of assumptions from above, we describe the system as three coupled differential equations, where each equation gives the rate of change of the particular cell population in terms of growth and death, cell–cell kill, cell recruitment, and cell inactivation. In particular:

Rate of change of tumor cell population =

(Growth and death rate)− (Cell–cell kill rate)

Rate of change of active effector cell populations =

(Growth and death rate) + (Recruitment rate)− (Inactivation rate)

The mathematical forms of the growth and death terms for tumor and immune cell populations will reflect Assumptions (1), (4) and (5). Assumption (2) is reflected in the cell–cell kill term, Assumption (3) gives rise to the effector cell recruitment terms, and Assumption (6) is incorporated through the effector inactivation terms.

Immune recruitment terms are generally assumed to be of a Michaelis–Menten form, (see, e.g., [46] in which Michaelis–Menten dynamics are derived for immune cell recruitment by cancer cells). See, for example, Eq. (4). These dynamics are commonly used in mathematical tumor models that include an immune component, since they allow for a saturation effect (see, e.g., [42]). In the case of the $CD8^+$ T cells, in addition to being recruited by interactions with T-cell processed tumor cells through a Michaelis–Menten dynamic, additional $CD8^+$ T cells are stimulated by the interaction of NK cells with tumor cells. This NK stimulation is represented by the rNT term in Eq. (11). The term rNT, representing a fraction of the number of interactions between NK cells and tumor cells, is the vehicle through which we model the fact that the specific immune response of the $CD8^+$ T cells is activated only after the activation of the earlier response of innate immunity.

Substituting specific mathematical forms for each of the growth, death, recruitment, and inactivation terms yields the following system of equations:

Three-dimensional model:

$$\frac{dT}{dt} = aT(1-bT) - cNT - DT \tag{9}$$

$$\frac{dN}{dt} = \sigma - fN + \frac{gT^2}{h+T^2}N - pNT \tag{10}$$

$$\frac{dL}{dt} = -mL + \frac{jD^2}{k+D^2}L - qLT + rNT \tag{11}$$

(continued)

where

$$D = d\frac{\left(\frac{L}{T}\right)^{\lambda}}{s + \left(\frac{L}{T}\right)^{\lambda}} \tag{12}$$

From [24] we were able to get data on the growth curves in the absence of an immune response, which allowed us to estimate parameters a and b. These model parameters were estimated from the data in [24] by minimizing the least-squares distance from the simulated values to the data. Data measuring the percent of IFN-γ producing immune cells as a function of ligand expression allowed us roughly to estimate immune recruitment rates stimulated both by ligand-transduced and control-transduced tumor cells. Other parameters, such as the background source rate for NK cells (σ) and death rates for immune cells (f and m), were taken from the literature, e.g. [46, 73]. Although some of these parameters are rough estimates, and may deviate from other specific data, the model as a whole qualitatively describes the observed data both in the mouse and in the human experiments.

Table 3 provides a detailed listing of the parameters in this model, along with their units, descriptions, numerical values for the simulations, and reference sources from which these values were taken. Detailed development of all terms, except for the new fractional cell kill term D which was descried in Sect. 5, can be found in [16].

6.3 Simulating Immunotherapy: Enhancing Ligand Expression

The three-dimensional model can be used to simulate the effect of enhancing ligand expression on tumor cells by allowing the relevant parameters to depend on the tumor cell type. The relevant parameters in this model are c and d, the effectiveness of the immune cells, along with g and j, the recruitment parameters.

Figure 5 (top) plots the effector:target lysis data from [24] for NK cells, along with our simulated model curves. The ligand transduced tumor cells are lysed at a higher rate by NK cells than those that are control transduced. The two values of NK-lysis parameter c estimated from the two sets of data accurately reproduce the effects of this ligand transduction.

In the bottom two rows of Fig. 5, effector:target lysis data and simulations for the $CD8^+$ T cells are presented. For our experiments, four $CD8^+$ T cell lysis parameters were determined through fitting to the four ligand transduction data sets of [24], and these are all able to capture the different experimental outcomes. For brevity, only

the two cases representing priming and rechallenge with control-transduced cells and priming and rechallenge with ligand-transduced cells are presented in Fig. 5. Figure 5 shows the experimental data against the mathematical model prediction using the best-fit parameter values for both the power form and the new rational form of the competition term. Note that in Fig. 5 (center row) in which we compare fits to data for non-ligand transduced cells, although the difference between the fit achieved by the traditional power kill law and by the new rational kill law is not clearly visible, the numerical difference in the error term is present. This can be seen in Fig. 7. Here, we plot the numerical errors between the predictions and the data, allowing a comparison between the goodness-of-fit of the power form and rational form of the competition term. In the bottom row of Fig. 5, the superiority of the fit achieved by the rational kill law over the power kill law is visible and striking. Similarly, the numerical error bars of the right panel of Fig. 7, reflect the much smaller error achieved by the rational kill law. It appears that it is critical to employ the rational law to fit ligand transduced cell data, whereas the use of either the rational or the power law for non-ligand transduced data will give us an acceptable fit. This may indicate that the more effective the immune cells are at lysing their target cells, the more they follow a rational law dynamic.

The simulations show what this model would predict under three different experimental scenarios similar to those reported in [24]. These simulations explain some of the reported experimental observations (see [24], Figs. 2 and 3, pp. 167–168). Ligand transduced cells stimulate the immune response sufficiently to control tumor growth (Fig. 8, top right), while control-transduced tumor cells escape immune defenses (Fig. 8, top left). In the top left panel of Fig. 8, the immune system is rechallenged at day 10 after priming with control-transduced cells, and the tumor escapes surveillance. In the top right panel of Fig. 8, the immune system is again rechallenged at day 10 with control-transduced cells, but the primary challenge was with ligand-transduced cells. This simulation shows that the tumor is controlled, indicating the development of immunity. Changing ligand levels on the cells requires changes to the model parameters d, λ, and s (all the parameters involved in the rational T cell kill term D), as well as c (strength of NK cell kill), g (NK cell recruitment rate), and j ($CD8^+$ T cell recruitment rate). Numerical values for these parameters with varying ligand levels are provided in Table 3.

Simulations generated by a validated mathematical model can be used to detect thresholds for immune efficacy. In Fig. 8 (bottom row), we reproduce with a computational solution of our mathematical model the qualitative results of three sets of experiments that were presented in Fig. 2, p. 167 of [24]. For the experiments in [24], groups of mice were challenged with either 10^4, 10^5 or 10^6 ligand-transduced tumor cells, then tumor establishment was tracked. For our in silico simulations, we also challenge the mathematical system with these three levels of tumor cells. Figure 8 (bottom left) shows simulated tumor cell growth over time

in response to these three initial levels of tumor burden in the absence of $CD8^+$ T cell activity, reflecting the experiments in which the mice were depleted of $CD8^+$ T cells. This simulation represents a system lacking a strong antigen-specific immune response. The system can control a small tumor, but tumor challenges of 10^5 cells or more escape the immune system's control.

Figure 8 (bottom center) shows simulated tumor growth outcomes for the same three experiments done in the absence of NK cells, reflecting the experiments with mice depleted of NK cells. The system is now able to control initial tumor burdens of up to 10^5 cells, but a larger challenge of 10^6 cells escapes immunosurveillance.

Figure 8 (bottom right) shows simulated results with both NK and $CD8^+$ T cells active, reflecting the experiments on mice with intact immune systems. With both the NK cells and the $CD8^+$ T cells working together, initial tumor burdens of up to 10^6 cells are controlled.

6.4 Sensitivity Analysis

In order to discover which components of the model contribute most significantly to determining final tumor size, we performed a sensitivity analysis. Model sensitivity was assessed by measuring the effect of small parameter changes on the final volume of the tumor as represented by a simulation of the system's evolution over 25 days. Since ultimately we are interested in predicting a patient's response to immunotherapy treatment, we used human data for the sensitivity study. In particular, the parameter set from patient 9, available in [26], and for whom lysis data are plotted with squares in Fig. 6, was used as the base point. Each parameter was perturbed from its estimated value by 1%, and the corresponding percent change in final tumor volume was calculated.

The results of this parameter sensitivity analysis for the mathematical model are shown in Fig. 9. The system in this case is found to be most sensitive to the exponent in the $CD8^+$ T lysis term, λ, as well as to the tumor growth parameter a. This suggests that, in addition to the aggressiveness of the tumor, as represented by growth parameter a, even very small changes in the cytolytic effectiveness of tumor-specific T cells, as represented by shifts in the value of λ, can affect clinical outcome. This would indicate that any treatment which might enhance this effectiveness should aggressively be pursued. By contrast, the size of the tumor after 25 days is not very sensitive to the NK cell competition parameter, c. According to this model, then, the cytolytic activity of the NK cell population alone is not a determining factor in the eventual size of the tumor, and should be considered in conjunction with $CD8^+$ cell activity.

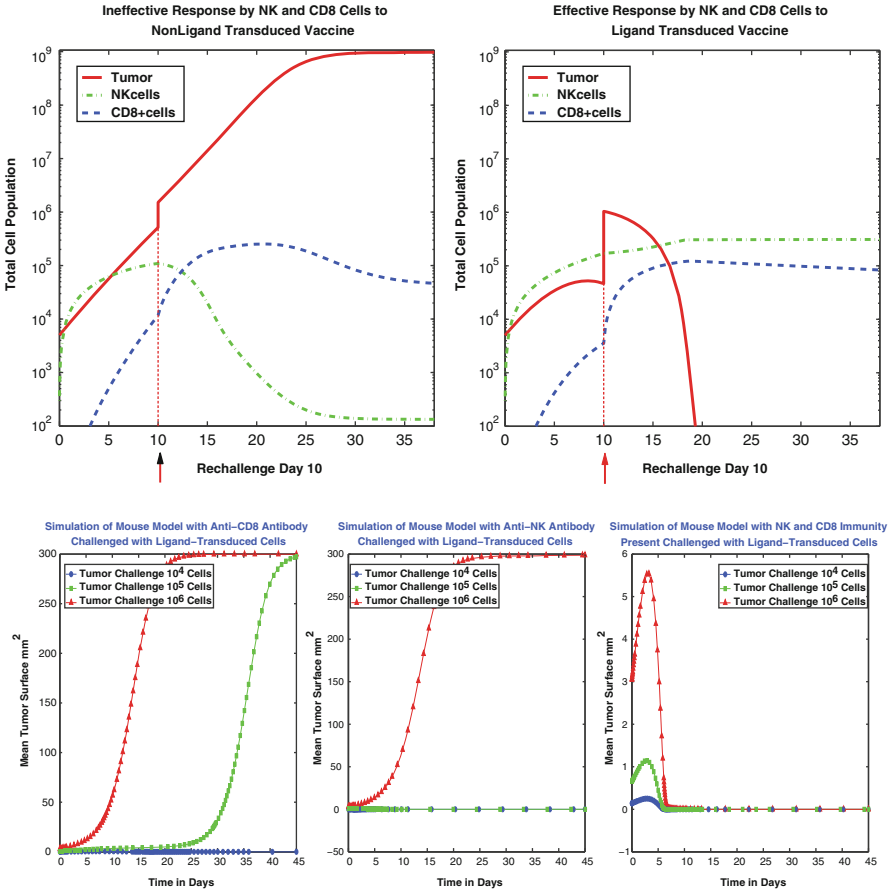

Fig. 8 Simulations of (tumor cell)–(NK cell)–(T cell) mutual interactions over time. *Top left* System evolution with control-transduced primary inoculation. Ineffective response by NK cells and $CD8^+$ T cells to non-ligand transduced challenge. *Top right* System evolution with ligand-transduced primary inoculation. Effective response by NK and $CD8^+$ T cells to non-ligand transduced challenge following priming with ligand-transduced cells. Both systems are rechallenged with control-transduced cells after 10 days. *Bottom row* The simulations presented in these graphs are based on data provided in [24]. In each of the three cases tumor growth is plotted over time starting with three different initial tumor challenges: 10^4, 10^5, and 10^6 cells. In the plots, cell populations are converted to mean surface values. *Bottom left* Simulation of Tumor–NK interactions in a system with $CD8^+$ T cells depleted. The simulation shows that in the absence of $CD8^+$ T cells, only a tumor inoculation of up to 10^4 cells is suppressed, whereas larger challenges escape immunosurveillance. *Bottom center* Simulation of Tumor-($CD8^+$ T cell) interactions in a system with NK cells depleted. The simulation shows that in the absence of NK cells, tumor inoculations of up to 10^5 cells are suppressed, whereas a larger challenge of 10^6 cells escapes immunosurveillance. *Bottom right* Simulation of Tumor-($CD8^+$) T–NK interactions in a system with all immune components intact. Note that the maximum mean tumor surface area achieved in this plot is only 6 mm^2, as compared with 300 mm^2 in the previous two plots. Tumor populations of this small size are not clearly visible in the data plots provided in [24], Fig. 2, p. 167. The simulation shows that when both NK cells and $CD8^+$ T cells are present, tumor inoculations of up to 10^6 cells are suppressed

6.5 *Bifurcation Analysis*

In addition to a parameter sensitivity analysis of the type described in Sect. 6.4, we can gain a better understanding of the overall dynamics of the system, by performing a bifurcation analysis of the system. This type of analysis gives us a global view of the system, identifying the regions in parameter space that correspond to a "health" or "diseased" state. Furthermore, if specific parameters have been identified as being critical to the progression of the disease, or if a particular treatment affects one set of parameters, a bifurcation analysis can pinpoint values of these parameters that serve as thresholds beyond which the patient's system enters the basin of attraction of a "healthy" stable fixed point. These bifurcation points could become the goal of therapy design. We will illustrate this idea with some specific parameter sets, guided in part by the those parameters identified as "sensitive" in Sect. 6.4.

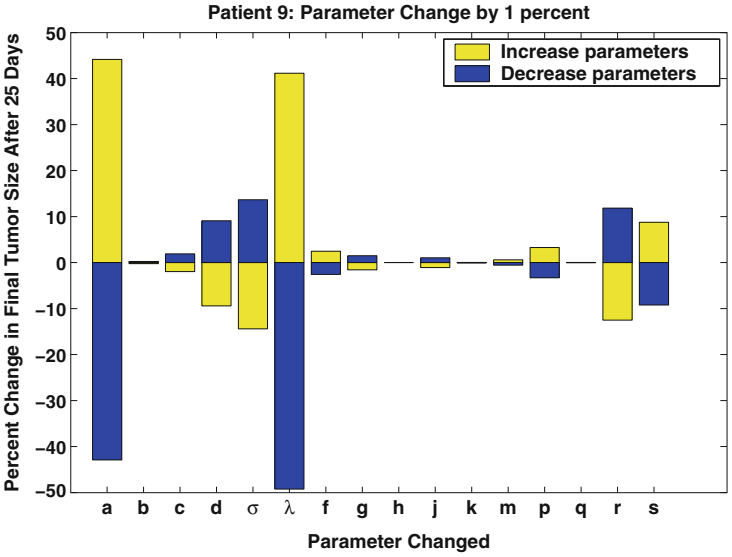

Fig. 9 This analysis shows that the tumor size is most sensitive to the $CD8^+$ T cell kill parameter, λ, as well as to the tumor growth rate parameter a

Before performing the bifurcation analysis, we add a bit more realism to the model. This model expansion is motivated by our goal of exploring the effect of different treatment strategies on the progression of the tumor, which we will pursue in Sect. 7. The expanded model will reflect two additional assumptions:

1. Circulating lymphocyte levels can be used as a measure of patient health (see, e.g., [33, 50, 56]). The source of the NK cell population can be represented as a fraction of the circulating lymphocyte population, a simplification meant to represent the complex cascade of biological events that leads to NK cell stimulation (see, e.g., [10]).

2. NK cells, circulating lymphocytes and tumor cells are components of the process of stimulation and elimination of activated effector cells, a model simplification meant to reflect the self-regulatory nature of the immune system (see, e.g., [26, 31, 39]).

Assumption (1) leads to the introduction of a new state variable, C, representing the population of circulating lymphocytes, or white blood cells. These circulating lymphocytes are assumed to be replenished at a constant rate, and die off at a constant rate, unaffected by the presence of the tumor. The constant source term for the NK-cells is replaced by a source term proportional to $C(t)$. Assumption (2) leads to a additional positive and negative terms in the $CD8^+$, or $L(t)$ equation. With these modifications, the expanded model is:

Four-dimensional model:

$$\frac{dT}{dt} = aT(1-bT) - cNT - DT \tag{13}$$

$$\frac{dN}{dt} = eC - fN + g\frac{T^2}{h+T^2}N - pNT \tag{14}$$

$$\frac{dL}{dt} = -mL + j\frac{D^2T^2}{k+D^2T^2}L - qLT + (r_1N + r_2C)T - uNL^2 \tag{15}$$

$$\frac{dC}{dt} = \alpha - \beta C \tag{16}$$

where D is the de Pillis–Radunskaya Law, given in Eq. (12).

6.5.1 Finding Equilibria

The first step in understanding the long-term behavior of the tumor–immune system is to identify the equilibria, and to determine their stability. Equilibria are found by setting the right-hand side of Eqs. (13)–(15) to zero. We first note that Eq. (16) decouples from (13)–(15), so that, at equilibrium we have $C_E = \alpha/\beta$.

Equation (13) has one zero at the "tumor-free" equilibrium at $T_E = 0$, and possibly several nonzero tumor equilibria. Setting $T = 0$ in (14) and (15) yields one non-negative tumor-free equilibrium in four-dimensions:

$$E_0 = (T_E, N_E, L_E, C_E) = (0, \frac{e\alpha}{\beta f}, 0, \frac{\alpha}{\beta}).$$

In the case where $T_E \neq 0$, the equilibria are again determined by finding the simultaneous solutions of Eqs. (13)–(16), but the values of the nonzero tumor equilibrium points must be found numerically.

In particular, setting Eq. (14) to zero and solving for N yields

$$N_E = \frac{eC_E(h + T^2)}{fh + (f - g)T^2 + phT + pT^3} \tag{17}$$

Similarly, requiring that Eq.(13) equal zero (where $T \neq 0$) gives

$$D_E = a - abT - cN_E \tag{18}$$

Using this expression in Eq. (12) gives an expression for the equilibrium value of L in terms of T:

$$L_{E1} = \left(\frac{D_E s T^\lambda}{d - D_E}\right)^{1/\lambda}, \tag{19}$$

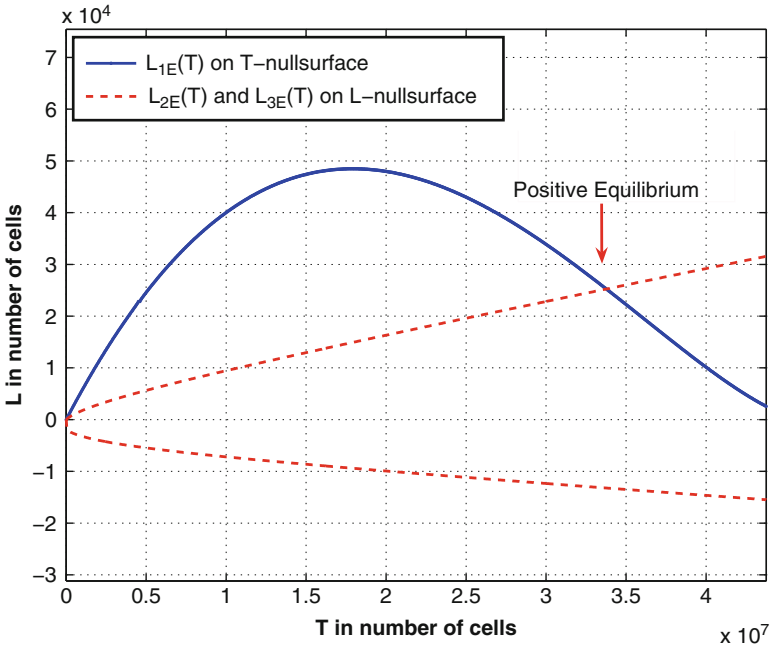

Fig. 10 The nonzero equilibria are the intersections of the graphs of the functions $L(T)$ obtained by finding the equations of the null-surfaces. There is only one nonzero positive equilibrium for the estimated parameter set

Finally, setting Eq. (15) to zero gives

$$L^2(uN_E) + \left(m - \frac{jD_E^2T^2}{k + D_E^2T^2} + qT\right)L - (r_1N_E + r_2C_E)T = 0, \tag{20}$$

which is quadratic in L. Equation (20) has two solutions for each value of T, which we shall denote $L_{E2}(T)$ and $L_{E3}(T)$. Equilibrium points of the system are found by determining the T-values at which the graphs of $L_{E2}(T)$ and $L_{E3}(T)$ intersect the graph of $L_{E1}(T)$. These T values can then be used to find the equilibrium values of N and L using Eqs. (17) and (19).

Observe that there could be multiple nonzero values of T that simultaneously satisfy Eqs. (19) and (20). However, these solutions could be negative or complex-valued. For example, using the estimated set of mouse parameters given in Table 5, we find two solutions, only one of which is biologically relevant (see Fig. 10). As a system parameter is changed, other nonzero equilibria can appear (see Fig. 11), or negative equilibria can become positive, and therefore biologically feasible.

6.5.2 Stability of Equilibria

A system will move towards an equilibrium point if that point is stable, so the next step in the analysis of the long-term dynamics of the system is to investigate the stability of all equilibria. The effect of the stability of the tumor-free equilibrium on the progression of the disease is illustrated in the lower graph of Fig. 11, dashed line. For this set of parameter values, the tumor-free equilibrium is unstable, while the high-tumor equilibrium is stable. The stability of the high-tumor equilibrium implies that, in the absence of treatment, the system will inevitably return to the high-tumor state, i.e., the tumor will escape immune surveillance *unless every single tumor cell is killed*. Thus, in a case such as ours for which there are only two equilibria, if the tumor-free equilibrium is unstable, then in order to realistically effect a cure, any treatment must not only reduce the tumor burden, but it must also change the parameters of the system itself. The role of immunotherapy, therefore, might be interpreted in this context as a treatment which changes system parameters by, for example, permanently raising the cytolytic potential of the natural killer cells [the parameter "c" in Eq. (13)]. We note that if the system were one that admitted a very small but stable tumor, then another "healthy" state might be one for which it is possible to maintain the system at this low tumor level.

The stability of an equilibrium is typically determined by linearizing the system about the calculated values, and by determining the stability of the linearized system by explicitly solving it. (See any textbook on differential equations, for example, [6].) However, the term D in Eq. (13) poses a problem since it is not differentiable at the tumor-free equilibrium $E_0 = (0, \frac{e\alpha}{\beta f}, 0, \frac{\alpha}{\beta})$, so we cannot use this technique to determine the stability of the tumor-free state.

However, we can make some relevant observations without linearizing. Suppose T is positive. We see that $\frac{dT}{dt}$ is negative if

$$a(1-bT) - cN - D < 0 \Leftrightarrow cN > a(1-bT) - D$$

If we assume that N is near its value at the tumor-free equilibrium: $N_E = \frac{e\alpha}{f\beta}$, then we get a sufficient condition for stability. Suppose $N > 0.5N_E$ then:

$$c > \frac{2a}{N_E} \Rightarrow cN > c(.5N_E) > a > a(1-bT) - D.$$

Thus, if c is sufficiently large relative to the intrinsic growth rate of the tumor cells, a small tumor can be controlled by the innate immune response: the tumor population will decrease towards zero, and the tumor-free equilibrium is *stable*.

Similarly, suppose we assume a small tumor population: $T < \frac{1}{b} \times 10^{-3}$ (for typical values of the intrinsic carrying capacity, b, this corresponds to a tumor of fewer than 10^5 cells, below the level of detection). Noting that $D = \frac{dL^\lambda}{sT^\lambda + L^\lambda} < d$, we get a condition for *instability*.

$$c < \frac{.999a - d}{N} \Rightarrow a(1-bT) > 0.999a > cN + d > cN + D$$

$$\Rightarrow \frac{dT}{dt} = T\,(a(1-bT) - cN - D) > 0$$

Thus, for small enough values of c, the tumor will escape immune surveillance and the disease will progress. Note that we must have $d < 0.999\,a$ in order for there to be a positive value of c that satisfies the first inequality above. This makes sense, since a small value of d corresponds to a low kill-rate by the $CD8^+$ T cells, reflecting a less effective immune response.

By simulating the four-dimensional model with initial values close to the tumor-free equilibrium and with gradually increasing values of c, we can estimate the critical value of c, the *bifurcation point*, at which the tumor-free equilibrium becomes unstable. Figure 11 shows that the bifurcation point is at approximately $c_{crit} = 4.86 \times 10^{-10}\text{cell}^{-1}\text{day}^{-1}$, somewhat smaller than the base value of 7.13×10^{-10} shown in Table 5. For this bifurcation diagram, the parameter d is set to $0.9a \approx 0.39$. All other parameters are those given in Table 5. Similar observations and experiments can be made with other key parameters, such as the parameter d, the maximum kill rate by $CD8^+$ cells. See [15] for other examples.

At nonzero equilibrium points, a linear stability analysis can be performed since the right-hand sides of all of the differential equations are differentiable away from $T = 0, L = 0$. As an illustrative example, we show the results of this analysis as we vary the NK-cell kill rate parameter, c, from zero to a relatively large value. For very small values of c, the tumor-free equilibrium is unstable, and there is

a stable, high-tumor equilibrium. This corresponds to a system with a very weak innate immune response to the tumor, and one tumor cell will reproduce, initiating the development of a large tumor. As the parameter c increases, the tumor-free equilibrium becomes stable, and a small number of tumor cells can be controlled by the immune system. The system returns to the tumor-free equilibrium, even in the absence of any treatment (Fig. 11, bottom panel).

When the tumor-free equilibrium becomes stable, a nonzero, unstable equilibrium appears, separating the two stable equilibria. The system is now *bi-stable*, and the goal of treatment should be to get the system into the basin of attraction of the zero-tumor equilibrium. At $c \approx 1.45 \times 10^{-5}$, the nonzero equilibria disappear in a saddle-node bifurcation. For larger values of c the system has only the stable zero-tumor equilibrium, and the disease will not progress.

Similar analyses can be performed using any of the system parameters in order to determine conditions for the appearance or disappearance of equilibria and to determine equilibrium stability. See [15] for a bifurcation analysis of the adaptive response parameter, j.

Two bifurcations are evident in the diagram in Fig. 11. The first is a *transcritical* bifurcation, where the negative equilibrium becomes positive, and the zero-tumor equilibrium changes its stability. (This bifurcation occurs at values that are too small to distinguish on the diagram). Before the bifurcation, the zero-tumor equilibrium is strictly unstable: even one tumor cell will result in the system moving toward the high-tumor equilibrium. After the bifurcation, the immune system is able to control small initial tumor populations. Initial tumor populations which are controlled are said to be in the *basin of attraction* of the zero-tumor equilibrium. On the other hand, those which escape immune surveillance, leading the system toward the high-tumor equilibrium, are said to be in the basin of attraction of the high-tumor equilibrium. These basins are shown in Fig. 12. Note that since the state-space of the system is actually four-dimensional, what is depicted in Fig. 12 is the projection of the basins onto the Tumor-NK plane, where the values of L and C are kept at their zero-equilibrium values. Figure 12 illustrates the consequences of *bi-stability*, the co-existence of two, stable fixed points. If the tumor is initially very small, the tumor will be controlled by the level of immune response represented by this parameter set. However, if the tumor somehow grows larger than this threshold, perhaps due to a temporarily weakened immune system or environmental factors, then the tumor will grow to a dangerous size, even in the renewed presence of an adequate immune response. Figure 12 shows two scenarios, where the system starts in identical states, except that in one case (the dashed red line in the lower panel), the initial tumor has *exactly one* additional cell. This tiny change in initial values results in a drastically different outcome for the patient. The location of the basin boundary is therefore crucial in determining the outcome of the disease. In the case of a patient who has undergone chemotherapy which reduces both tumor and immune cell levels, if these levels place the system above the basin boundary then even an undetectable tumor will regrow. However, if the patient is given immunotherapy subsequent to chemotherapy, thereby pushing NK levels to the right of the basin boundary,

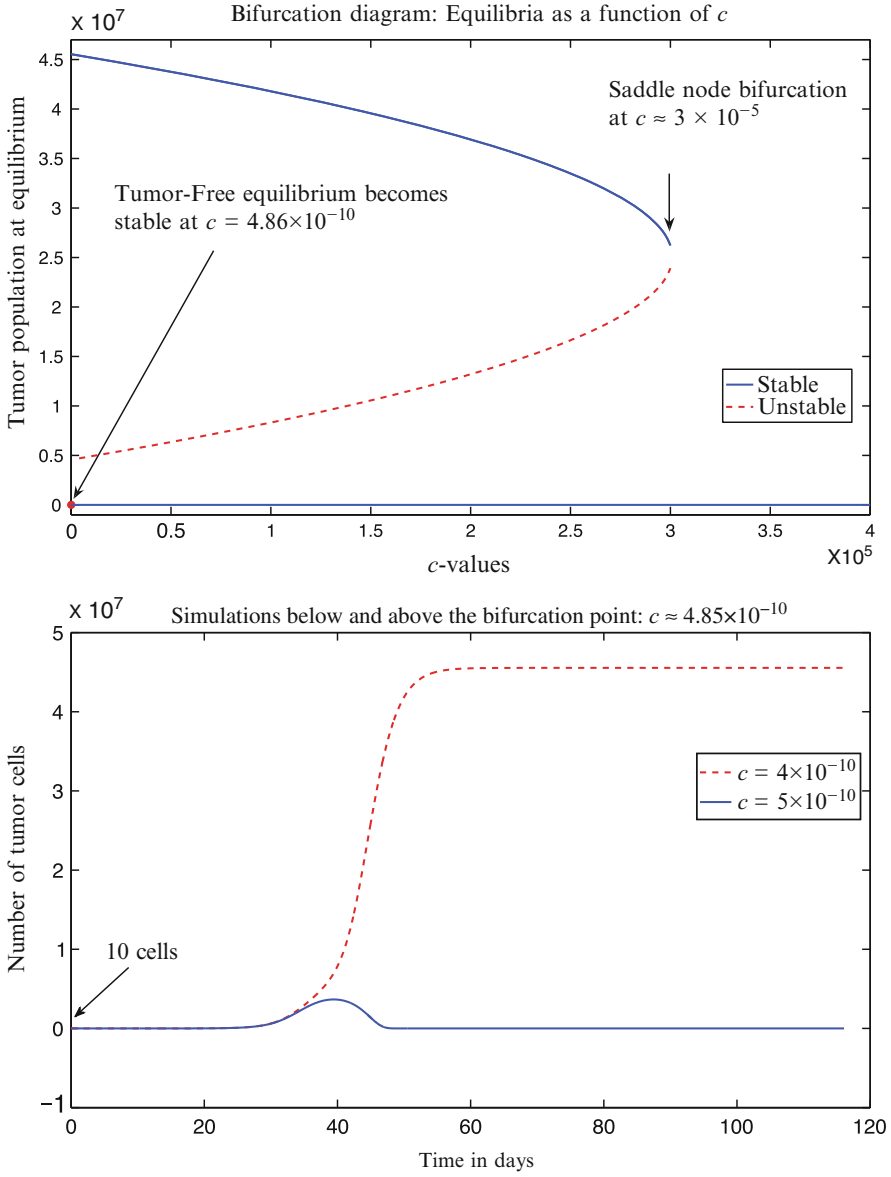

Fig. 11 (*Top*) Bifurcation diagram showing the effect of varying the NK-kill rate, c. As c increases from zero, the tumor-free equilibrium becomes stable in a transcritical bifurcation at $c_{trans} \approx 4.86 \times 10^{-10}$, and an unstable, nonzero equilibrium appears. In this regime the system is bi-stable. At $c_{sad} \approx 3.0 \times 10^{-5}$ the high, stable equilibrium and the unstable equilibrium coalesce and disappear in a saddle-node bifurcation. (*Bottom*) Two solutions of the system showing tumor growth over time for two values of c, one below the transcritical bifurcation, and one above. For the smaller value of c, the small initial tumor consisting of 10 cells grows to the high tumor equilibrium, while for the larger value of c, the immune system is able to drive the tumor back to the tumor-free equilibrium. In *both panels*, other parameters are from Table 5, except for d, which is set to 0.3877. Initial values for the *lower panel* are: $(10, \frac{e\alpha}{f\beta}, 0, \frac{\alpha}{\beta})$

the system will evolve toward the stable zero-tumor equilibrium, and the tumor will not regrow. This hypothetical scenario emphasizes the potential importance of combination therapy.

7 Model Extension to Simulate Chemotherapy and Immunotherapy

The next step in model development is to add terms that reflect treatment therapies. Therefore, in addition to the list of assumptions about tumor and immune system evolution given in Sects. 6.1 and 6.5, we add assumptions used in the development of therapeutic terms: Full model development and analysis details can be found in [15].

- The fraction of the tumor population killed by chemotherapy depends on the amount of drug in the system. The fraction killed has a maximum less than one, since only tumor cells in certain stages of development can be killed by chemotherapy [60].
- A fraction of NK cells, $CD8^+$ T cells, and circulating lymphocytes are also killed by chemotherapy, according to a similar fractional kill curve [29].

Our model, when extended to include treatment terms, not only tracks cell populations: tumor cells (T) and immune cells (circulating lymphocytes: C, NK cells: N, and cytotoxic $CD8^+$ T-cells: L), but in addition will track the total number of circulating lymphocytes (or total white blood cell count in the blood stream), $C(t)$, a chemotherapy drug blood concentration $M(t)$ and an immunotherapy drug blood concentration $I(t)$. In our examples, the chemotherapy term represents a non-targeted cytotoxic medication such as doxorubicin, and the immunotherapy term represents an interleukin such as IL-2.

Since broadly cytotoxic chemotherapy is damaging to all cells in the system, we include a chemotherapy drug kill term in each of the cell population equations. We use a saturation term $1 - e^{-M}$ to represent the chemotherapy fractional cell kill, noting that the effectiveness of chemotherapy is bounded: At relatively low concentrations of drug, the kill rate is nearly linear, while at higher drug concentrations, the kill rate plateaus. The mathematical term we use reflects the dose–response curves suggested by the literature [29]. We then subtract the term $K_\phi(1 - e^{-}M)\phi$, from each the four cell population equations, where $\phi = T, N, L, C$.

For immunotherapy treatment, we allow for $CD8^+$ T activation by interleukin-2 (IL-2) immunotherapy. This "drug" is actually a naturally occurring cytokine in the human body, and its effect on the immune system's efficacy is described mathematically with a Michaelis–Menten interaction term in the equation for L. The presence of IL-2 stimulates the production of $CD8^+$ T cells, and the cascade

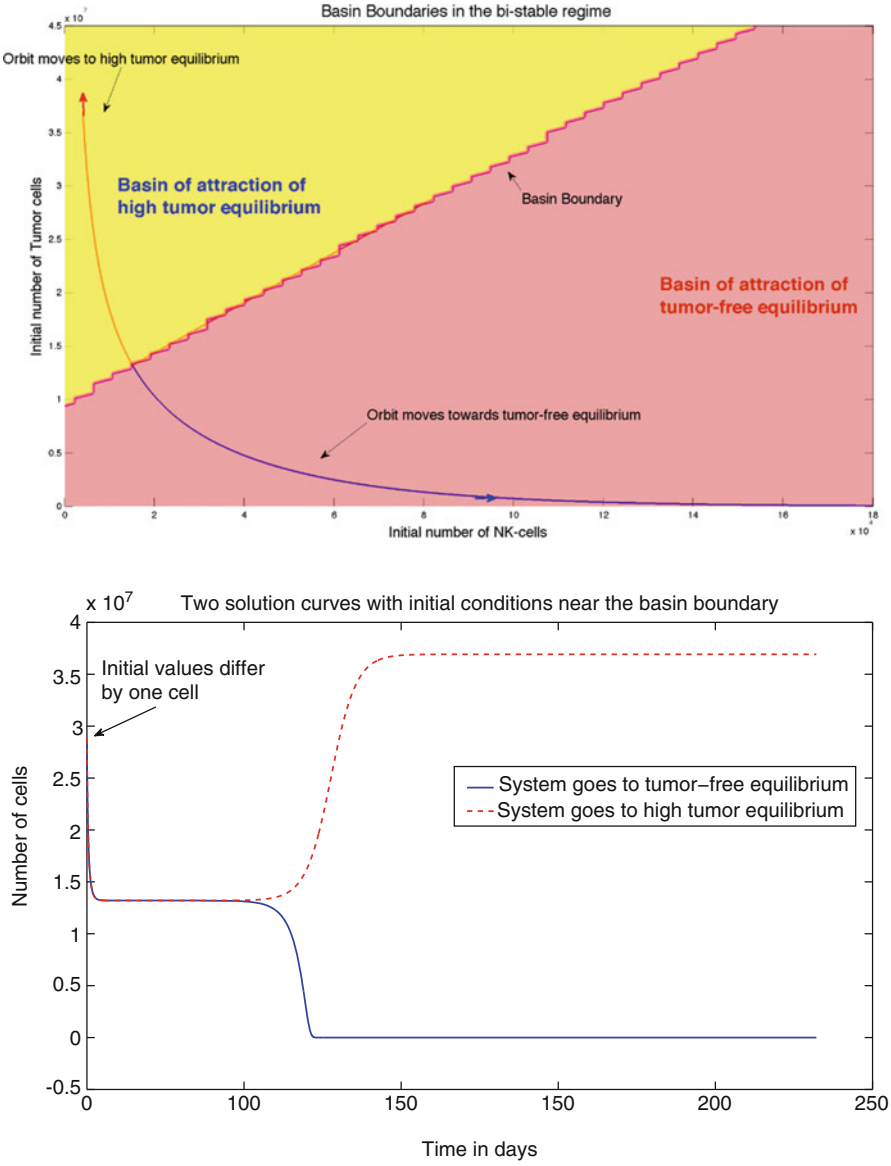

Fig. 12 (*Top*) Basins of attraction of the zero-tumor and high-tumor equilibria in the bi-stable regime. Two orbits are shown that start near the basin boundary, with initial populations differing by only one tumor cell. (*Bottom*) Solution curves showing the evolution of the tumor population over time for the two orbits shown in the *upper graph* with initial values near the basin boundary. The two initial conditions are: $T_1(0) = 2.8817259 \times 10^7$ (*solid blue line*) and $T_2(0) = 2.8815260 \times 10^7$. Other initial values are $N(0) = 8.201 \times 10^4, L(0) = 0, C(0) = 1.0083 \times 10^7$. Parameters used in these simulations: $c = 1.0 \times 10^{05}, d = 0.387702$. Other parameters are those listed in Table 5

of effects requires that we modify certain terms in the equations for T, N and L, in addition to including new treatment term equations. Details of those modifications can be found in [15]. The extended system of equations becomes:

Model with chemotherapy and immunotherapy:

$$\frac{dT}{dt} = aT(1-bT) - cNT - DT - K_T(1-e^{-M})T \tag{21}$$

$$\frac{dN}{dt} = eC - fN + g\frac{T^2}{h+T^2}N - pNT - K_N(1-e^{-M})N \tag{22}$$

$$\begin{aligned}\frac{dL}{dt} &= -mL + j\frac{D^2T^2}{k+D^2T^2}L - qLT + (r_1N + r_2C)T \\ &\quad - uNL^2 - K_L(1-e^{-M})L + \frac{p_I LI}{g_I + I} + v_L(t)\end{aligned} \tag{23}$$

$$\frac{dC}{dt} = \alpha - \beta C - K_C(1-e^{-M})C \tag{24}$$

$$\frac{dM}{dt} = -\gamma M + v_M(t) \tag{25}$$

$$\frac{dI}{dt} = -\mu_I I + v_I(t) \tag{26}$$

$$D = d\frac{(L/T)^\lambda}{s + (L/T)^\lambda} \tag{27}$$

7.1 Tumor Growth Response to Treatments: Mouse Data

For the following set of numerical experiments, our model parameter values are determined using published data both from murine experimental studies [24] and from human clinical trials [26]. When necessary, we also use previous model parameters that have been fitted to experimental curves [17, 18, 22, 46]. Tables 5 and 6 provide a full listing of all of the parameters with their units and descriptions. Full descriptions of parameter derivation for the following set of experiments can be found in [15].

The first simulation we run represents an in silico mouse that has an immune response and has been challenged with a tumor, but no treatments are administered. Simulation results are shown in Fig. 13, top left. The parameter set and initial

conditions yield a scenario representing an in silico mouse in which the immune system is not strong enough to stop tumor growth. The tumor reaches carrying capacity, and we assume the mouse dies under this extreme tumor burden. The initial conditions for this situation are chosen to be a tumor of size 10^6 cells, a circulating lymphocyte population of 1.1×10^7, a natural killer cell population of 5×10^4, and a population of 100 $CD8^+$ T cells. With the set of parameters in Table 5, the outcome of the simulation is sensitive to the initial conditions chosen. This set of initial conditions is meant to reflect a laboratory mouse experiment, in which an initial tumor challenge of 10^6 cells is directly implanted into the mouse, and then the progression of the tumor is observed.

The next two simulations employ either chemotherapy or immuotherapy treatments. The chemotherapy treatment approach involves administering seven pulsed doses of chemotherapy, each dose represented by setting $v_M(t) = 1$ in Eq. (25) for 1 day, and given in a 14 day cycle. The immunotherapy treatment approach involves injecting 8×10^8 highly activated $CD8^+$ T cells from day 7 to day 8. This $CD8^+$ injection is meant to represent the TIL treatments used for certain patients (see, for example, [26]).

For an initial tumor challenge of 10^6 cells, the tumor survives despite either method of intervention. These experiments are pictured in Fig. 13, top right and bottom left.

There are also cases in which chemotherapy alone or immunotherapy alone can be effective in killing a tumor that the immune system could not kill on its own. These experimental results are not pictured here. However, the range of initial conditions for which mono-therapies are effective is relatively small in comparison to the greater effectiveness of combination treatments. This result is consistent with experimental investigations (see, for example, [49]). The next simulation represents an in silico mouse treated with both chemotherapy and immunotherapy. The chemotherapy and immunotherapy treatments given as mono-therapies above are now given simultaneously, and initial population sizes are set to the same values as in the previous experiments. Results are displayed in the bottom right image in Fig. 13.

In these simulations, combination therapy is clearly more effective in controlling tumor growth than is either individual of treatment alone. The synergistic effect of combination treatment that we observe reflects the outcomes of some laboratory studies (see, e.g., [49, 72]). In vivo, these treatments do cause undesirable side effects, some of which are due to the damage caused to the immune cells. With this model, the circulating lymphocyte level can be used as a proxy to indicate at least whether the immune health of the mouse has been damaged too much during treatment, and dosing can be modified accordingly.

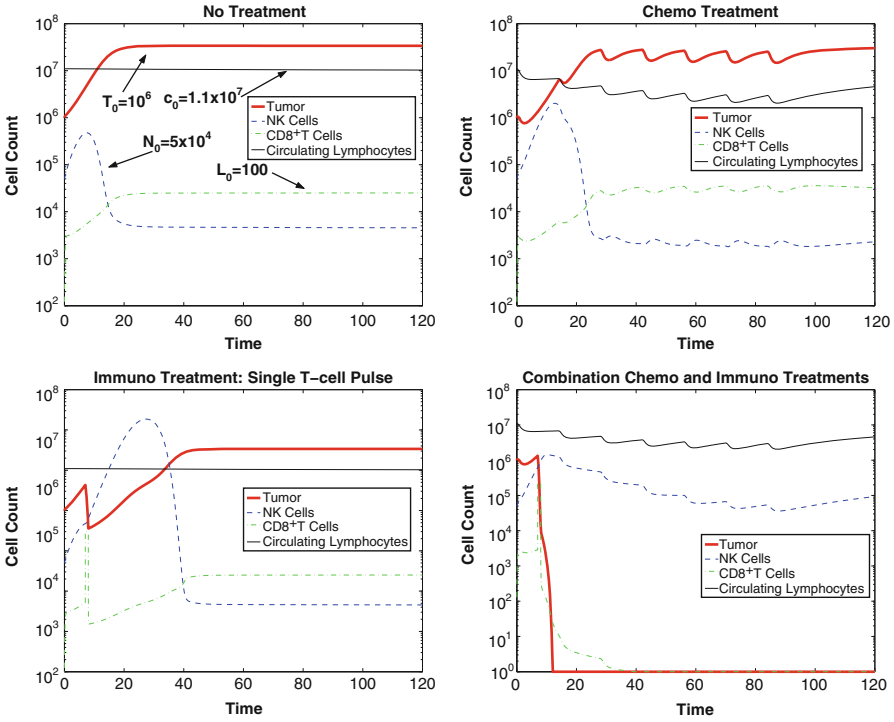

Fig. 13 Mouse data. *Top left* No treatment. Immune system without intervention where the tumor reaches carrying capacity and the mouse "dies". *Top right* Chemotherapy. The immune system response to high tumor with chemotherapy administered for 1 day in a 14 day cycle. *Bottom left* Immunotherapy. Immune system response to high tumor with the administration of immunotherapy from days 7 to 8. *Bottom right* Combination therapy. Chemotherapy and immunotherapy as previously described given simultaneously effectively control of the tumor. Parameters for all simulations are provided in Table 5

7.2 Tumor Growth Response to Treatments: Human Data

We next run model simulations using parameters taken from experimental results of two patients—"Patient 9" and "Patient 10"—from a study by Rosenberg et al. on metastatic melanoma [26]. Model parameters for both Patients 9 and 10 are summarized in Table 6.

We first look at the "human" system without treatment. In the simulations using human parameters, we set an initial tumor burden of 10^6 cells. This experiment represents a situation in which the immune system has not become activated against the tumor cell population until the population has reached 10^6 cells, a size which in many cases is still considered to be below the threshold of clinical detectability in a human. For this tumor, immune system strength is very important in determining whether or not the body can eliminate a tumor in the absence of treatment interventions. Simulations show that an immune system with initial values

of 1×10^5 natural killer cells, 1×10^2 $CD8^+$ T cells, and 6×10^{10} circulating lymphocytes can be considered "healthy," and is, in fact, sufficient to control the growth of a 10^6 tumor challenge (images not shown). However, when the immune system is weakened, a tumor of the same 10^6 size grows to a dangerous level in the absence of treatment interventions. A "weakened" immune system in this case has initially values set to 1×10^3 NK cells, 10 $CD8^+$ T cells, and 6×10^8 circulating lymphocytes. We note that if we challenge even the "healthy" immune system with 10^7 tumor cells (an order of magnitude larger than the 10^6 challenge), even the healthy immune system is unable to control the tumor. This indicates that the earlier the immune system can be activated against a growing tumor, the better. We will also use the 10^7 size challenge to test the results of treatment interventions.

Simulations of treatments show similar outcomes to the mouse experiments: We can easily find scenarios in which chemotherapy alone or immunotherapy alone is not sufficiently effective in controlling tumor growth when initial tumor size is 10^7 cells, but in combination the therapies can successfully eliminate a tumor. We do not include all the experiments here. The reader can refer to [15] in which a larger range of simulations is presented. Here we will focus on experiments that highlight how certain treatment scenarios can differ from patient to patient, and how outcomes will be affected if a patient's immune system is compromised. Measuring certain patient-specific immune response parameters can be important in helping to predict whether an individual will respond well to treatments.

As a proxy representing a patient's immunological health we use the number of circulating lymphocytes in the body, and do not allow the circulating lymphocytes to drop below a threshold for which the risk of infection may be too high. In our experiments, we chose that threshold to be on the order of 10^8 cells. This amount reflects a fraction of approximate normal white blood cell levels in an adult human (see, e.g., [63]).

Simulation results for combination treatment on Patient 9 are shown in Fig. 14, left. The combination treatment is able to eliminate a tumor of initial size 10^7 cells, a tumor cell count that is likely to be clinically detectable. The chemotherapy regimen is given in 9 pulsed doses total, with dose strength $v_M(t) = 5$, and doses given once every 10 days. Initial immune strength is 1×10^3 NK cells, 10 $CD8^+$ T cells, and 6×10^8 circulating lymphocytes. Immunotherapy consists of a TIL injection followed by short doses of IL-2. This mirrors the treatment that was given to Patients 9 and 10 in Rosenberg's experiments [26], the difference being that the patients in the clinical trial were first administered immuno-depleting chemotherapy before the administration of TIL therapy. IL-2 and chemotherapy concentrations are shown in Fig. 14, right. The combination treatment given is simply a superposition of these separate chemotherapy and immunotherapy regimens. We note that, when administered separately as monotherapies, the chemotherapy treatment alone or the immunotherapy treatment alone is unsuccessful in controlling tumor.

We next run these treatment simulations using the patient specific parameters extracted from the Rosenberg et al. study [26] for Patient 10. We use the same initial conditions for the state of the immune system and the initial tumor challenge. However, several of the immune response parameters for Patient 10 (such as d and λ) differ from those of Patient 9, causing Patient 10's CTL response to tumor

cell growth to be slower. As opposed to the positive response to the combination treatment approach for Patient 9 (see Fig. 14), the parameter set for Patient 10 allows continued growth of the tumor, as seen in in Fig. 15, top left. If we wish to control the tumor, we must modify the treatment. One approach is to administer additional immunotherapy in the form of more IL-2 doses. This expansion in treatment does lead to tumor death in silico, as shown in Fig. 15, top right. It is interesting to note that in this case, tumor behavior seems to reflect tumor dormancy followed by relapse. The tumor appears to have completely died out by day 22. However, around day 79, the tumor begins to re-emerge. Without the additional IL-2 treatment given at day 80, the tumor would regrow. In order to see longer term outcomes, we ran the simulation for 2,000 days, and the tumor did re-emerge, but at levels generally considered below detectability thresholds. The tumor subsequently died out again and did not reappear. See Fig. 15, bottom left. These results indicate that the tumor population has been drawn into the stable zero tumor equilibrium at this point. Such a case in the clinic would likely be viewed as a successful case of complete remission.

Clearly, the immune system's tumor handling capacity and response to treatment is patient specific. This is not surprising, since the combination therapy administered to thirteen patients in the Rosenberg et al. study [26] gave rise to objective clinical responses in only 6 of the 13 patients.

8 Discussion

The first model presented in this chapter incorporates tumor–immune interactions and highlights the qualitative difference in kill rates between the innate immune response (the effect of the NK cells) and the adaptive response (the effect of the $CD8^+$ cells). The model, with its two different functional forms for the kill rates, provides a good fit with experimental data resulting from priming and rechallenge with different combinations of tumor cell types. The fact that two different functional forms are needed to describe the interactions between tumor cells and the two branches of the immune system suggests that laboratory experiments might be designed to illuminate the mechanisms behind the different cell interaction dynamics. Lessons might also be learned by looking at examples in ecology in which predator–prey kill rates can obey either a rational law or a power law [2]. We hypothesize that the more effective the immune cell is at killing, the more closely it follows a rational law dynamic, as given in Eq. (8).

The experimental and simulated results that were presented in this chapter, along with the parameter sensitivity analysis, highlight the importance of $CD8^+$ T cell activation on the time course of the disease. Model results appear to indicate that in order to promote tumor regression, it may be necessary (although perhaps not sufficient) to focus on increasing $CD8^+$ T cell activity. In fact, we propose that there may be a direct positive correlation between the patient-specific efficacy of the $CD8^+$ T cell response as measured by cytotoxicity assays, and the likelihood of a patient responding favorably to certain immunotherapy treatments.

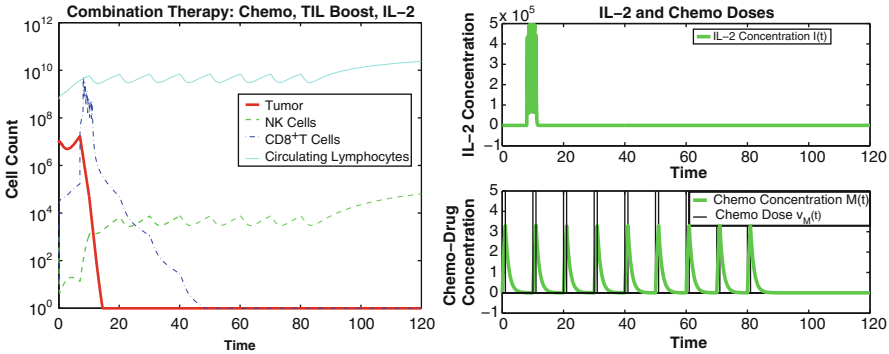

Fig. 14 Human data, Patient 9. Combining the separately unsuccessful therapies for a 10^7 size tumor succeeds in eliminating the tumor. *Left* A 10^7 cell tumor is successfully eliminated by combining nine 1-day chemotherapy doses of strength $v_M(t) = 5$ every 10 days, with a boost of TILs and IL-2. 10^9 TILs are administered from day 7 through 8. IL-2 is administered in 6 pulses from day 8 to day 11 at concentration $v_I(t) = 5 \times 10^5$ per pulse. Initial conditions are: 10^7 Tumor cells, 1×10^3 NK cells, 10 $CD8^+$ T cells, 6×10^8 circulating lymphocytes. Patient 9 parameters for these simulations are in Table 6. *Right* Drug concentrations for IL-2 and chemotherapy

In the final sections of the chapter, we extended the first model to include immuno-modulating therapies. With this extended model, we could test treatment strategies that used immunotherapies and cancer vaccines in conjunction with chemotherapy.

Through an analysis of the system of equations in the absence of chemotherapy or immunotherapy, we determined the equilibrium points of the system along with the criteria for stability. In some parameter ranges, the system exhibited bi-stability, where two stable equilibria co-exist. One of these stable equilibria represents a disease-free state with no tumor cells, and the other represents an unhealthy state where the tumor grows to a significant size. In this bistable situation, a treatment that moves the system into the basin of attraction of the stable tumor-free equilibrium by, for example, reducing the tumor population (through surgery or radiation) and/or by increasing the number of immune cells (through adoptive cell transfer) could lead to a "cured" state. Once the system has moved across the boundary into the zero-tumor basin of attraction, small tumors that arise can be controlled by the immune response—as long as the system parameters do not change too much.

In other parameter regimes, the tumor-free equilibrium is *unstable*, and therefore it is not sufficient merely to reduce the tumor size. In this case of an unstable tumor-free equilibrium, even a few tumor cells will be able to escape the immune surveillance. A successful treatment must be able to change the system parameters in order to force this equilibrium to become stable. We note that in [30], a similar conclusion is reached through a different modeling approach: in this case, too, it is shown that unless system parameters are altered in some way, cytotoxic drugs alone are often not sufficient to control even a very small tumor.

As can be seen in Figs. 14 and 15, simulations using parameter sets from two different patients [26] show that treatment efficacy depends strongly on

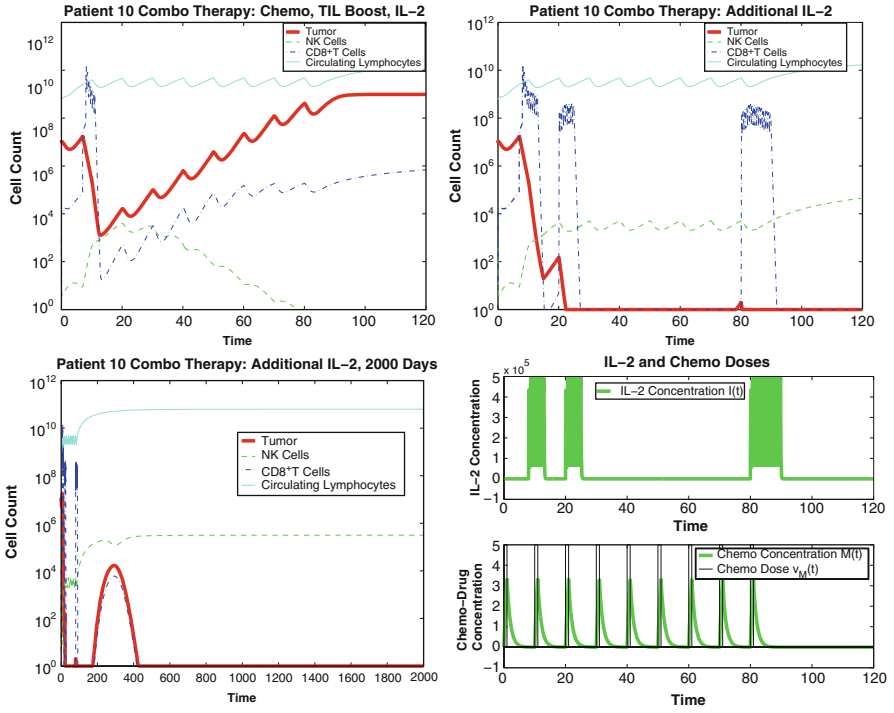

Fig. 15 Human data, Patient 10. *Top left* Combination therapy fails to eliminate the 10^7 cell tumor in Patient 10 with more slowly responding immune system, and initial immune strength of 10^3 NK cells, 10 $CD8^+$ T cells, and 6×10^8 circulating lymphocytes. 10^9 TILs are administered from days 7 through 8. IL-2 is administered in 6 pulses from day 8 to day 11 at concentration $v_I(t) = 5 \times 10^6$ per pulse. *Top right* Combination therapy kills the 10^7 cell tumor in Patient 10. Treatment is identical to that in the *top left panel*, with the exception that additional pulses of IL-2 are administered from days 8 through 13, 20 through 25 and 80 through 90. *Bottom left* The same effective combination therapy as given in the *top right panel* and as shown in the *bottom right panel*, but viewed over 2,000 days. Tumor is eventually eliminated. *Bottom right* Concentrations for IL-2 and chemotherapy implemented in the simulations shown in the *top right and bottom left panels*. Patient 10 parameters are provided in Table 6

patient-specific parameter values. Assays exist that allow for measurement of some of the significant patient specific parameters used. For example, through chromium release assays one can measure patient specific immune-tumor lysis rates, while tumor cell reproduction rates can also be observed and measured in the laboratory. Changes in these measurable parameters clearly affect system outcomes. Although not all system parameters are yet measurable, those that are help to provide a good start in designing customized treatment protocols for individuals.

The development of combination immunotherapy–chemotherapy protocols for treating certain forms of cancer is a promising strategy in cancer treatment research. In some preliminary clinical studies, immunotherapy has been found to be most effective when administered in conjunction with chemotherapy [49], and this

qualitative result has been borne out in our mathematical simulations, as shown in Figs. 14 and 15. In this chapter, combination treatments included vaccine therapy, activated anticancer-cell transfer (TIL injections), and activation-protein injections (IL-2 injections) together with chemotherapy. Mathematical models of other forms of immunotherapy and combination chemo-immunotherapy (such as dendritic cell treatments, regulatory T cell suppression, and targeted monoclonal antibody therapies) can be found in the works of, for example, [13, 14, 21]. The mathematical models presented in this chapter can be used as a springboard for further study and development of patient-specific cancer treatment protocols.

Appendix: Nomenclature and Parameter Values

Here we list all of the parameters used in the model, their meaning and their estimated values. Tables 3 and 4 are fits to the three-dimensional model, while Tables 5 and 6 are fits to the four-dimensional model. Tables 3 and 5 are used in the experiments run to simulate the mouse experiments from [24]. Tables 4 and 6 apply to the human data from [26]. For detailed derivations, see [15, 23].

Table 3 Estimated parameter values: based on mouse experiments provided in [24]

Param.	Units	Description	Estimated value	Source
a	day^{-1}	Tumor growth rate	5.14×10^{-1}	[24]
b	cells^{-1}	$1/b$ is tumor carrying capacity	1.02×10^{-9}	[24]
$c(n)$	$\text{cell}^{-1}\ \text{day}^{-1}$	Fractional (non)-ligand-transduced tumor cell kill by NK cells	3.23×10^{-7}	[24]
$c(l)$			3.50×10^{-6}	
$d(nn)$	day^{-1}	Saturation level of fractional tumor cell kill by $CD8^+$ T cells nn, nl, ln, ll: primed with (non)-ligand-transduced cells, challenged with (non)-ligand-transduced cells	1.43	[24]
$d(nl)$			3.60	
$d(ln)$			3.51	
$d(ll)$			7.17	
$\lambda(nn)$	none	Exponent of fractional tumor cell kill by $CD8^+$ T cells nn, nl, ln, ll: primed with (non)-ligand-transduced cells, challenged with (non)-ligand-transduced cells	5.80×10^{-1}	[24]
$\lambda(nl)$			4.60×10^{-1}	
$\lambda(ln)$			9.00×10^{-1}	
$\lambda(ll)$			7.50×10^{-1}	

(continued)

Table 3 (continued)

Param.	Units	Description	Estimated value	Source
$s(nn)$	none	Steepness coefficient of the Tumor-($CD8^+$ T cell) competition term nn, nl, ln, ll: primed with (non)-ligand-transduced cells, challenged with (non)-ligand-transduced cells. (Smaller $s \Rightarrow$ steeper curve)	2.73	[24]
$s(nl)$			1.61	
$s(ln)$			5.07	
$s(ll)$			4.00×10^{-1}	
e	cells day^{-1}	Constant source of NK cells	1.30×10^4	[46]
f	day^{-1}	Death rate of NK cells	4.12×10^{-2}	[46]
$g(n)$	day^{-1}	Maximum NK cell recruitment rate by (non)-ligand-transduced tumor cells	2.5×10^{-2}	[24, 46]
$g(l)$			$4g(n) = 2 \times 10^{-1}$	
h	cell^2	Steepness coefficient of the NK cell recruitment curve	2.02×10^7	[46]
p	$\text{cell}^{-1}\text{day}^{-1}$	NK cell inactivation rate by Tumor cells	1.0×10^{-7}	[24]
m	day^{-1}	Death rate of $CD8^+$ T cells	2.0×10^{-2}	[73]
$j(nn)$	day^{-1}	Maximum $CD8^+$ T cell recruitment rate nn, nl, ln, ll: primed with (non)-ligand-transduced cells, challenged with (non)-ligand-transduced cells	3.75×10^{-2}	[24, 46]
$j(nl)$			3.75×10^{-2}	
$j(ln)$			$3j(nn) = 1.13 \times 10^{-1}$	
$j(ll)$			$8j(nn)$	
$j(ll)$			$= 3.0 \times 10^{-1}$	
k	cell^2	Steepness coefficient of the $CD8^+$ T cell recruitment curve	2.02×10^7	[24, 46]
q	$\text{cell}^{-1}\ \text{day}^{-1}$	$CD8^+$ T cell inactivation rate by Tumor cells	3.42×10^{-10}	[46]
r	$\text{cell}^{-1}\ \text{day}^{-1}$	Rate at which tumor-specific $CD8^+$ T cells are stimulated to be produced as a result of tumor cells killed by NK cells	1.1×10^{-7}	[47, 73]

Table 4 Estimated parameter values: patient specific parameters used based on data in [26] and other sources

Parameter	Patient 9	Patient 10	Source
a	5.14×10^{-1}	5.14×10^{-1}	Estimated from [24]
b	1.02×10^{-9}	1.02×10^{-9}	Estimated from [24]
c	3.23×10^{-7}	3.23×10^{-7}	Estimated from data in [24, 26]
d	5.80	4.23	Fit to data from [26]
e	1.3×10^{4}	1.3×10^{4}	Parameter from [46]
λ	1.36	1.43	Fit to data from [26]
f	4.12×10^{-2}	4.12×10^{-2}	Parameter from [46]
g	2.5×10^{-2}	2.5×10^{-2}	Estimated from data in [24, 26]
h	2.02×10^{7}	2.02×10^{7}	Parameter from [46]
j	3.75×10^{-2}	3.75×10^{-2}	Estimated from data in [24, 26]
k	2.0×10^{7}	2.0×10^{7}	Estimated from data in [24, 26]
m	2.00×10^{-2}	2.00×10^{-2}	Estimated from data in [73]
q	3.42×10^{-10}	3.42×10^{-10}	Estimated from data in [46]
p	1.00×10^{-7}	1.00×10^{-7}	Estimated from data in [24]
s	2.5×10^{-1}	3.6×10^{-1}	Fit to data in [26]
r	1.1×10^{-7}	1.1×10^{-7}	Estimated from data in [47, 73]

Table 5 Estimated mouse parameter values

Param.	Units	Description	Estimated value	Source
a	day^{-1}	Tumor growth rate	4.31×10^{-1}	[24]
b	cells^{-1}	1/b is tumor carrying capacity	2.17×10^{-8}	[24]
c	$\text{cell}^{-1}\ \text{day}^{-1}$	Fractional (non)-ligand-transduced tumor cell kill by NK cells	7.13×10^{-10}	[24]
d	day^{-1}	Saturation level of fractional tumor cell kill by $CD8^+$ T cells. Primed with ligand-transduced cells, challenged with ligand-transduced cells	8.17	[24]
λ	none	Exponent of fractional tumor cell kill by $CD8^+$ T cells. Primed with ligand-transduced cells, challenged with ligand-transduced cells	6.57×10^{-1}	[24]
s	none	Steepness coefficient of the Tumor-($CD8^+$ T cell) lysis term D. Primed with ligand-transduced cells, challenged with ligand-transduced cells. (Smaller $s \Rightarrow$ steeper curve)	6.18×10^{-1}	[24]
e	day^{-1}	Fraction of circulating lymphocytes that become NK cells	1.29×10^{-3}	[46]
f	day^{-1}	Death rate of NK cells	4.12×10^{-2}	[46]
g	day^{-1}	Maximum NK cell recruitment rate by ligand-transduced tumor cells	4.98×10^{-1}	[24, 46]
h	cell^2	Steepness coefficient of the NK cell recruitment curve	2.02×10^{7}	[46]

(continued)

Table 5 (continued)

Param.	Units	Description	Estimated value	Source
p	$\text{cell}^{-1}\ \text{day}^{-1}$	NK cell inactivation rate by Tumor cells	1.0×10^{-7}	[24]
m	day^{-1}	Death rate of $CD8^+$ T cells	2.0×10^{-2}	[73]
j	day^{-1}	Maximum $CD8^+$ T cell recruitment rate. Primed with ligand-transduced cells, challenged with ligand-transduced cells	9.96×10^{-1}	[24, 46]
k	cell^2	Steepness coefficient of the $CD8^+$ T cell recruitment curve	3.03×10^5	[24, 46]
q	$\text{cell}^{-1}\ \text{day}^{-1}$	$CD8^+$ T cell inactivation rate by Tumor cells	3.42×10^{-10}	[46]
r_1	$\text{cell}^{-1}\ \text{day}^{-1}$	Rate at which $CD8^+$ T cells are stimulated to be produced as a result of tumor cells killed by NK cells	1.1×10^{-7}	[47, 73]
r_2	$\text{cell}^{-1}\ \text{day}^{-1}$	Rate at which $CD8^+$ T cells are stimulated to be produced as a result of tumor cells interacting with circulating lymphocytes	3.0×10^{-11}	No data found
u	$\text{cell}^{-2}\ \text{day}^{-1}$	Regulatory function by NK-cells of $CD8^+$ T-cells	1.80×10^{-8}	No data found
K_T	day^{-1}	Fractional tumor cell kill by chemotherapy	9.00×10^{-1}	[61]
K_N, K_L, K_C	day^{-1}	Fractional immune cell kill by chemotherapy	6.00×10^{-1}	[61]
α	cell day^{-1}	Constant source of circulating lymphocytes	1.21×10^5	[3, 36]
β	day^{-1}	Natural death and differentiation of circulating lymphocytes	1.20×10^{-2}	[3, 36]
γ	day^{-1}	Rate of chemotherapy drug decay	9.00×10^{-1}	[8]

Table 6 Estimated human parameter values

Patient 9	Patient 10	Source
$a = 4.31 \times 10^{-1}$	$a = 4.31 \times 10^{-1}$	[24]
$b = 1.02 \times 10^{-9}$	$b = 1.02 \times 10^{-9}$	[24]
$c = 6.41 \times 10^{-11}$	$c = 6.41 \times 10^{-11}$	[24, 26]
$d = 2.34$	$d = 1.88$	[26]
$e = 2.08 \times 10^{-7}$	$e = 2.08 \times 10^{-7}$	[46]
$\lambda = 2.09$	$\lambda = 1.81$	[26]
$f = 4.12 \times 10^{-2}$	$f = 4.12 \times 10^{-2}$	[46]
$g = 1.25 \times 10^{-2}$	$g = 1.25 \times 10^{-2}$	[24, 26]
$h = 2.02 \times 10^7$	$h = 2.02 \times 10^7$	[46]
$j = 2.49 \times 10^{-2}$	$j = 2.49 \times 10^{-2}$	[24, 26]
$k = 3.66 \times 10^7$	$k = 5.66 \times 10^7$	[24, 26]

(continued)

Table 6 (continued)

Patient 9	Patient 10	Source
$m = 2.04 \times 10^{-1}$	$m = 9.12$	[73]
$q = 1.42 \times 10^{-6}$	$q = 1.59 \times 10^{-6}$	[46]
$p = 3.42 \times 10^{-6}$	$p = 3.59 \times 10^{-6}$	[24]
$s = 8.39 \times 10^{-2}$	$s = 5.12 \times 10^{-1}$	[26]
$r_1 = 1.10 \times 10^{-7}$	$r_1 = 1.10 \times 10^{-7}$	[47, 73]
$r_2 = 6.50 \times 10^{-11}$	$r_2 = 6.50 \times 10^{-11}$	No data found
$u = 3.00 \times 10^{-10}$	$u = 3.00 \times 10^{-10}$	No data found
$K_T = 9.00 \times 10^{-1}$	$K_T = 9.00 \times 10^{-1}$	[61]
$K_N = K_L = K_C = 6 \times 10^{-1}$	$K_N = K_L = K_C = 6 \times 10^{-1}$	[61]
$\alpha = 7.50 \times 10^{8}$	$\alpha = 5.00 \times 10^{8}$	[3, 36]
$\beta = 1.20 \times 10^{-2}$	$\beta = 8.00 \times 10^{-3}$	[3, 36]
$\gamma = 9.00 \times 10^{-1}$	$\gamma = 9.00 \times 10^{-1}$	[8]
p_I: Maximum $CD8^+$T-cell recruitment rate by IL-2. Units: day^{-1}		
$p_I = 1.25 \times 10^{-1}$	$p_I = 1.25 \times 10^{-1}$	[42]
g_I: Steepness of $CD8^+$T-cell recruitment curve by IL-2. Units: $cell^2$		
$g_I = 2.00 \times 10^{7}$	$g_I = 2.00 \times 10^{7}$	[42]
μ_I: Rate of IL-2 drug decay. Units: day^{-1}		
$\mu_I = 1.00 \times 10^{1}$	$\mu_I = 1.00 \times 10^{1}$	[42]

References

1. Adam, J.A., Bellomo, N.: A Survey of Models for Tumor Immune Systems Dynamics. Springer, New York (1997)
2. Akçakaya, H., Arditi, R., Ginzburg, L.R.: Ratio-dependent predation: an abstraction that works. Ecology **76**, 995–1004 (1995)
3. Bannock, L.: Nutrition (2002). Found at http://www.doctorbannock.com/nutrition.html. Accessed January 2013
4. Bellomo, N., Preziosi, L.: Modelling and mathematical problems related to tumor evolution and its interaction with the immune system. Math. Comput. Model. **32**(3–4), 413–452 (2000)
5. Blattman, J., Greenberg, P.: Cancer immunotherapy: a treatment for the masses. Science **305**, 200–205 (2004)
6. Borrelli, R., Coleman, C.: Differential Equations: A Modeling Perspective. Wiley, New York (1998)
7. Britton, N.: Essential Mathematical Biology. Springer, London (2003)
8. Calabresi, P., Schein, P. (eds.).: Medical Oncology: Basic Principles and Clinical Management of Cancer, 2nd edn. McGraw-Hill, New York (1993)
9. Coldman, A.J., Goldie, J.H.: A stochastic model for the origin and treatment of tumors containing drug-resistant cells. Bull. Math. Biol. **48**(3 − 4), 279–292 (1986); Simulation in cancer research (Durham, 1986)
10. Cooper, M., Fehniger, T., Caligiuri, M.: The biology of human natural killer-cell subsets. Trends Immunol. **22**(11), 633–640 (2001)
11. Couzin, J.: Select T cells, given space, shrink tumors. Science **297**, 1973 (2002)
12. Dalgleish, A.G., O'Byrne, K.J.: Chronic immune activation and inflammation in the pathogenesis of AIDS and cancer. Adv. Cancer Res. **84**, 231–276 (2002)

13. de Pillis, L., Caldwell, T., Sarapata, E., Williams, H.: Mathematical modeling of the regulatory T cell effects on renal cell carcinoma treatment. Discr. Contin. Dyn. Syst. Ser. B **18**(4), 915–94 (2013)
14. de Pillis, L., Gallegos, A., Radunskaya, A.: A model of dendritic cell therapy for melanoma. Front. Oncol. **3**(56), 1–14 (2013). http://www.frontiersin.org/molecular_and_cellular_oncology/10.3389/fonc.2013.00056/abstract. Accessed January 2013
15. de Pillis, L., Gu, W., Radunskaya, A.: Mixed immunotherapy and chemotherapy of tumors: modeling applications and biological interpretations. J. Theor. Biol. **238**(4), 841–862 (2006)
16. de Pillis, L., Radunskaya, A.: A mathematical tumor model with immune resistance and drug therapy: an optimal control approach. J. Theor. Med. **3**, 79–100 (2001)
17. de Pillis, L., Radunskaya, A.: Immune response to tumor invasion. In: Bathe, K., (ed.) Computational Fluid and Solid Mechanics, vol. 2, pp. 1661–1668. MIT, Cambridge (2003)
18. de Pillis, L.G., Radunskaya, A.: The dynamics of an optimally controlled tumor model: a case study. Math. Comput. Model. **37**, 1221–1244 (2003)
19. de Pillis, L., Radunskaya, A.: Some promising approaches to tumor-immune modeling. Math. Stud. Hum. Dis. Dyn. **410**, 89–112 (2006)
20. de Pillis, L., Radunskaya, A.: Best practices in mathematical modeling. In: Mayeno, A., Reisfeld, B., (eds.) Computational Toxicology, Methods in Molecular Biology, vol. 929, Part 2, pp. 51–74. Springer, New York (2012)
21. de Pillis, L.G., Radunskaya, A.E., Savage, H.: Mathematical model of colorectal cancer with monoclonal antibody treatments. Br. J. Med. Med. Res. **4**(16), 3101–3131 (2014)
22. de Pillis, L., Radunskaya, A., Wiseman, C.: A validated mathematical model of cell-mediated immune responses to tumor invasion and vaccine therapy in mice and humans. Invited Poster, Society of Biological Therapy 17th Annual Meeting (2003)
23. de Pillis, L.G., Radunskaya, A.E., Wiseman, C.L.: A validated mathematical model of cell-mediated immune response to tumor growth. Cancer Res. **65**(1), 7950–7958 (2005)
24. Diefenbach, A., Jensen, E., Jamieson, A., Raulet, D.: Rae1 and H60 ligands of the NKG2D receptor stimulate tumor immunity. Nature **413**, 165–171 (2001)
25. Donnelly, J.: Cancer vaccine targets leukemia. Nat. Med. **9**(11), 1354–1356 (2003)
26. Dudley, M., Wunderlich, J., Robbins, P., Yang, J., Hwu, P., Schwartzentruber, D., Topalian, S., Sherry, R., Restifo, N., Hubicki, A., Robinson, M., Raffeld, M., Duray, P., Seipp, C., Rogers-Freezer, L., Morton, K., Mavroukakis, S., White, D., Rosenberg, S.: Cancer regression and autoimmunity in patients after clonal repopulation with antitumor lymphocytes. Science **298**(5594), 850–854 (2002)
27. Eisen, M.: Mathematical Models in Cell Biology and Cancer Chemotherapy. Springer, Berlin (1979)
28. Farrar, J., Katz, K., Windsor, J., Thrush, G., Scheuermann, R., Uhr, J., Street, N.: Cancer dormancy. VII. A regulatory role for CD8+ T cells and IFN-gamma in establishing and maintaining the tumor-dormant state. J. Immunol. **162**(5), 2842–9 (1999)
29. Gardner, S.N.: A mechanistic, predictive model of dose-response curves for cell cycle phase-specific and nonspecific drugs. Cancer Res. **60**, 1417–1425 (2000)
30. Gatenby, R., Vincent, T.: Application of quantitative models from population biology and evolutionary game theory to tumor therapeutic strategies. Mol. Cancer Ther. **2**(9), 919–927 (2003)
31. Germain, R.: An innately interesting decade of research in immunology. Nat. Med. **10**(12), 1307–1320 (2004)
32. Gilks, W.: Markov Chain Monte Carlo. Encyclopedia of Biostatistics. Wiley Online Library, MRC Biostatistics Unit, Cambridge (2005)
33. Glas, R., Franksson, L., Une, C., Eloranta, M., Ohlen, C., Orn, A., Karre, K.: Recruitment and activation of natural killer (NK) cells in vivo determined by the target cell phenotype: an adaptive component of NK cell-mediated responses. J. Exp. Med. **191**(1), 129–138 (2000)
34. Hadj, T.: Alemtuzumab for B-cell chronic lymphocytic leukemia. Issues Emerg. Health Technol. **66**, 1–4 (2005)

35. Hart, D., Shochat, E., Agur, Z.: The growth law of primary breast cancer as inferred from mammography screening trials data. Br. J. Cancer **78**(3), 382–387 (1998)
36. Hauser, B.: Blood tests. Tech. rep., International Waldenstrom's Macroglobulinemia Foundation (2001). Available at http://www.iwmf.com/Blood_Tests.pdf. Accessed May 2005
37. Henderson, D., Jacobson, S., Johnson, A.: The theory and practice of simulated annealing. In: Glover, F., Kochenberger, G., (eds.) Handbook of Metaheuristics, International Series in Operations Research & Management Science, vol. 57, pp. 287–319. Springer US (2003). doi:10.1007/0-306-48056-5_10
38. Institute, C.R.: Cancer and the immune system: The vital connection. Web page publication of the Cancer Research Institute (2000). http://www.cancerresearch.org. Available at http://www.cancerresearch.org/immunology/immuneindex.html. Accessed May 2005
39. Jiang, H., Chess, L.: An integrated view of supporessor T cell subsets in immunoregulation. J. Clin. Invest. **114**(9), 1198–1208 (2004)
40. Kawarada, Y., Ganss, R., Garbi, N., Sacher T. ad Arnold, B., Hammerling, G.: NK- and CD8+ T cell-mediate eradication of established tumors by peritumoral injection of CpG-containing oligodeoxynucleotides. J. Immunol. **167**(1), 5247–5253 (2001)
41. Kieper, W., Prlic, M., Schmidt, C., Mescher, M., Jameson, S.: Il-12 enhances CD8+ T cell homeostatic expansion. J. Immunol. **166**, 5515–5521 (2001)
42. Kirschner, D., Panetta, J.: Modeling immunotherapy of the tumor-immune interaction. J. Math. Biol. **37**(3), 235–52 (1998)
43. Kolmogorov, A.: Sulla teoria di volterral della lotta per l'esistenza. Giornale Istituto Ital. Attuari **7**, 74–80 (1936)
44. Kuznetsov, V.: Basic models of tumor-immune system interactions—identification, analysis and predictions. In: Adam, J., Bellomo, N., (eds.) A Survey of Models for Tumor-Immune System Dynamics, pp. 237–294. Springer, Berlin (1997)
45. Kuznetsov, V., Makalkin, I.: Bifurcation-analysis of mathematical-model of interactions between cytotoxic lymphocytes and tumor-cells—effect of immunological amplification of tumor-growth and its connection with other phenomena of oncoimmunology. Biofizika **37**(6), 1063–70 (1992)
46. Kuznetsov, V., Makalkin, I., Taylor, M., Perelson, A.: Nonlinear dynamics of immunogenic tumors: Parameter estimation and global bifurcation analysis. Bull. Math. Biol. **56**(2), 295–321 (1994)
47. Lanzavecchia, A., Sallusto, F.: Dynamics of T-lymphocyte responses: intermediates, effectors, and memory cells. Science **290**, 92–97 (2000)
48. Li, J., Guo, K., Koh, V., Tang, J., Gan, B., Shi, H., Li, H., Zeng, Q.: Generation of PRL-3- and PRL-1-specific monoclonal antibodies as potential diagnostic markers for cancer metastases. Clin. Cancer Res. **11**(6), 2195–2204 (2005)
49. Machiels, J., Reilly, R., Emens, L., Ercolini, A., Lei, R., Weintraub, D., Okoye, F., Jaffee, E.: Cyclophosphamide, doxorubicin, and paclitaxel enhance the antitumor immune response of granulocyte/macrophage-colony stimulating factor-secreting whole-cell vaccines in HER-2/*neu* tolerized mice. Cancer Res. **61**(9), 3689–3697 (2001)
50. Melichar, B., Dvorak, J., Jandik, P., Touskova, M., Solichova, D., Megancova, J., Z., V.: Intraarterial chemotherapy of malignant melanoma metastatic to the liver. Hepatogastroenterology **48**(42), 1711–1715 (2001)
51. Meyskens, F.J., Thomson, S.P., Moon, T.E.: Quantitation of the number of cells within tumor colonies in semisolid medium and their growth as oblate spheroids. Cancer Res. **44**, 271–277 (1984)
52. Morecki, S., Pugatsch, T., Levi, S., Moshel, Y., Slavin, S.: Tumor-cell vaccination induces tumor dormancy in a murine model of B-cell leukemia/lymphoma (BCL1). Int. J. Cancer **65**(2), 204–8 (1996)
53. Muller, M., Gounari, F., Prifti, S., Hacker, H., Schirrmacher, V., Khazaie, K.: EblacZ tumor dormancy in bone marrow and lymph nodes: active control of proliferating tumor cells by CD8+ immune T cells. Cancer Res. **58**(23), 5439–46 (1998)
54. Murphy, K.: Janeway's Immunobiology, 8th edn. Garland Science, New York (2011)

55. Murray, J.M.: Mathematical Biology, 2nd edn. Springer, Berlin (1993)
56. Mustafa, M., Buchanan, G., Winick, N., McCracken, G., Tkaczewski, I., Lipscomb, M., Ansari, Q., Agopian, M.: Immune recovery in children with malignancy after cessation of chemotherapy. J. Pediatr. Hematol. Oncol. **20**(5), 451–457 (1998)
57. O'Byrne, K.J., Dalgleish, A.G., Browning, M.J., Steward, W.P., Harris, A.L.: The relationship between angiogenesis and the immune response in carcinogenesis and the progression of malignant disease. Eur. J. Cancer **36**, 151–169 (2000)
58. Osada, T., Nagawa, H., Shibata, Y.: Tumor-infiltrating effector cells of α-galactosylceramide-induced antitumor immunity in metastatic liver tumor. J. Immune Based Ther. Vaccines **2**(7), 1–9 (2004)
59. Pardoll, D.: Cancer vaccines. Nat. Med. **4**(5), 525–531 (1998) (Vaccine Supplement)
60. Pazdur, R., Hoskins, W., Wagman, L., Coia, L. (eds.): Cancer Management: A Mulitdisciplinary Approach, 8th edn., chap. Principles of Chemotherapy. Oncology Publishing Group of CMP Healthcare Media (2004). Available at http://www.cancernetwork.com/handbook/contents.htm. Accessed May 2005
61. Perry, M. (ed.): The Chemotherapy Source Book, 3rd edn. Lippincott Williams & Wilkins, Philadelphia (2001)
62. Qu, Z., Griffiths, G., Wegener, W., Chang, C., S.V., G., Horak, I., Hansen, H., Goldenberg, D.: Development of humanized antibodies as cancer therapeutics. Methods **36**(1), 84–95 (2005). doi:10.1016/j.ymeth.2005.01.008
63. Roitt, I., Brostoff, J., Male, D.: Immunology. Mosby, St. Louis (1993)
64. Rosenbaum, E., Rosenbaum, I.: Everyone's Guide to Cancer Supportive Care: A Comprehensive Handbook for Patients and Their Families. Andrews McMeel, Kansas (2005)
65. Rosenberg, S., Yang, J., Restifo, N.: Cancer immunotherapy: moving beyond current vaccines. Nat. Med. **10**(9), 909–915 (2004)
66. Sarapata, E., de Pillis, L.: A comparison and catalog of intrinsic tumor growth models. arXiv:1312.4857v1 [q-bio.CB] pp. 1–73 (2013). Preprint, http://arxiv.org/abs/1312.4857
67. Sen, M.K., Stoffa, P.L.: Global Optimization Methods in Geophysical Inversion. Cambridge University Press, Cambridge (2013)
68. Skipper, H.E.: On mathematical modeling of critical variables in cancer treatment (goals: better understanding of the past and better planning in the future). Bull. Math. Biol. **48**(3–4), 253–278 (1986); Simulation in cancer research (Durham, 1986)
69. Stewart, T.: Immune mechanisms and tumor dormancy. Medicina (Buenos Aire) **56**(1), 74–82 (1996)
70. The MathWorks, I.: Matlab (2012b)
71. Volterra, V.: Variazioni e fluttuazioni del numero d'individui in specie animali conviventi. Mem. Acad. Lincei Roma **2**, 31–113 (1926)
72. Wheeler, C., Asha, D., Gentao, L., Yu, J., Black, K.: Clinical responsiveness of glioblastoma multiforme to chemotherapy after vaccination. Clin. Cancer Res. **10**, 5316–5326 (2004)
73. Yates, A., Callard, R.: Cell death and the maintenance of immunological memory. Discr. Contin. Dyn. Ser. B **1**(1), 43–59 (2002)

The Mathematics of Drug Delivery

Peter Hinow and Ami E. Radunskaya

Abstract There are a variety of devices for the delivery of pharmaceutical substances, tablets of course being the most prominent. Pharmaceutical scientists and physicians have formulated goals, such as release of a drug in a controlled fashion over an extended period of time or the targeted delivery of a drug to a specific site in a patient's body. Since experiments with these delivery devices can be costly and sometimes only partially conclusive, mathematical modeling can play a role in understanding the mechanisms behind experimental release profiles and in developing delivery systems. Here we review mathematical models for drug delivery by matrix tablets and liposomes.

1 Introduction

Pharmaceutical scientists are concerned with the delivery of drugs to a patients body in an efficient and safe manner. Dictated by the nature of the ailment and the drug to treat it, there are several routes of delivery, such as oral, nasal, intravenous, and transdermal routes to name just a few. Most well known of course is oral administration and there the most prevalent form of delivery is via tablets. Simple and convenient to use, they also allow fairly exact measuring of the dose of active ingredient in each tablet. As we shall see in this chapter, it is often the case that only a part of the drug load of the tablet is released. With modern drugs being very expensive it is obvious that the fraction of drug released should be as high as possible. Another objective is to release the drug load in a controlled fashion so that the levels of the drug in the body remain in a narrow therapeutic range: levels

P. Hinow (✉)
Department of Mathematical Sciences, University of Wisconsin,
P.O. Box 413, Milwaukee, WI 53201-0413, USA
e-mail: hinow@uwm.edu

A.E. Radunskaya
Department of Mathematics, Pomona College, 610 N. College Ave.,
Claremont, CA 91711, USA
e-mail: aer04747@pomona.edu

A. Eladdadi et al. (eds.), *Mathematical Models of Tumor-Immune System Dynamics*, Springer Proceedings in Mathematics & Statistics 107,
DOI 10.1007/978-1-4939-1793-8_5

of drug that are too low are sub-therapeutic, and levels that are too high carry the obvious danger of harmful side effects.

A second, more recently developed delivery device that we will discuss in this chapter are liposomes. Liposomes are artificially prepared vesicles consisting of a lipid bilayer that encapsulates the drug in a solution. The lipid bilayer is similar in nature to those that make up cytoplasmic and nuclear membranes of the cells. Thus liposomes have the potential to be incorporated by cells through endocytosis and in addition may be directed towards specific target sites in the body. They further offer protection of hydrophilic drugs from dissolving before they reach their target zone in the body. The goal of pharmaceutical scientists is to control the permeability of the liposome membrane to the drug cargo. One way to accomplish this is with the help of bile salts that bind to the membrane. Different bile salts act differently on the liposome membrane, depending of course also on their concentrations. This is another part of our mathematical modeling efforts to be reviewed in this chapter.

The importance of mathematical modeling of drug delivery has long been recognized. While early attempts [13] consisted still largely of phenomenological expressions, in the past decades the need for a deeper understanding of the physical processes inside a tablet or liposome became clear. In this chapter we review our own works concerning drug release from matrix tablets [3, 4] and modulation of liposome permeability [15]. The mathematical tools employed include ordinary and partial differential equation models, random walks, and cellular automata. The chapter ends with an outlook on present challenges and the concept of "triggered" delivery.

2 Drug Release from Matrix Tablets

Matrix tablets are drug delivery devices that release a water-soluble drug over an extended period of time. Such matrix tablets are formulated from mixtures of polymer, drug, and excipient powders, of which the latter two are water soluble. The composition of the powder mixture as well as the choice of compaction pressures and optional curing temperatures allow variation in the drug release profile of the tablet. To determine the release profiles experimentally, a tablet fabricated in this manner is placed into a rotating basket apparatus and the release of the drug over time is monitored. Earlier mathematical models focused on random walks on cubic lattices [29, 30], Monte Carlo simulations [18], and percolation theory [6]. A common observation in many works is that there exists a critical fraction of polymer powder in the mixture below which the release of the drug is complete or nearly complete. If the polymer fraction is increased above that fraction, the drug release remains incomplete, say 40–60% of the total load. Frequently expressions such as the *Higuchi law*, *Peppas equation*, or *Weibull equation*, namely

$$M(t) = K\sqrt{t}, \qquad M(t) = Kt^n, \qquad M(t) = K(1 - \exp(-at^b)),$$

respectively, are fit to the simulated release curves. In these expressions, $M(t)$ is the fraction released at time t, and K, n, a and b are model parameters. While these expressions allow for easy comparison of different curves, the precise meaning of the fitted parameters often remains unclear. Subsequent authors have worked with partial differential equations for diffusion and erosion processes [19, 25]. These powerful models remain challenging to construct, to parametrize, and to implement. During the release process, the matrix porosity increases and the topology of the channel network available for diffusion changes as well. We will address this issue briefly below.

2.1 The Discrete Model

In [3] we propose two mathematical models for drug release from a matrix tablet, one discrete and one continuous. The discrete model begins with the construction of a graph as the contact graph of a random dense sphere packing. Dense sphere packings are a highly interesting topic in their own right [9, 14, 27] and have found many applications in statistical physics [20] and space engineering [17]. We use the "stochastic billiard" method proposed by Lubachevsky and Stillinger [21] where a certain number of spheres move and grow in a container. The spheres are initialized with small radii, randomly placed in a container, with random initial velocities. The spheres then undergo elastic collisions with one another and with the walls, while the radii grow at constant rates. By assigning different rates to different spheres, packings with spheres of different sizes can be created. Since the walls of the container are fixed, the growing spheres have less and less room to move in, and the collisions become more and more frequent. The process is stopped once the collision frequency exceeds a certain bound. The spheres in the packing are then labeled "polymer," "drug," and "excipient" according to the composition of the powder mixture that we want to simulate.

From the sphere packing, we construct a *contact graph*. The contact graph consists of a node for each particle (sphere), with edges between nodes that are less than a prescribed minimum distance apart. Under the assumption that dissolved drug and excipient particles can diffuse through the tablet, we model the escape of drug by a random walk along the edges of the contact graph. However, all edges emanating from a node labeled "polymer" are removed, to represent the insolubility of polymer. The production process can contain a step of heating of the tablet which causes polymer to melt and leads to a closer encapsulation of the drug. In order to model this, we allow for an additional random removal of edges between neighboring non-polymer spheres. We now begin a random walk on the contact graph that begins at every drug node and terminates at one of the boundary nodes. Since edges to polymer nodes have already been removed, only nodes labeled "drug" or "excipient" are accessible to the random walker. The number of steps of each walk is counted and the cumulative distribution function is taken as a

prediction of the release curve. To avoid endless loops, a walk is also terminated once a maximum number of steps has been reached. Figure 1 illustrates the random walk in two dimensions.

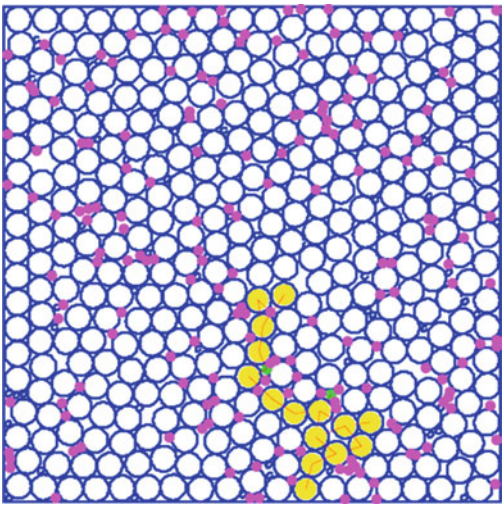

Fig. 1 Graphical illustration of one random walk through the contact graph. The polymer particles are the *smaller, solid, spheres*. The walk terminates when the "walker" reaches the boundary of the tablet

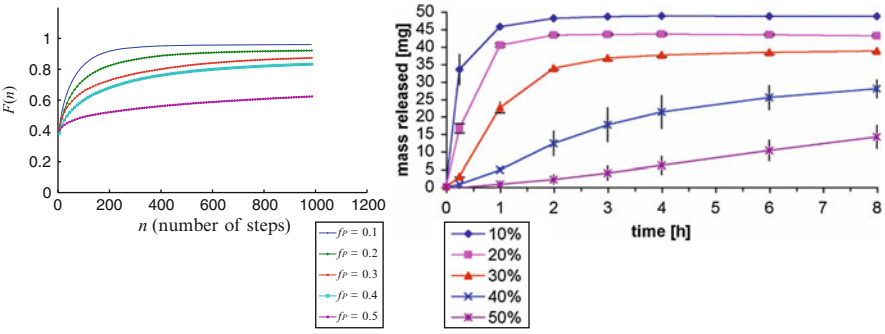

Fig. 2 *(Left)* Simulated release curves for powder mixtures with five different polymer fractions. The mass fraction is kept constant at 10 %, the remainder of the tablet is comprised of water soluble, pharmaceutically inactive excipient. *(Right)* Experimental release of indomethacin (mass fraction 10 %) from Eudragit RLPO matrix tablets containing mannitol (90–125 μm particle diameter) as plastic excipient. The tablets were cured at 40°C for 24 h. Figures are taken from [3] and [8]

The simulation method in [3] is quite capable of reproducing the delayed and only partial release of drug as the polymer fraction in the powder mixture is increased. As we mentioned above, heating of the tablet can be simulated by additional edge removal [3, not shown]. This results in pockets of drug particles that are completely surrounded by polymer particles and thus unable to escape. The fact

that the simulated release curves in the left panel of Fig. 2 begin at approximately one-half of the total amount of drug contained is due to the fact that the sphere packings used in [3] were relatively small, about 2,000 spheres. Thus surface effects are more prominent as a lot of drug particles are already situated on the boundary of the tablet. A more critical shortcoming of the simulated release curves is that they do not show the change from convex to concave that is visible in some of the experimental release profiles in the right panel of Fig. 2. This shape is due to the fact that after the tablet is initially placed in the fluid, some time is required for the fluid to penetrate the tablet and to dissolve the drug. Moreover, the initial model did not take into account the rearrangement of the polymer matrix during the process of powder compaction. To address these problems, in [4] we introduce a cellular automaton model that we describe in Sect. 2.3.

2.2 The Continuous Model

The second model in [3] is based on a system of reaction-diffusion partial differential equations for the concentrations of dissolved and undissolved drug and excipient, respectively. The spatial domain Ω is a cylinder of radius R and height H. It is therefore convenient to introduce cylindrical coordinates and to make the plausible assumption that all dissolution and diffusion processes possess rotational symmetry, so that the angular variable θ can be omitted. We denote by v_1 and v_2 the concentration of dissolved drug in the solvent and the content of undissolved drug in the tablet, respectively, with similar expressions u_1 and u_2 for dissolved and undissolved excipient. The porosity of the tablet is denoted by $\kappa \in [0, 1]$ and this will increase as excipient and drug are dissolved in the solvent. The diffusion of the dissolved substance follows the classical Fick's law, while the dissolution of undissolved substance is possible only as long as the surrounding fluid is not already saturated with dissolved substance. Under these assumptions we obtain a system of the following type

$$\begin{aligned} &\frac{\partial}{\partial t}(\kappa(u_2, v_2)v_1) - \nabla_{(r,z)} \cdot (D_v \kappa(u_2, v_2)\nabla v_1) = \alpha_v \kappa(u_2, v_2)\left(1 - \frac{v_1}{C^v_{\max}}\right) v_2, \\ &\frac{\partial}{\partial t} v_2 = -\alpha_v \kappa(u_2, v_2)\left(1 - \frac{v_1}{C^v_{\max}}\right) v_2, \end{aligned} \tag{1}$$

with a similar pair (but with possibly different constants) for the dynamics of the excipient. Here α_v denotes the rate of drug dissolution. Note that the porosity of the tablet, which itself changes over time, influences the dissolution process due to the changing contact area between drug and fluid. The porosity function is given by

$$\kappa(u_2, v_2) = (\kappa_0 - \kappa_{end})\frac{u_2 + v_2}{u_2^0 + v_2^0} + \kappa_{end},$$

where κ_0 and κ_{end} are the initial and terminal porosities, respectively. The parameter, κ_{end}, reflects the amount of polymer in the tablet: when all of the drug and excipient have dissolved and diffused out of the table, a higher polymer content will yield a less porous tablet. In other words, κ_{end} *decreases* as the fraction of polymer in the tablet increases. Initially all drug and excipient are bound and uniformly distributed across the tablet so that

$$u_1^0 = v_1^0 = 0, \quad u_2^0(x) \equiv u_2^0, \quad \text{and} \quad v_2^0(x) \equiv v_2^0.$$

Finally, we assume that any dissolved drug and excipient that have reached the boundary of the tablet are immediately carried away so that the model is completed by homogeneous Dirichlet boundary conditions for the diffusing substances. The integral of $\kappa(u_2, v_2)u_1 + u_2$ gives the total amount of drug still in the tablet so that its antiderivative is the complement of the cumulative release function. A few numerical solutions are shown in Fig. 3. As can be seen in this figure, the partial differential equation model captures the change from convex to concave in the release profiles. This further underscores the importance of including the dissolution process in any model. On the other hand, this model does not provide an easy way to quantitatively represent the different possible powder compositions, nor does it reproduce the partial release in the case of high polymer load. To produce both features, namely the concavity changes and the saturation of the release profiles, we develop a cellular automaton model.

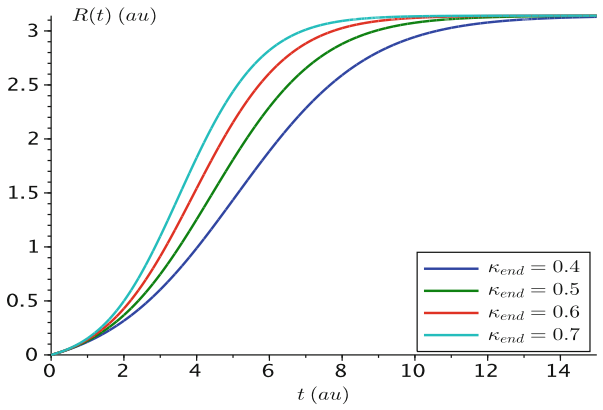

Fig. 3 Release profiles predicted by the continuous model (1) as the final porosity κ_{end} varies. The dimensionless parameters used in this example are $\kappa_0 = 0.02$, $D_u = 0.3$, $D_v = 0.5$ $\alpha_u = \alpha_v = 1.5$ and $C^u_{\max} = C^v_{\max} = u_2^0 = v_2^0 = 1$

2.3 The Cellular Automaton Model

Cellular automata (CA) were first conceived by Stanislaw Ulam and John von Neumann in the 1940s at a time when computing technology was yet in its infancy. Since then they have been put to good use in the simulation of traffic networks [22], neural networks [12], tumor growth [10, 16] and statistical mechanics, to name but a few examples. In a standard CA, the computational domain (in this context, the three-dimensional volume taken up by the tablet) is divided into "cells." Each cell can be in one of a finite number of states. Rules governing transitions between states depend on the state of the cell and on the states of its neighbors. In our case of matrix tablets it is natural to create cells that are empty, occupied by solid substance (drug, polymer, or excipient), or by water, which in turn carries the dissolved drug and excipients.

To represent the tablet, the cells of the automaton are arranged on a cubical lattice filling out a cylinder. Each cell can be in one of five states *drug* (D), *polymer* (P), *excipient* (X), *empty* (E), and *water* (W). Every cell filled with water is in addition characterized by the concentrations of dissolved drug and excipient, relative to a saturation concentration. The polymer, drug and excipient cells are present in their relative concentrations in the powder mixture while the empty sites are created during the simulation of the compaction process by breaking drug cells into smaller pieces. The effect of compaction and curing on the polymer cells is to allow polymer to move into adjacent empty spaces, with a preference for spaces occupied by polymer. This part of the initialization process allows the user to simulate a variety of preparation scenarios, since the polymer particles deform under pressure, and fuse together when heated. Initially, there are no water cells inside the tablet but it is surrounded at all times by cells filled with water.

In each simulated time step after the initialization step, there are three sub-processes that are modeled by the cellular automaton rules:

1. *Dissolution*: the number of wet cells are updated, and the concentration of dissolved drug and excipient is calculated. Empty cells can be filled with water if they have water cells as neighbors. Cells occupied by drug or excipient can be replaced by water if they have water cells as neighbors and these cells have still some dissolution capacity. Once a drug or excipient cell is replaced by water, the amount of drug or excipient is then dissolved in the newly formed water cell.
2. *Diffusion*: Dissolved drug and excipient diffuse freely between neighboring water cells in accordance with Fick's law.
3. *Transport away from the boundary*: The entire tablet is surrounded by a layer of water cells in which the dissolved substances are diffusing. We simulate some common experimental setups where the external fluid is stirred by further diluting the concentrations of drug end excipient in the external boundary layer. This eases further diffusion of dissolved substances from the interior of the tablet.

A simulation of a small tablet is shown in Fig. 4 to illustrate these steps.

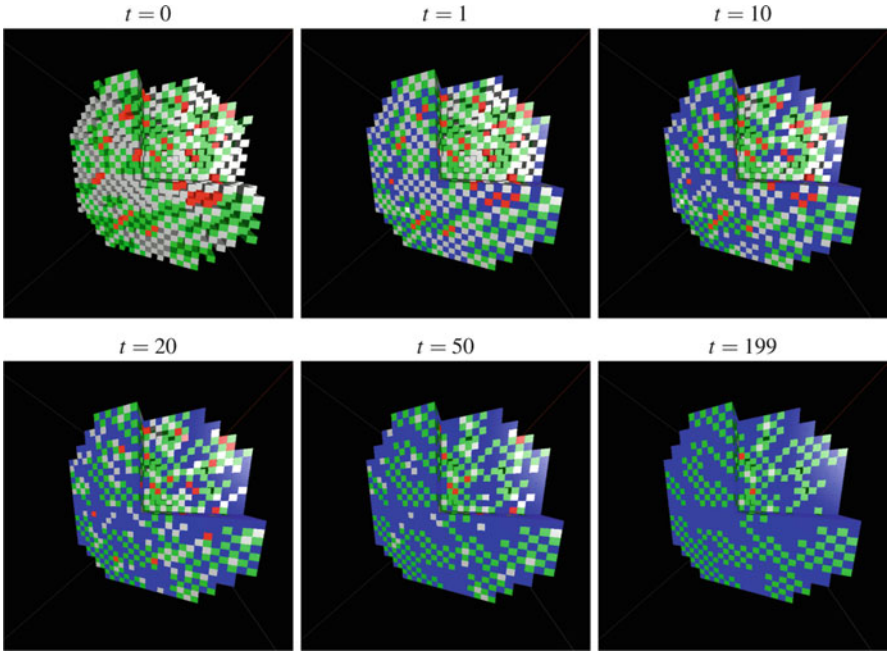

Fig. 4 Snapshots of the states of the tablet CA for a very small tablet to illustrate the updating rules. Part of the tablet is cut away so that we can visualize what is happening in the interior. The states are represented by different colors: *red* (drug), *green* (polymer), *grey* (excipient), water (*blue*) and empty (*black*). Initially ($t = 0$) the tablet contains no water, and we see the randomly placed particles of solid drug, excipient and polymer, with a few empty cells. As the tablet is immersed in the water medium, water cells enter the empty spaces ($t = 1$), but the interior still consists of solid particles. Excipient and drug cells then begin to dissolve, and we see the corresponding *grey* and *red* cells becoming *blue* ($t = 10, 20, 50$). Finally, all of the accessible drug and excipient is dissolved, and we see that only a few drug (*red*) and excipient (*grey*) cells remain: those that are surrounded by polymer (*green*) ($t = 199$). Note that this visualization does not show the outer boundary layer of water

One key observation from the experimental data is the initially slow release of drug from the tablet, especially at high polymer fractions, (see Fig. 2, right panel, lower graph). One explanation for this very slow release is the formation of a polymer "shell" when the tablet is thermally cured (heated), [2]. We can represent this in the model by allowing a layer of polymer cells to form on the outside of the simulated tablet. A user-specified parameter allows the simulation of polymer shells of different thickness, so that polymers with varying thermal reactivity can be modeled. The left panel of Fig. 5 shows a cross-section of a tablet in which a shell has formed.

All parameters of the CA model have straightforward physical interpretations such as the geometric dimensions of the tablet, the mass of the particles, and the diffusion rates of dissolved drug and excipient. The entire CA model, beginning with the initialization of the tablet has been implemented in `C++` and is available

from the authors upon request. For further details we refer to [4]. In the right panel of Fig. 5 we see a good qualitative agreement between the simulated release profiles and the experimental data from the right panel of Fig. 2. This agreement consists of the ordering of the release profiles according to the polymer content in the matrix, the change from a convex to a concave phase and the general time scale of approximately 8 h. It is straightforward to study the influence of the respective parameters on the release profiles [4, not shown].

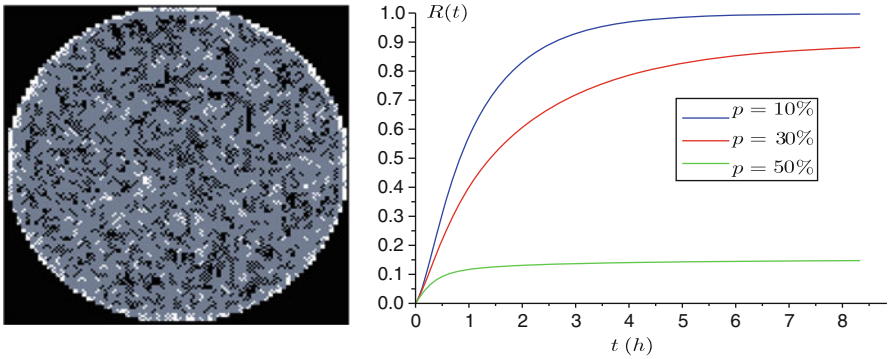

Fig. 5 *(Left)* Simulated formation of an exterior polymer shell due to thermal curing (*white squares*). *(Right)* Release curve produced by the cellular automaton model for a tablet of 8 mm diameter and 2 mm height. The drug content is 10 % in all cases while the polymer fraction varies. The unit of time is 1 h. This figure should also be compared to the experimental data in the right panel of Fig. 2. The parameters for this figure are taken from [4, Table 1]

Both the experimental data and the simulations reveal a challenge in the matrix tablets as they are currently formulated. This challenge comes from two competing goals: the first is to design a tablet so that all of the drug is released. The second goal is to have the release occur steadily over a fixed amount of time: in the case of ingested tablets, the best we can hope for is a steady release over 8 h, since the tablet itself will be eliminated from the system after that. Using our CA model, we were able to experiment with changing the key parameters: polymer content, curing temperature (which affects the polymer spreading), and shell formation (which is affected by the choice of polymer as well as the curing temperature). Based on these experiments, we found that a polymer concentration of 30 % in a tablet manufactured at low temperature and cured at low temperature resulted in a release profile with the desired characteristics, shown in Fig. 6. With this CA tool, pharmaceutical researchers can easily do experiments *in silico* that will suggest which powder mixtures and manufacturing procedures result in an optimal matrix tablet.

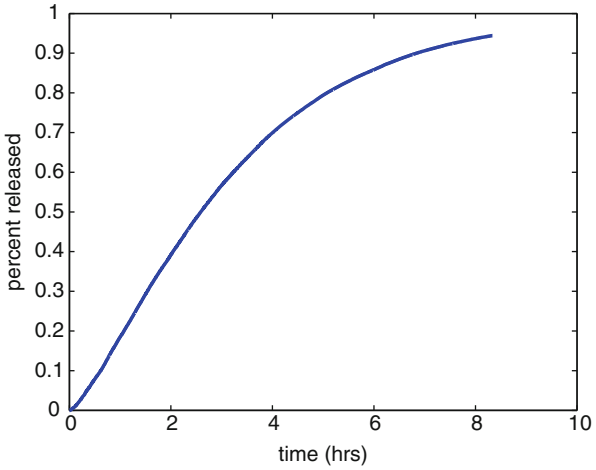

Fig. 6 Release profile from a simulated CA tablet that shows near complete release of the drug load at a fairly steady rate over an 8 h period. The parameters used here represent a low curing temperature, a low pressure compaction process, and a tablet with 30 % polymer

3 Permeability of Liposome Membranes

The matrix tablets described in the previous section are relatively inexpensive to manufacture and can be "tuned" to have the desired release profiles. However, they are only useful for drugs that are to be delivered via the gastrointestinal tract. In some cases, as in the case of many tumors, drugs need to be delivered to a specific site in the body, and then released there. One way to accomplish this targeted delivery is to load the drug into small vesicles that have low permeability in the blood, but whose permeability can be affected by the micro-environment. Hence, by manipulating this micro-environment, drugs can be delivered to specific sites, and in specific doses. One promising type of vesicle used for drug delivery are *liposomes*.

Liposomes are artificially prepared nano-spheres consisting of a lipid bilayer. They are currently being investigated as potential drug delivery devices [11, 26] and as model biological membranes. The permeability of the liposome bilayer membrane can be modified by binding of suitable bile salts. These bile salts occur naturally in the gastrointestinal tract where they play a central role in the digestion of dietary fats. This poses the danger of premature degradation of drug-carrying liposomes. On the other hand, they can also enhance transport across biological barriers [31]. The release of drugs from liposomes can be experimentally studied by measuring the release profiles of fluorescent dyes from the nano-particles under different experimental conditions. In [15] we combined mathematical modeling and experiments to study the release of carboxyfluorescein from liposomes.

Carboxyfluorescein (CF) is a fluorescent dye which is non-fluorescent when it is encapsulated at high concentrations inside the liposomes. Once CF has been

released from the liposomes, the concentration is sufficiently low that it can be made visible by excitation with light. The level of fluorescence is taken as a measure for the concentration of CF outside the liposomes. Bile salts, such as cholate (C), deoxycholate (DC) and monoketocholate (MKC) act as permeability enhancer by binding to the lipid bilayer. We have created a compartmental model for the concentrations of bile salts in the exterior space, the leaflets of the liposomes and the interior volumes [4]. Let V_i, V_s and V_o denote the total volumes of the combined liposome interiors, the inner and outer leaflets and the exterior volume, respectively. Further, let $w(t)$, $x(t)$, $y(t)$ and $z(t)$ denote the concentrations of bile salt in the combined interior liposome volume, the combined inner leaflet volume, the combined outer leaflet volume and the exterior volume, respectively. Then we have the system of differential equations

$$\begin{aligned} V_i w'(t) &= k_{-1}x - k_1 w, \\ V_s x'(t) &= k_1 w + k_2 y - (k_{-1} + k_{-2})x, \\ V_s y'(t) &= k_{-2}x + k_1 z - (k_{-1} + k_2)y, \\ V_o z'(t) &= k_{-1}y - k_1 z, \end{aligned} \tag{2}$$

where the k's are the rate constants. The binding of bile salt to a leaflet of the membrane occurs with rate k_1 while its release occurs with rate k_{-1}. It is not assumed that flipping between inner and outer leaflet occurs at equal rates, so $k_2 \neq k_{-2}$ is possible. In principle there could be also different binding and release rates at the outer and the inner leaflet (due to different curvature), but we wish to keep the total number of parameters low, as they will be determined by curve fitting. The concentration of the drug in the interior of all liposomes is denoted by c_i and that in the common exterior by c_o. The membrane permeability P depends on the concentration of bile salt in the outer and inner leaflets in two ways. On the one hand, it can depend on the total concentration of bile salts in both leaflets, on the other hand it can depend on the difference between these concentrations. We assume the functional form

$$P(x, y) = p_1|y - x|^{a_1} + p_2(x + y)^{a_2},$$

where p_1, p_2, a_1 and a_2 are constants to be determined from the experimental data. With the convention that the flux of CF is from the interior to the exterior, we obtain from Fick's law

$$V_i \frac{dc_i}{dt} = AP(x, y)(c_o - c_i),$$

where A is the combined liposome membrane area. Finally, the fluorescence output is given by

$$F(t) = F_0 + Kc_o(t),$$

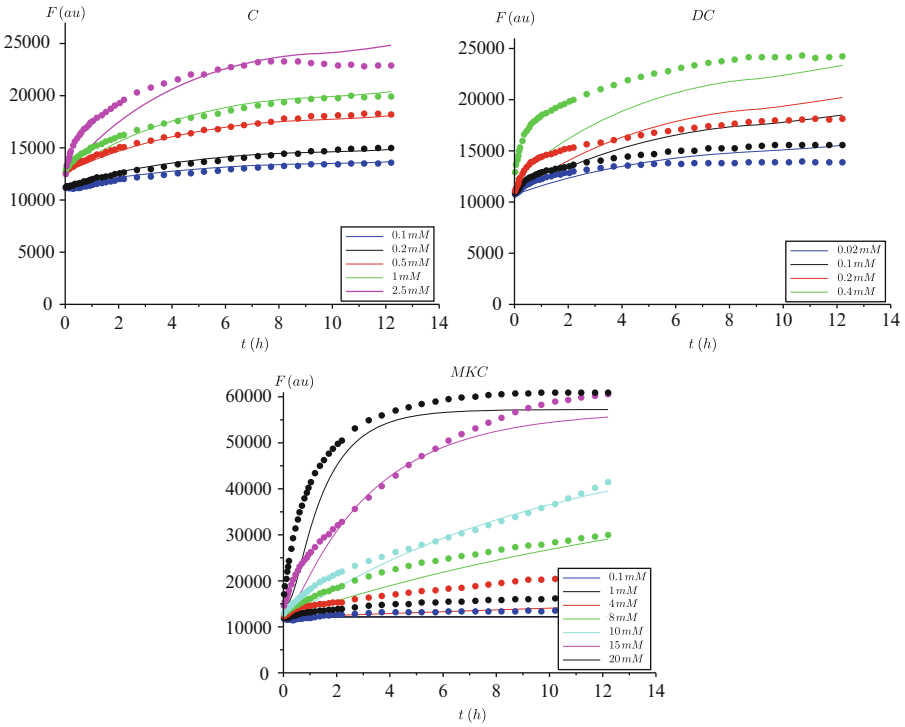

Fig. 7 Optimal least-square fit of the release *curves* for the bile salts cholate (C), deoxycholate (DC) and monoketocholate (MKC) at different concentrations of bile salts. The *dotted* experimental and *solid fitted curves* of the same color belong together. Each *dot* represents a fluorescence measurement

with background fluorescence level F_0 and proportionality constant K. For the experimental part of the work, liposomes were prepared from soybean phosphatidylcholine (SPC) lipids. For more details on the preparation, see [15]. The experimental release curves for three different bile salts and their numerical recreations are shown in Fig. 7, where optimal parameters were determined using the Metropolis Monte Carlo method. Despite uncertainties about certain parameters of the experiment such as the initial drug concentration inside the liposomes and the exact dependence of the fluorescence signal on the concentration of CF in the exterior space, some conclusions can be drawn from the optimal fits. Firstly, we obtained for all types of bile salts that $p_1/p_2 \approx 10^3$. This suggests that the membrane permeability depends much more strongly on the difference of the bile salt concentrations in the inner and outer leaflets, rather than on the total amount of bile salt in both leaflets. Secondly, for the bile salts cholate and deoxycholate we obtained that $k_2 \approx k_{-2}$ which implies that the equilibrium concentrations of bile salt in both leaflets are approximately equal. This results in an end of leakage of CF after approximately 3–5 h and hence in an entrapment of the drug cargo in the liposomes. In contrast we

have for monoketocholate that $k_2/k_{-2} \approx 10$ and hence the concentrations in both leaflets are noticeably distinct. This results in a positive steady state permeability and allows a complete release of the drug cargo on a reasonable timescale (12–24 h, say).

4 Outlook

In the preceding sections we have described several mathematical approaches to modeling of drug delivery. In the realm of modeling the drug release from matrix tablets, our cellular automaton (CA) model has shown the best results and is ready for more concrete applications. It can be trained with experimental release data and has the potential to be used as a predictive tool. The software is written in `C++` and available at [5]. In the future, simulations can be sped up by parallelization of the code. The model itself can be improved in various directions. For example, currently the dissolution of a drug or excipient cell results in complete and immediate replacement of this cell by a water cell which then carries a completely saturated solution. The assumption that one water cell can dissolve a drug cell of equal volume is clearly not realistic.

Many modern drugs have very specific action sites and it is desirable to deliver them in a highly localized manner. This includes, but is not restricted to, anti-tumor vaccines and drugs used to treat neurological disorders such as Parkinson's disease and dementia. This has given rise to the concepts of "targeted" and "triggered" delivery. Liposomes are ideal delivery devices since they are made of naturally occurring lipid bilayers. Antibodies and ligands attached to the liposome surface or magnetic nanoparticles can be used to target liposomes to specific cells [1, 24]. Even without such targeting, it is possible to trigger the release of the drug cargo at a certain specific site [23]. Potential signals for drug release are, for example, an acidic tumor micro-environment, heat or low-frequency ultrasound. A particular challenge is the delivery of drugs to the brain, as the brain is protected by the blood–brain barrier [7, 28]. Here the effect of triggered delivery would be most beneficial as it would be possible to create a high concentration of the drug in the capillaries of the brain. However, ultrasound as the triggering signal results in delivery of energy to the brain and may not be without harmful side effects. An experimentally validated mathematical model has the power do yield signaling schedules that maximize the release of encapsulated drug while at the same time minimize the exposure to the low-frequency ultrasound. This is the topic of ongoing research.

Acknowledgements The authors have been supported by the grant "Collaborative Research: Predicting the Release Kinetics of Matrix Tablets" (DMS 1016214 to Peter Hinow and DMS 1016136 to Ami Radunskaya) of the National Science Foundation of the United States of America. We thank Boris Bäumer (Department of Mathematics and Statistics), Lipika Chatterjee, Lin Yang, and Ian Tucker (School of Pharmacy) at the University of Otago in Dunedin, New Zealand, Aisha Nájera (Claremont Graduate University) and Ezra Buchla for inspiring and cheerful collaboration. We thank Max Strater (Pomona College) for generating the images in Fig. 4. We thank the School

of Pharmacy at the University of Otago in Dunedin, New Zealand, for hospitality during several collaboration visits. The original Workshop on the Application of Mathematics to Problems in Biomedicine (December 17–19, 2007) at the University of Otago in Dunedin, New Zealand was supported by NSF grant DMS-0737537. Peter Hinow thanks Amina Eladdadi and Peter Kim for organizing the Workshop on Mathematical Modeling of Tumor–Immune System Dynamics at the University of Sydney, Australia, in January 2013. Much of the material presented here appears in [3, 4] and [15].

References

1. Altin, J.G., Parish, C.R.: Liposomal vaccines–targeting the delivery of antigen. Methods **40**, 39–52 (2006)
2. Azarmi, S., Farid, J., Nokhodchi, A., Bahari-Saravi, S.M., Valizadeh, H.: Thermal treating as a tool for sustained release of indomethacin from Eudragit RS and RL matrices. Int. J. Pharm. **246**, 171–177 (2002)
3. Baeumer, B., Chatterjee, L., Hinow, P., Rades, T., Radunskaya, A., Tucker, I.: Predicting the drug release kinetics of matrix tablets. Discr. Contin. Dyn. Sys. B **12**, 261–277 (2009)
4. Buchla, E., Nájera, A., Hinow, P., Radunskaya, A.: Swallowing a cellular automaton pill: predicting drug release from a matrix tablet. Simulation **90**, 227–237 (2014). Available at http://arxiv.org/abs/1208.3447
5. Buchla, E.: `Celldiff`. Available at https://github.com/catfact/celldiff (2012)
6. Caraballo, I., Millan, M., Rabasco, A.M.: Relationship between drug percolation threshold and particle size in matrix tablets. Pharm. Res. **13**, 387–390 (1996)
7. Cecchelli, R., Berezowski, V., Lundquist, S., Culot, M., Renftel, M., Dehouck, M.-P., Fenart, L.: Modelling of the blood-brain barrier in drug discovery and development. Nat. Rev. Drug Discov. **6**, 650–661 (2007)
8. Chatterjee, L., Baier, A.-K., Rades, T., Tucker, I.G.: Effect of particle size of mannitol on polymethacrylate matrices prepared by direct compression. 35th Controlled Release Society Annual Meeting, New York (2008)
9. Donev, A., Torquato, S., Stillinger, F.H., Conelly, R.: Jamming in hard sphere and disk packings. J. Appl. Phys. **95**, 989–999 (2004)
10. DuBois, C., Farnham, J., Aaron, E., Radunskaya, A.: A multiple time-scale computational model of a tumor and its micro environment. Math. Biosci. Eng. **10**, 121–150 (2013)
11. Enden, G., Schroeder, A.: A mathematical model of drug release from liposomes by low frequency ultrasound. Ann. Biomed. Eng. **37**, 2640–2645 (2009)
12. Goltsev, A.V., de Abreu, F.V., Dorogovtsev, S.N., Mendes, J.F.F.: Stochastic cellular automata model of neural networks. Phys. Rev. E **81**, 061921 (2010)
13. Higuchi, T.: Mechanism of sustained medication: theoretical analysis of rate release of solid drugs dispersed in solid matrices. J. Pharm. Sci. **52**, 1145–1149 (1963)
14. Hinow, P.: A nonsmooth program for jamming hard spheres. Optim. Lett. **8**, 13–33 (2014)
15. Hinow, P., Radunskaya, A., Tucker, I., Yang, L.: Kinetics of bile salt binding to liposomes revealed by carboxyfluorescein release and mathematical modeling. J. Liposome Res. **22**, 237–244 (2012)
16. Kavousanakis, M.E., Liu, P., Boudouvis, A.G., Lowengrub, J., Kevrekidis, I.G.: Efficient coarse simulation of a growing avascular tumor. Phys. Rev. E **85**, 031912 (2012)
17. Knott, G.M., Jackson, T.L., Buckmaster, J.: Random packings of heterogeneous propellants. AIAA J. **39**, 678–686 (2001)
18. Kosmidis, K., Argyrakis, P., Macheras, P.: Fractal kinetics in drug release from finite fractal matrices. J. Chem. Phys. **119**, 6373–6377 (2003)

19. Lemaire, V., Bélair, J., Hildgen, P.: Structural modeling of drug release from biodegradable porous matrices based on a combined diffusion/erosion process. Int. J. Pharm. **258**, 95–107 (2003)
20. Löwen, H.: Fun with hard spheres. In: Statistical Physics and Spatial Statistics. Lecture Notes in Physics, vol. 554, pp. 295–331. Springer, New York/Berlin/Heidelberg (2000)
21. Lubachevsky, B.D., Stillinger, F.H.: Geometric properties of random disk packings. J. Stat. Phys. **60**, 561–583 (1990)
22. Nowak, S., Schadschneider, A.: Quantitative analysis of pedestrian counterflow in a cellular automaton model. Phys. Rev. E **85**, 066128 (2012)
23. Oude Blenke, E., Mastrobattista, E., Schiffelers, R.M.: Strategies for triggered drug release from tumor targeted liposomes. Expert Opin. Drug Deliv. **10**, 1399–1410 (2013)
24. Richardson, G., Kaouri, K., Byrne, H.M.: Particle trapping by an external body force in the limit of large Peclet number: applications to magnetic targeting in the blood flow. Eur. J. Appl. Math. **21**, 77–107 (2010)
25. Siepmann, J., Peppas, N.A.: Hydrophilic matrices for controlled drug delivery: an improved mathematical model to predict the resulting drug release kinetics (the "Sequential Layer" Model). Pharm. Res. **17**, 1290–1298 (2000)
26. Torchilin, V.P.: Recent advances with liposomes as pharmaceutical carriers. Nat. Rev. Drug Discov. **4**, 145–160 (2005)
27. Torquato, S., Truskett, T.M., Debenedetti, P.G.: Is random close packing of spheres well defined? Phys. Rev. Lett. **84**, 2064–2067 (2000)
28. Tucker, I., Yang, L., Mujoo, H.: Delivery of drugs to the brain via the blood brain barrier using colloidal carriers. J. Microencapsul. **29**, 475–486 (2012)
29. Villalobos, R., Ganem, A., Cordero, S., Vidales, A.M., Domínguez, A.: Effect of the drug-excipient ratio in matrix-type-controlled release systems: Computer simulation study. Drug Dev. Ind. Pharm. **31**, 535–543 (2005)
30. Villalobos, R., Cordero, S., Vidales, A.M., Domínguez, A.: In silico study on the effects of matrix structure in controlled drug release. Physica A **367**, 305–318 (2006)
31. Yang, L., Zhang, H., Fawcett, J.P., Mikov, M., Tucker, I.G.: Effect of bile salts on the transport of morphine-6-glucuronide in rat brain endothelial cells. J. Pharm. Sci. **100**, 1516–1524 (2011)

The Role of the miR-451-AMPK Signaling Pathway in Regulation of Cell Migration and Proliferation in Glioblastoma

Yangjin Kim, Hyunji Kang, and Sean Lawler

Abstract Glioblastoma is the most aggressive type of brain cancer with a median survival time of 1 year. A particular microRNA, miR-451, and its counterpart, AMPK complex are known to play a key role in controlling the balance between rapid proliferation and aggressive invasion in response to metabolic stress in the microenvironment. The present paper develops a hybrid model of glioblastoma that identifies a key mechanism behind the molecular switches between proliferative phase and migratory phase in response to metabolic stress and biophysical interaction between cells. We first focus on the core miR-451-AMPK control system and show how up- or down-regulation of components of these pathways affects cell proliferation and migration. We then examine a hybrid model for the biomechanical interaction between invasive and proliferative cells, in which all cells are modeled individually, and show how biophysical properties of cells and the core miR-451-AMPK control system affect the growth/invasion patterns of glioma spheroids in response to various glucose levels in the microenvironment. The model predicts that cell migration depends not only on glucose availability but also on mechanical constraints between cells. The model predicts various invasion patterns and cell speeds under normal and low glucose conditions. The hybrid model also predicts that introduction of chemoattractants at the resection site may lead to the localization

Y. Kim (✉)
Department of Mathematics, Konkuk University, 120 Neungdong-ro, Gwangjin-gu, Seoul, 143-701, Republic of Korea

Department of Mathematics, Ohio State University, Columbus OH, 43210, USA
e-mail: ahyouhappy@konkuk.ac.kr

H. Kang
Department of Mathematics, Konkuk University, 120 Neungdong-ro, Gwangjin-gu, Seoul, 143-701, Republic of Korea
e-mail: gagul0618@gmail.com

S. Lawler
Department of Neurosurgery, Brigham and Women's Hospital, Harvard Medical School, 4 Blackfan Circle., HIM 930A, Boston MA, 02115, USA
e-mail: SLAWLER@partners.org

A. Eladdadi et al. (eds.), *Mathematical Models of Tumor-Immune System Dynamics*, Springer Proceedings in Mathematics & Statistics 107,
DOI 10.1007/978-1-4939-1793-8_6

of infiltrating tumor cells back to the periphery of the resected area, which may lead to possible follow-up treatment options such as the subsequent surgeries and optimized elimination of the infiltrating glioma cells.

1 Introduction

1.1 Glioblastoma

Glioblastoma multiforme (GBM) is the most common malignant brain tumor with a median survival time of approximately 1 year from the time of diagnosis [18,36,77]. These tumors are characterized by the hallmarks of rapid proliferation and their invasiveness into surrounding normal brain tissue, which results in inevitable tumor recurrence after surgery [10]. Surgery is the main treatment option, generally followed by radiotherapy and chemotherapy. Therapeutic approaches are needed that target the invading cells, in order to improve clinical outcome [16]. Tumor cells may face challenges such as hypoxia, acidity, and limited nutrient availability as they grow. In order to maintain rapid growth, glioblastoma cells must adapt to these changes in the challenging microenvironment [27]. In order to sustain their rapid proliferation, cancer cells shift their metabolic machinery from oxidative phosphorylation and anaerobic glycolysis to high levels of glucose uptake and lactate production (the *Warburg Effect*) [42, 84].

The tricarboxylic acid (TCA), or Krebs, cycle (Fig. 1) is a key step for generating an energy source, ATP, in nonhypoxic normal cells. While differentiated cells favor this mode of metabolism (Fig. 1a), tumor cells adapt aerobic glycolysis [83] (Fig. 1b) that appears to be a less efficient way of metabolism due to consumption of large amounts of glucose and production of lactic acid [42]. Using this aerobic glycolysis [24], cancer cells may have an advantage of not having to depend on oxygen for energy especially in the hostile (hypoxic) tumor microenvironment, leading to improved survival [24, 42]. Better understanding of glycolysis in cancer cells may lead to better treatment of the disease. For instance, drug resistance could be prevented by inhibition of glycolysis [86].

To ensure an adequate glucose supply, cancer cells adapt by increasing angiogenesis and invasion [27]. However, cellular responses to glucose withdrawal are critical for cancer cell survival in the challenging microenvironment where glucose levels may fluctuate. In order to survive periods of metabolic stress and maintain viability as cells accumulate, cancer cells therefore engage strategies of metabolic adaptation [38]. The 5′-adenosine monophosphate activated protein kinase (AMPK) pathway, the major cellular sensor of energy availability [30], is activated by metabolic stress to promote glucose uptake and energy conservation [30]. Cancer cells adapt to periods of low energy availability through this conserved cellular energy sensor, thus avoiding bioenergetic catastrophe and cell death.

1.2 Role of miRNA in Cancer Development

MiRNAs, key regulators of gene expression, are approximately 22 nucleotide single-stranded non-coding RNAs [4]. Dysregulation of miRNAs has been associated with tumor suppressor and oncogenic activities [20] in many types of cancer, including glioblastoma where altered miRNA expression favors tumorigenesis [28, 51]. miRNAs also regulate aerobic glycolysis in cancer development [73]. Glioma invasion is promoted by miR-21 through downregulation of matrix metalloprotease (MMP) inhibitors [21]. However, many alterations and functional significance of these miRNAs are not clearly understood [27].

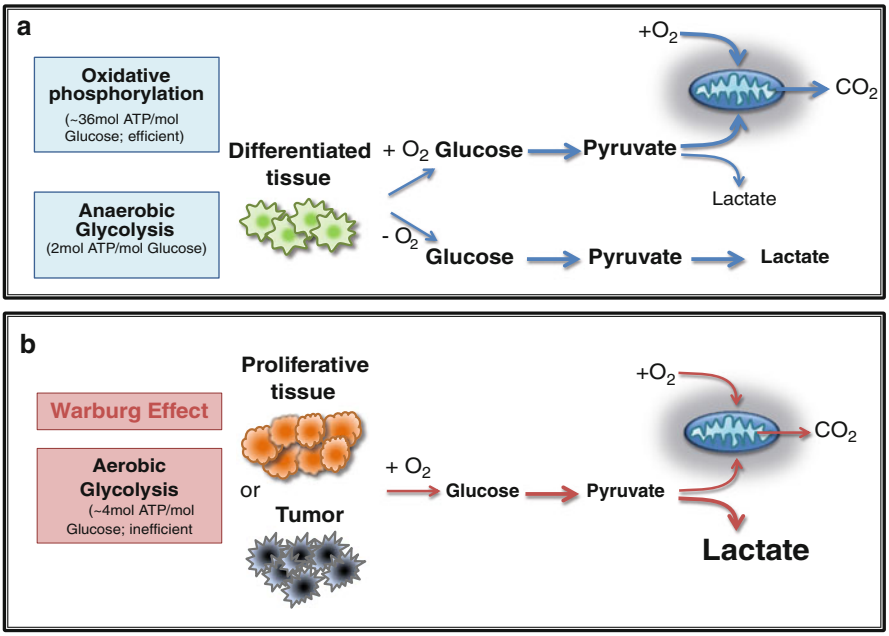

Fig. 1 Schematics of oxidative phosphorylation, anaerobic glycolysis, and aerobic glycolysis [42, 46, 83, 84]. (**a**) Differentiated cells favor oxidative phosphorylation and anaerobic glycolysis. (**b**) In response to rapid growth and proliferation, tumor cells shift their metabolic machinery toward high levels of glucose uptake and lactate production (Warburg effect; aerobic glycolysis) [42, 83, 84]

1.3 Role of miR-451 in Cell Proliferation and Invasion in Glioblastoma

There has been discrepancy in the role of miR-451 in regulation of tumor growth and invasion in glioblastoma, i.e., as tumor suppressive [90] and oncogenic roles [22] in GBM [52, 59]. While miR-451 was over-expressed in GBM cell lines [28]

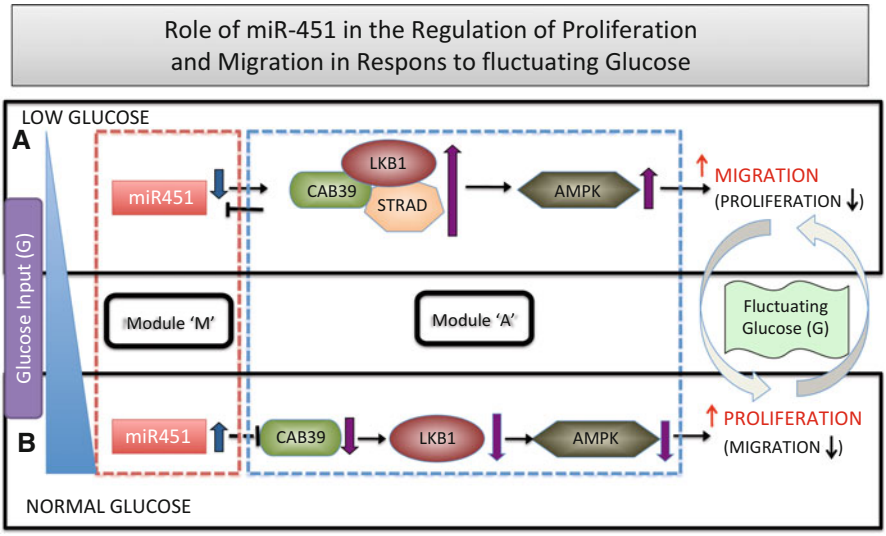

Fig. 2 Proposed role of miR-451 in the regulation of LKB1/AMPK signaling in response to high and low glucose levels [46]. miR-451 levels determine cell migration or proliferation in response to glucose (*red triangle on the left*) via AMPK complex on the right module [27]. (**a**) Normal glucose levels upregulate miR-451, which in turn leads to increased proliferation and decreased cell migration by inhibiting the CAB39-LKB1-AMPK pathway. (**b**) Low glucose levels reduce miR-451 levels, resulting in upregulation of AMPK activity. This leads to enhanced cell motility and reduced cell proliferation. Schematic components of miR-451 and the CAB39/LKB1/AMPK complex is represented by modules 'M' (box with *brown dotted line*) and 'A' (box with *blue dotted line*) in our theoretical framework. *Blue arrows* on the *right* indicate the switching behavior between the proliferative state in (**a**) and the migratory state in (**b**) in response to fluctuating glucose

including CD133, it was down-regulated in three other GBM cell lines [22, 60]. Godlewski et al. [27] identified a novel mechanism in which miR-451 determines glioma cell survival, motility, and proliferation. They found that (1) miR-451 regulates AMPK signaling in response to various glucose levels in glioblastoma cells. (2) CAB39 was identified as a target of miR-451 and CAB39 was up-regulated when cells invade surrounding collagen gel. (3) The effects of miR-451 are mediated by the LKB1/AMPK pathway through the direct targeting of CAB39. In particular, they [27] found that normal glucose levels up-regulate miR-451, leading to elevated proliferation and decreased cell migration while low glucose levels induce down-regulation of miR-451, which in turn promotes cell motility and inhibits cell proliferation via AMPK signaling, mediated by direct targeting CAB39 [25, 26, 59]. Their model is shown schematically in Fig. 2. This finding emphasizes the adaptation to altered energy availability under dynamic metabolic stress that is commonly found in rapidly growing tumors like GBM [38].

1.4 Infiltrating Glioma

Invasion of glioma cells is a major reason for treatment failure since the migratory cells are not completely eliminated by standard surgical resection of the tumor, causing tumor recurrence [10]. Variations are seen in number of invading cells and patterns of migration [44]. Several factors may contribute to glioma cell migration in the brain. Extracellular matrix (ECM) may stimulate cell migration in a process known as haptotactic migration. While the haptotactic process is known to be activated by pre-existing brain components, it is also greatly influenced by remodeling of the ECM through the secretion of proteases such as the MMPs [10, 12, 35]. Glioma cell motility is also stimulated by various chemotactic factors, which include ligands of the EGF family [56], the TGF-β family [61], scatter factor/hepatocyte growth factor (SF/HGF) [50], SDF-1 [91], and certain lipids [88]. In particular, other authors studied the action of HGF or scatter factor as a migration switch [55, 75, 79, 81] and Scianna et al. [69] investigated different behaviors of colonies of two cell lines (ARO and MLP-29) in response to HGF using cellular Potts models. Other cell types such as microglia can be attracted to the tumor and secrete chemoattractants and matrix components [85], providing indirect stimulation of cell migration. In patients, glioma cells usually follow preferred dispersion routes, for example, the basal lamina of brain blood vessels or white matter tracts. This implies that glioma cell migration may be controlled by specific substrates and structures in the brain. Indeed there are several publications based on a diffusion model [32, 78]. See a general review on hybrid models of tumor growth [63].

The chapter is organized as follows: In Sect. 2 we present and analyze a population model based on partial differential equations (PDEs) that take into account the core miR-451-AMPK system. We investigate the effect of glucose fluctuation on regulation of the core control system, miR-451-AMPK, and explore the system behavior in response to several different therapeutic interventions in the signaling pathways. We develop and analyze a hybrid model in Sect. 3. In Sect. 4, we discuss similarities and differences between the population model and hybrid approaches and suggest possible directions for future work.

2 A Population Model Via the miR-451-AMPK Signaling

2.1 Mathematical Model of the miR-451-AMPK Signaling Network

In order to incorporate the signaling network shown in Fig. 3a into our model of cell migration, we began by simplifying this network. As indicated in the introductory section, two key players in the intracellular network are miR-451 and AMPK complex. We get a simplified representation in Fig. 3b from the complex network in Fig. 3a by merging all complex networks between CAB39/LKB1/STRAD and

AMPK/MARK into one component (AMPK complex; blue dotted box in Fig. 3a) and keeping miR-451 in one module (brown dotted box in Fig. 3a). We refer to the interactions represented by edges in Fig. 3b as the core miR-451-AMPK control system. By convention, kinetic interpretation of arrows and hammerheads in the network represents induction (arrow) and inhibition (hammerhead). Two variables m and a represent activities of miR-451 and the AMPK complex, respectively.

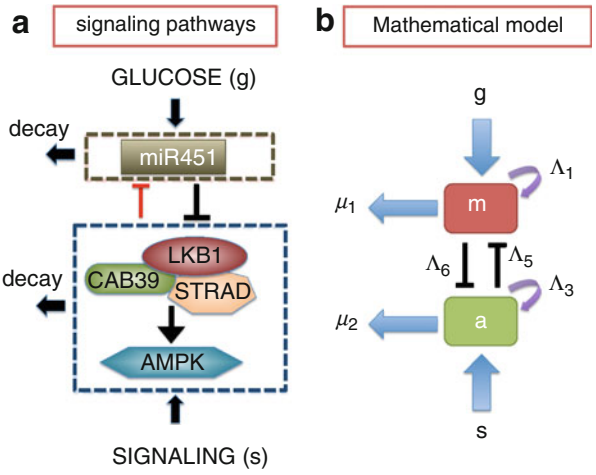

Fig. 3 (**a**) Conceptual model: regulation of miR451-AMPK signaling pathways in glioma cell migration and proliferation [25, 27]. (**b**) Cartoon mathematical model [46]: miR-451 level and activity of its target complex (CAB39/LKB1/AMPK) were represented by 'm' and 'a', respectively

Based on the signaling network shown in Fig. 3b, we write the phenomenological equations for the rate change of those key molecules (m, a) as follows:

$$\frac{dm}{dt} = f(g) + \frac{\Lambda_1 \Lambda_2^2}{\Lambda_2^2 + \Lambda_5 F(a)} - \mu_1 m, \tag{1}$$

$$\frac{da}{dt} = h(s) + \frac{\Lambda_3 \Lambda_4^2}{\Lambda_4^2 + \Lambda_6 H(m)} - \mu_2 a, \tag{2}$$

where g represents the signaling pathways from glucose to miR-451, s represents the signaling pathways to AMPK, Λ_1 and Λ_3 are the autocatalytic enhancement parameters for miR-451 and AMPK complex, respectively, Λ_2 and Λ_4 are the Hill-type inhibition saturation parameters from the counterpart of miR-451 and AMPK complex, respectively, Λ_5 is the inhibition strength of miR-451 by the AMPK complex, Λ_6 is the inhibition strength of the AMPK complex by miR-451, μ_1 and μ_2 are microRNA/protein degradation rates of miR451 and AMPK complex, respectively. The glucose signal g increases the rate of miR-451 levels through a function $f(g)$, while the AMPK signal s increases the AMPK activity through

another function $h(s)$. A requirement on these functions is

$$\frac{\partial f}{\partial g} > 0, \ \forall g \geq 0, \quad \text{and} \quad \frac{\partial h}{\partial s} > 0, \ \forall s \geq 0. \tag{3}$$

AMPK-dependent inhibition of miR-451 and miR-451-dependent suppression of AMPK activity are through increasing functions $F(a)$ and $H(m)$ in the denominators in Eqs. (1) and (2), respectively. These functions also have to satisfy

$$\frac{\partial F}{\partial a} > 0, \ \forall a \geq 0 \quad \text{and} \quad \frac{\partial H}{\partial m} > 0, \ \forall m \geq 0. \tag{4}$$

Our following phenomenological assumptions $f(g) = g$, $F(a) = a^2$, $h(s) = s$, $H(m) = m^2$ satisfy these conditions (3)–(4) and computational results from the model are in good agreement with experimental data [27] . By non-dimensionalizing the Eqs. (1)–(2) with these assumption we have the governing equations as follows:

$$\frac{dM}{dt} = G + \frac{k_1 k_2^2}{k_2^2 + \alpha A^2} - M, \tag{5}$$

$$\epsilon \frac{dA}{dt} = S + \frac{k_3 k_4^2}{k_4^2 + \beta M^2} - A. \tag{6}$$

The parameters appearing in Eqs. (5)–(6) and Table 1 are referred to as essential control parameters.

Nondimensionalization and Parameter Estimate

The following dimensionalization was performed to get the dimensionless key control equations in the main section

$$T = \mu_1 t, \ M = \frac{m}{m^*}, \ A = \frac{a}{a^*}, \ G = \frac{g}{\mu_1 m^*}, \ S = \frac{s}{\mu_2 a^*}, \ k_1 = \frac{\Lambda_1}{\mu_1 m^*}, \tag{7}$$

$$k_2 = \Lambda_2, \ k_3 = \frac{\Lambda_3}{\mu_2 a^*}, \ k_4 = \Lambda_4, \ \alpha = \Lambda_5 (a^*)^2, \ \beta = \Lambda_6 (m^*)^2, \ \epsilon = \frac{\mu_1}{\mu_2}. \tag{8}$$

miRs are typically more stable than their targets [40, 87] and the parameter ϵ is small [1]. While the typical half-life of AMPK is short (∼6 h) [14], the half-life of a miRNA is much larger (101–225 h) [23]. By taking a slightly larger half-life (290 h) of miR-451, we get a small relative ratio, $\epsilon = \frac{\mu_1}{\mu_2} = 0.02$. miRNA concentrations in an animal cell (assuming 1,000–25,000 μm^3 volume) were estimated to be 80 pM–2.2 μM [62] and we take our reference value $m^* = 1.0$ μM. Based on the high (4.5 g/l) and low (0.3 g/l) glucose level in [27] and m^*, we estimate glucose supply rate through several pathways $g = (2.4 \times 10^{-5} - 2.4 \times 10^{-3})$ μM/h resulting

in a range of dimensionless glucose input levels $G = \frac{g}{\mu_1 m^*} = 0.01 - 1.0$. AMPK concentration was measured as 35–150 nM in rat liver [31] and we take $a^* = 100$ nM. We take the signal source of the AMPK complex, $s = 2.4$ nM/h leading to $S = \frac{s}{\mu_2 a^*} = 0.2$. The autocatalytic rate (Λ_1) of miR-451 is assumed to be fourfold larger than its negative contribution ($\mu_1 m^*$) from its decay in the absence of inhibition pathway from the AMPK module, $k_1 = \frac{\Lambda_1}{\mu_1 m^*} = 4.0$ (Similarly for its counterpart, the AMPK complex, we take $k_3 = \frac{\Lambda_3}{\mu_2 a^*} = 4.0$). Finally, the inhibition strength ($\alpha = 1.6$) of miR-451 by the AMPK complex was assumed to be a bit stronger than the inhibition strength ($\beta = 1.0$) of the AMPK complex by miR-451.

Once the parameters above were determined, we fitted the data in the level of LKB1/AMPK activity in [27] in response to negative control and over expressed levels of miR-451 (Fig. 5b in [27]) in the following way: The steady state of AMPK complex (A^s) in terms of miR-451 level (M^s) and other parameters in the miR-451-AMPK model can be rewritten by

$$A^s = S_1 + \frac{\lambda_3 \lambda_4^2}{\lambda_4^2 + \beta (M^s)^2} = 0.2 + \frac{4}{1 + \beta (M^s)^2}. \tag{9}$$

The up-regulated AMPK complex level (∼500 pmol of phosphate incorporated in a dimensional form) for negative control of miR-451 was down-regulated (∼100 pmol of phosphate incorporated in a dimensional form). Using Eq. (9) above, we estimated the parameter value of β to be 1.0 which gives the low AMPK complex activity ($\sim A^s = 0.9$) in response to a high dimensionless miR-451 level ($M^s = 4.2$) and the high AMPK complex activity ($A^s = 4.2$) in response to negative control of the miR-451 level ($M^s = 0.0$), resulting in a reasonable ∼4.7-fold difference in the AMPK complex activities as seen in the experiments in [27]. Finally, by observing the behavior of the system and experimental data, we assume that the inhibition strength ($\alpha = 1.6$) of miR-451 by the AMPK complex is bit larger than the inhibition strength ($\beta = 1.0$) of the AMPK complex by miR-451 [45, 46].

Table 1 Parameters that are used in the core control model (miR-451-AMPK system)

Parameter	Description	Value[a]	Refs.
k_1	miR-451 autocatalytic production rate	4.0	[45, 46]
k_2	Hill-type coefficient	1.0	[45, 46]
α	Inhibition strength of miR-451 by AMPK complex	1.6	[45, 46]
k_3	AMPK autocatalytic production rate	4.0	[45, 46]
k_4	Hill-type coefficient	1.0	[45, 46]
β	Inhibition strength of AMPK complex by miR-451	1.0	[45, 46]
S	Signaling source of AMPK	0.2	[45, 46]
ϵ	Scaling factor (slow dynamics)	0.02	[1, 14, 23, 45, 46]
th_M	Threshold of miR-451 for invasion/growth switch	2.0	[45, 46]

[a] Dimensionless value

2.1.1 Analysis and Implications

We recall (see Fig. 2) that low (or high) levels of miR-451 imply reduced (or elevated) cell proliferation and increased (or decreased) migration in response to the low (or high) glucose level. The effect of glucose in regulation of miR-451 level and AMPK activity in our model was tested. Figure 4a–c shows three different patterns and time flow of the dynamics of the steady state (SS; circles) of the core control system in response to low ($G = 0.1$), intermediate ($G = 0.45$), and high ($G = 1.0$) levels of glucose in the M-A phase plane, respectively. By taking the appropriate thresholds, th_M (= 2.0) of miR-451 and th_A (=2.0) of AMPK, we can define the migratory region $\mathbb{T}_m$ by $\mathbb{T}_m = \{(M, A) \in \mathbb{R}^2 : M < th_M,\ A > th_A\}$ (dotted pink box in Fig. 4d) and the proliferative region $\mathbb{T}_p$ by $\mathbb{T}_p = \{(M, A) \in \mathbb{R}^2 : M > th_M,\ A < th_A\}$ (solid box in Fig. 4d). There exists only one SS (blue filled circle) in the $\mathbb{T}_m$-zone under the glucose withdrawal condition ($G = 0.1$; Fig. 4a) while the unique SS (blue filled circle) exists in the $\mathbb{T}_p$-zone when normal glucose is provided ($G = 1.0$; Fig. 4c). For an intermediate level of glucose ($G = 0.45$), there exists three SS: two stable SS (two blue filled circles; one in $\mathbb{T}_p$ and one in $\mathbb{T}_m$) and one unstable SS (larger empty red circle) in the middle. This leads to a bi-stable system shown in Fig. 4b. From these observations, we anticipate to see a hysteresis bifurcation curve with respect to glucose G. Indeed, we get a hysteresis bifurcation curve in Fig. 4e by solving miR-451 SS values (M^s) as a function of G when the core control system (5)–(6) is in equilibrium. While the lower and upper branches are stable, the middle branch is unstable. When G is small, then the system stays in the lower branch ($\mathbb{T}_m$). So, glioma cells are in the migratory phase in response to slow increase in G until it reaches the right knee point of the curve ($\sim$0.6) where M jumps to the upper branch, putting cells are in the $\mathbb{T}_p$-phase. As G is decreased due to glucose consumption by cells, the miR-451 level remains elevated, until it hits the left knee point of the curve ($\sim$0.4), at which time the M jumps down to the lower branch, putting cells back to $\mathbb{T}_m$-phase. These two-way transitions between $\mathbb{T}_m$ and $\mathbb{T}_p$ naturally define a bi-stability window ($W_\sigma = [\sigma_w^\dagger, \sigma_w^\ddagger]$). The size of the window ($|W_\sigma|$) depends on other parameters and may even disappear for some parameter set. So, the effect of glucose is history dependent: when $G \in W_\sigma$ (bi-stable mode in Fig. 4b), the cells are in the $\mathbb{T}_m$- and $\mathbb{T}_p$-phase if $dG/dt > 0$ and $dG/dt < 0$, respectively.

2.1.2 Comparison with Experiments

In the experiments by Godlewski et al. [27], there was a reduction in miR-451 levels by 78–82 % when cells (U251 and LN229 in Fig. 5) were cultured in glucose withdrawal (0.3 g/l; gray) and normal glucose (4.5 g/l; black) conditions. Simulation results from the model are in good agreement with these experimental results [27], i.e., there was significant reduction in miR-451 levels in response to glucose deprivation relative to the control case. See Fig. 5.

2.1.3 Sensitivity Analysis

In the mathematical model developed in this paper, there are a number of parameters for which no experimental data are available but they may significantly affect the system behaviors. We performed sensitivity analysis for key parameters (G, S, k_1, k_2, k_3, k_4, α, β, ϵ) in order to see how sensitive is the core system at a given time to these parameters. As a usual step, we have chosen a biologically relevant range for each of these parameters and divided each range into 1,000 intervals of uniform length. Then, a partial rank correlation coefficient (PRCC) value is calculated. PRCC values lie between -1 and 1 with the sign determining whether an increase in the parameter value will decrease $(-)$ or increase $(+)$ the miR-451 expression and AMPK activity at a given time [57]. Figure 6 shows the PRCC values for the miR-451 level and AMPK activity at $t = 100$. The miR-451 level turns out to be positively correlated to G, k_1, k_2 but is very weakly correlated to $k_3, k_4, \beta, \epsilon$.

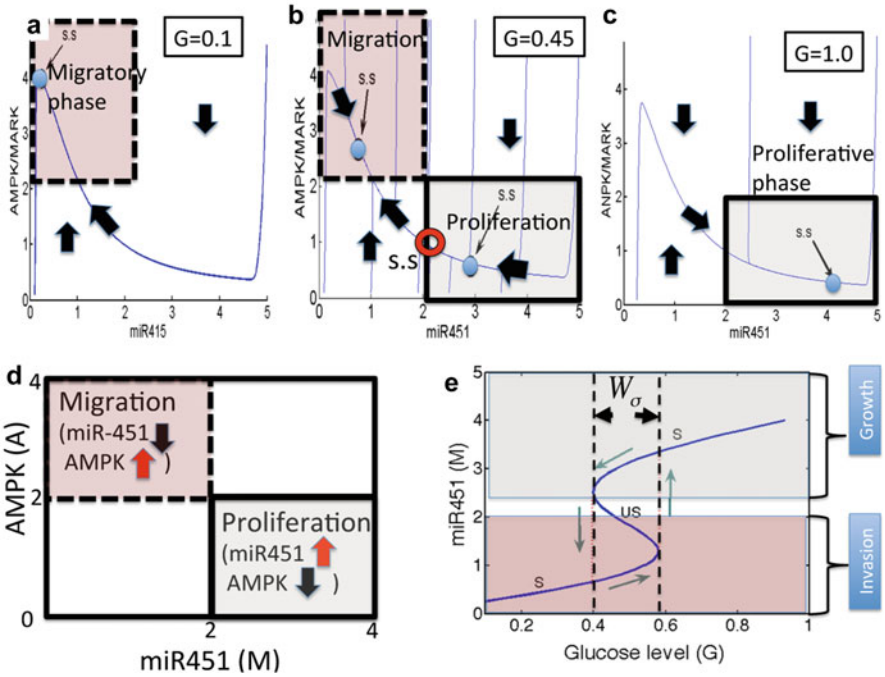

Fig. 4 (**a**–**c**) Dynamic behaviors of the core control system in the M-A phase plane in response to low [$G = 0.1$ in (**a**)], intermediate [$G = 0.45$ in (**b**)], and high [$G = 1$ in (**c**)] levels of glucose signals. *Blue filled circles* = steady states (SS), *red empty circle* in (**b**) = unstable SS. (**d**) A schematic of proliferative ($M > th_M$, $A < th_A$) and migratory ($M < th_M$, $A > th_A$) and regions in the M-A plane. $th_M = 2.0$, $th_A = 2.0$. All other parameters are fixed as in Table 1. (**e**) High and low glucose signals (G) provide an on-off switch of miR-451 over-expression and determine the dichotomous behavior: cell proliferation or migration [46]. $W_\sigma = [\sigma_w^\dagger, \sigma_w^\ddagger]$ = a window of bi-stability

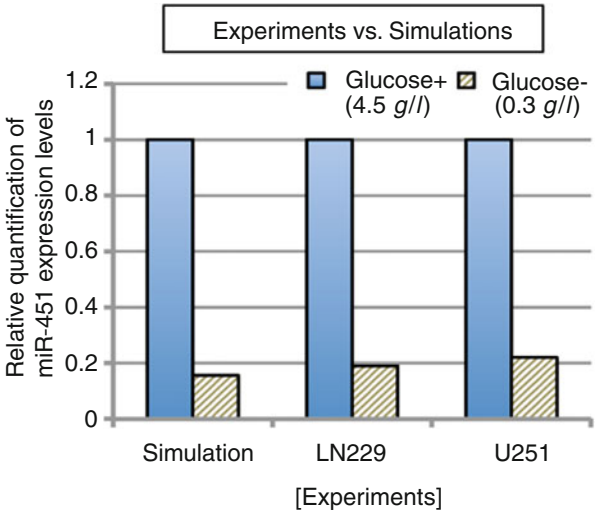

Fig. 5 Simulation results versus experimental observation: miR-451 expression level in response to high (+, 4.5 g/l) and low (−, 0.3 g/l) glucose

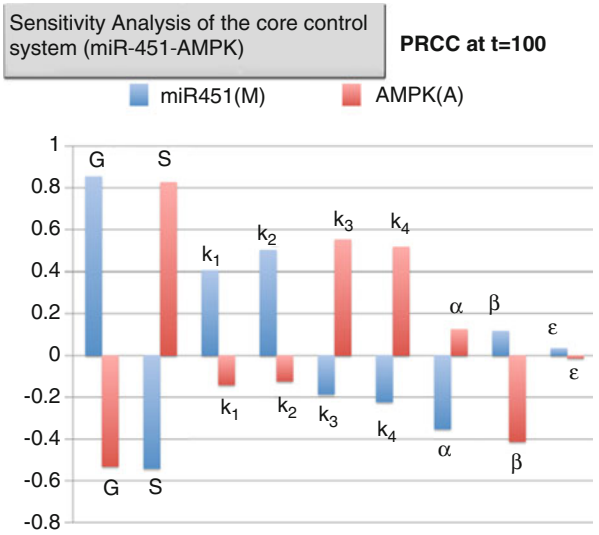

Fig. 6 Sensitivity analysis: the y-value indicates partial rank correlation coefficient (PRCC) values of the miR-451 level and AMPK activity for the perturbed model parameters $(G, S, k_1, k_2, k_3, k_4, \alpha, \beta, \epsilon)$ at $t = 100$. The analysis was carried out using the general Latin hypercube sampling (LHS) scheme in [57] with the sample size 1,000

In particular, the miR-451 level will increase significantly if glucose signal G is enhanced. On the other hand, the miR-451 expression is negatively correlated to the S, α, i.e., miR-451 level would be decreased if either S or α is increased. AMPK activity is positively (negatively) correlated to S, k_3, k_4 (G, β) as expected due to mutual antagonism between miR-451 and AMPK complex.

2.2 *Analysis of miR-451-AMPK Core Control System for Time-Dependent Input*

Tumor cells are exposed to fluctuating glucose levels and they must adapt to the new microenvironment via signaling pathways such as miR-451-AMPK core control system. We mimic the periodically fluctuating glucose levels as follows

$$\frac{dG}{dt} = \sum_{i=1}^{N_g} g_s I_{[t_i, t_i + h_d]} - \mu_g G. \tag{10}$$

where N_g is the number of glucose infusion, g_s is the glucose signal on the time interval $[t_i, t_i + h_d]$, $i = 1, \ldots, N_g$, for a time duration h_d and period τ $(= t_{i+1} - t_i,\ i = 1, \ldots, N_g - 1; h_d < \tau)$ between those intervals, $I[\cdot]$ is the indicator function, μ_g is the decay rate of glucose. Figure 7a, b shows time courses of miR-451 level, AMPK activity in response to fluctuating glucose level from Eq. (10). While the system stays in the proliferative phase in response to frequent glucose infusion ($\tau = 15$; Fig. 7a), it alternates between proliferative and migratory phases with less frequent glucose supply ($\tau = 30$; Fig. 7b).

In the same vein, another way of lowering AMPK activities and up-regulation of miR-451 is to block the signals to the AMPK complex module in a periodic fashion using some drugs. We assume that this signal to the AMPK module is completely blocked N_s-times over the time interval $[t_i, t_i + h_s]$, $i = 1, \ldots, N_s$ with a duration h_d and period τ $(= t_{i+1} - t_i,\ i = 1, \ldots, N_s - 1)$. Thus, we consider the following modified version of the Eq. (6),

$$\epsilon \frac{dA}{dt} = \sum_{i=1}^{N_s} S_s (1 - I_{[t_i, t_i + h_s]}) + \frac{k_3 k_4^2}{k_4^2 + \beta M^2} - A, \tag{11}$$

where S_s is the signaling strength to the AMPK complex, $I(\cdot)$ is the indicator function. Figure 7(c, d) shows growth-invasion patterns in a parameter space S_s-h_d and S_s-τ, respectively. While larger duration (h_d) and lower AMPK source S_s lead to growth (Fig. 7c), shorter period (τ) and lower AMPK source is required to induce anti-invasive effect (Fig. 7d). These results suggest possible therapeutic anti-invasive strategies at the molecular level.

2.3 PDE Model

Governing equations for the tumor density ($n(x,t)$), concentrations of the ECM ($\rho(x,t)$), MMP ($P(x,t)$), glucose ($G(x,t)$), miR-451 ($M(x,t)$), and AMPK ($A(x,t)$) are given by

$$\frac{\partial n}{\partial t} = \left[D_n \Delta n - \nabla \cdot \left(\chi_n \frac{n \nabla G}{\sqrt{1+\lambda_G |\nabla G|^2}} \right) - \nabla \cdot \left(\chi_n^1 \frac{n \nabla \rho}{\sqrt{1+\lambda_\rho |\nabla \rho|^2}} \right) \right] I_{M<th_M} + \lambda_{11} n(1 - n/n_0) I_{M>th_M}, \tag{12}$$

$$\frac{\partial \rho}{\partial t} = -\lambda_{21} P \rho + \lambda_{22} \rho (1 - \rho/\rho_0), \tag{13}$$

$$\frac{\partial P}{\partial t} = D_P \Delta P + \lambda_{31} n \rho - \lambda_{32} P, \tag{14}$$

$$\frac{\partial G}{\partial t} = D_G \Delta G - \lambda_{41}\, nG + \sum_{j=0}^{N-1} \lambda_{42} I_j, \tag{15}$$

$$\frac{\partial M}{\partial t} = (G + \frac{k_1 k_2^2}{k_2^2 + \alpha A^2} - M) \frac{n}{n_0}, \tag{16}$$

$$\epsilon \frac{\partial A}{\partial t} = (S + \frac{k_3 k_4^2}{k_4^2 + \beta M^2} - A) \frac{n}{n_0}, \tag{17}$$

where $I_{M>th_M}$ is the indicator function of growth region (where miR-451 level (M) is greater than a threshold value (th_M)) and $I_{M<th_M}$ is the indicator function of the invasive region (where miR-451 level is below the threshold (th_M)). Here all parameter values ($D_n, \chi_n, \lambda_G, \chi_n^1, \lambda_\rho, \lambda_{11}, n_0, \lambda_{21}, \lambda_{22}, D_P, \lambda_{31}, \lambda_{32}, D_G, \lambda_{41}, \lambda_{42}$) are positive.

The first three terms in the Eq. (12) represent random motility, chemotaxis, and haptotaxis, respectively, when the tumor cell is in the migratory phase ($\mathbb{T}_m$). Here, chemotaxis (or haptotaxis) is the cell movement in response to a chemical stimulus such as gradients of glucose (∇G) with the chemotactic sensitivity (χ_n) (or adhesive stimulus in the ECM ($\nabla \rho$) with the haptotactic sensitivity (χ_n^1)). On the other hand, the last term indicates tumor cell proliferation when the cell is in the proliferative condition ($\mathbb{T}_p$). ECM is degraded by tumor-secreted MMPs at a rate λ_{21}. MMPs and glucose diffuse throughout the domain with the diffusion coefficients, D_P, D_G ($D_P \leq D_G$), respectively. Glucose is consumed by tumor cells at a rate (λ_{41}) but is injected at a rate λ_{42}. The core control system (16)–(17) acts on the system in the presence of the tumor cell density ($n/n_0 \neq 0$).

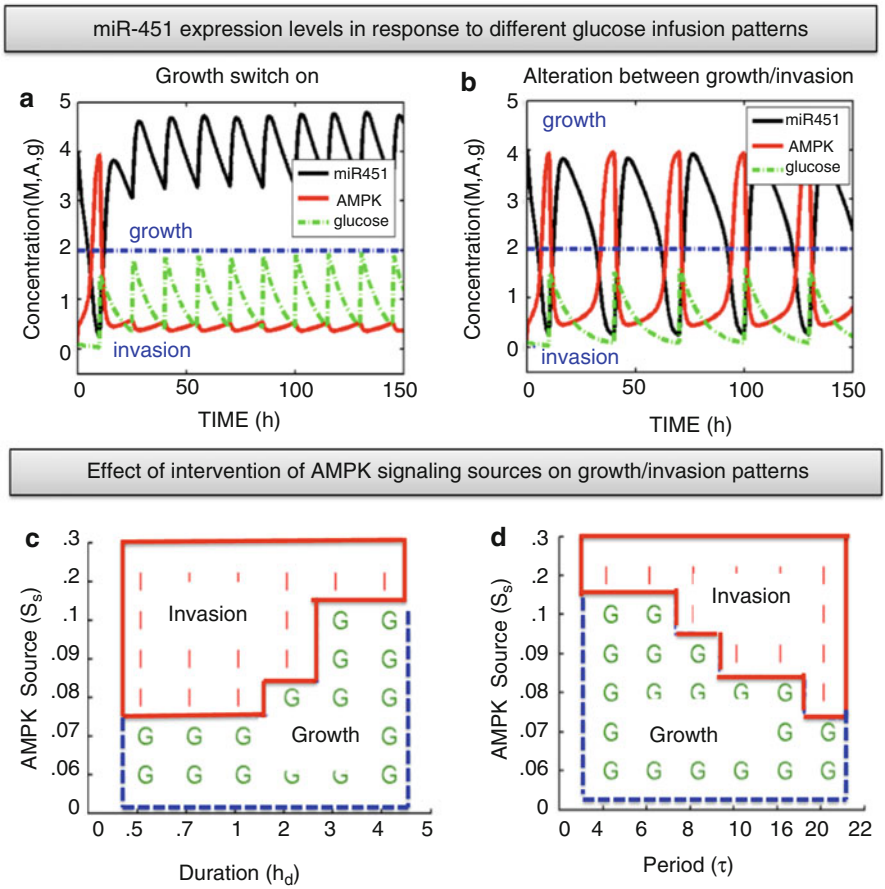

Fig. 7 (**a**, **b**) Time courses of the miR-451 level, AMPK activity, and glucose level for fluctuating glucose supply with the period $\tau = 15$ (**a**), 30 (**b**). *Dotted blue line* $= th_M = 2.0$. Parameters: $g_s = 3.0$, $h_d = 0.5$, $\mu_g = 0.1$. Initial conditions: $M(0) = 4.0$, $A(0) = 0.1$, $G(0) = 0.1$. Initial injection time: $t_1 = 10$. All other parameters are fixed as in Table 1. (**c**, **d**) growth (*blue dotted boxes*) and invasion (*red solid boxes*) patterns in the h_d-S_s-plane [(**c**); $\tau = 10$ fixed] and τ-S_s-plane [(**d**); $h_d = 2.0$ fixed] in response to a periodic intervention of signals to the AMPK complex. Signals to the AMPK complex (S) were partially blocked in a periodic fashion with various period τ, duration h_d, and various signal strength (S_s). Initial conditions: $M(0) = 0.1$, $A(0) = 4.0$. Parameters: glucose level = 0.5, other parameters are same as in Table 1

Parameter Estimation

(1) D_n : For EC cells migrating in a culture containing angiogenic factor, Stokes and Lauffenburger [76] measured the diffusion coefficient to be 7×10^{-9} cm^2/s. A 'typical' cell motility coefficient has been estimated to be 5×10^{-10} cm^2/s [6]. A smaller value, 10^{-10} cm^2/s, was used in [2]. While the experimental results for motility of human glioma [19] and glioblastoma cells [33] in 2D substrate suggest a

value of D_n in the range of $1.16 \times 10^{-10} - 2.31 \times 10^{-9}$ cm^2/s, Stein et al. [74] used a tenfold higher value of D_n (=2.31×10^{-8} cm^2/s) in order to get a better fit to the experimental data. Burgess et al. [7] took $D_n = 1.7 \times 10^{-9}$ cm^2/s, but Sander and Deisboeck [67] argued that D_n should be much smaller, namely, 10^{-12} cm^2/s. We shall take $D_n = 10^{-11}$ cm^2/s. (2) D_P : In experiments of the movement of MMP-1 in the collagen fibril, Saffarian et al. [66] estimated the diffusion coefficient to be $(8 \pm 1.5) \times 10^{-9}$ cm^2/s for wild-type activated MMP-1 and $(6.7 \pm 1.5) \times 10^{-9}$ cm^2/s for inactive mutant. In our simulation, we take $D_P = 5 \times 10^{-11}$ cm^2/s. (3) D_G : The diffusion coefficient of G was measured as 6.7×10^{-7} cm^2/s in the brain [37] and 1.3×10^{-6} cm^2/s in collagen gel [64]. The diffusion coefficient in a growing tumor spheroid or aggregate is much smaller than the one in the medium, and so we take $D_G = 2.31 \times 10^{-7}$ cm^2/s. (4) χ_n: In the presence of EGF, glioma cells traveled a distance 0.4–0.5 cm in 150 h [9]; glioma cells in agar containing EGF traveled faster, covering a distance of 1.25 cm in 150 h, while in plain agar they traveled only 0.75 cm during the same period. In experiments with U87MGmEGFR spheroid growth, Deisboeck et al. [17] calculated the cell velocity to be in the range of 50–110 μm/24 h. Kim et al. [44] assumed that gradient of the glucose concentration was $3 \times 10^{-3} - 10^{-4}$ g/cm^4 and a drift velocity 25–110 μm/24 h of mobile cells to compute an intermediate value of $\chi_n = \frac{velocity}{gradient} = 2.76 \times 10^{-4}$ cm^5/(g · s). We assume that the chemotactic sensitivity is relatively small due to the fluctuating glucose level. We take χ_n=1.86×10^{-7} cm^5 g^{-1} s^{-1}. (5) χ_n^1: For the haptotactic sensitivity, we take $\chi_n^1 = 4.17 \times 10^{-5}$ cm^5/(g · s). (6) λ_{11}: Doubling time were in the range from 27 h (U87MG) to 60 h (LN405) for human glioma cells [58]; this translates into proliferation rate of $(7.1\text{–}8) \times 10^{-6}$ s^{-1}. Measured values of proliferation rate were reported as 1/day, or 8×10^{-6} s^{-1}, in typical experiments in [67]. Taking into consideration the large flux of glucose being supplied periodically in our system, we take $\lambda_{11} = 1.112 \times 10^{-4}$ s^{-1}. (7) λ_{31}: It is difficult to measure the MMP production rate directly. The range of $(1.11\text{–}6.94) \times 10^{-8}$ s^{-1} was estimated in [44] for sparsely seeded migrating cells. The MMP production rate, written as $\lambda(n, \rho)$, was modeled by $\lambda_{31} n$ in [44] where $\lambda_{31} = 6.94 \times 10^{-8}$ s^{-1}. Here, we model it as $\lambda_{31} n \rho$, because ρ is expected to oscillate quite significantly. In order to adjust to the order of magnitude of MMP production in [44], we take an estimated value, $\lambda_{31} = 6.95 \times 10^{-5}$ cm^3 g^{-1} s^{-1}; see also [58]. (8) λ_{32}: MMP is secreted by a tumor cell and is highly localized (fast decay) in the invading front of migrating tumor cells. We assume half-life of MMP to be very short (approximately 3.8 h) so that $\lambda_{32} = 5.0 \times 10^{-5}$ s^{-1}. (9) λ_{41}: Nutrient consumption rate was measured as $\alpha = 1.6$ pg/cell/min in [53]. We compute λ_{41} from $\lambda_{41} G^\dagger = \alpha$ when $G^\dagger = 8.9 \times 10^{-4}$ g/cm^3 is between high (4.5×10^{-3} g/cm^3) and low (3.0×10^{-4} g/cm^3). Hence, $\lambda_{41} = \frac{\alpha}{G^\dagger} = 0.3$ cm^3/(g · s).

Table 2 lists parameter values used in the model.

2.4 Simulation Results

Figure 8 shows a time course of total tumor population, concentration of glucose, miR-451 levels, and AMPK activity. Fluctuating glucose levels (dash-dotted line) in Fig. 8a lead to peaks of miR-451 levels and low AMPK activity in Fig. 8b. In turn, fluctuating AMPK levels give rise to the plateau invasion phase and creeping growth phase of the tumor cells due to infiltrating cells near the surface of the tumor core when the AMPK level is high.

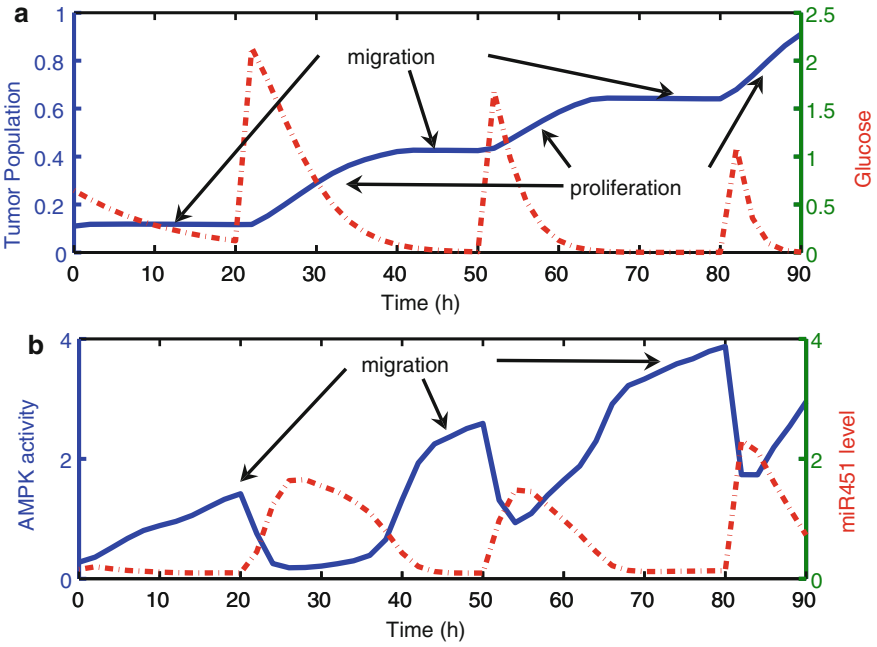

Fig. 8 Dynamics of tumor invasion and growth in response to fluctuating glucose. (**a**) Time courses of tumor population and glucose level. (**b**) Time courses of miR-451 level and AMPK activity in response to fluctuating glucose in (**a**). Tumor cells adapt proliferative ($\mathbb{T}_p$; high miR-451, low AMPK) and migratory phase ($\mathbb{T}_m$; low miR-451, high AMPK) via the core control system in response to high and low glucose levels, respectively

We now test our hypothesis on growth-invasion patterns of tumor spheroids under the fluctuating (Fig. 9a) and steady-state glucose conditions (Fig. 9b) when the total supply of glucose is fixed. Figure 9c shows that the overall growth rate of the tumor (black solid line) in response to glucose fluctuation is larger than one with fixed supply of glucose (dotted black line) after 100 h.

Figure 10b shows the effect of inhibition strength (α) of miR-451 by the AMPK complex on the tumor population. In contrast to the control case ($\alpha = 1.6$), the AMPK activity does not fluctuate (Fig. 10a; circle) when α is low ($\alpha = 0.16$),

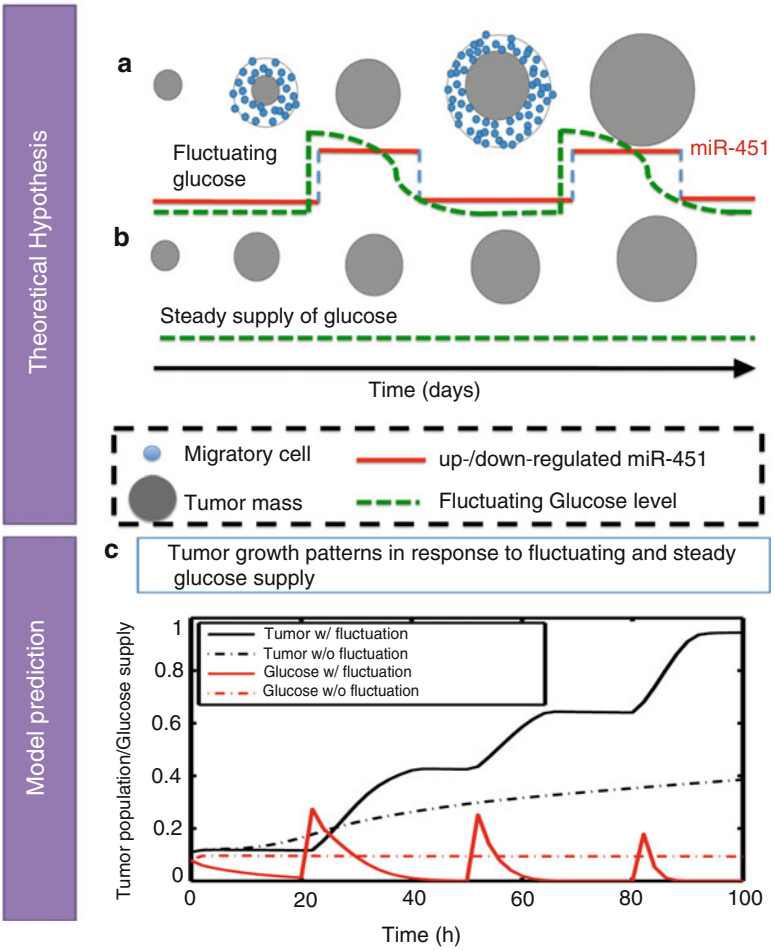

Fig. 9 Theoretical hypothesis and model prediction on two different growth schemes of tumors with the same initial size in response to steady and fluctuating glucose. (**a**) Cycle of invasion and growth in response to fluctuating glucose. (**b**) Monotonic growth in response to steady glucose; the total supply of glucose is the same as in (**a**). Hypothesis: enhanced growth of tumor spheroids with fluctuating glucose in (**a**). (**c**) Model prediction: time courses of tumor populations (*black lines*) in responds to periodic injection of high glucose (*red solid line*) and steady supply of glucose (*red dotted line*)

which leads to slower tumor growth. Since lower values of the inhibition strength α lead to higher levels of miR-451 and low AMPK activity (Fig. 10a), blocking miR-451 along the pathways from CAB39/LKB1/STRAD/AMPK to miR-451 could be a possible therapeutic target of an anti-invasion drug. On the other hand, one would achieve the similar anti-invasive effect by increasing the inhibition strength (β) of the AMPK complex by miR-451, i.e., down-regulation of AMPK activities and

up-regulation of miR-451 (the base value ($\beta = 1.0$; solid line) $\rightarrow$ $\beta = 10$ (circle) in Fig. 10c). An increase in β also leads to slower tumor growth. Figure 10d shows tumor populations at $t = 0, 50, 100$ for various parameter values $\beta = 1.0, 1.2, 10$. In contrast to the control case ($\beta = 1.0$), there is a significant decrease in tumor population and it does not generate invasion-growth patterns when β is large β=10. For an intermediate value of $\beta = 1.2$, a periodic fluctuation of AMPK levels is observed but the duration of high AMPK activities is not as long as one in the case of the control ($\beta = 1.0$). These results are due to the fact that higher values of the inhibition strength β lead to lower AMPK activity and over-expression of miR-451. Thus, this increase in β also suggests another possible anti-invasion target.

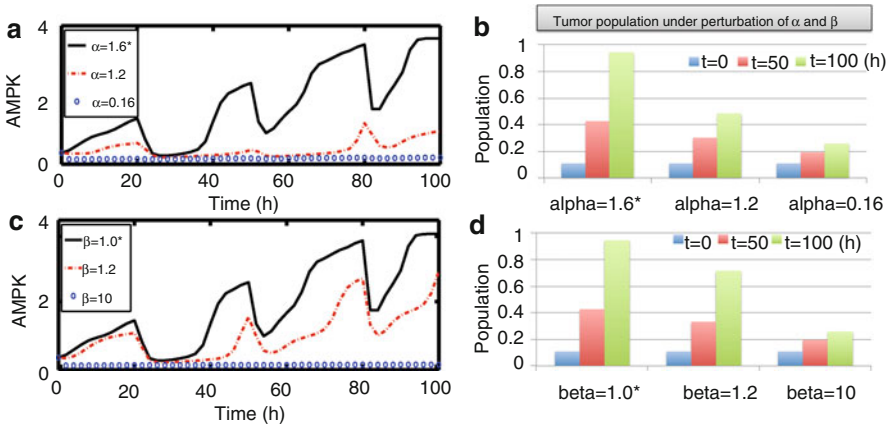

Fig. 10 Effect of inhibition strength α and β on tumor invasion and growth. (**a**) Time course of total AMPK activity within the system for different values of α=1.6* (*solid black*), 1.2 (*dotted red*), 0.16 (*blue circle*). (**b**) Tumor populations at time $t = 0, 50, 100$ for each case in (A). (**c**) Time course of total AMPK activity within the system for different values of β=1.0* (*solid black*), 1.2 (*dotted red*), 10 (*blue circle*). (**d**) Tumor populations at time $t = 0, 50, 100$ for each case in (**c**). *The control case was marked as star (*) for each subfigure

3 Hybrid Model

3.1 Cell-Mechanics Model

The behavior of individual cells is based on the models developed by Dallon and Othmer [15] (DO model) and Kim et al. [47, 48]. The model essentially takes into account the following forces: (1) the active forces $\mathbf{T}_i$ exerted on the substrate or neighboring cells and the reaction force ($\mathbf{M}_{j,i}$), (2) the dynamic drag forces from adhesive bonds with neighboring cells, (3) static friction force $\mathbf{S}_{j,i}$ for rigid

Table 2 Parameters that are used in the PDE model

Parameter	Description	Value*	Refs.
D_n	Random motility of tumor cells	10^{-11} cm^2/s	[44]
D_P	Diffusion coefficient of MMPs	5×10^{-11} cm^2/s	[44, 66, 71]
D_G	Diffusion coefficient of glucose	2.31×10^{-7} cm^2/s	[44, 64],TW
λ_{11}	Tumor cell growth rate	1.112×10^{-4} s^{-1}	[58, 67], TW
n_0	Carrying capacity of tumor cells	1.0×10^{-3} g/cm^3	TW
λ_{21}	ECM degradation rate	1.41×10^{3} cm^3 g^{-1} s^{-1}	[44],TW
λ_{22}	ECM release/reconstruction rate	5.0×10^{-5} s^{-1}	[44],TW
ρ_0	ECM carrying capacity	1.0×10^{-3} g/cm^3	[39, 44, 74]
λ_{31}	MMP production rate	6.95×10^{-5} cm^3 g^{-1} s^{-1}	TW
λ_{32}	MMP decay rate	5.0×10^{-5} s^{-1}	[44],TW
λ_{41}	Glucose consumption rate	0.3 cm^3/(g $\cdot$ s)	[53, 67], TW
λ_{42}	Glucose injection rate	1.25×10^{-6} g/(cm^3 $\cdot$ s)	TW
χ_n	Chemotactic sensitivity parameter	1.86×10^{-7} cm^5 g^{-1} s^{-1}	TW
χ_n^1	Haptotactic parameter	4.17×10^{-5} cm^5/(g $\cdot$ s)	[44],TW

*TW = This work

attachment between cells or between a cell and the substrate. (See DO for a more detailed discussion of all forces involved.) The total force on the ith cell is then given by

$$\mathbf{F}_i = \sum_{j \in \mathcal{N}_i^a} \mathbf{M}_{j,i} + \sum_{j \in \mathcal{N}_i^a} \mathbf{T}_i + \sum_{j \in \mathcal{N}_i^d} \mu_{ij} (\mathbf{v}_j - \mathbf{v}_i) + \sum_{j \in \mathcal{N}_i^s} \mathbf{S}_{j,i} \tag{18}$$

where $\mathcal{N}_i^a$ denotes the neighbors of i, including the substrate, upon which it can exert traction, $\mathcal{N}_i^d$ is the set of "cells" (which includes substrate and extracellular matrix ECM) that interact with i via a frictional force, and $\mathcal{N}_i^s$ denotes the set of cells that statically bind to cell i. These force balance equations allow us to calculate all forces involved and track down locations of all cells in addition to biophysical response of the cells. These forces are expressed in terms of cell velocity ($\mathbf{v}_i$) and integrating these forces also generates measurable quantities such as the cell velocity, which can be compared to the experimental data.

There are two kinds of glioma cell involved: proliferative and motile one. The cells are treated as oriented ellipsoids and cytoplasm is considered as an incompressible, viscoelastic solid [15, 47]. We assume the multiplicative form of the growth rate function for the i-th axis of the cell given by

$$(u_i^g)' = f(\sigma) P(M, A)$$

where σ is the force acting on the cell and P is a function of the miR451 activity (M) and AMPK levels (A). The growth function $f(\sigma)$ is defined so that cells can grow under sufficiently small tensile and compressive forces [47,48]. We also assume that

the cell proliferation is determined by the core control system, i.e., a cell proliferates when miR-451 is up-regulated and AMPK activity is down-regulated at the cell site:

$$P(M,A) = \begin{cases} 1 & \text{if } M > th_M,\ A < th_A \\ 0 & \text{otherwise} \end{cases} \tag{19}$$

where th_M, th_A are threshold values of the miR-451 and AMPK levels. The active force $\mathbf{T}_i$ of cell i is given by

$$\mathbf{T}_i = \phi(M_i)\frac{\nabla C}{\sqrt{K_C + |\nabla C|^2}} \tag{20}$$

where C is the concentration of a chemoattractant. Here, the indicator function $\phi(M)$ is given by

$$\phi(M) = \begin{cases} r_n F_0 & \text{if } M < th_M, A > th_A, \text{ cell without physical constraints,} \\ 0 & \text{otherwise,} \end{cases} \tag{21}$$

where F_0 is the basal magnitude of the active force ($0 \le |\mathbf{T}_i| \le F_0$) and r_n is a random number in [0.8, 1.2]. Therefore, the active force is completely turned off for proliferative cells ($M_i > th_M, A < th_A$), cells under physical constraints (a cell completely surrounded by neighboring cells), or in the absence of chemotactic signal ($\nabla C = 0$).

3.2 Reaction-Diffusion

We let $G(\mathbf{x},t), C(\mathbf{x},t)$ be the concentrations of glucose and chemoattractant, respectively, at space $\mathbf{x}$ and time t. Governing equations of all variables are given by

$$\frac{\partial G}{\partial t} = D_G \Delta G + \sum_{j=1}^{N_G} \lambda_{in}^G I_{[t_j^G, t_j^G + \tau_d^G]\times\Omega_\epsilon} + \lambda_b \eta_1(x,G) - \lambda_c \eta_2(x,G) - \mu_G G, \tag{22}$$

$$\frac{\partial C}{\partial t} = D_C \Delta C + \sum_{j=1}^{N_C} \lambda_{in}^C I_{[t_j^C, t_j^C + \tau_d^C]\times\Omega_\epsilon} - \mu_C C \tag{23}$$

where D_G, D_C are the diffusion coefficients of glucose and chemoattractant, respectively, λ_{in}^G (λ_{in}^C) is the glucose (chemoattractant) injection rate on a subdomain Ω_ϵ over time intervals $[t_j^G, t_j^G + \tau_d^G]$, $j = 1, \ldots, N_G$ ($[t_j^C, t_j^C + \tau_d^C]$, $j = 1, \ldots, N_C$) with a period τ^G (τ^C) and duration τ_d^G (τ_d^C) after the initial surgery at $t = t_S$ ($t_1^G > t_S$), λ_b is the glucose flux from blood flow, λ_c is the consumption rate of glucose by tumor cells, μ_G is the glucose removal rate from the system via

blood flow and glucose consumption in the surrounding tissue [3, 11, 29, 65, 82], μ_C is the decay rate of the chemoattractant. Here, indicator functions (η_1, η_2) are given by

$$\eta_1(x, G) = \begin{cases} 1 & \text{blood vessel} \\ 0 & \text{otherwise} \end{cases}, \quad \eta_2(x, G) = \begin{cases} 1 & \text{tumor} \\ 0 & \text{otherwise.} \end{cases}$$

We also assume no flux (Neumann) boundary conditions ($\frac{\partial G}{\partial \nu} = 0$, $\frac{\partial C}{\partial \nu} = 0$, on $\partial\Omega$). The reaction-diffusion equations (22)–(23) are solved on the regular grid using the alternating-direction implicit (ADI) method and the nonlinear solver *nksol* for algebraic systems. A typical spatial grid size used is $h_x = h_y = 0.01$ on a square domain $[0, 1] \times [0, 1]$. An adaptive time stepping method is used. Table 3 lists parameter values used in the model.

Table 3 Parameters that are used in the hybrid model

Parameter	Description	Value*	Refs.
D_G	Diffusion coefficient of glucose	6.7×10^{-7} cm^2/s	[37]
D_C	Diffusion coefficient of chemoattractant (EGF)	1.66×10^{-6} cm^2/s	[80]
λ_c	Glucose consumption rate by tumor	0.8 pg/cell/min	TW
μ_G	Removal rate of glucose in brain tissue	0.0034 min^{-1}	TW
μ_C	Decay rate of chemoattractant (EGF)	8.02×10^{-6} s^{-1}	[49]

*TW = This work

3.3 Results

We investigate growth/invasion dynamics of a tumor spheroid in response to high and low glucose levels. Figure 11a–c shows spatial patterns of glioma cells in response to a high glucose level ($G_0 = 0.6$) at time $t = 0, 10, 32$ h. The miR451 level stays high and AMPK activity is still low at $t = 10$ h (Fig. 11d) and all cells are proliferating in the spherical core without much migration. However, some cells on the surface begin to migrate away from the core due to the lowered miR-451 level near $t = 30$ h. Figure 11d shows a time course of the miR-451 level and AMPK activity at the site of a cell on the surface of the core (black arrowhead in Fig. 11b, c, e, f). The miR-451 level in this cell is decreased until it drops below the threshold ($th_M = 2.0$) around 30 h for a phenotypic switch to a migratory state. See Fig. 11g–i for relatively high glucose profiles at $t = 0.1, 6.6, 30$ h. On the other hand, when the glucose level is low ($G_0 = 0.2$), cells on the surface of the spherical core shed from the core due to the low level of miR-451 and high AMPK activity at $t = 10, 32$ h (Fig. 11e, f). (See profiles of glucose at $t = 0.1, 6.6, 30$ h in Fig. 11j–l.) For example, the same cell (200th cell; arrowhead) in Fig. 11b, c migrated far away at the final time ($t = 32$ h) in response to the low glucose level

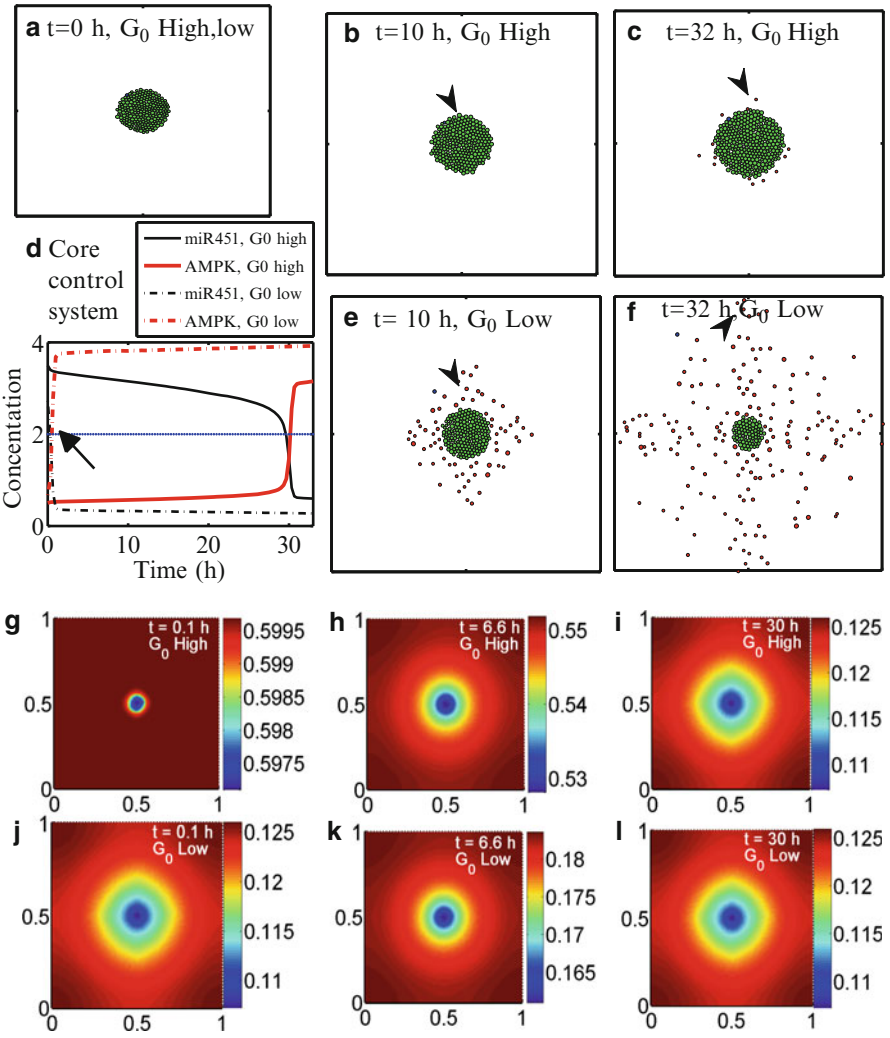

Fig. 11 (**a**–**c**, **e**, **f**) Spatial patterns of tumor spheroids in response to high (**a**–**c**) and low (**a**, **e**, **f**) glucose levels at $t = 0, 10, 32$ h. (**d**) Time courses of core control system (the miR451 level and AMPK activity) for high (*solid*) and low (*dotted*) levels of glucose at a cell site [200th cell marked by b*lack arrowhead* in (**b**, **c**, **e**, **f**)]. (**g**–**i**) Profiles of glucose at $t = 0.1, 6.6, 30$ h corresponding to the high initial glucose level ($G_0 = 0.6$) in (**a**–**c**). (**j**–**l**) Profiles of glucose at $t = 0.1, 6.6, 30$ h corresponding to the low initial glucose level ($G_0 = 0.2$) in (**a**, **e**, **f**)

(arrowhead in Fig. 11f). The miR-451 level dropped below the threshold (th_M) at an early time ($t = 1$ h) and the cell (arrowhead in Fig. 11e) is in the migratory phase at $t = 10$. However, this cell did not migrate due to the physical constraints from its neighboring cells in the tumor core. After shedding of all neighboring cells, the cells finally are free from the physical constraints and began to migrate

(Fig. 11f). The reduction of cell motility with the down-regulated miR-451 level was also observed in [27]. Godlewski et al. [27] observed that a cell line (U251 cells) stably expressing miR-451 (miR-451^{+}) grows faster than negative control (miR-451^{-}). In our case, cells maintain high (or low) miR-451 levels for most of the time in the case of high (or low) glucose level.

This effect of cell mechanics on glioma cell shedding is illustrated in Fig. 12. When the glucose level is low ($G_0 = 0.2$), the core control system (miR-451, AMPK) induces the migratory signal of the most of cells. However, cells inside the spherical core fail to escape due to mechanical constraints and strong adhesion forces between them. Only the cells on the surface of the spherical core are able to migrate in response to the 'escape' signal ($M < th_M, A > th_A$) from low glucose levels. For example, more than 70 % of cells inside the spheroid are in the migratory phase but do not migrate away even at early times of simulation ($\sim$1 h). However, under normal glucose conditions ($G_0 > 0.6$), all cells are in the proliferative phase and this relative number of trapped cells with the migratory signal is zero until the glucose level becomes sufficiently low around t= 27 h due to glucose consumption by tumor cells. The relative number of trapped cells is increased up to 70 % at $t = 31$ h due to increased number of cells in the core with the migratory signal.

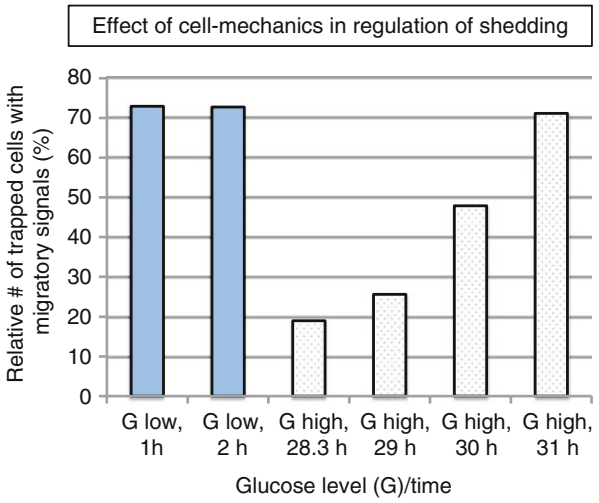

Fig. 12 Effect of mechanics on cell invasion [ratio of 'trapped' cells (%) with the migratory signals ($M < th_M, A > th_A$) within the spherical core]

Figure 13a shows the area of the migratory zone at $t = 6, 20$ h for various glucose conditions ($G_0 = 0.1, 0.2, 0.3.0.4, 0.5$). While tumor cells migrate aggressively across large areas (Fig. 11e, f) outside the core under glucose withdrawal conditions ($G_0 = 0.1 - 0.4$), cell motility is significantly decreased when the glucose level is high ($G_0 = 0.5$) as observed in experiments [27]. Calculated cell speeds in the hybrid model are also in good agreement with measured values in experiments (see Fig. 13b): 39–45 μm/h in 2D barrier-free culture condition and 15–20 μm/h in

3D glioblastoma cell culture in the absence/presence of EGF-stimulation [41], 15–25 μm/h in glioblastoma cells with/without α-actinin isoforms [70], 15–48 μm/h for cells embedded in collagen I matrix [39].

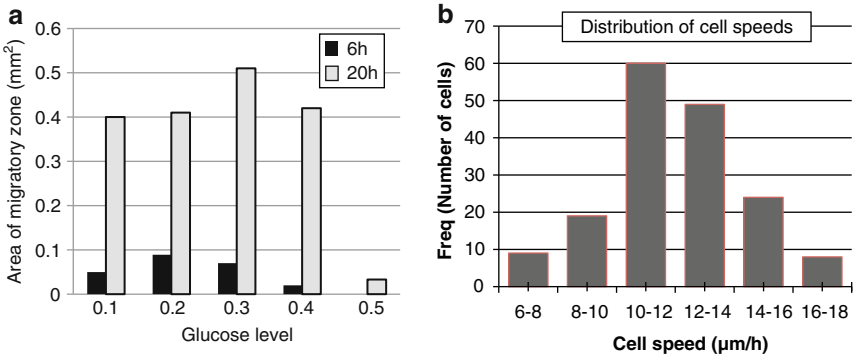

Fig. 13 (**a**) Cell motility (area of migratory zone; A_{mz}) in response to various glucose levels ($G_0 = 0.1$–0.5) at time t = 6, 20 h. (**b**) Distribution of average cell speeds from the hybrid model

Finally we tested some hypotheses on localization of invasive glioma cells after conventional surgery at $t = 0$ h [43]. Figure 14a–d shows profiles of migratory and proliferative cells at $t = 0, 8, 16, 24$ h when a chemoattractant and glucose were injected at the center of the domain at $t = 0$ h and $t = 17$ h, respectively. Invasive tumor cells initially respond to the chemoattractant. Then, most of migratory cells switch to proliferative ones around $t = 17$ h (Fig. 14e) when low miR-451 levels jump to higher value $M > 5 > th_M$ (Fig. 14f), forming a visible larger tumor mass (Fig. 14d), in response to glucose injections. Most of these proliferative cells may enter the migratory phase ($M < th_M, A > th_A$) again when glucose levels are lowered due to consumption of glucose from the growing tumor mass. It was assumed that a cell can sense the microenvironment and the active force of a migratory cell is set to be zero when the cell reaches the periphery of the resection bed. So, cells stop the migration process on the periphery of the resected area and are localized near the surgical site, increasing chances of elimination of invasive tumor cells via the second treatment options such as the follow-up surgery or radiotherapy if feasible.

4 Discussion and Conclusions

Tumor cell proliferation and migration depend on the type of tumor cells and on the tumor microenvironment. In this work we focused on tumor cells from glioblastoma. One of the major obstacles in treatment of glioblastoma is that by the time the disease is diagnosed glioma cells have already spread into the surrounding brain tissue and the incomplete elimination of cancer cells by conventional therapeutic approaches leads to regrowth of these invasive cells, leading to the poor survival

rate. Infiltrating glioma cells can be cultured from biopsies up to 4 cm away from the main bulk tumor [72]. Like the guerilla warriors, the glioma cells seem to posses specific characteristics that allow for diffusive infiltration [13].

We first developed an intracellular model of the miR-451-AMPK core control system within a glioma cell and population model of tumor cell proliferation and invasion. Then, we developed a hybrid model where glioma cells are modeled as an individual unit embedded in the microenvironment and biophysical and biochemical properties of all cells are taken into account.

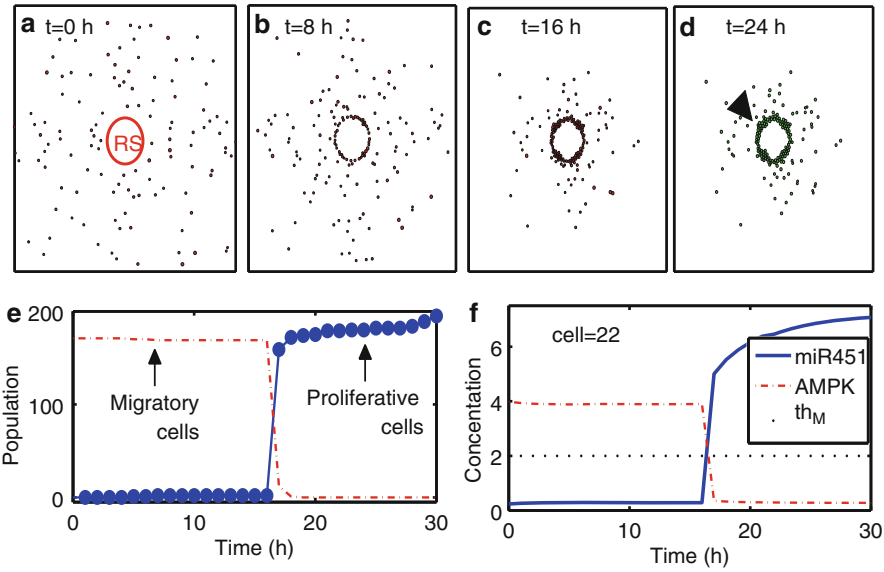

Fig. 14 (**a**–**d**) Migration-proliferation profiles of tumor cells at $t = 0, 8, 16, 24$ h in response to injection of a chemoattractant at $t = 0$ h and glucose at $t = 17$ h after initial surgery at $t = 0$ h. *Solid circle* in (**a**) = resected area after the first surgery (RS). (**e**) A time course of cell populations: proliferative (*circle*) and migratory (*dash-dotted*) cells. (**f**) Time course of miR-451 (*solid*) and AMPK activity (*dash-dotted*) at a cell site [cell id = 22; *arrow* in (**d**)]. *Dotted black line* in the middle = threshold value of miR-451 ($th_M = 2.0$). Parameters used: $t_1^G = 17\ h, \tau_d^G = 24$ h

Simulation of the population model shows how variations in glucose significantly affect the level of miR-451and, in turn, cell migration. By changing the level of glucose through periodic injections, the cancer cells will alternate between migration to proliferation modes via the miR-451-AMPK system. The model simulation predicts that oscillations in the levels of glucose lead to the faster growth of the primary tumor relative steady supply of glucose. The model also suggests that drugs which upregulate miR-451, or block other components of the CAB39/AMPK pathway, will slow down glioma cell migration, a possible target for anti-invasion drugs. The miR-451 as well as the downstream signaling molecules (AMPK, mTOR) was identified as a novel target for growth control in colorectal carcinoma [8, 54]. For instance, mTOR inhibitors such as rapamycin or RAD001

and AMPK activator such as AICAR reversed miR-451's effect on tumor growth [8]. In general, AMPK pathways have been identified as an emerging drug target for metabolic syndrome as well [89]. These drugs could be used to control the cell migration or proliferation in glioblastoma.

The hybrid model was able to reproduce the spatial invasion patterns and cell motility of glioma cells under normal and low glucose conditions observed in the *in vitro* experiment [27] and correct cell speeds in the experiments [39, 41, 70]. Due to its biophysical properties of the individual cells, the hybrid model can capture biomechanical properties of a growing tumor. For instance, cell–cell adhesion between tumor cells plays a significant role in regulation of shedding properties from the primary spheroid core [45].

For therapeutic strategies, the model suggests that (1) Injection of chemoattractant at the surgical site may attract invasive tumor cells back to the tumor site, leading to localization of these invasive tumor cells. This may lead to a follow-up surgery for eradication of the *invisible* tumor cells that managed to survive from the first surgery [43]. (2) Introduction of glucose at the center of the surgical site may increase the visibility of invisible cells by the up-regulation of miR-451 and downregulation of AMPK activity. Multiple microsurgical resections for glioblastoma have been proven to be effective and useful [34]. We also note that introduction of glucose at the wrong time and locations, for instance presence of blood vessels on the routes, may interfere this localization strategy and this may lead to undesirable results (i.e., the proliferation of dispersed infiltrative glioma cells). Optimal control theories have been applied to optimize expenses on glucose injections for this strategy i.e., maintaining unregulated status of miR-451 levels to increase visibility of the tumor near the resection site after localization [68].

Glioma cell migration through a narrow intercellular space between normal brain cells is an extremely complex process that involves deformation of both cell body and nucleus via the complex regulation of acto-myosin dynamics [5]. There is currently only a limited understanding of the complex relationship between the tumor cells and the host cells in the microenvironment. A better understanding of this relationship and cell motility may lead to new therapeutic approaches that target stromal elements instead of, or in addition to, tumor cells. We hope to address these situations in future work.

Acknowledgements YJK and HJK were supported by the Basic Science Research Program through the National Research Foundation of Korea by the Ministry of Education and Technology (2012R1A1A1043340).

References

1. Aguda, B.D., Kim, Y., Hunter, M.G., Friedman, A., Marsh, C.B.: MicroRNA regulation of a cancer network: consequences of the feedback loops involving miR-17-92, E2F, and Myc. PNAS **105**(50), 19678–19683 (2008)
2. Anderson, A.R.A., Chaplain, M.A.J.: Continuous and discrete mathematical models of tumor-induced angiogenesis. Bull. Math. Biol. **60**, 857–900 (1998)

3. Aronen, H.J., Pardo, F.S., Kennedy, D.N., Belliveau, J.W., Packard, S.D., Hsu, D.W., Hochberg, F.H., Fischman, A.J., Rosen, B.R.: High microvascular blood volume is associated with high glucose uptake and tumor angiogenesis in human gliomas. Clin. Cancer Res. **6**(6), 2189–200 (2000)
4. Bartel, D.P.: Micrornas: target recognition and regulatory functions. Cell **136**(2), 215–33 (2009)
5. Beadle, C., Assanah, M.C., Monzo, P., Vallee, R., Rosenfield, S.S., Canoll, P.: The role of myosin II in glioma invasion of the brain. Mol. Biol. Cell **19**, 3357–3368 (2008)
6. Bray, D.: Cell Movements: From Molecules to Motility. Garland, New York (2000)
7. Burgess, P.K., Kulesa, P.M., Murray, J.D., Alvord, Jr., E.C.: The interaction of growth rates and diffusion coefficients in a three-dimensional mathematical model of gliomas. J. Neuropathol. Exp. Neurol. **56**(6), 704–713 (1997)
8. Chen, M.B , Wei, M.X., Han, J.Y., Wu, X.Y., Li, C., Wang, J., Shen, W., Lu, P.H.: MicroRNA-451 regulates AMPK/mTORC1 signaling and fascin1 expression in HT-29 colorectal cancer. Cell. Signal. **26**(1), 102–109 (2014)
9. Chicoine, M.R., Madsen, C.L., Silbergeld, D.L.: Modification of human glioma locomotion in vitro by cytokines EGF, bFGF, PDGFbb, NGF, and TNF alpha. Neurosurgery **36**(6), 165–70 (disbrain cancer) (1995)
10. Chintala, S.K., Tonn, J.C., Rao, J.S.: Matrix metalloproteinases and their biological function in human gliomas. Int. J. Dev. Neurosci. **17**(5–6), 495–502 (1999)
11. Chiro, D.G., DeLaPaz, R.L., Brooks, R.A., Sokoloff, L., Kornblith, P.L., Smith, B.H., Patronas, N.J., Kufta, C.V., Kessler, R.M., Johnston, G.S., Manning, R.G., Wolf, A.P.: Glucose utilization of cerebral gliomas measured by [18f] fluorodeoxyglucose and positron emission tomography. Neurology **32**(12), 1323–1329 (1982)
12. Choe, G., Park, J.K., Jouben-Steele, L., Kremen, T.J., Liau, L.M., Vinters, H.V., Cloughesy, T.F., Mischel, P.S.: Active matrix metalloproteinase 9 expression is associated with primary glioblastoma subtype. Clin. Cancer Res. **8**(9), 2894–2901 (2002)
13. Claes, A., Idema, A.J., Wesseling, P.: Diffuse glioma growth: a guerilla war. Acta Neuropathol. **114**(5), 443–458 (2007)
14. Crute, B.E., Seefeld, K., Gamble, J., Kemp, B.E., Witters, L.A.: Functional domains of the alpha1 catalytic subunit of the amp-activated protein kinase. J. Biol. Chem. **273**(52), 35347–35354 (1998)
15. Dallon, J.C., Othmer, H.G.: How cellular movement determines the collective force generated by the dictyostelium discoideum slug. J. Theor. Biol. **231**, 203–222 (2004)
16. Davis, F.G., McCarthy, B.J.: Current epidemiological trends and surveillance issues in brain tumors. Exp. Rev. Anticancer Ther. **1**(3), 395–401 (2001)
17. Deisboeck, T.S., Berens, M.E., Kansal, A.R., Torquato, S., Stemmer-Rachamimov, A.O., Chiocca, E.A.: Pattern of self-organization in tumour systems: complex growth dynamics in a novel brain tumour spheroid model. Cell Prolif. **34**, 115–134 (2001)
18. Demuth, T., Berens, M.E.: Molecular mechanisms of glioma cell migration and invasion. J. Neurooncol. **70**(2), 217–228 (2004)
19. Demuth, T., Hopf, N.J., Kempski, O., Sauner, D., Herr, M., Giese, A., Perneczky, A.: Migratory activity of human glioma cell lines in vitro assessed by continuous single cell observation. Clin. Exp. Metastasis **18**(7), 589–597 (2000)
20. Esquela-Kerscher, A., Slack, F.J.: Oncomirs - micrornas with a role in cancer. Nat. Rev. Cancer **6**(4), 259–269 (2006)
21. Gabriely, G., Wurdinger, T., Kesari, S., Esau, C.C., Burchard, J., Linsley, P.S., Krichevsky, A.M.: Microrna 21 promotes glioma invasion by targeting matrix metalloproteinase regulators. Mol. Cell Biol. **28**(17), 5369–5380 (2008)
22. Gal, H., Pandi, G., Kanner, A.A., Ram, Z., Lithwick-Yanai, G., Amariglio, N., Rechavi, G., Givol, D.: Mir-451 and imatinib mesylate inhibit tumor growth of glioblastoma stem cells. Biochem. Biophys. Res. Commun. **376**, 86–90 (2008)

23. Gantier, M.P., McCoy, C.E., Rusinova, I., Saulep, D., Wang, D., Xu, D., Irving, A.T., Behlke, M.A., Hertzog, P.J., Mackay, F., Williams, B.R.: Analysis of microrna turnover in mammalian cells following dicer1 ablation. Nucleic Acids Res. **39**(13), 5692–5703 (2011)
24. Gatenby, R.A., Gillies, R.J.: Why do cancers have high aerobic glycolysis? Nat. Rev. Cancer **4**(11), 891–899 (2004)
25. Godlewski, J., Bronisz, A., Nowicki, M.O., Chiocca, E.A., Lawler, S.: microRNA-451: a conditional switch controlling glioma cell proliferation and migration. Cell Cycle **9**(14), 2742–2748 (2010)
26. Godlewski, J., Newton, H.B., Chiocca, E.A., Lawler, S.E.: MicroRNAs and glioblastoma; the stem cell connection. Cell Death Differ. **17**(2), 221–228 (2010)
27. Godlewski, J., Nowicki, M.O., Bronisz, A., Palatini, G.N.J., Lay, M.D., Brocklyn, J.V., Ostrowski, M.C., Chiocca, E.A., Lawler, S.E.: MircroRNA-451 regulates LKB1/AMPK signaling and allows adaptation to metabolic stress in glioma cells. Mol. Cell **37**, 620–632 (2010)
28. Godlewski, J., Nowicki, M.O., Bronisz, A., Williams, S., Otsuki, A., Nuovo, G., Raychaudhury, A., Newton, H.B., Chiocca, E.A., Lawler, S.: Targeting of the Bmi-1 oncogene/stem cell renewal factor by microRNA-128 inhibits glioma proliferation and self-renewal. Cancer Res. **68**(22), 9125–9130 (2008)
29. Goldman, S., Levivier, M., Pirotte, B., Brucher, J.M., Wikler, D., Damhaut, P., Stanus, E., Brotchi, J., Hildebrand, J.: Regional glucose metabolism and histopathology of gliomas. a study based on positron emission tomography-guided stereotactic biopsy. Cancer **78**(5), 1098–1106 (1996)
30. Hardie, D.G.: AMP-activated/SNF1 protein kinases: conserved guardians of cellular energy. Nat. Rev. Mol. Cell Biol. **8**(10), 774–785 (2007)
31. Hardie, D.G., Salt, I.P., Hawley, S.A., Davies, S.P.: AMP-activated protein kinase : an ultrasensitive system for monitoring cellular energy charge. Biochem. J. **338**, 717–722 (1999)
32. Harpold, H.L., Alvord, Jr., E.C., Swanson, K.R.: The evolution of mathematical modeling of glioma proliferation and invasion. J. Neuropathol. Exp. Neurol. **66**(1), 1–9 (2007)
33. Hegedus, B., Zach, J., Czirok, A., Lovey, J., Vicsek, T.: Irradiation and taxol treatment result in non-monotonous, dose-dependent changes in the motility of glioblastoma cells. J. Neurooncol. **67**(1–2), 147–157 (2004)
34. Hong, B., Wiese, B., Bremer, M., Heissler, H.E., Heidenreich, F., Krauss, J.K., Nakamura, M.: Multiple microsurgical resections for repeated recurrence of glioblastoma multiforme. Am. J. Clin. Oncol. **36**(3), 261–268. doi:10.1097/COC.0b013e3182467bb1 (2013)
35. Jaalinoja, J., Herva, R., Korpela, M., Hoyhtya, M., Turpeenniemi-Hujanen, T.: Matrix metalloproteinase 2 (MMP-2) immunoreactive protein is associated with poor grade and survival in brain neoplasms. J. Neurooncol. **46**(1), 81–90 (2000)
36. Jacobs, V.L., Valdes, P.A., Hickey, W.F., De Leo, J.A.: Current review of in vivo GBM rodent models: emphasis on the CNS-1 tumour model. ASN NEURO **3**(3), e00063 (2011)
37. Jain, R.K.: Transport of molecules in the tumor interstitium: a review. Cancer Res. **47**(12), 3039–3051 (1987)
38. Jones, R.G., Thompson, C.B.: Tumor suppressors and cell metabolism: a recipe for cancer growth. Genes Dev. **23**(5), 537–548 (2009)
39. Kaufman, L.J., Brangwynne, C.P., Kasza, K.E., Filippidi, E., Gordon, V.D., Deisboeck, T.S., Weitz, D.A.: Glioma expansion in collagen I matrices: analyzing collagen concentration-dependent growth and motility patterns. Biophys. J. BioFAST **89**, 635–650 (2005)
40. Khanin, R., Vinciotti, V.: Computational modeling of post-transcriptional gene regulation by micrornas. J. Comput. Biol. **15**(3), 305–316 (2008)
41. Kim, H.D., Guo, T.W., Wu, A.P., Wells, A., Gertler, F.B., Lauffenburger, D.A.: Epidermal growth factor-induced enhancement of glioblastoma cell migration in 3D arises from an intrinsic increase in speed but an extrinsic matrix and proteolysis-dependent increase in persistence. Mol. Biol. Cell **19**, 4249–4259 (2008)
42. Kim, J.W., Dang, C.V.: Cancer's molecular sweet tooth and the Warburg effect. Cancer Res. **66**(18), 8927–8930 (2006)

43. Kim, Y.: Regulation of cell proliferation and migration in glioblastoma: new therapeutic approach. Front. Mol. Cell. Oncol. **3**, 53 (2013)
44. Kim, Y., Lawler, S., Nowicki, M.O., Chiocca, E.A., Friedman, A.: A mathematical model of brain tumor : pattern formation of glioma cells outside the tumor spheroid core. J. Theor. Biol. **260**, 359–371 (2009)
45. Kim, Y., Roh, S.: A hybrid model for cell proliferation and migration in glioblastoma. Discr. Contin. Dyn. Syst. B **18**(4), 969–1015 (2013)
46. Kim, Y., Roh, S., Lawler, S., Friedman, A.: miR451 and AMPK/MARK mutual antagonism in glioma cells migration and proliferation. PLoS One **6**(12), e28293 (2011)
47. Kim, Y., Stolarska, M., Othmer, H.G.: A hybrid model for tumor spheroid growth in vitro I: theoretical development and early results. Math. Models Methods Appl. Sci. **17**, 1773–1798 (2007)
48. Kim, Y., Stolarska, M., Othmer, H.G.: The role of the microenvironment in tumor growth and invasion. Prog. Biophys. Mol. Biol. **106**, 353–379 (2011)
49. Kudlow, J.E., Cheung, C.Y., Bjorge, J.D.: Epidermal growth factor stimulates the synthesis of its own receptor in a human breast cancer cell line. J. Biol. Chem. **261**(9), 4134–4138 (1986)
50. Lamszus, K., Schmidt, N.O., Jin, L., Laterra, J., Zagzag, D., Way, D., Witte, M., Weinand, M., Goldberg, I.D., Westphal, M., Rosen, E.M.: Scatter factor promotes motility of human glioma and neuromicrovascular endothelial cells. Int. J. Cancer **75**(1), 19–28 (1998)
51. Lawler, S., Chiocca, E.A.: Emerging functions of micrornas in glioblastoma. J. Neurooncol. **92**(3), 297–306 (2009)
52. LeBrun, D.G., Li, M.: Micrornas in glioblastoma multiforme: profiling studies and therapeutic impacts. Mol. Cell. Pharmacol. **3**(3), 93–105 (2011)
53. Li, C.K.: The glucose distribution in 9L rat brain multicell tumor spheroids and its effect on cell necrosis. Cancer **50**(10), 2066–2073 (1982)
54. Li, H.Y., Zhang, Y., Cai, J.H., Bian, H.L.: MicroRNA-451 inhibits growth of human colorectal carcinoma cells via downregulation of PI3K/AKT pathway. Asian Pac. J. Cancer Prev. **14**(6), 3631–3634 (2013)
55. Luca, A.D., Arena, N., Sena, L.M., Medico, E.: Met overexpression confers HGF-dependent invasive phenotype to human thyroid carcinoma cells in vitro. J. Cell. Physiol. **180**(3), 365–371 (1999)
56. Lund-Johansen, M., Bjerkvig, R., Humphrey, P.A., Bigner, S.H., Bigner, D.D., Laerum, O.D.: Effect of epidermal growth factor on glioma cell growth, migration, and invasion in vitro. Cancer Res. **50**(18), 6039–6044 (1990)
57. Marino, S., Hogue, I.B., Ray, C.J., Kirschner, D.E.: A methodology for performing global uncertainty and sensitivity analysis in systems biology. J. Theor. Biol. **254**(1), 178–196 (2008)
58. Mercapide, .J., Cicco, R., Castresana, J.S., Klein-Szanto, A.J.: Stromelysin-1/matrix metalloproteinase-3 (MMP-3) expression accounts for invasive properties of human astrocytoma cell lines. Int. J. Cancer **106**(5), 676–682 (2003)
59. Moller, H.G., Rasmussen, A.P., Andersen, H.H., Johnsen, K.B., Henriksen, M., Duroux, M.: A systematic review of microrna in glioblastoma multiforme: micro-modulators in the mesenchymal mode of migration and invasion. Mol. Neurobiol. **47**(1), 131–44 (2013)
60. Nan, Y., Han, L., Zhang, A., Wang, G., Jia, Z., Yang, Y., Yue, X., Pu, P., Zhong, Y., Kang, C.: Mirna-451 plays a role as tumor suppressor in human glioma cells. Brain Res. **1359**, 14–21 (2010)
61. Platten, M., Wick, W., Weller, M.: Malignant glioma biology: role for TGF-beta in growth, motility, angiogenesis, and immune escape. Microsc. Res. Tech. **52**(4), 401–410 (2001)
62. Ragan, C., Zuker amd, M., Ragan, M.A.: Quantitative prediction of mirna-mrna interaction based on equilibrium concentrations. PLoS Comput. Biol. **7**(2), e1001090. doi:10.1371/journal.pcbi.1001090 (2011)
63. Rejniak, K.A., Anderson, A.R.A.: Hybrid models of tumor growth. WIRES Syst. Biol. Med. **3**, 115–125 (2011)

64. Rong, Z., Cheema, U., Vadgama, P.: Needle enzyme electrode based glucose diffusive transport measurement in a collagen gel and validation of a simulation model. Analyst **131**(7), 816–821 (2006)
65. Rozental, J.M., Levine, R.L., Nickles, R.J.: Changes in glucose uptake by malignant gliomas: preliminary study of prognostic significance. J. Neurooncol. **10**(1), 75–83 (1991)
66. Saffarian, S., Collier, I.E., Marmer, B.L., Elson, E.L., Goldberg, G.: Interstitial collagenase is a brownian ratchet driven by proteolysis of collagen. Science **306**(5693), 108–111 (2004)
67. Sander, L.M., Deisboeck, T.S.: Growth patterns of microscopic brain tumors. Phys. Rev. E **66**, 051901 (2002)
68. Schattler, H., Kim, Y., Ledzewicz, U., de los Reyes V.A.A., Jung, E.: On the control of cell migration and proliferation in glioblastoma. In: Proceeding of the IEEE Conference on Decision and Control, 978-1-4673-5716-6, vol. 13, pp. 1810–1815 (2013)
69. Scianna, M., Merks, R.M., Preziosi, L., Medico, E.: Individual cell-based models of cell scatter of ARO and MLP-29 cells in response to hepatocyte growth factor. J. Theor. Biol. **260**(1), 151–60 (2009)
70. Sen, S., Dong, M., Kumar, S.: Isoform-specific contributions of a-actinin to glioma cell mechanobiology. PLoS One **4**(12), e8427 (2009)
71. Sherratt, J.A., Murray, J.D.: Models of epidermal wound healing. Proc. R. Soc. Lond. B **241**, 29–36 (1990)
72. Silbergeld, D.L., Chicoine, M.R.: Isolation and characterization of human malignant glioma cells from histologically normal brain. J. Neurosurg. **86**(3), 525–531 (1997)
73. Singh, P.K., Mehla, K., Hollingsworth, M.A., Johnson, K.R.: Regulation of aerobic glycolysis by micrornas in cancer. Mol. Cell Pharmacol. **3**(3), 125–134 (2011)
74. Stein, A.M., Demuth, T., Mobley, D., Berens, M., Sander, L.M.: A mathematical model of glioblastoma tumor spheroid invasion in a three-dimensional in vitro experiment. Biophys. J. **92**(1), 356–365 (2007)
75. Stella, M.C., Comoglio, P.M.: HGF: a multifunctional growth factor controlling cell scattering. Int. J. Biochem. Cell Biol. **31**(12), 1357–1362 (1999)
76. Stokes, P.M., Lauffenburger, D.A.: Analysis of the roles of microvessel endothelial cell random motility and chemotaxis in angiogenesis. J. Theor. Biol. **152**, 377–403 (1991)
77. Stylli, S.S., Kaye, A.H., MacGregor, L., Howes, M., Rajendra, P.: Photodynamic therapy of high grade glioma - long term survival. J. Clin. Neurosci. **12**(4), 389–398 (2005)
78. Swanson, K.R., Alvord, E.C., Murray, J.D.: Virtual resection of gliomas: effect of extent of resection on recurrence. Math. Comput. Model. **37**, 1177–1190 (2003)
79. Tamagnone, L., Comoglio, P.M.: Control of invasive growth by hepatocyte growth factor (HGF) and related scatter factors. Cytokine Growth Factor Rev. **8**(2), 129–142 (1997)
80. Thorne, R.G., Hrabetova, S., Nicholson, C.: Diffusion of epidermal growth factor in rat brain extracellular space measured by integrative optical imaging. J. Neurophysiol. **92**(6), 3471–3481 (2004)
81. Trusolino, L., Comoglio, P.M.: Scatter-factor and semaphorin receptors: cell signalling for invasive growth. Nat. Rev. Cancer **2**(4), 289–300 (2002)
82. Valle-Casuso, J.C., Gonzalez-Sanchez, A., Medina, J.M., Tabernero, A.: HIF-1 and c-Src mediate increased glucose uptake induced by endothelin-1 and connexin43 in astrocytes. PLoS One **7**(2), e32448 (2012)
83. Vander Heiden, M.G., Cantley, L.C., Thompson, C.B.: Understanding the warburg effect: the metabolic requirements of cell proliferation. Science **324**(5930), 1029–1033 (2009)
84. Warburg, O.: On the origin of cancer cells. Science **123**(3191), 309–314 (1956)
85. Watters, J.J., Schartner, J.M., Badie, B.: Microglia function in brain tumors. J. Neurosci. Res. **81**(3), 447–455 (2005)
86. Xu, R.H., Pelicano, H., Zhou, Y., Carew, J.S., Feng, L., Bhalla, K.N., Keating, M.J., Huang, P.: Inhibition of glycolysis in cancer cells: a novel strategy to overcome drug resistance associated with mitochondrial respiratory defect and hypoxia. Cancer Res. **65**(2), 613–621 (2005)
87. Yao, G., Lee, T.J., Mori, S., Nevins, J.R., You, L.: A bistable Rb-E2F switch underlies the restriction point. Nat. Cell Biol. **10**(4), 476–482 (2008)

88. Young, N., Brocklyn, J.R.: Roles of sphingosine-1-phosphate (S1P) receptors in malignant behavior of glioma cells. differential effects of S1P2 on cell migration and invasiveness. Exp. Cell Res. **313**(8), 1615–1627 (2007)
89. Zhang, B.B., Zhou, G., Li, C.: AMPK: an emerging drug target for diabetes and the metabolic syndrome. Cell Metab. **9**(5), 407–416 (2009)
90. Zhou, X., Ren, Y., Moore, L., Mei, M., You, Y., Xu, P., Wang, B., Wang, G., Jia, Z., Pu, P., Zhang, W., Kang, C.: Downregulation of miR-21 inhibits EGFR pathway and suppresses the growth of human glioblastoma cells independent of PTEN status. Lab. Invest. **90**(2), 144–155 (2010)
91. Zhou, Y., Larsen, P.H., Hao, C., Yong, V.W.: CXCR4 is a major chemokine receptor on glioma cells and mediates their survival. J. Biol. Chem. **277**(51), 49481–49487 (2002)

An Optimal Control Approach to Cancer Chemotherapy with Tumor–Immune System Interactions

Urszula Ledzewicz and Heinz Schättler

Abstract We review some results about the structure of optimal chemotherapy protocols in the presence of tumor immune system interactions that can be derived from population-based mathematical models using optimal control.

1 Introduction

The question how chemotherapeutic agents should be administered to achieve optimal effects is a difficult one and conclusive answers have not yet been given. It is a common medical approach to start treatment with maximum tolerated dose (MTD) strategies: give as much of a cytotoxic drug as is safely possible and give it right away. The underlying rationale is that cancer is often only diagnosed in the later stages of the disease and thus immediate and significant action is required. Mathematically, the scheduling of therapeutic agents over time in order to optimize some objective related to tumor burden (e.g., tumor volume) and quality of life of the patient (e.g., some measure of the toxic side effects of treatment) while the underlying system follows some dynamics (in this case determined by the processes of tumor development and treatment interactions) is an optimal control problem. Within such a framework an MTD strategy can be shown to be the mathematically optimal solution for models that only consider homogeneous tumor populations of chemotherapeutically sensitive cells (e.g., see [10, 30, 31, 35, 51, 53, 54, 56]). However, as soon as heterogeneous structures are considered—tumor populations with varying sensitivities or that may also include drug resistant populations—then this is not necessarily the case. For example,

U. Ledzewicz (✉)
Department of Mathematics and Statistics, Southern Illinois University, Edwardsville, IL 62026, USA
e-mail: uledzew@siue.edu

H. Schättler
Department of Electrical and Systems Engineering, Washington University, St. Louis, MO 63130, USA
e-mail: hms@wustl.edu

A. Eladdadi et al. (eds.), *Mathematical Models of Tumor-Immune System Dynamics*, Springer Proceedings in Mathematics & Statistics 107,
DOI 10.1007/978-1-4939-1793-8_7

as resistance builds up, protocols that administer drugs at lower than maximum dose rates become candidates for optimality. Intuitively, as chemotherapy destroys the sensitive population, over time the proportion of resistant cells becomes dominant and then the harm to the healthy cells done by full dose chemotherapy outweighs the increasingly diminishing returns that can be achieved with chemotherapy. In such a case, it will simply be better (in terms of the overall quality of life of the patient measured by a quantitative objective) to proceed with less toxic lower dose rates [24,33]. Chemotherapy at significantly reduced dose rates also has attracted medical research interest in the past 10 years because it has important secondary effects on the tumor microenvironment. In several medical papers, both antiangiogenic and immune stimulatory effects of low dose chemotherapy have been recorded [15, 22, 41, 43] having led to a reevaluation of an MTD thinking and the notion that "more is not necessarily better" [14, 15, 17, 42]. Alternative protocols that administer chemotherapy at reduced less toxic dose rates and basically without any prolonged interruptions have become an intense focus of medical research known as "metronomic dosing" (e.g., see [1,41] and the many references therein).

All this has led to a reexamination of the question how one can optimize the antitumor, antiangiogenic, and pro-immune effects of therapy by modulating dose and administration schedule. Rather than merely focussing on the cytotoxic effects of chemotherapy, a more holistic approach needs to be taken and its effects on the other components of the tumor microenvironment need to be considered. One major such component is the immune system and in this paper we consider the structure of optimal chemotherapy protocols when tumor immune system interactions are taken into account. The immune system's first response to its environment is on the basis of a discrimination between "own" and "foreign" objects [40] and while some tumor cells may simply be classified as "own" and thus tolerated, generally tumor cells also exhibit a large number of abnormalities (such as mutated proteins, under- or over-expressed normal proteins and many more) that lead to the appearance of specific antigens that will be classified as "foreign" and thus do trigger reactions by both the innate and adaptive immune system [19, 52]. The empirical hypothesis of *immunosurveillance*, i.e., that the immune system may act to eliminate or control tumors, is well established in the medical community.

The competitive interaction between tumor cells and the immune system is complex, to say the least, and still is the topic of vast current medical research. It involves an immense number of events with the kinetics of the interplay strongly nonlinear and characterized by multi-stability, i.e., persistence of both benign and malignant scenarios. The possible outcome of this interplay thus is not only constituted by either tumor suppression or tumor outbreak, but there exist lots of intermediate scenarios. Depending on the aim of a mathematical analysis, a more detailed and precise model need not necessarily be better since it may simply obscure, or even hide the main features.[1] Especially, if the aim is to study treatment protocols, and even more so if we are just interested in general structures rather than

[1]The short fragment "On Exactitude in Science" by Jorge Luis Borges is of interest here.

particular cases, then low-dimensional cell population-based mathematical models that try to capture the essence of the interactions in a few parameters are preferred. For this reason, here we use some versions of Stepanova's classical model [50] for tumor immune system interactions as the vehicle to describe the structure of optimal therapy protocols. This classical model does capture the main features that we want to discuss here (such as immunosurveillance and *tumor dormancy*) while being low-dimensional and minimally parameterized. This has the advantage of allowing us to easily visualize the associated geometric features (regions of attractions, stability boundaries, etc.) that are connected with the various stable behaviors.

Stepanova's model has been the source of various generalizations, most notably the paper [23] by Kuznetsov, Makalkin, Taylor and Perelson. In this paper, using a classical logistic model for cancer growth, the authors estimate the parameters based on in vivo data of B-lymphoma BCL_1 in the spleen of mice and analyze both local and global bifurcations. De Vladar and González [57] carry out a similar analysis replacing logistic growth on cancer cells with a Gompertzian model. In each case, the models exhibit both stable microscopic and macroscopic equilibria and a comprehensive analysis of the dynamic behavior of the underlying systems and its bifurcations is carried out in the respective papers. More recently, d'Onofrio generalized these structures in a unifying meta model [36, 37] that incorporates all these dynamical models and has similar qualitative features. In Stepanova's model the actions of the immune system are agglomerated into one numerical quantity termed the immunocompetent cell density. Different generalizations of Stepanova's underlying model, such as the one given in the paper by Kirschner and Panetta [20], in order to better model the complex interactions that make up the actions of the immune system, break up this quantity into T-cells, effector cells, killer cells, and more. This approach is also taken in the papers by de Pillis, Radunskaya, and Wiseman [44, 46, 47] who analyze the underlying problem from an optimal control perspective as it will be done here, albeit using a different type of objective. Structured population models are considered, for example, by Delitalia and Lorenzi in [8]. We refer the reader to the review article by Eftimie, Bramson, and Earn [9] for a more general discussion of other non-spatial mathematical models. Spatial methods on tumor immune interactions described by partial differential equations have been considered, for example, in the research of A. Friedman and coworkers in the context of macrophage activities [7] as well as for specific diseases (e.g., glioma [12]). Tumor growth under the influence of the full microenvironment is considered in papers by Friedman and Kim [11, 18]. Even more intricate mathematical models that try to capture the increasingly complex interactions both within the immune system itself and with the tumor are based on cellular automata such as in the work of Mallet, de Pillis and Radunskaya [34, 45]. Here our intention is to describe some of the fundamental aspects of tumor immune system interactions and their implications on the qualitative structure of optimal therapy protocols. For this purpose, Stepanova's low-dimensional model along with some minor variations such as done in the papers [23, 39, 57] appears adequate.

In Sect. 2 we briefly describe the underlying concepts from dynamical systems theory that allow a geometric formulation for the problem of treating cancer as

moving the state of the system from a malignant region of cancerous growth into a benign region of tumor dormancy or immunosurveillance. This transfer then is induced by the solution of an optimal control problem formulated in Sect. 3. Here the objective function is tailored to the underlying multi-stable structure of the system with tumor–immune interactions. As one particular scenario, in Sect. 4 we then develop further the problem of chemotherapy with a strongly targeted cytotoxic agent and a rudimentary immune boost. For such a model, optimal treatment protocols switch after a brief administration of maximum dose chemotherapy to giving significantly lower dose rates. In the medical literature such protocols have been tested and sometimes are referred to as *"chemo-switch" protocols* [2, 43]. Clearly, in these solutions the tumor microenvironment plays a major role: the initial chemotherapy is designed to move the state of the dynamics into a region where the immune system is potent enough to control (possibly not to eliminate or eradicate) the cancer and then much lower doses of chemotherapy are sufficient. In fact—but such a structure is not included in the model—higher doses may be harmful in that they might adversely effect the immune system which otherwise would have come to the assistance in combating the tumor.

2 Multistability and Immune Surveillance

In her 1980 paper [50], Stepanova formulated a by now classical mathematical model of two ordinary differential equations that aggregate the interactions between tumor cell growth and the activities of the immune system during the development of cancer. Precisely because of its simplicity—a few parameters incorporate many medically important features—the underlying equations have been widely accepted as a basic model. There exist numerous extensions and generalizations of this model, e.g., [20, 23, 36, 37, 57], that all share in similar qualitative findings: while the immune system can be effective in the control of small cancer volumes, for large volumes the cancer dynamics suppresses the immune dynamics and the two systems effectively become separated [57, appendix B]. In the first case, so-called *immunosurveillance*, what medically would be considered cancer never develops; in the latter case, therapeutic action is needed to cure the disease. However, as will be seen, the persistence of both benign and malignant scenarios significantly affects the structure of optimal chemotherapy protocols.

We briefly recall Stepanova's model. Let x denote the *tumor volume* with a fixed finite carrying capacity $x_\infty < \infty$ and let y be a nondimensional, order of magnitude variable related to the activities of various types of T-cells activated during the immune reaction referred to as the *immunocompetent cell density*. While Stepanova used an exponential model for the growth of the tumor, here we consider an arbitrary growth rate F depending on the tumor volume x, $F(x)$, only assuming that F is a positive, nondecreasing, twice continuously differentiable function defined on an interval $(0, x_\infty)$ that satisfies $F(x_\infty) = 0$. We shall generally use Gompertzian,

logistic or generalized logistic growth models in our simulations. The dynamical equations of the model are given by

$$\dot{x} = \mu_C x F(x) - \gamma x y, \tag{1}$$

$$\dot{y} = \mu_I \left(x - \beta x^2\right) y - \delta y + \alpha, \tag{2}$$

with all Greek letters denoting constant coefficients. Equation (2) summarizes the main features of the immune system's reaction to cancer. Several organs such as the spleen, thymus, lymph nodes, and bone marrow each contribute to the development of immune cells in the body and the parameter α models a combined rate of influx of T-cells generated through these primary organs; δ is simply the rate of natural death of the T-cells. The first term in this equation models the proliferation of lymphocytes. For small tumors, it is stimulated by the tumor antigen which is assumed to be proportional to the tumor volume x. It is argued in [50] that large tumors suppress the activity of the immune system. The reasons lie in an inadequate stimulation of the immune forces as well as a general suppression of immune lymphocytes by the tumor (see [50] and the references therein). This feature is expressed in the model through the inclusion of the term $-\beta x^2$. Thus $1/\beta$ corresponds to a threshold beyond which the immunological system becomes depressed by the growing tumor. The coefficients μ_I and β are used to calibrate these interactions and in the product with y collectively describe a state-dependent influence of the cancer cells on the stimulation of the immune system. The first equation, (1), models tumor growth. The coefficient γ denotes the rate at which cancer cells are eliminated through the activity of T-cells and the term $\gamma x y$ thus models the beneficial effect of the immune reaction on the cancer volume. Lastly, μ_C simply is a tumor growth coefficient. This parameter could have been subsumed in the functional form F, but we prefer to leave the definition of F to account only for the qualitatively different structures that specify various growth models for the cancer cells. In Stepanova's original formulation this term F is simply given by $F_E(x) \equiv 1$, i.e., exponential growth of the cancer cells was considered, but here we are interested in models with finite carrying capacities and use the Gompertzian growth model $F_G(x) = -\ln(x/x_\infty)$ or logistic and generalized logistic models of the form $F_L(x) = 1 - (x/x_\infty)^\nu$, $\nu > 0$.

In Table 1 we summarize the numerical values that were used for the computations and illustrations shown in this chapter. They almost exclusively are taken from the paper [23] by Kuznetsov, Makalkin, Taylor, and Perelson who estimate these parameters based on in vivo experimental data for B-lymphoma BCL_1 in the spleen of mice. In that paper, a classical logistic term is used for cancer growth and we adjusted the growth rates to account for Gompertzian growth using linear data fitting [28]. Also, the functional form $\left(x - \beta x^2\right) y$ used in Stepanova's model in Eq. (2) is a quadratic expansion of the term used in [23]. Following [23], x is given in multiples of 10^6 cells and y is a dimensionless quantity that describes the immuno-competent cell density on an order of magnitude basis relative to base

value 1. The time scale is taken relative to the tumor cell cycle in mice and and is in terms of 0.11 days [23]. However, these values are only used for a numerical illustration of our analytical results.

Table 1 Variables and parameter values used in numerical computations

Symbol	Interpretation	Value	Dimension	Reference
x	Tumor volume		10^6 cells	[50]
x_0	Initial value for x	600	10^6 cells	
y	Immuno-competent cell density		Orders of magnitude Non-dimensional	[50]
y_0	Initial value for y	0.10	Non-dimensional	
α	Rate of influx	0.1181	Non-dimensional	[23]
β	Inverse threshold for tumor suppression	0.00264	Non-dimensional	[23]
γ	Interaction rate	1	10^7 cells/day	[23]
δ	Death rate	0.37451	Non-dimensional	[23]
μ_C	Tumor growth parameter	0.5618	10^7 cells/day	[28]
μ_I	Tumor stimulated proliferation rate	0.00484	Non-dimensional	[28]
x_∞	Fixed carrying capacity	780	10^6 cells	

2.1 Regions of Attraction and Stable Manifolds of Equilibria

We briefly review some fundamental concepts and results from dynamical systems theory that we shall be using. Given a general differential equation of the form $\dot{x} = f(x)$ with $f : G \to \mathbb{R}^n$ a continuously differentiable vector field defined on some open set $G \subset \mathbb{R}^n$, it follows from standard results on ordinary differential equations that the initial value problem with initial condition $x(0) = x_0 \in G$ has a unique solution $x = x(t; x_0)$ which is defined on a maximal open interval $I \subset \mathbb{R}$. The solution curves in the state space, $x(\cdot; x_0) : I \to G, t \mapsto x(t; x_0)$, are called the *trajectories* of the system and the totality of all solution curves for $x_0 \in G$ is called the *phase portrait* of the dynamical system. If $f(x_*) = 0$, then this solution curve is just the point $x(t; x_*) \equiv x_*$ defined for $I = \mathbb{R}$ and x_* is called an *equilibrium point*. In this case, the linear system $\dot{y} = Ay$ with $A = Df(x_*)$, the Jacobian matrix of f at x_*, is called the linearization around the equilibrium point. The eigenvalues of the matrix A are also called the eigenvalues of f at x_*. An equilibrium point x_* is said to be *hyperbolic* if none of its eigenvalues lies on the imaginary axis. Hyperbolic equilibria play an important role in the theory of dynamical systems since the local properties of the system near such a point are "stable" in the sense that they do not change if small changes in the dynamics (such as in values of parameters that define the vector field f) occur. For example, local stability properties can be determined

in terms of its eigenvalues: if all eigenvalues of $A = Df(x_*)$ have negative real part, then x_* is locally asymptotically stable while it is unstable if there exists an eigenvalue with positive real part.

Definition 1 (Region of Attraction). Let x_* be a locally asymptotically stable equilibrium point for $\dot{x} = f(x)$. Its region of attraction, $A(x_*)$, consists of all initial conditions x_0 for which the corresponding solution exists for all $t \geq 0$ and converges to x_* as $t \to \infty$,

$$A(x_*) = \left\{ x_0 \in G : x(t; x_0) \text{ exists for all } t > 0 \text{ and } \lim_{t \to \infty} x(t; x_0) = x_* \right\}.$$

It is not difficult to see that the region of attraction of a locally asymptotically stable equilibrium point is an open and connected subset of the state space. If the equilibrium point is unstable, then there still exist points on a lower dimensional manifold for which a similar convergence result holds true.

Definition 2 (Local Stable Manifold). Given a hyperbolic equilibrium point x_* and a sufficiently small neighborhood U of x_*, the local stable manifold of x_* in U is defined as the set of all initial conditions $x_0 \in U$ such that the corresponding solution $x(t; x_0)$ exists and lies in U for all $t > 0$ and converges to x_* as $t \to \infty$,

$$W^s_{loc}(x_*; U) = \left\{ x_0 \in U : x(t; x_0) \in U \text{ for all } t > 0 \text{ and } \lim_{t \to \infty} x(t; x_0) = x_* \right\}.$$

Theorem 1 ([13]). *Let x_* be a hyperbolic equilibrium point and let W denote the k-dimensional linear subspace of $\mathbb{R}^n$ generated by all eigenvectors and generalized eigenvectors of the matrix $Df(x_*)$ that correspond to eigenvalues with negative real parts. Then, for U sufficiently small, the local stable manifold of x_* in U is a k-dimensional embedded submanifold and its tangent space at x_* is given by W.*

The global stable manifold of x_* is then defined by propagating the solutions that lie in a local stable manifold backward in time. If we denote the flow of the differential equation by Φ_t, then we simply have that $\Phi_t(x_0) = x(t; x_0)$ for $t \in I$. Thus we get the following definition:

Definition 3 (Global Stable Manifold). Given a hyperbolic equilibrium point x_*, let $W^s_{loc}(x_*; U)$ denote the local stable manifold for a sufficiently small neighborhood U of x_*. The global stable manifold is then defined as

$$W^s(x_*) = \cup_{t \leq 0} \{ \Phi_t(x_0) : x_0 \in W^s_{loc}(x_*; U) \}.$$

Unfortunately, by propagating trajectories backward, nice geometric properties may be lost and global stable manifolds need no longer be embedded submanifolds, but are only what are called immersed submanifolds. For example, a dense line on a torus might arise.

Local and global unstable manifolds are defined by reversing the orientation of time.

2.2 Benign and Malignant Regions for Tumor–Immune System Interactions

We return to our discussion of the system (1)–(2). There always exists a *disease free equilibrium point* at $(x_f, y_f) = (0, \frac{\alpha}{\delta})$ which is locally asymptotically stable if $\mu_C F(0) < \frac{\alpha\gamma}{\delta}$ and unstable if $\mu_C F(0) > \frac{\alpha\gamma}{\delta}$. The latter case includes the Gompertzian model when $\lim_{x\to 0+} F(x) = +\infty$. Essentially, if the initial tumor growth rate $\mu_C F(0)$ is small enough, then the beneficial effects of the immune system are able to eliminate the cancerous growth near the tumor free equilibrium point in an extreme form of immunosurveillance. However, if there also exist equilibria with positive x-values (and this is the scenario if the disease free equilibrium point is unstable) then there is always the danger that, even if the disease free equilibrium is locally stable, that a strong enough perturbation (event) may dislocate the state out of the region of attraction of this equilibrium point. Note that the positive half-line $\{x = 0, y > 0\}$ is invariant and forms the stable manifold of the disease free equilibrium point if $\mu_C F(0) > \frac{\alpha\gamma}{\delta}$.

Typically there also exist equilibria with positive tumor volumes. Figure 1 shows the phase portrait of the system (1) and (2) for a Gompertzian growth rate and the parameters listed in Table 1. There is a locally asymptotically stable focus at $(x_b, y_b) = (72.961, 1.327)$ (marked by a green star), a saddle point at $(x_s, y_s) = (356.174, 0.439)$ (marked by a black star) and a second asymptotically stable node at $(x_m, y_m) = (737.278, 0.032)$ (marked by a red star). In the diagram we also marked the stable manifold of the saddle as the red curve and the unstable manifold of the saddle as the green curve. Both of these, since the dimension is 2, are differentiable curves. Indeed, these curves play the most important roles in the overall tumor–immune system dynamics: it is the stable manifold of the saddle that separates the benign from the malignant behavior and it is the unstable manifold of the saddle that for realistic initial conditions determines the steady-state behavior of the uncontrolled system. Similar geometric structure are also valid for higher dimensional systems which are called Morse-Smale systems [13].

Note that the tumor volume for the stable equilibrium point (x_m, y_m) is close to the carrying capacity and that it is by an order of magnitude larger than for the equilibrium point (x_b, y_b). For a typical set of parameter values, these values might be interpreted as a *microscopic* and a *macroscopic locally asymptotically stable equilibrium point* with the high value clearly indicating that the patient will succumb to the disease.

Definition 4 (Benign and Malignant Equilibria). We call a locally asymptotically stable equilibrium point (x_*, y_*) of the Eqs. (1) and (2) malignant if the corresponding tumor volume x_* is close to the carrying capacity of the system, benign if it is by an order of magnitude smaller. We call the region of attraction of a malignant, respectively benign equilibrium point the malignant, respectively benign region.

In case of a microscopic benign equilibrium, this region can be interpreted as the set of all states of the system where the immune system is able to control the cancer. This is one possible way of describing geometrically what medically has been called

immunosurveillance. On the other hand, the region of attraction of the macroscopic equilibrium point corresponds to conditions when the system has escaped from this immunosurveillance and the disease will become lethal. Obviously, the boundary between these two behaviors is the critical mathematical object to study and it is formed by the stable manifold of the saddle point. Reality is far more complicated than accounted for in this model and constantly random (and otherwise not modeled)

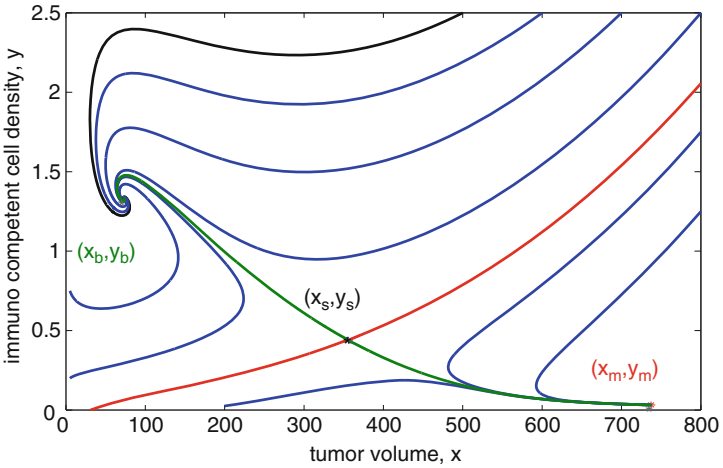

Fig. 1 Phaseportrait of the uncontrolled system (1) and (2) for a Gompertzian growth rate $F(x) = -\log(x/x_\infty)$ and the parameter values in Table 1. The *green star* marks the benign equilibrium point (x_b, y_b) and the *red star* marks the malignant equilibrium point (x_m, y_m). Their regions of attractions are separated by the stable manifold (shown as the *solid red curve*) of the saddle point (marked by the *black star*). The *solid green curve* is the unstable manifold of the saddle point which represents the steady-state (long term) behavior of the system for initial points in the benign, respectively malignant regions

events will take place that move the state of the system around in the state-space. Once a temporary disturbance has passed, the system will again settle down to follow the trajectories in the phase portrait. This may lead to the escape of the system from immunosurveillance, but it also opens up the possibility of moving the state of the system from a malignant position into the benign region through therapy. This naturally leads to an optimal control formulation that will be discussed in Sect. 3.

2.3 Benign and Malignant Regions for Generalized Logistic Growth

We still analyze the dynamics of the system for a generalized logistic growth rate

$$F(x) = 1 - \left(\frac{x}{x_\infty}\right)^\nu, \qquad \nu > 0,$$

and, especially, how the benign and malignant regions change with the parameter ν. This exponent largely determines the rate of tumor growth: for small values of ν, the term $(x/x_\infty)^\nu$ will be close to 1 and the model reflects a slowly growing tumor while tumor growth accelerates with increasing values of ν reaching unrestricted exponential growth in the limit $\nu \to \infty$. We only remark that if the function F is multiplied with a tumor growth parameter ξ, and if this coefficient is made to depend on the parameter ν in the order of $\xi = O(\frac{1}{\nu})$, then a Gompertzian model is obtained in the limit $\nu \to 0$. In this sense, the generalized logistic rate function F interpolates between Gompertzian growth as $\nu \to 0$ and exponential growth as $\nu \to \infty$ with the parameter ν determining the speed of tumor growth.

For a generalized logistic growth model, the disease free equilibrium point is locally asymptotically stable for $\mu_C < \frac{\alpha\gamma}{\delta}$ and unstable for $\mu_C > \frac{\alpha\gamma}{\delta}$. We shall see below that there are no other equilibria for ν close to 0 and in these cases the disease free equilibrium point is globally asymptotically stable, i.e., every solution converges to (x_f, y_f). This simply corresponds to a scenario when the immune system is able to control the cancerous growth. If $\mu_C > \frac{\alpha\gamma}{\delta}$, there will always exists at least one equilibrium point with positive x-value. Solving the equation $\dot{x} = 0$ for y and substituting into the relation $\dot{y} = 0$, these equilibria are determined by the solutions of the nonlinear equation

$$\mu_C \left(1 - \left(\frac{x}{x_\infty}\right)^\nu\right)\left(\mu_I\left(x - \beta x^2\right) - \delta\right) + \alpha\gamma = 0. \tag{3}$$

in the interval $(0, x_\infty)$. Note that zeros x_* can only lie where the quadratic polynomial

$$q(x) = \mu_I\left(x - \beta x^2\right) - \delta$$

is negative. Thus, if $\mu_I \geq 4\beta\delta$, then all zeros x_* lie in the intervals $(0, x_1)$ or (x_2, x_∞) with $x_1 < x_2$ the positive roots of q given by

$$x_1 = \frac{1}{2\beta}\left(1 - \sqrt{1 - 4\frac{\beta\delta}{\mu_I}}\right) \qquad \text{and} \qquad x_2 = \frac{1}{2\beta}\left(1 + \sqrt{1 - 4\frac{\beta\delta}{\mu_I}}\right);$$

for $\mu_I < 4\beta\delta$, the polynomial q is always negative and thus the location of the roots in $(0, x_\infty)$ is not restricted. But in any case, there will never be more than three roots.

Proposition 1. *For a generalized logistic growth rate $F(x) = 1-(x/x_\infty)^\nu$ and for all values of $\nu > 0$, there exist at most three equilibria for the dynamical system (1)–(2) that have positive x-values. If $\mu_C > \frac{\alpha\gamma}{\delta}$, then at least one such equilibrium point exists.*

Proof. Rewrite Eq. (3) in the following form defining the polynomial P_ν and the rational function R,

$$P_\nu(x) = 1 - \left(\frac{x}{x_\infty}\right)^\nu = \frac{\alpha\gamma}{\mu_C}\frac{1}{\mu_I\,(\beta x^2 - x) + \delta} = R(x).$$

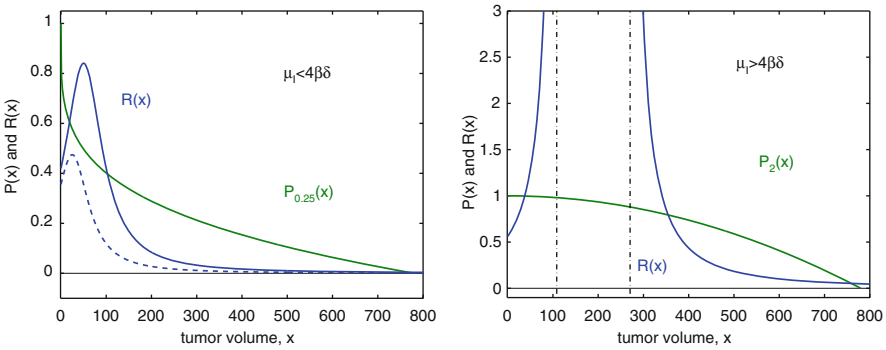

Fig. 2 Illustration of the possible number of equilibria for a generalized logistic growth rate $F(x) = 1 - (x/x_\infty)^\nu$ in the cases $\mu_I < 4\beta\delta$ (*left*) and $\mu_I > 4\beta\delta$ (*right*)

First consider the case when $\mu_I < 4\beta\delta$. Under this assumption, R is positive on $[0, \infty)$ with a global maximum for $\tilde{x} = \frac{1}{2\beta}$. Since $P_\nu(x) = 1 - (x/x_\infty)^\nu$ is a decreasing function, it follows that there exists at most one equilibrium point in the interval $[0, \frac{1}{2\beta}]$, possibly none. In the interval $[\frac{1}{2\beta}, \infty)$, the function R has a unique inflection point $\hat{x}$ and is strictly concave over the interval $[\frac{1}{2\beta}, \hat{x})$ and strictly convex over $[\hat{x}, \infty)$. Coupled with monotonicity and convexity properties of the function P, it follows that there can be no more than two additional zeroes on the interval $[\frac{1}{2\beta}, \infty)$ for at most three possible zeros. Note that it is possible that there are no solutions for certain parameter values, but there will always exist at least one positive solution if $R(0) = \frac{\alpha\gamma}{\delta\mu_C} < 1$ simply since, in this case, we have that $R(0) < 1 = P(0)$ while $R(x_\infty) > 0 = P_\nu(x_\infty)$.

In the case when $\mu_I > 4\beta\delta$, the function R has simple poles at x_1 and x_2 and is positive and strictly monotonically increasing over $(0, x_1)$ and positive and strictly monotonically decreasing over (x_2, x_∞). Again it follows from monotonicity properties that there can be at most one zero on $(0, x_1)$ and since $\lim_{x\to x_1-} R(x) = +\infty$, it is clear that there exists a solution in this interval if and only if $R(0) = \frac{\alpha\gamma}{\delta\mu_C} \le 1$. Similarly, R is monotonically decreasing and convex over the interval (x_2, x_∞). This allows for at most two more solutions. However, there may be none, especially if ν becomes very small. The underlying geometric properties are illustrated in Fig. 2. □

Figure 3 shows the values of the equilibria as a function of ν for the data from Table 1. We have $\mu_C > \frac{\alpha\gamma}{\delta}$ and thus the disease free equilibrium point $(x_f, y_f) = (0, \frac{\alpha}{\delta})$ is unstable. For small values of ν, $\nu < \nu_* = 0.40355$, there only exists one globally asymptotically stable equilibrium point with small x-value that corresponds to a microscopic benign state. These parameter values medically reflect a situation where tumor growth is slow and the reaction of the immune system is able to control the tumor. For $\nu_* = 0.40355$ the system undergoes a saddle-node bifurcation [13,21] and two additional equilibria, one stable (malignant), the other unstable, are created and the system becomes multi-stable for $\nu > \nu_*$ with three equilibria. The benign equilibrium point (x_b, y_b) is a *stable focus* whose values are represented by the green curves in Fig. 3 and the malignant equilibrium point (x_m, y_m) is a *stable node* whose values are represented by the red curves; the values for the *saddle*

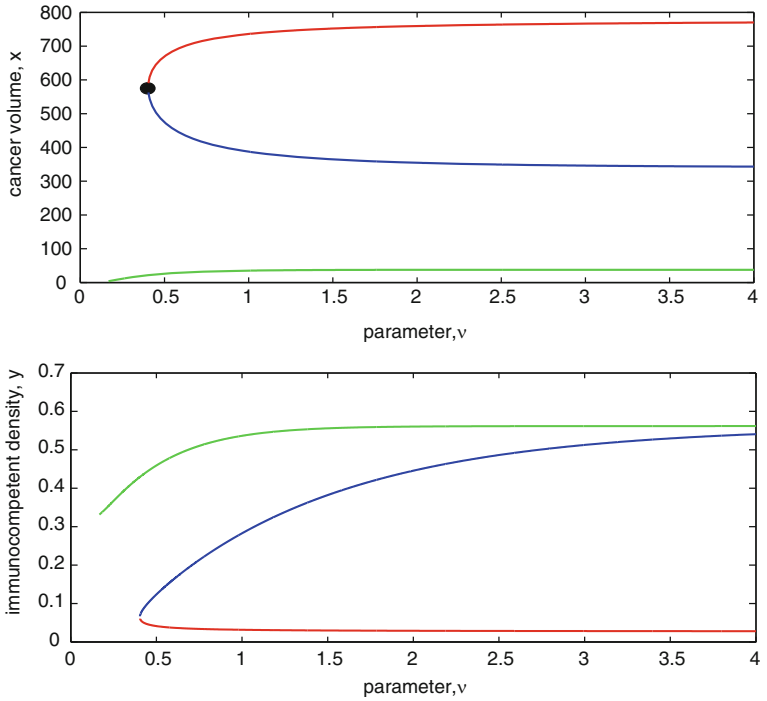

Fig. 3 Values of the non disease free equilibria for the system (1) and (2) with a generalized logistic growth rate $F(x) = 1-(x/x_\infty)^\nu$ as a function of ν. The values for the benign equilibrium point are shown as the *green curve*, for the saddle point as the *blue curve* and for the malignant equilibrium point as the *red curve* with the x-values given in the figure on the *top* and the y-values in the figure at the *bottom*. A saddle-node bifurcation occurs for $\nu_* = 0.40355\ldots$ and for $\nu < \nu_*$ there exists only a globally asymptotically stable benign equilibrium. This scenario geometrically represents the medical concept of immunosurveillance. (Reproduced with permission from [29], ©2012, AIMS)

point (x_s, y_s) are represented by the blue curves. For example, for classical logistic growth ($\nu = 1$) the numerical values are given by $(x_b, y_b) = (35.158, 0.537)$, $(x_s, y_s) = (387.527, 0.283)$ and $(x_m, y_m) = (736.102, 0.032)$.

Figure 4 illustrates the phaseportraits for the values $\nu = 0.75$ and 5. In each figure we have highlighted the stable manifold of the saddle (x_s, y_s), which forms the stability boundary for the benign and malignant regions, as a thick solid red line. These phase portraits show the decrease of the benign region at the expense of the malignant regions as the parameter ν increases reflecting the fact that the immune system becomes increasingly overwhelmed by a fast growing tumor. In the limit $\nu \to \infty$ the malignant region converges to the region of uncontrolled growth for the exponential model. This region differs little from the one for $\nu = 5$. The benign equilibrium point (x_b, y_b) converges to the disease free equilibrium point (x_f, y_f) as $\nu \to \infty$.

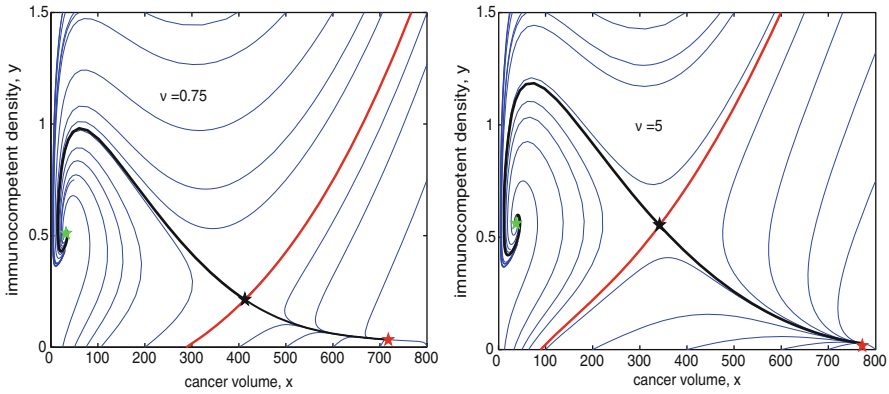

Fig. 4 Phase portraits of the system (1) and (2) with a generalized logistic growth rate $F(x) = 1 - (x/x_\infty)^\nu$ for $\nu = 0.75$ (*left*) and $\nu = 5$ and the parameter values from Table 1. As ν increases (a model for faster growing tumors), the malignant region increases in size

3 Therapy as an Optimal Control Problem: Transfer of the State from the Malignant into the Benign Region

We consider therapy with both a chemotherapeutic agent and some rudimentary immunotherapy in the form of an immune boost. Following the log-kill hypothesis, we assume that the elimination of tumor cells is proportional to the tumor volume x and the concentration of the chemotherapeutic agent which we denote by u. The effects of the chemotherapeutic agent on the immune system are complex and are more difficult to assert. It is natural to model the effects on existing cells of the immune system by a log-kill term in the equation for $\dot{y}$, but the negative side effects of chemotherapy also generally cause a lower influx of T-cells from the primary organs that are effected by chemotherapy, especially the

bone marrow. These can be modeled by reducing the factor α that models this influx. For simplicity, we do not include a pharmacokinetic model and identify dose rates with concentrations. (Generally, the changes in the optimal controls are of the same nature as, for example, discussed in the papers [25, 32, 38].) We also include a rudimentary immunotherapy in the form of an immune boost which is added as a positive term to Eq. (2). Overall, the controlled equations with treatment take the form

$$\dot{x} = \mu_C x F(x) - \gamma x y - \kappa x u, \tag{4}$$

$$\dot{y} = \mu_I \left(x - \beta x^2\right) y - \delta y - \eta y u + \alpha \left(1 - \xi u\right) + \rho y v. \tag{5}$$

Admissible controls are Lebesgue measurable functions u and v which take values in the interval $[0, 1]$. Since no pharmacokinetic model is included, without loss of generality we normalize the maximum values for the controls to 1 and subsume the maximum dose rates/concentrations in the coefficients for the pharmacodynamic model (κ, ξ, η and ρ). As before, all Greek letters denote constant positive coefficients and in addition we have that $\xi < 1$. The state space for the problem is given by $\mathbb{M} = \{(x, y) : 0 < x < x_\infty, 0 < y\}$ and we assume that initial conditions lie in $\mathbb{M}$. We also restrict the tumor growth rate F to Gompertzian, logistic or generalized logistic models. For each of these the carrying capacity is finite and we have that $F(x_\infty) = 0$.

Proposition 2. *The region $\mathbb{P}$ is positively invariant for the control system, i.e., given arbitrary admissible controls $u : [0, T] \to [0, 1]$ and $v : [0, T] \to [0, 1]$ defined over an interval $[0, T]$, $T \leq \infty$, the solution to the dynamics (4) and (5) exists on $[0, T]$ and the corresponding trajectory lies in $\mathbb{M}$.*

Proof. Since $\dot{y}_{|y=0} = \alpha \left(1 - \xi u\right) > \alpha \left(1 - \xi\right) > 0$, it follows that the y-components of the solution is always positive. Furthermore, for any control u, $x \equiv 0$ is an equilibrium solution to Eq. (4) and we also have that $\dot{x}_{|x=x_\infty} < 0$. Hence the x-component of the solution cannot leave the finite open interval $(0, x_\infty)$. It follows that the right hand side of the dynamics is linearly bounded and, by a standard argument of ODEs, this implies that solutions exist on all of $[0, T]$. □

The practical aim of therapy thus becomes to move an initial state (x_0, y_0) of the system that lies in the malignant region of the uncontrolled system into the region of attraction of the stable, benign equilibrium point while keeping side effects tolerable. This can be formulated as the following optimal control problem:

[CI] for a free terminal time T, minimize the objective

$$J = Ax(T) - By(T) + \int_0^T \left(Cu(t) + Dv(t) + S\right) dt, \tag{6}$$

over all Lebesgue measurable functions $u : [0, T] \to [0, 1]$ and $v : [0, T] \to [0, 1]$ subject to the dynamics (4) and (5) and initial conditions $x(0) = x_0$ and $y(0) = y_0$.

The objective function consists of three separate components: (1) the penalty term $Ax(T) - By(T)$ at the final time is designed to induce the state of the system to move from the malignant into the benign region, (2) the integrals $\int_0^T u(t)dt$ and $\int_0^T v(t)dt$ measure the total amounts of drugs given, and (3) the penalty term ST on the final time is included to make the mathematical problem well-posed. All coefficients are positive. The choice of the weights aims at striking a balance between the benefit at the terminal time T, $Ax(T) - By(T)$, and the overall side effects measured by the total amount of drugs given, while it guarantees the existence of an optimal solution by also penalizing the free terminal time T. We emphasize that the coefficients in the objective (6) are variables of choice and should be fine tuned to calibrate the system's optimal response. We discuss the rationale behind each term.

(1) The main feature here is to formulate the objective (6) in such a way that minimization induces a transfer of the system from the malignant into the benign region of the state space. For this, it may no longer be adequate to just minimize the tumor volume since, as can be seen in the phaseportraits, small tumor volumes are possible that lie in the malignant region if the immune system is depressed. Rather, the geometric shape of the separatrix matters. Ideally, if a functional description of this manifold could be given, one would minimize or maximize the level sets of this function to achieve a transfer into the benign region. But these are generally highly transcendental equations that cannot be solved explicitly. On the other hand, local approximations for the separatrix at the saddle point are easily obtained. It follows from Theorem 1 that the stable eigenspace at the saddle is the tangent space to the separatrix. This tangent line is easily computed and its normal vector can serve as a reasonable direction in which we want the system to move. A second natural option is to take the direction of the (correctly oriented) unstable eigenvector at the saddle since this is the path which uncontrolled trajectories in the benign region will closely follow. It follows from the geometric properties of the system near the saddle that the coefficients A and B are positive in both cases. Minimizing this quantity thus creates the necessary incentive for the system to move into the benign region.

(2) The model does not include a separate compartment of healthy cells to describe the side effects of treatment. These are only measured indirectly through the total amounts of drugs administered. Following standard pharmacological practice, these are represented by the AUC (area under the curve) and we thus include the term $\int_0^T Cu(t) + Dv(t)dt$ in the objective as a so-called soft constraints. Clinical data as to the severity of the drugs should be reflected in the choices for C and D. Naturally, the specific type of tumor and stage of cancer will enter into the choice of these coefficients. In a more advanced stage, higher side effects will need to be tolerated and smaller values of C would be taken.

(3) The last term in the objective function, which can be written either under the integral or as a separate penalty term ST, is included to give a mathematically well-posed problem formulation. Indeed, the existence of the asymptotically stable, benign equilibrium point generates controlled trajectories that improve the value $Ax(T) - By(T)$ of the objective along the trivial controls $u = 0$ and $v = 0$. If no penalty is imposed on the terminal time, then this creates a "free pass" structure in which the value of the objective can be improved without incurring a cost. As a result of this feature, an optimal solution may not exist. Intuitively, the controls switch to $(u, v) = (0, 0)$ immediately as the separatrix is crossed and then take an increasingly longer time as they pass near the saddle point with the infimum arising in the limit $T \to \infty$. The infimum arises as the control switches to follow $u = 0$ when the controlled trajectory intersects the separatrix, then follows the separatrix for an infinite time to the saddle and then again leaves this saddle point along the unstable manifold, once more taking an infinite time. This indeed would be the "optimal" solution for this problem formulation, but it is not an admissible trajectory in our system. From a practical point of view, it clearly is undesirable for the system to move along the boundary between benign and malignant behaviors. In view of imprecise and mathematically unmodeled dynamics and other random perturbations, the addition of this term provides desired robustness and stability properties for the underlying real system. Thus it makes perfect sense, both mathematically and practically, to include a penalty term on the final time in the objective. This creates a well-posed mathematical problem for which the existence of solutions follows from standard theory.

3.1 Necessary Conditions for Optimality: Bang-Bang and Singular Controls

We write the state of the system as $z = (x, y)^T$ and express the dynamics in the vector field form

$$\dot{z} = f(z) + ug_1(z) + vg_2(z) \tag{7}$$

with drift vector field

$$f(z) = \begin{pmatrix} \mu_C x F(x) - \gamma xy \\ \mu_I \left(x - \beta x^2\right) y - \delta y + \alpha \end{pmatrix} \tag{8}$$

and control vector fields

$$g_1(z) = -\begin{pmatrix} \kappa x \\ \eta y + \alpha\xi \end{pmatrix} \qquad \text{and} \qquad g_2(z) = \begin{pmatrix} 0 \\ \rho y \end{pmatrix} \tag{9}$$

For a two-dimensional row-vector $\lambda = (\lambda_1, \lambda_2)$, we define the Hamiltonian

$$H = H(\lambda, x, y, u, v)$$

as

$$\begin{aligned} H = {} & Cu + Dv + S + \lambda_1 \left(\mu_C x F(x) - \gamma x y - \kappa x u\right) \\ & + \lambda_2 \left(\mu_I \left(x - \beta x^2\right) y - \delta y - \eta y u + \alpha \left(1 - \xi u\right) + \rho y v\right) \end{aligned} \tag{10}$$

or, equivalently, in terms of the drift and control vector fields as

$$H = S + \langle \lambda, f(z) \rangle + u \left(C + \langle \lambda, g_1(z) \rangle\right) + v \left(D + \langle \lambda, g_2(z) \rangle\right).$$

If (u_*, v_*) is an optimal control defined over an interval $[0, T]$ with corresponding trajectory $z_* = (x_*, y_*)^T$, then it follows from the Pontryagin maximum principle [48] (for some more recent references on the topic, see [5,6,49]) that there exists an absolutely continuous covector $\lambda = (\lambda_1, \lambda_2)$, $\lambda : [0, T] \to \left(\mathbb{R}^2\right)^*$, that satisfies the adjoint equations

$$\begin{aligned} \dot{\lambda}_1(t) &= -\frac{\partial H}{\partial x}(\lambda(t), x_*(t), y_*(t), u_*(t), v_*(t)) \\ &= -\lambda_1(t) \left\{\mu_C \left(x_*(t) F'(x_*(t)) + F(x_*(t))\right) - \gamma y_*(t) - \kappa u_*(t)\right\} \\ &\qquad -\lambda_2(t) \mu_I \left(1 - 2\beta x_*(t)\right) y_*(t) \end{aligned} \tag{11}$$

$$\begin{aligned} \dot{\lambda}_2(t) &= -\frac{\partial H}{\partial y}(\lambda(t), x_*(t), y_*(t), u_*(t), v_*(t)) \\ &= \lambda_1(t) \gamma x_*(t) - \lambda_2 \left\{\mu_I \left(x_*(t) - \beta x_*(t)^2\right) - \delta - \eta u_*(t) + \rho v_*(t)\right\} \end{aligned} \tag{12}$$

with terminal conditions $\lambda_1(T) = A$ and $\lambda_2(T) = -B$ such that for almost every time $t \in [0, T]$, the optimal controls $(u_*(t), v_*(t))$ minimize the Hamiltonian H along $(\lambda(t), x_*(t), y_*(t))$ over the control set $[0, 1] \times [0, 1]$ with the minimized Hamiltonian being constant and equal to 0,

$$H(\lambda(t), x_*(t), y_*(t), u_*(t), v_*(t)) \equiv 0.$$

Controlled trajectories $(z, (u, v))$ for which there exists a multiplier λ such that these conditions are satisfied are called *extremals* and the triple $(z, (u, v), \lambda))$ including the multiplier is called an *extremal lift*. Note that the adjoint equation is a homogeneous linear equation that can succinctly be written in the form

$$\dot{\lambda}(t) = -\lambda(t) \left(Df(z_*(t)) + u_*(t) Dg_1(z_*(t)) + v_*(t) Dg_2(z_*(t))\right). \tag{13}$$

The transversality condition on $\lambda(T)$ implies the following statement:

Corollary 1. *The multiplier λ is nontrivial, i.e., $\lambda(t) \neq 0$ for all $t \in [0, T]$.*

Since the Hamiltonian H is linear in the controls and the control set is a compact interval in $\mathbb{R}^2$, the minimization decouples and can be carried out separately. Defining the *switching functions* Φ_1 for u and Φ_2 for v as

$$\Phi_1(t) = C + \langle \lambda(t), g_1(z_*(t)) \rangle = C - \lambda_1(t)\kappa x_*(t) - \lambda_2(t)\,(\eta y_*(t) + \alpha\xi)\,, \tag{14}$$

and

$$\Phi_2(t) = D + \langle \lambda(t), g_2(z_*(t)) \rangle = D + \lambda_2(t)\rho y_*(t), \tag{15}$$

it follows that

$$u_*(t) = \begin{cases} 0 & \text{if} \quad \Phi_1(t) > 0, \\ 1 & \text{if} \quad \Phi_1(t) < 0, \end{cases} \qquad \text{and} \qquad v_*(t) = \begin{cases} 0 & \text{if} \quad \Phi_2(t) > 0, \\ 1 & \text{if} \quad \Phi_2(t) < 0. \end{cases} \tag{16}$$

A priori the control is not determined at times τ where the switching function vanishes, $\Phi_i(\tau) = 0$, with every value possible in principle. However, if the derivative of the switching function is nonzero, $\frac{d\Phi_i}{dt}(\tau) \neq 0$, then Φ_i changes sign at τ and the control is discontinuous with a switch between the boundary values of the control interval. Controls which only have switchings of this type are called *bang-bang* and we also refer to the constant controls given by 0 or 1 as bang controls. The other extreme arises if a switching function Φ_i vanishes identically over a nonempty open interval I. In this case also all its derivatives must vanish on I and differentiating the switching functions while enforcing the dynamics until the controls explicitly appear typically allows to compute controls u_* and v_* that generate such behavior. A different procedure is employed in [55]. If these controls take values in the control set, they are admissible and often become the prime candidates for optimality. Such controls are called *singular* for historical reasons which have to do with the fact that the matrix of the second derivatives of H with respect to the controls becomes singular, in fact, is identically zero in our case. Additional necessary conditions for optimality, the so-called generalized Legendre-Clebsch conditions [5, 49], allow to distinguish between locally minimizing and maximizing controls. Here, since we consider a multi-input optimal control problem, it is even possible that both controls would be singular at the same time in which case the controls are called totally singular.

Overall, optimal controls need to be synthesized from the constant bang and singular controls. This generally is a highly nontrivial task and requires to analyze the zero sets of the switching functions. For this, it is imperative to have a transparent procedure to compute the derivatives of the switching function and this is provided with the help of the Lie bracket of vector fields.

Definition 5 (Lie Bracket of Vector Fields). Given two differentiable vector fields f and g defined on some open set $G \subset \mathbb{R}^n$, $f, g : G \to \mathbb{R}^n$, their Lie bracket $[f, g]$ is another vector field defined on G by

$$[f, g](x) = Dg(x)f(x) - Df(x)g(x).$$

We only mention the most important structural properties of the Lie bracket. It is clear that the Lie bracket is anti-commutative, i.e., for all vector fields we have that $[f, g] = -[g, f]$ and a simple computation verifies that for any vector fields f, g and h the Lie bracket satisfies the Jacobi identity

$$[f, [g, h]] + [g, [h, f]] + [h, [f, g]] \equiv 0.$$

Proposition 3. *Let $z(\cdot)$ be a solution of the dynamics (7) for the controls u and v and let λ be a solution of the corresponding adjoint Eq. (13). For a continuously differentiable vector field h, let*

$$\Psi(t) = \langle \lambda(t), h(z(t)) \rangle = \lambda(t)h(z(t)). \tag{17}$$

The derivative of Ψ is then given by

$$\dot{\Psi}(t) = \langle \lambda(t), [f + ug_1 + vg_2, h](z(t)) \rangle . \tag{18}$$

Proof. Dropping the argument t, along the solutions of the dynamics and adjoint equation, we have that

$$\begin{aligned}
\dot{\Psi} &= \dot{\lambda}h(z) + \lambda Dh(z)\dot{z} \\
&= -\lambda \left(Df(z) + uDg_1(z) + vDg_2(z)\right) h(z) + \lambda Dh(z) \left(f(z) + ug_1(z) + vg_2(z)\right) \\
&= \lambda \left(Dh(z)f(z) - Df(z)h(z)\right) + u\lambda \left(Dh(z)g_1(z) - Dg_1(z)h(z)\right) \\
&\qquad + v\lambda \left(Dh(z)g_2(z) - Dg_2(z)h(z)\right) \\
&= \langle \lambda, [f + ug_1 + vg_2, h](z) \rangle .
\end{aligned}$$

For example, since $[h, h] \equiv 0$ for any vector field h, the first derivatives of the switching functions Φ_1 and Φ_2 are thus given by

$$\dot{\Phi}_1(t) = \langle \lambda(t), [f + vg_2, g_1](z_*(t)) \rangle$$

and

$$\dot{\Phi}_2(t) = \langle \lambda(t), [f + ug_1, g_2](z_*(t)) \rangle .$$

The commutator of the control vector fields is easily computed to be

$$[g_1, g_2](z) = \begin{pmatrix} 0 \\ \rho\alpha\xi \end{pmatrix}, \tag{19}$$

and thus is a constant vector field. For $\xi = 0$, i.e., when the effects of chemotherapy on the constant influx of immune cells from the primary organs are not considered (or are small), the two control vector fields commute and this considerably simplifies the mathematical analysis. Generally, an analysis of the necessary conditions for optimality of the maximum principle needs to be carried out to obtain information as to the concatenation structure of optimal controls. We show how such an analysis is carried out for two simpler models when we neglect the effects of chemotherapy on the immune system or simply assume that these are small. Such an assumption can be justified for so-called strongly targeted drugs.

4 Optimizing Cancer Chemotherapy with Strongly Targeted Cytotoxic Drugs

In this simplified version of model (4) and (5) we only consider a chemotherapeutic agent and assume that its effects on the immune system are small and thus in a first approximation can be ignored. In this case, the dynamics simplifies to

$$\dot{x} = \mu_C x F(x) - \gamma x y - \kappa x u, \qquad x(0) = x_0, \tag{20}$$

$$\dot{y} = \mu_I \left(x - \beta x^2\right) y - \delta y + \alpha, \qquad y(0) = y_0. \tag{21}$$

We shall analyze the structure of optimal controls for both a Gompertzian ($F_G(x) = -\ln(x/x_\infty)$) and generalized logistic growth model ($F_L(x) = 1-(x/x_\infty)^\nu$, $\nu > 0$) and it will be seen that the results for the Gompertzian model relate to the limiting behavior of the results for the generalized logistic model as $\nu \to 0$. The drift and control vector fields are

$$f(z) = \begin{pmatrix} \mu_C x F(x) - \gamma x y \\ \mu_I \left(x - \beta x^2\right) y - \delta y + \alpha \end{pmatrix} \qquad \text{and} \qquad g(z) = \begin{pmatrix} -\kappa x \\ 0 \end{pmatrix}.$$

Since the Hamiltonian vanishes identically, it follows from the terminal conditions $\lambda_1(T) = A$ and $\lambda_2(T) = -B$ that the terminal points of optimal controlled trajectories need to lie on specific curves. We thus get the following transversality conditions for the terminal points.

Lemma 1. *If the optimal control ends with a segment where $u = 0$ or the control is singular, $u = u_{\text{sing}}$, then the terminal point $(x_*(T), y_*(T))$ lies on the curve*

$$A\left(-\mu_C x \ln\left(\frac{x}{x_\infty}\right) - \gamma x y\right) - B\left(\mu_I \left(x - \beta x^2\right) y - \delta y + \alpha\right) + S = 0; \tag{22}$$

if the optimal control ends with a segment for $u = 1$, then it lies on the curve

$$A\left(-\mu_C x \ln\left(\frac{x}{x_\infty}\right) - \gamma x y - \kappa x\right) - B\left(\mu_I\left(x - \beta x^2\right) y - \delta y + \alpha\right) + C + S = 0. \tag{23}$$

4.1 Singular Controls and Arcs

If an optimal control u_* is singular on an open interval I, then the switching function Φ,

$$\Phi(t) = C + \langle \lambda(t), g\left(z_*(t)\right)\rangle = C - \lambda_1(t)\kappa x_*(t),$$

and all its derivatives vanish on I. Furthermore, the Hamiltonian H vanishes identically over $[0, T]$ and thus we also have that

$$H = S + \langle \lambda(t), f(z_*(t))\rangle + u_*(t)\Phi(t) \equiv 0.$$

Along a singular arc it therefore follows that

$$H = S + \langle \lambda(t), f(z_*(t))\rangle \equiv 0$$

and combining this relation with $\Phi(t) \equiv 0$, we obtain

$$\langle \lambda(t), Cf(z_*(t))\rangle \equiv -CS \equiv \langle \lambda(t), Sg\left(z_*(t)\right)\rangle$$

so that

$$\langle \lambda(t), Cf(z_*(t)) - Sg(z_*(t))\rangle \equiv 0.$$

Furthermore, it follows from Proposition 3 that

$$\dot{\Phi}(t) = \langle \lambda(t), [f, g](z_*(t))\rangle \equiv 0$$

on I. Since $\lambda \in \left(\mathbb{R}^2\right)^*$ is nontrivial, the vector fields $Cf - Sg$ and $[f, g]$ must be linearly dependent when the optimal control is singular. Hence a singular arc must lie in the curve determined by

$$\det\left(Cf(z) - Sg(z), [f, g](z)\right) = 0. \tag{24}$$

Proposition 4. *For the optimal control problem [CI], any singular arc is contained in the zero set $\mathscr{S}$ of the following quadratic function in y,*

$$P(x, y) = p_2(x)y^2 + p_1(x)y + p_0(x),$$

with coefficients that are functions of x given by

$$p_0(x) = -C\alpha\mu_C x F'(x),$$
$$p_1(x) = [C\mu_C F(x) + S\kappa]\,\mu_I(x - 2\beta x^2) - \mu_C x F'(x) C\left(\mu_I\left(x - \beta x^2\right) - \delta\right),$$
$$p_2(x) = -C\gamma\mu_I\left(x - 2\beta x^2\right).$$

Proof. A direct calculation verifies that the Lie bracket $[f, g]$ is given by

$$[f, g](z) = Dg(z) f(z) - Df(z)g(z) = \kappa x \begin{pmatrix} \mu_C x F'(x) \\ \mu_I(1 - 2\beta x) y \end{pmatrix}.$$

Hence we have that

$$\begin{aligned} &\det\left(Cf(z) - Sg(z), [f, g](z)\right) \\ &\quad = \kappa x \begin{vmatrix} C\left(\mu_C x F(x) - \gamma x y\right) + S\kappa x & \mu_C x F'(x) \\ C\left(\mu_I\left(x - \beta x^2\right) y - \delta y + \alpha\right) & \mu_I(1 - 2\beta x) y \end{vmatrix} \\ &\quad = \kappa x \cdot P(x, y) \end{aligned}$$

with the function P defined by the determinant on the right-hand side. Multiplying out the terms verifies the functional form and the coefficients specified above. □

Since P is quadratic in y, for every fixed value x the singular curve $\mathscr{S}$ contains at most two points in $\mathbb{M}$. For a Gompertzian growth model, we have that $xF_G'(x) \equiv -1$ and for the generalized logistic model we get $xF_L'(x) = -\nu(x/x_\infty)^\nu$. In either case, the coefficient $p_0(x)$ is always positive. The quadratic coefficient $p_2(x)$ does not depend on the growth function and is negative for $x < \frac{1}{2\beta}$ and positive for $x > \frac{1}{2\beta}$. In particular, for $x < \frac{1}{2\beta}$ there exist two real solutions, one positive, one negative. Only the positive one is of interest for the problem and thus the singular curve $\mathscr{S}$ is the graph of a function over the interval $(0, \frac{1}{2\beta})$. Whether solutions exist for $x > \frac{1}{2\beta}$ depends on the actual parameter values. Analytic formulas for y as a function of x can still be written down, but they get unwieldy.

For a singular trajectory to be optimal, it must satisfy the *Legendre-Clebsch condition* for optimality [5, 49]. In its simplest version it states that

$$\langle\lambda(t), [g, [f, g]](z_*(t))\rangle \leq 0 \tag{25}$$

along the extremal lift associated with the singular control (while this quantity is nonnegative along maximizing controls). A direct calculation shows that

$$[g, [f, g]](z) = D\left([f, g]\right)(z) g(z) - Dg(z)[f, g](z)$$

$$= -\kappa^2 x \begin{pmatrix} \mu_C \left(xF'(x) + x^2 F''(x) \right) \\ \mu_I \left(1 - 4\beta x \right) y \end{pmatrix},$$

but we now need to analyze the different growth functions separately.

For a *Gompertzian model*, $F_G(x) = -\ln(x/x_\infty)$, we have that

$$xF_G'(x) \equiv -1 \qquad \text{and} \qquad xF_G'(x) + x^2 F_G''(x) \equiv 0$$

and thus the Lie brackets are given by

$$[f, g](z) = \kappa x \begin{pmatrix} -\mu_C \\ \mu_I (1 - 2\beta x) y \end{pmatrix}$$

and

$$[g, [f, g]](z) = -\kappa^2 x \begin{pmatrix} 0 \\ \mu_I \left(1 - 4\beta x \right) y \end{pmatrix}.$$

The vector fields g and $[f, g]$ are linearly independent unless $x = \frac{1}{2\beta}$. For $x = \frac{1}{2\beta}$ there does not exist a point on the singular curve: it follows from $\dot{\Phi}(t) = -\lambda_1(t)\frac{\kappa\mu_C}{2\beta} = 0$ that $\lambda_1(t) = 0$ and thus $\Phi(t) = C > 0$. For $x \neq \frac{1}{2\beta}$, we can express the second-order brackets $[f, [f, g]]$ and $[g, [f, g]]$ as linear combinations of this basis in the form

$$[f, [f, g]](z) = \varphi_1(z) g(z) + \varphi_2(z)[f, g](z) \tag{26}$$

and

$$[g, [f, g]](z) = \theta_1(z) g(z) + \theta_2(z)[f, g](z). \tag{27}$$

Along a singular arc we have that

$$\langle \lambda(t), g\left(z_*(t)\right) \rangle = -C < 0$$

and

$$\langle \lambda(t), [f, g]\left(z_*(t)\right) \rangle = 0.$$

Hence

$$\langle \lambda(t), [g, [f, g]]\left(z_*(t)\right) \rangle = -C\theta_1(z_*(t))$$

and thus the Legendre-Clebsch condition is satisfied if and only if $\theta_1(z_*(t))$ is nonnegative. It is not difficult to see that

$$\theta_1(z) = \kappa\mu_C \frac{1-4\beta x}{1-2\beta x} \qquad \text{and} \qquad \theta_2(z) = -\kappa \frac{1-4\beta x}{1-2\beta x}$$

so that the strengthened Legendre-Clebsch condition is satisfied for $0 < x < \frac{1}{4\beta}$ and $\frac{1}{2\beta} < x$ and it is violated for $\frac{1}{4\beta} < x < \frac{1}{2\beta}$.

By solving the equation

$$\ddot{\Phi}(t) = \langle \lambda(t), [f,[f,g]](z_*(t)) \rangle + u(t) \langle \lambda(t), [g,[f,g]](z_*(t)) \rangle = 0 \tag{28}$$

for the control u, the singular control can formally be expressed as

$$u_{\text{sing}}(t) = -\frac{\langle \lambda(t), [f,[f,g]]\,(z_*(t)) \rangle}{\langle \lambda(t), [g,[f,g]]\,(z_*(t)) \rangle}.$$

Using the representations for the second order brackets, this simplifies to

$$\begin{aligned} u_{\text{sing}}(t) &= -\frac{\varphi_1(z_*(t))\,\langle \lambda(t), g(z_*(t)) \rangle + \varphi_2(z_*(t))\,\langle \lambda(t), [f,g](z_*(t)) \rangle}{\theta_1(z_*(t))\,\langle \lambda(t), g(z_*(t)) \rangle + \theta_2(z_*(t))\,\langle \lambda(t), [f,g](z_*(t)) \rangle} \\ &= -\frac{\varphi_1(z_*(t))}{\theta_1(z_*(t))}. \end{aligned} \tag{29}$$

Overall, we therefore have the following result:

Proposition 5 ([28]). *For the optimal control problem [CI] with a Gompertzian growth rate, $F_G(x) = -\ln(x/x_\infty)$, the control that keeps the singular curve $\mathscr{S}$ invariant is given in feedback form as*

$$u_{\text{sing}}(t) = -\frac{\varphi_1(z_*(t))}{\theta_1(z_*(t))}$$

with the coefficients φ_1 and θ_1 defined through the relations (26) and (27). This control is admissible if and only if its value lies in the interval $[0,1]$. The strengthened Legendre-Clebsch condition is satisfied for $x < \frac{1}{4\beta}$ and $\frac{1}{2\beta} < x$, and it is violated for $\frac{1}{4\beta} < x < \frac{1}{2\beta}$.

Based on the formulas derived above, the singular arc, the singular control, and their admissible portions can easily be evaluated numerically. Note that, given a point $z_*(t) \in \mathscr{S}$, the equations $\Phi(t) = 0$ and $\dot{\Phi}(t) = 0$ have a unique solution for the multiplier $\lambda(t)$ and if the singular control is admissible, this locally defines a singular arc along which the strengthened Legendre-Clebsch condition is satisfied. In Fig. 5 we illustrate the structure of the singular curve for the data from Table 1 and parameter values $(C, S) = (0.05, 0.05)$.

For the *generalized logistic growth* rate, $F_L(x) = 1 - (x/x_\infty)^\nu$, $\nu > 0$, we have that

$$xF_L'(x) = -\nu\left(\frac{x}{x_\infty}\right)^\nu \qquad \text{and} \qquad x^2F_L''(x) = -\nu\,(\nu-1)\left(\frac{x}{x_\infty}\right)^\nu$$

and thus

$$[f,g](z) = \kappa x\begin{pmatrix} -\mu_C\,\nu\left(\frac{x}{x_\infty}\right)^\nu \\ \mu_I\,(1-2\beta x)\,y\end{pmatrix}$$

and

$$[g,[f,g]](z) = -\kappa^2 x\begin{pmatrix} -\mu_C\,\nu^2\left(\frac{x}{x_\infty}\right)^\nu \\ \mu_I\,(1-4\beta x)\,y\end{pmatrix}.$$

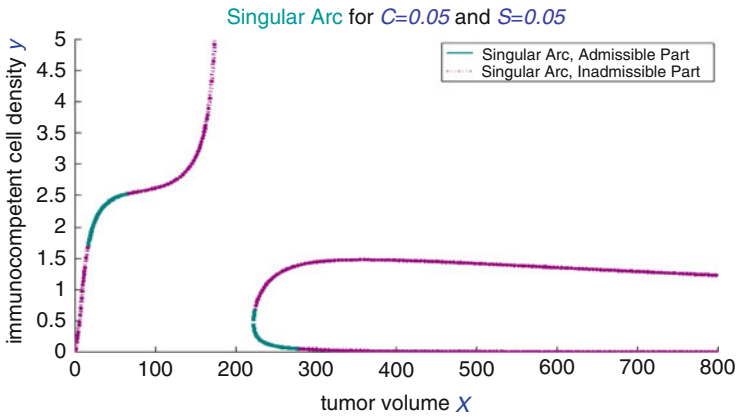

Fig. 5 Example of singular curves for problem [CI] with a Gompertzian growth rate $F_G(x) = -\ln(x/x_\infty)$. The admissible portions (where the values of the control lie in the interval $[0,1]$) are identified by the *solid green* segments. Only these segments represent actual trajectories of the system

Proposition 6 ([29]). *For the optimal control problem [CI] with a generalized logistic growth rate $F_L(x) = 1-(x/x_\infty)^\nu$, $\nu > 0$, the strengthened Legendre-Clebsch condition is satisfied if and only if*

$$\nu < \frac{1-4\beta x_*(t)}{1-2\beta x_*(t)}. \tag{30}$$

Proof. Suppose the control u_* is singular over an open interval I. Then $\Phi(t) \equiv 0$ on I, i.e., $\lambda_1(t)\kappa x_*(t) \equiv C > 0$, implies that λ_1 is positive along a singular arc. Furthermore, $\dot\Phi(t) \equiv 0$ on I gives that

$$\lambda_2(t)\mu_I\,(1-2\beta x_*(t))\,y_*(t) \equiv \lambda_1(t)\mu_C\,\nu\left(\frac{x_*(t)}{x_\infty}\right)^\nu > 0.$$

Evaluating the Legendre-Clebsch condition, and using the above relation to eliminate the multiplier λ_2, we obtain that

$$\begin{aligned}
&\langle\lambda(t),[g,[f,g]](z_*(t))\rangle \\
&\quad= \kappa^2\left\{\lambda_1(t)\mu_C\left(\frac{x_*(t)}{x_\infty}\right)^\nu \nu^2 x_*(t) + \lambda_2(t)\mu_I\left(4\beta x_*^2(t) - x_*(t)\right)y_*(t)\right\} \\
&\quad= \kappa^2\lambda_1(t)x_*(t)\left\{\mu_C\left(\frac{x_*(t)}{x_\infty}\right)^\nu \nu^2 + \frac{\mu_C\left(\frac{x_*(t)}{x_\infty}\right)^\nu \nu}{1-2\beta x_*(t)}\left(4\beta x_*(t)-1\right)\right\} \\
&\quad= \kappa^2\lambda_1(t)\mu_C\left(\frac{x_*(t)}{x_\infty}\right)^\nu \nu x_*(t)\left\{\nu - \frac{1-4\beta x_*(t)}{1-2\beta x_*(t)}\right\}. \qquad (31)
\end{aligned}$$

Since $\lambda_1(t)$ is positive along a singular arc, this implies that condition (25) holds if and only if (30) is satisfied. □

This determines the following intervals along which an optimal control can be singular dependent on the parameter ν.

Corollary 2 ([29]). *Suppose an optimal control u_* for the optimal control problem [CI] with a generalized logistic growth rate is singular at time t. Then, it follows that*

1. *if $0 < \nu < 1$, we have either $0 \le \beta x_*(t) < \frac{1}{2}\frac{1-\nu}{2-\nu} < \frac{1}{4}$ or $\frac{1}{2} < \beta x_*(t)$,*
2. *if $1 \le \nu \le 2$, then $\frac{1}{2} < \beta x_*(t)$ and*
3. *if $\nu > 2$, then $\frac{1}{2} < \beta x_*(t) < \frac{1}{2}\frac{1-\nu}{2-\nu}$.* □

These relations readily follow from condition (30) and are illustrated in Fig. 6. In the limiting case $\nu \to 0$ we obtain that the Legendre-Clebsch condition is satisfied for βx in the intervals $[0, \frac{1}{4}) \cup (\frac{1}{2}, \infty)$ and this agrees with Proposition 5 for a Gompertzian growth function. As ν increases, these intervals shrink until, in the limit $\nu \to \infty$, for exponential growth singular controls no longer are optimal. The computation of the singular control is exactly as for the case of a Gompertzian function and the same formula (29) is valid, albeit with different functions θ_1 and φ_1.

4.2 Optimal Controlled Trajectories for a Gompertzian Growth Function

We give some examples of optimal controlled trajectories for different scenarios that show the structure of the solutions [28]. Optimal controls for problem [CI]

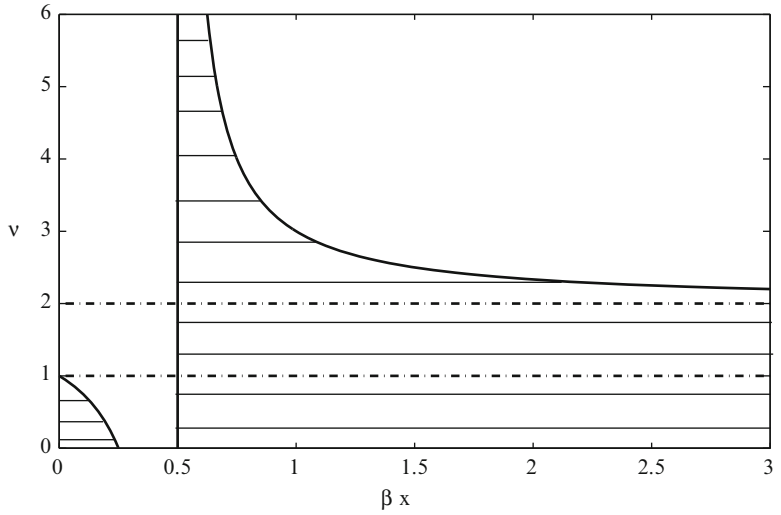

Fig. 6 The highlighted region for fixed value of ν (plotted *vertically*) represents the intervals (*horizontally*) scaled in terms of βx on which the Legendre-Clebsch condition for minimality of singular arcs is satisfied. As ν increases, these intervals become smaller and in the limit $\nu \to \infty$ (exponential growth) singular controls are not optimal. (Reproduced with permission from [29], ©2012, AIMS)

typically contain a singular arc and its presence makes numerical computations challenging. The numerical difficulties lie with the fact that singular controls are only optimal on lower dimensional submanifolds and without any a priori information about these structures, numerical algorithms have extreme difficulties finding these sets. A numerically computed "optimal" solution often simply shows numerical chattering, i.e., controls that seemingly switch rapidly between various values, not necessarily the extreme points 0 and 1 of the control interval. These are tell-tale signs of optimal singular arcs. In the computations below (which are reproduced from the papers [26] and [28]) the classical ε-approach was used in which a quadratic penalty term $\varepsilon \int_0^T u^2(t)dt$ is added to the objective and then the optimal controls for the underlying problem are recovered in the limit as $\varepsilon \to 0$. For the actual computations GPOPS (*G*eneral *P*seudo-spectral *OP*timal Control *S*oftware), an open-source MATLAB optimal control software that implements the Gauss hp-adaptive pseudo-spectral methods (http://www.gpops.org/) was used. These methods approximate the state using a basis of Lagrange polynomials and collocate the dynamics at the Legendre-Gauss nodes [3, 4, 16]. The continuous-time optimal control problem is then transformed into a finite-dimensional nonlinear programming problem that is being solved using standard algorithms. These type of algorithms are especially effective to find controls that lie in the interior of the control set like the singular controls for our problem. The analytical formulas derived above allowed us to verify that the numerically found solutions indeed were accurate in the sense that the corresponding controlled trajectories followed the

singular curve $\mathscr{S}$ along singular controls. In some simple cases, which arise when the coefficients C and S in the objective (6) skew the importance of the side-effects versus the terminal time, optimal controls give full-dose chemotherapy over the full interval $[0, T]$. But aside for such special scenarios, optimal solutions always contain a time interval when the control is singular.

We illustrate the changes in the structure of optimal controls as we vary the coefficients C and S in the objective. The coefficients A and B related to the stable eigenvector of the saddle are kept constant as $A = 0.00192$ and $B = 1$ and the numerical value chosen for κ is $\kappa = 1$. In our computations, we use the same initial condition given by $(x_0, y_0) = (600, 0.1)$. The initial tumor volume x_0 is given as a multiple of some reference value and represents a tumor cell count that is 600 times higher than some chosen base value (10^6 cells); y_0 is a dimensionless, order-of-magnitude quantity that represents a depletion of the immuno-competent cell densities to 10 % of a nominal value. These initial conditions lie well within the malignant region and initially in each scenario considered below the control is given by $u \equiv 1$ for some interval $[0, t_1]$.

Scenario 1: If the penalty on the terminal time T is taken large relative to the side-effects of treatment, $S \gg C$, this term becomes dominant and the optimal control is simply constant given by full dose treatment, $u \equiv 1$. Figure 7 shows such an example when $S = 0.28$ and $C = 0.001$. In the figure, the initial and terminal points are labeled $w_0 = (x_0, y_0)$ and $w_T = (x_T, y_T)$, respectively. It is noticeable that with such a high cost on the terminal time, the optimal trajectory barely crosses into the benign region. A blow-up of the trajectory near the terminal point is given in the small box inserted into the figure.) Yet, assuming the dynamics follows the uncontrolled system after the final time T, the state then converges to the benign equilibrium point. The figure also shows the potential singular arc for these coefficients which in this range is the graph of a function with its admissible portion identified by the solid green segment. For these parameter values the optimal solution terminates exactly at the time when the singular arc is reached, but this is a mere coincidence without significance. The figure also shows the terminal curves defined by the transversality conditions (22) and (23) and in this case the terminal point lies at the intersection of the singular curve with the curve defining the transversality condition for $u = 1$.

Scenario 2: As the penalty S on the time used is decreased, optimal controlled trajectories starting from the initial condition (x_0, y_0) give an initial maximum dose chemotherapy, $u \equiv 1$, until the singular curve $\mathscr{S}$ is reached. If the corresponding singular control is admissible, at that time the optimal control switches to the singular control. Optimal controlled trajectories then follow the singular arc from the malignant into the benign region across the separatrix. In the benign region, at a certain time τ administration of chemotherapy stops, i.e., the control switches to $u \equiv 0$ and follows the uncontrolled trajectory towards the benign equilibrium point. If the penalty on the chemotherapeutic agent is not too high, then optimal controls will switch one more time to give a short full dose chemotherapy segment at the end of treatment, possibly after

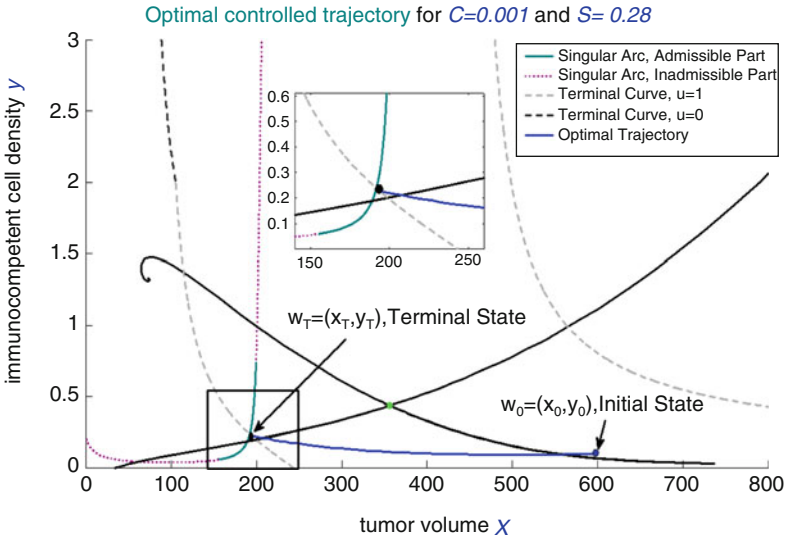

Fig. 7 Optimal controlled trajectory for Scenario 1. The optimal control is constant given by $u_*(t) \equiv 1$

a prolonged period of rest. We use the notation **1s0**, respectively **1s01**, to label such concatenation sequences for the optimal controls. That is, an **1s01**-trajectory starts with an interval $[0, t_1]$ when the control is at maximum dose rate, $u \equiv 1$, followed by an interval $[t_1, \tau]$ where the control is singular and the trajectory follows an admissible singular arc. The optimal behavior then includes a rest period over an interval $[\tau, \sigma]$ when no drugs are given, $u \equiv 0$, and may end with another short burst of full dose chemotherapy over a final interval $[\sigma, T]$. Such a structure can also be used to define a three-dimensional minimization problem over the variables (τ, σ, T) whose numerical solution defines the optimal control. Overall, a concatenation sequence for the control of at most the form **1s01** results. Figure 8 shows an example of such a numerically computed optimal controlled trajectory for $(C, S) = (0.01, 0.2)$. As before, we label the initial and terminal conditions by $w_0 = (x_0, y_0)$ and $w_T = (x_T, y_T)$, respectively, and we denote the consecutive switching points by w_1, w_2 and w_3. In the range where the singular arc comes into play, it is the graph of a function and the figure also identifies its admissible segment as the solid green segment of the curve.

Scenario 3: If the penalty on the chemotherapeutic agent is increased further, the last full dose therapy segment disappears and the structure of optimal controlled trajectories reduces to **1s0**. Increasing the parameter C gives a more prominent role to the side effects and in this case the optimal trajectory ends on the curve (22) that defines the terminal values for the control $u = 0$. This situation is rather typical and we illustrate it for the case $(C, S) = (0.05, 0.01)$ in Fig. 9.

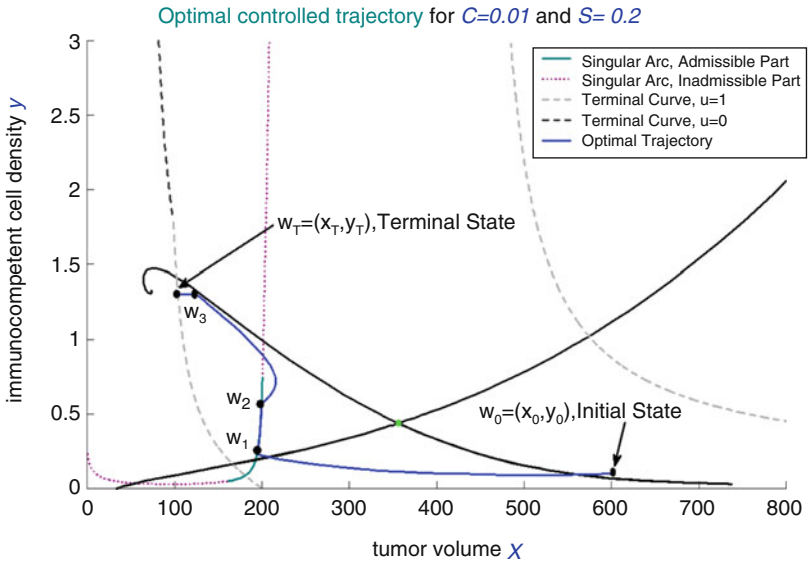

Fig. 8 Optimal controlled trajectory for Scenario 2. Following an initial full dose chemotherapy segment, the optimal control switches to the singular control as the singular arc is reached and then follows the singular arc. After a prolonged rest period, another short burst of chemotherapy is given at the end. Note that the tumor volume initially increases along the rest period, but as the immune system becomes stronger this trend is reversed

4.3 Comments and Interpretation

There are some interesting theoretical insights about optimal therapies in the presence of tumor immune interactions that can be drawn from these numerical computations. By including a penalty term on the final time T, we have given a well-posed formulation for which optimal controls exist. If a strong emphasis is put onto this penalty, optimal controls simply will be constant maximum dose therapies. Thus, if time is of the essence, give as much as you can as soon as you can. However, if a longer time horizon is permissible and the coefficient at the terminal time T is lowered, optimal controls become concatenations that start with a full dose therapy session to reduce the high initial tumor burden, but then switch to reduced dose rates according to the singular control. During such a period (see scenario 2) it is even possible that the tumor volume x increases again. But the immunocompetent density y increases as well and since the states already lie in the benign region, this eventually leads to a better outcome with the trajectories converging to the benign equilibrium point. Note that optimal controls no longer aim at eradicating the tumor, but rather are content to move the state of the system into a region where the innate beneficial actions of the immune system are able to maintain the cancer at a low level reminiscent of tumor dormancy and/or immune surveillance. In the medical literature, such protocols that initially apply a burst of MTD chemotherapy to reduce

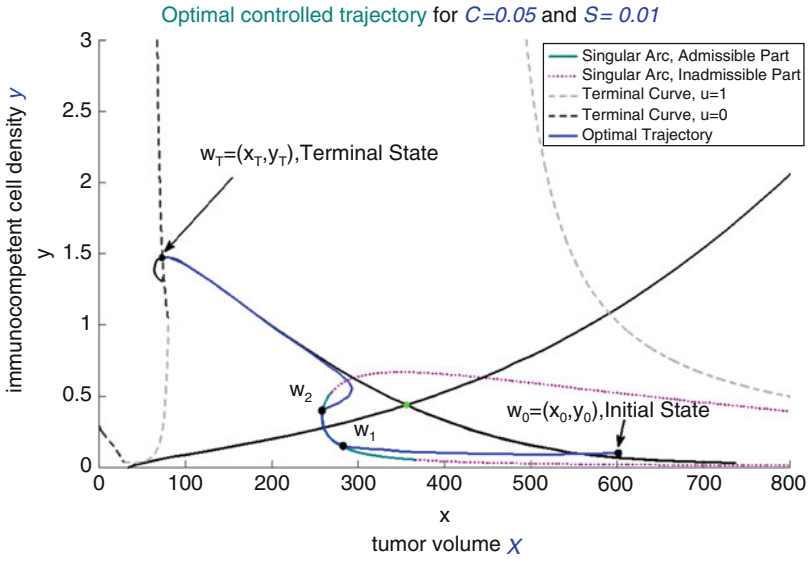

Fig. 9 Optimal controlled trajectory for Scenario 3. Following an initial full dose chemotherapy segment, the optimal control switches to the singular control as the singular arc is reached and then follows the singular arc from the malignant into the benign region. Because of stronger side effects, no additional chemotherapy is given at the end. Again note that the tumor volume also increases initially along the rest period and again this trend is reversed as the immune system becomes stronger

the tumor volume and then sustain a smaller volume with reduced dosages have been considered under the terminology of *"chemo-switch"* strategies [2, 43]. The additional and usually very short burst of full dose chemotherapy that marks the end of some of these therapies also is quite interesting. While this may appear a bit odd, such strategies seem to represent a common pattern pursued in some chemotherapies based on physicians' experience. Thus, despite the model's simplicity, its solutions give some interesting practical insights into how to schedule therapies over time.

With the prominent role played by the singular arc, these solutions for model [CI] contrast with the optimal bang-bang controls for cell-cycle specific models for cancer chemotherapy [30, 31, 53, 54, 56] when optimal controls are bang-bang with upfront dosing, i.e., confirm the MTD paradigm. In both types of models it is implicitly assumed that the tumor population consists of chemotherapeutically sensitive cells, but here it is the mitigating influence of the immune system which for smaller tumor volumes leads to the abandonment of the strict bang-bang scheme that is seen in the cell-cycle specific models. Intuitively, if the system is in a condition where it is able to manage the cancer by itself, why administer chemotherapy? Indeed, if negative influences of the chemotherapy on the immune system are added, high-dose chemotherapy precisely may destroy this innate ability of the organism.

4.4 *Optimizing Combination Treatment: Targeted Chemotherapy with Immune Boost*

We close with giving optimal solutions when we add some rudimentary form of immunotherapy in the form of an immune boost to the model [26]. For example, this can be provided by the application of a drug based on the interleukin family. In this case [CI] is a multi-input optimal control problem with controls u and v. Figure 10 shows the phaseportrait for the corresponding system for a Gompertzian growth function when only an immune boost at constant maximum dose is used. As before, the parameters for the dynamics are from Table 1 and in the control vector field for the immune boost we choose $\rho = 1$. The uncontrolled system shows the same bistable behavior as described in Sect. 2.2. The malignant region shrinks with the immune boost, but immunotherapy alone is not able to eliminate it and thus control the tumor. The stable manifold of the saddle at $(x_s, y_s) = (555.1, 0.191)$ still separates a region where the immune system aided by the immune boost can eliminate the cancer (here the y-values of the system approach $+\infty$ while x converges to 0 from the right) from a region where the cancer eventually will dominate and trajectories converge to the asymptotically stable malignant equilibrium point $(x_m, y_m) = (715.6, 0.048)$. Thus chemotherapy is needed.

An important feature of this formulation is that the control vector fields g_1 and g_2 commute [see (19)]. This implies that the derivatives of the switching functions, $\Phi_1(t) = C + \langle \lambda(t), g_1(z_*(t)) \rangle$ for u and $\Phi_2(t) = D + \langle \lambda(t), g_2(z_*(t)) \rangle$ for v, are given by

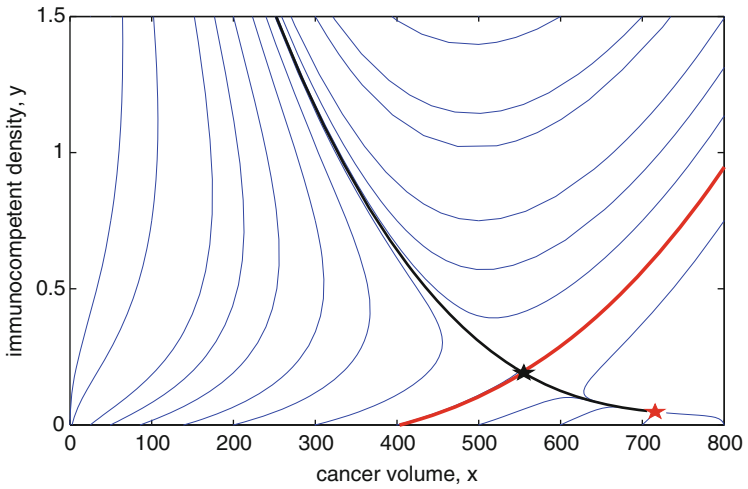

Fig. 10 Phaseportrait for the system (1) and (2) for a Gompertzian growth rate $F(x) = -\log(x/x_\infty)$ with full dose immune boost only (i.e., $u \equiv 0$ and $v \equiv 1$). The malignant region becomes smaller, but persists. Chemotherapy is needed to move initial conditions in the malignant region into the benign region

$$\dot{\Phi}_i(t) = \langle \lambda(t), [f, g_i](z(t)) \rangle , \qquad i = 1, 2. \tag{32}$$

In particular, these derivatives do not depend on the controls u or v and thus are absolutely continuous functions that can be differentiated further. It follows from Proposition 3 that

$$\ddot{\Phi}_i(t) = \langle \lambda(t), [f + ug_1 + vg_2, [f, g_i]](z(t)) \rangle , \qquad i = 1, 2.$$

From above, we have that

$$[f, g_1](z) = \kappa x \begin{pmatrix} \mu_C x F'(x) \\ \mu_I (1 - 2\beta x) y \end{pmatrix}$$

and another computation verifies that

$$[f, g_2](z) = Dg_2(z) f(z) - Df(z) g_2(z) = \rho \begin{pmatrix} \gamma x y \\ \alpha \end{pmatrix}$$

which does not depend on the particular growth model F used. Furthermore, a direct computation verifies that the Lie brackets $[g_1, [f, g_2]]$ and $[g_2, [f, g_1]]$ vanish identically. Thus, regardless of the tumor growth model used, the second derivatives of the switching functions are given by

$$\ddot{\Phi}_1(t) = \langle \lambda(t), [f + ug_1, [f, g_1]](z_*(t)) \rangle \tag{33}$$

and

$$\ddot{\Phi}_2(t) = \langle \lambda(t), [f + vg_2, [f, g_2]](z_*(t)) \rangle . \tag{34}$$

The Lie bracket relations of the vector fields therefore decouple the controls u and v in the first two derivatives of the switching functions. In particular, the general formulas derived above for a singular control for the chemotherapeutic agent u remain valid, but with the one change that the equation $H \equiv 0$ now involves the second control v_* and thus reads

$$H = S + \langle \lambda(t), f(z_*(t)) \rangle + v_*(t) \left(D + \langle \lambda(t), g_2(z_*(t)) \rangle \right) \equiv 0.$$

Proposition 7 ([26]). *Optimal controls v_* are not singular on any interval.*

Proof. Suppose the control v_* is singular on an open interval I. Regardless of the specific form of the control u_*, by the Legendre-Clebsch condition, it is a necessary condition for optimality of v_* that

$$\langle \lambda(t), [g_2, [f, g_2]](z(t)) \rangle \leq 0 \qquad \text{on} \quad I.$$

On I we have that

$$\Phi_2(t) = D + \langle \lambda(t), g_2(z_*(t)) \rangle \equiv 0 \quad \text{and} \quad \dot{\Phi}_2(t) = \langle \lambda(t), [f, g_2](z_*(t)) \rangle \equiv 0.$$

The vector fields g_2 and $[f, g_2]$ are linearly independent on $\mathbb{M}$ and can therefore be used as a basis for the higher order Lie brackets. We write the second-order Lie bracket $[g_2, [f, g_2]]$ as a linear combination of g_2 and $[f, g_2]$ in the form

$$[g_2, [f, g_2]](z) = \psi_1(z) g_2(z) + \psi_2(z) [f, g_2](z)$$

with smooth functions ψ_1 and ψ_2. A simple computation verifies that

$$[g_2, [f, g_2]](z) = \rho^2 \begin{pmatrix} \gamma x y \\ -\alpha \end{pmatrix},$$

and solving the equations

$$\rho \begin{pmatrix} \gamma x y \\ -\alpha \end{pmatrix} = \psi_1(z) \begin{pmatrix} 0 \\ y \end{pmatrix} + \psi_2(z) \begin{pmatrix} \gamma x y \\ \alpha \end{pmatrix}$$

gives

$$\psi_1(z) = -\frac{2\rho\alpha}{y} \qquad \text{and} \qquad \psi_2(z) = \rho.$$

Hence along a singular control v_* it follows that we have

$$\begin{aligned} &\langle \lambda(t), [g_2, [f, g_2]](z_*(t)) \rangle \\ &\quad = \psi_1(z_*(t)) \, \langle \lambda(t), g_2(z_*(t)) \rangle + \psi_2(z_*(t)) \, \langle \lambda(t), [f, g_2](z_*(t)) \rangle \\ &\quad = \psi_1(z_*(t)) \, (-D) + \psi_2(z_*(t)) \cdot 0 = \frac{2D\rho\alpha}{y_*(t)} > 0 \end{aligned}$$

violating the Legendre-Clebsch condition. □

Thus, an immune boost will be given in a bang-bang manner and for a possible singular control u_*, we only need to consider the two cases $v_* = 0$ and $v_* = 1$. If $v_* = 0$, this reduces to the earlier situation with the same formulas valid verbatim. For $v_* = 1$ we now obtain that

$$\det \left(C \, (f(z) + g_2 \, (z)) - (D + S) g_1(z), [f, g_1](z) \right) = 0$$

and this expression is equal to

$$\det \left(C f(z) - S g_1(z), [f, g_1](z) \right)$$

$$+C \det\left(g_2(z), [f, g_1](z)\right)$$
$$-D \det\left(g_1(z), [f, g_1](z)\right).$$

The first term corresponds to the expression computed earlier and the other terms are given by

$$\det\left(g_2(z), [f, g_1](z)\right) = \kappa\rho xy \begin{vmatrix} 0 & \mu_C x F'(x) \\ 1 & \mu_I(1-2\beta x)y \end{vmatrix} = -\kappa\rho\mu_C x^2 F'(x) y$$

and

$$\det\left(g_1(z), [f, g_1](z)\right) = \kappa x \begin{vmatrix} -\kappa x & \mu_C x F'(x) \\ 0 & \mu_I(1-2\beta x)y \end{vmatrix} = -\kappa^2\mu_I(x-2\beta x^2)xy.$$

Hence, if we write

$$\det\left(C\left(f(z)+g_2(z)\right) - (D+S)g_1(z), [f, g_1](z)\right)$$
$$= \kappa x \cdot Q(x, y) = \kappa x \cdot \left(q_2(x)y^2 + q_1(x)y + q_0(x)\right),$$

then Q differs from P only in the linear term which now is given by

$$q_1(x) = \mu_I(x-2\beta x^2)\left[C\mu_C F(x) + (D+S)\kappa\right]$$
$$-C\mu_C x F'(x)\left[\mu_I(x-\beta x^2) - \delta + \rho\right]$$

while $q_0(x) \equiv p_0(x)$ and $q_2(x) \equiv p_2(x)$.

Based on the formulas derived above, the singular arc, the singular control, and their admissible portions can easily be evaluated numerically. As an illustration, Fig. 11 shows how the singular curve $\mathscr{S}$ changes from $v \equiv 0$ (blue curve) to $v \equiv 1$ (red curve) for the parameter values from Table 1 for the dynamics, $\kappa = 2$ and $\rho = 1$, and the coefficients $C = 0.036$, $D = 0.007$ and $S = 0.036$ for the objective.

Scenario 4: Figure 12 shows an optimal control (top) and its corresponding trajectory (bottom) for the same parameter values for the dynamics as before and coefficients $\kappa = 2$ and $\rho = 1$ in the control vector fields. Also the initial condition is the same as before, $(x_0, y_0) = (600, 0.1)$. The objective again is defined with $A = 0.00192$ and $B = 1$ (coming from the stable eigenvector of the saddle for the uncontrolled system) and we have chosen the other weights as $C = 0.01$, $D = 0.025$ and $S = 0.001$. For these weights, both the side effects of chemotherapy and the immune boost are significant. Chemotherapy has overall the better effectiveness and becomes the dominant therapy. Initially chemotherapy is given at full dose without any immune boost. However, already after a brief time interval, as the state of the system nears the separatrix, chemotherapy is reduced drastically and is only administered at lower dose rates according to the singular control u_{sing}. Once more the *"chemo-switch"*

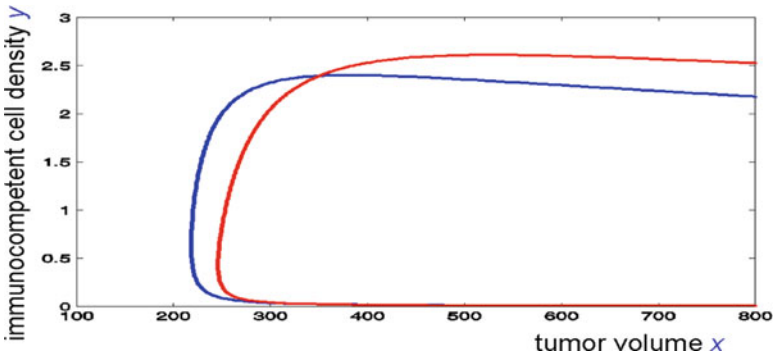

Fig. 11 Example of the changes in the singular curve $\mathscr{S}$ for the chemotherapeutic agent u without ($v \equiv 0$, *blue curve*) and with ($v \equiv 1$, *red curve*) immune boost

type behavior of administration of a chemotherapeutic agent is seen as optimal. In the figure of the trajectory the corresponding switching points are indicated on the trajectory by a red asterisk. Once a "safe" distance to the separatrix has been established, chemotherapy is switched off and the system follows the uncontrolled trajectory towards the benign stable equilibrium point. This portion of the trajectory closely follows the unstable manifold of the saddle for the uncontrolled system and is labeled as the "free pass" in Fig. 12. Along this trajectory, only a small penalty for the time is incurred. Towards the end, when the cancer volume is already quite small, it becomes beneficial to give an immune boost with the precise timing depending on the penalty S given to the terminal time. The two green asterisks on the corresponding trajectory mark the beginning and end of the arc generated by the action of the immune boost. Towards the end, as it was the case in scenario 2, another short full dose chemotherapy session starting at the point marked on the trajectory with a red star reduces the cancer volume further. Thus for this choice of weights in the objective, chemotherapy is the dominant treatment option and overall for the administration of the chemotherapeutic agent we again have a concatenation structure for the optimal controls of the form **1s01**. Immunotherapy is only used as an additional tool once the cancer volume has become small so that the tumor–immune interactions become significant and for the immune boost the concatenation structure for the controls is **010**.

Conclusion

We developed some results about the structure of optimal chemotherapy protocols when tumor–immune system interactions are included in the model. As vehicle for the mathematical analysis we chose the classical model by

(continued)

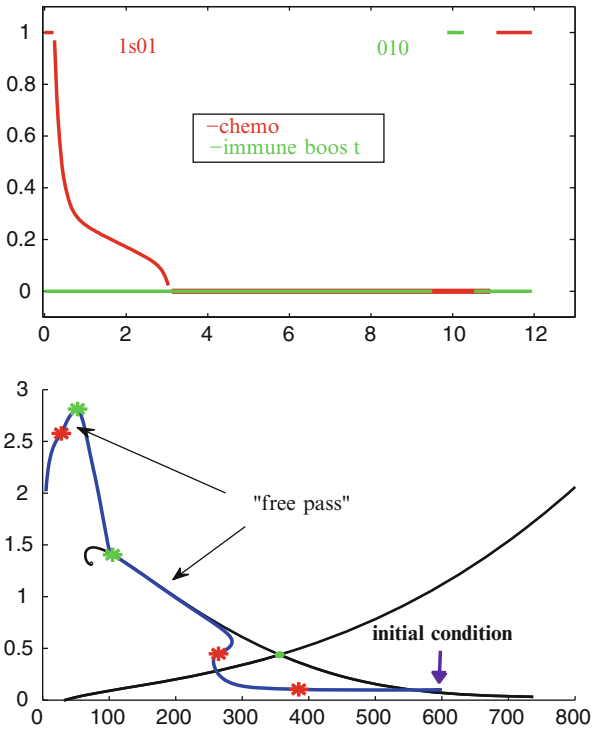

Fig. 12 Optimal controls (*top*) and corresponding trajectory (*bottom*) for scenario 4. The stars on the trajectory indicate the points when switchings in the optimal controls occur (*red asterisks* for switchings in the chemotherapy, *green asterisks* for switchings in the immunotherapy). Chemotherapy remains the dominant mode of administration with the immune boost only aiding towards the end. (Reproduced with permission from [26], ©2013, AIMS)

Stepanova [50], but the ideas that were presented, such as the concept of a malignant and benign region and viewing treatment as effecting the transfer from the malignant into the benign region, are generally valid. Most of the analysis presented and the numerical solutions shown are for the case of a strongly targeted chemotherapeutic agent when it is reasonable to neglect its effects on the immune system. Once such effects become stronger and are included in the mathematical analysis, the actual equations for the singular arc and singular control become more complex (c.f.,[27]). Research on the structure of optimal protocols in this case is still ongoing, but similar types of optimal structures are expected.

Acknowledgements The numerical computations of the optimal solutions reported on here were done by our former students Mohammad Naghneian, Mozhdeh Sadat Faraji Mosalman, and Omeiza Olumoye and are part of a larger research project presented in [26, 28, 29]. This material is based upon work supported by the National Science Foundation under collaborative research Grants Nos. DMS 1311729/1311733. Any opinions, findings, and conclusions or recommendations expressed in this material are those of the author(s) and do not necessarily reflect the views of the National Science Foundation.

References

1. André, N., Padovani, L., Pasquier, E.: Metronomic scheduling of anticancer treatment: the next generation of multitarget therapy? Fut. Oncol. **7**(3), 385–394 (2011)
2. Bellmunt, J., Trigo, J.M., Calvo, E., Carles, J., Pérez-Garcia, J.L., Virizuela, J.A., Lopez, R., Lázaro, M., Albanell, J.: Activity of a multi-targeted chemo-switch regimen (sorafenib, gemcitabine, and metronomic capecitabine) in metastatic renal-cell carcinoma: a phase-2 study (SOGUG-02-06). Lancet Oncol. **11**, 350–357 (2010)
3. Benson, D.A.: A Gauss pseudospectral transcription for optimal control. Ph.D. dissertation, Dept. of Aeronautics and Astronautics, MIT (2004)
4. Benson, D.A., Huntington, G.T., Thorvaldsen, T.P., Rao, A.V.: Direct trajectory optimization and costate estimation via an orthogonal collocation method. J. Guid. Control Dyn. **29**(6) 1435–1440 (2006)
5. Bonnard, B., Chyba, M.: Singular Trajectories and their Role in Control Theory. Mathematics and Applications, vol. 40. Springer, Berlin (2003)
6. Bressan, A., Piccoli, B.: Introduction to the Mathematical Theory of Control. American Institute of Mathematical Sciences (AIMS), Springfield (2007)
7. Chen, D., Roda, J.M., Marsh, C.B., Eubank, T.D., Friedman, A.: Hypoxia inducible factors mediate the inhibition of cancer by GM-CSF: a mathematical model. Bull. Math. Biol. **74**(11), 2752–2777 (2012) doi:10.1007/s11538-012-9776-3
8. Delitalia, M., Lorenzi, T.: Recognition and learning in a mathematical model for immune response against cancer. Discrete Cont. Dyn. Syst. Ser. B **18**, 891–914 (2013)
9. Eftimie, R., Bramson, J.l., Earn, D.J.D.: Interactions between the immune system and cancer: a brief review of non-spatial mathematical models. Bull. Math. Biol. **73**(1), 2–32 (2010)
10. Eisen, M.: Mathematical Models in Cell Biology and Cancer Chemotherapy. Lecture Notes in Biomathematics, vol. 30. Springer, Berlin (1979)
11. Friedman, A., Kim, Y.: Tumor cell proliferation and migration under the influence of their microenvironment. Math. Biosci. Eng. **8**(2), 371–383 (2011)
12. Friedman, A., Tian, J.P., Fulci, G., Chocca, E.A., Wang, J.: Glioma virotherapy: the effects of innate immune suppression and increased viral replication capacity, Canc. Res. **66**(4), 2314–2319 (2006)
13. Guckenheimer, J., Holmes, P.: Nonlinear Oscillations, Dynamical Systems, and Bifurcations of Vector Fields. Springer, New York (1983)
14. Hahnfeldt, P., Folkman, J, Hlatky, L.: Minimizing long-term burden: the logic for metronomic chemotherapeutic dosing and its angiogenic basis. J. Theor. Biol. **220**, 545–554 (2003)
15. Hanahan, D., Bergers, G., Bergsland, E.: Less is more, regularly: metronomic dosing of cytotoxic drugs can target tumor angiogenesis in mice, J. Clin. Investig. **105**(8), 1045–1047 (2000)
16. Huntington, G.T. Advancement and analysis of a Gauss pseudospectral transcription for optimal control. Ph.D. dissertation, Dept. of Aeronautics and Astronautics, MIT (2007)
17. Kamen, B., Rubin, E., Aisner, J., Glatstein, E.: High-time chemotherapy or high time for low dose? J. Clin. Oncol. **18**, 2935–2937 (2000)
18. Kim, Y., Friedman, A.: Interaction of tumor with its microenvironment: a mathematical model. Bull. Math. Biol. **72** 1029–1068 (2010)
19. Kindt, T.J., Osborne, B.A., Goldsby, R.A.: Kuby Immunology. W.H. Freeman, New York (2006)
20. Kirschner, D., Panetta, J.C.: Modeling immunotherapy of the tumor-immune interaction, J. Math. Biol. **37** 235–252 (1998)
21. Khalil, H.K.: Nonlinear Systems, 3rd. edn. Prentice Hall, Upper Saddle River (2002)
22. Klement, G., Baruchel, S., Rak, J., Man, S., Clark, K., Hicklin, D.J., Bohlen, P., Kerbel, R.S.: Continuous low-dose therapy with vinblastine and VEGF receptor-2 antibody induces sustained tumor regression without overt toxicity. J. Clin. Investig. **105**(8), R15–R24 (2000)

23. Kuznetsov, V.A., Makalkin, I.A., Taylor, M.A., Perelson, A.S.: Nonlinear dynamics of immunogenic tumors: parameter estimation and global bifurcation analysis. Bull. Math. Biol. **56**, 295–321 (1994)
24. Ledzewicz, U., Bratton, K., Schättler, H.: A 3-compartment model for chemotherapy of heterogeneous tumor populations. Acta Applicandae Matematicae (2014). doi:10.1007/s10440-014-9952-6
25. Ledzewicz, U., Faraji Mosalman, M.S., Schättler, H.: On optimal protocols for combinations of chemo- and immunotherapy. In: Proc. 51st IEEE Conference on Decision and Control, pp. 7492–7497, Maui, Hawaii (2012)
26. Ledzewicz, U., Faraji Mosalman, M.S., Schättler, H.: Optimal controls for a mathematical model of tumor-immune interactions under targeted chemotherapy with immune boost. Discrete Cont. Dyn. Syst. Ser. B **18**, 1031–1051 (2013). doi:10.3934/dcdsb.2013.18.1031
27. Ledzewicz, U., Naghnaeian, M., Schättler, H.: Bifurcation of singular arcs in an optimal control problem for cancer immune system interactions under treatment. In: Proc. 49th IEEE Conference on Decision and Control, , pp. 7039–7044, Atlanta (2010)
28. Ledzewicz, U., Naghnaeian, M., Schättler, H.: Optimal response to chemotherapy for a mathematical model of tumor-immune dynamics. J. Math. Biol. **64**, 557–577 (2012). doi:10.1007/s00285-011-0424-6
29. Ledzewicz, U., Olumoye, O., Schättler, H.: On optimal chemotherapy with a stongly targeted agent for a model of tumor-immune system interactions with generalized logistic growth. Math. Biosci. Eng. **10**(3) 787–802 (2012). doi:10.3934/mbe.2013.10.787
30. Ledzewicz, U., Schättler, H.: Optimal bang-bang controls for a 2-compartment model in cancer chemotherapy. J. Optim. Theory Appl. **114**, 609–637 (2002)
31. Ledzewicz, U., Schättler, H.: Analysis of a cell-cycle specific model for cancer chemotherapy. J. Biol. Syst. **10**, 183–206 (2002)
32. Ledzewicz, U., Schättler, H.: The influence of PK/PD on the structure of optimal control in cancer chemotherapy models. Math. Biosci. Eng. **2**(3), 561–578 (2005)
33. Ledzewicz, U., Schättler, H.: Drug resistance in cancer chemotherapy as an optimal control problem. Discrete Cont. Dyn. Syst. Ser. B **6**, 129–150 (2006)
34. Mallett, D.G., de Pillis, L.G.: A cellular automata model of tumor-immune system interactions. J. Theor. Biol. **239**, 334–350 (2006)
35. Martin, R.B.: Optimal control drug scheduling of cancer chemotherapy. Automatica **28**, 1113–1123 (1992)
36. d'Onofrio, A.: A general framework for modelling tumor-immune system competition and immunotherapy: Mathematical analysis and biomedial inferences. Physica D **208**, 202–235 (2005)
37. d'Onofrio, A.: Tumor-immune system interaction: modeling the tumor-stimulated proliferation of effectors and immunotherapy. Math. Models Methods Appl. Sci. **16**, 1375–1401 (2006)
38. d'Onofrio, A., Ledzewicz, U., Maurer, H., Schättler, H.: On optimal delivery of combination therapy for tumors. Math. Biosci. **222**, 13–26 (2009). doi:10.1016/j.mbs.2009.08.004
39. d'Onofrio, A., Ledzewicz, U., Schättler, H.: On the dynamics of tumor immune system interactions and combined chemo- and immunotherapy. In: d'Onofrio, A., Cerrai, P., Gandolfi., A. (eds.) New Challenges for Cancer Systems Biomedicine. SIMAI Springer series, vol. 1, pp. 249–266. Springer, Milan (2012)
40. Pardoll, D.: Does the immune system see tumors as foreign or self? Ann. Rev. Immun. **21**, 807–839 (2003)
41. Pasquier, E., Kavallaris, M., André, N.: Metronomic chemotherapy: new rationale for new directions. Nat. Rev. Clin. Oncol. **7**, 455–465 (2010)
42. Pasquier, E., Ledzewicz, U.: Perspective on "More is not necessarily better": metronomic chemotherapy. Newsletter Soci. Math. Biol. **26**(2), pp. 9–10 (2013)
43. Pietras, K., Hanahan, D.: A multi-targeted, metronomic and maximum tolerated dose "chemo-switch" regimen is antiangiogenic, producing objective responses and survival benefit in a mouse model of cancer. J. Clin. Oncol. **23**, 939–952 (2005)

44. de Pillis, L.G., Gu, W., Radunskaya, A.: Mixed immunotherapy and chemotherapy of tumors: modeling, applications and biological interpretations. J. Theor. Biol. **238**, 841–862 (2006)
45. de Pillis, L.G., Mallet, D.G., Radunskaya, A.E.: Spatial tumor-immune modeling, Special issue devoted to *Cancer and Medical Treatment Modelling*. J. Comput. Math. Methods Med. **7**, 159–176 (2006)
46. de Pillis, L.G., Radunskaya, A.: A mathematical tumor model with immune resistance and drug therapy: an optimal control approach. J. Theor. Med. **3**, 79–100 (2001)
47. de Pillis, L.G., Radunskaya, A., Wiseman, C.L.: A validated mathematical model of cell-mediated immune response to tumor growth. Canc. Res. **65**, 7950–7958 (2005)
48. Pontryagin, L.S., Boltyanskii, V.G., Gamkrelidze, R.V., Mishchenko, E.F.: The Mathematical Theory of Optimal Processes. MacMillan, New York (1964)
49. Schättler, H., Ledzewicz, U.: Geometric Optimal Control. Springer, New York (2012)
50. Stepanova, N.V.: Course of the immune reaction during the development of a malignant tumour. Biophysics. **24**, 917–923 (1980)
51. Swan, G.W.: Role of optimal control in cancer chemotherapy. Math. Biosci. **101**, 237–284 (1990)
52. Swann, J.B., Smyth, M.J.: Immune surveillance of tumors. J. Clin. Investig. **117**, 1137–1146 (2007)
53. Swierniak, A.: Optimal treatment protocols in leukemia - modelling the proliferation cycle. In: Proc. 12th IMACS World Congress, vol. 4, pp. 170–172, Paris (1988).
54. Swierniak, A.: Cell cycle as an object of control. J. Biol. Syst. **3**, 41–54 (1995)
55. Swierniak, A., Duda, Z.: Singularity of optimal control in some problems related to optimal chemotherapy. Mathl. Comput. Modeling. **19**, 255–262 (1994)
56. Swierniak, A., Ledzewicz, U., Schättler, H.: Optimal control for a class of compartmental models in cancer chemotherapy. Int. J. Appl. Math. Comput. Sci. **13**, 357–368 (2003)
57. de Vladar, H.P., González, J.A.: Dynamic response of cancer under the influence of immunological activity and therapy. J. Theor. Biol. **227**, 335–348 (2004)

Negative Feedback Regulation in Hierarchically Organized Tissues: Exploring the Dynamics of Tissue Regeneration and the Role of Feedback Escape in Tumor Development

Ignacio A. Rodriguez-Brenes, Natalia L. Komarova, and Dominik Wodarz

Abstract Hierarchically organized tissues are tightly regulated to maintain homeostasis under normal conditions and promote the rapid regeneration after injury. Negative feedback from the tissue itself plays an important role in establishing this control. In particular differentiated cells emit signals that down-regulate cell division and inhibit stem cell self-renewal. The mathematical analysis of how these two feedback mechanisms affect tissue regeneration and stability can provide important insights into the dynamics of tissue regulation. This topic is also important for the study of carcinogenesis, given that cancer development requires an escape from feedback control. Here we discuss various aspects of tissue regulation and the phenotypic evolutionary pathways that lead to escape from these feedback mechanisms. Furthermore, we discuss the various tumor growth patterns that arise through different feedback inactivations. Finally, by examining published clinical data we propose that the majority of tumor growth patterns found in the literature can be classified into five categories, which by themselves could reflect the different evolutionary events that drive tumor progression in different types of stem-cell-driven cancers.

1 Introduction

In cell lineages tissue development, maintenance and regeneration are highly regulated. In healthy tissue control loops ensure that the number of cells are kept at appropriate levels, precluding the appearance of abnormal cell growth and promoting the efficient regeneration after an injury [17,47]. Two types of feedbacks

I.A. Rodriguez-Brenes • N.L. Komarova
Department of Mathematics, University of California, Irvine, CA 92697, USA
e-mail: iarodrig@uci.edu; komarova@uci.edu

D. Wodarz (✉)
Department of Ecology and Evolution, University of California, Irvine, CA 92697, USA
e-mail: dwodarz@uci.edu

A. Eladdadi et al. (eds.), *Mathematical Models of Tumor-Immune System Dynamics*, Springer Proceedings in Mathematics & Statistics 107,
DOI 10.1007/978-1-4939-1793-8_8

have been identified: long-range and short-range [4]. The long-range feedbacks respond to the loss of mature cells during an injury, while the short-range feedbacks act in an autocrine fashion in stem cells [3, 6]. In this chapter we will focus on long-range feedbacks. In particular, two types of feedback loops have been suggested to be crucial: Differentiated cells secrete factors that inhibit the division of stem cells. In addition, differentiated cells secrete factors that suppress self renewal of stem cells and instead promote differentiation of the stem cells [26, 33, 60]. This stops the expansion of the stem cell population and leads to cell death through terminal differentiation, thus stopping tissue growth. Negative feedback regulators have been identified in a large number of tissues including muscle, liver, bone, hair, and the nervous and hematopoietic systems [13, 14, 33, 55, 61].

In this chapter we present a mathematical model, which includes feedback regulation in both the division rate and the self-renewal probability of stem cells. We find that the feedback on the self-renewal probability of stem cells is by itself sufficient to establish control. However, if feedback on the division rate is absent, tissue regeneration may lead to significant damped oscillations in the path back to recovery, which, in the worst case scenario, could even lead to the stochastic extinction of the cell population. We find that this oscillatory behavior is more pronounced when the number of stem cell is only a small fraction of the cell population. In general we find a trade-off between requiring a small equilibrium fraction of stem cells while avoiding oscillations and the speed at which the system is able to recover from a perturbation. Spatial interactions and the addition of feedback inhibition on the cell division rate reduce the amplitude of oscillations and contribute to the robustness of the system. In addition, feedback inhibition on the division rate also increases the speed of regeneration.

This discussion falls within the context of ongoing mathematical research on the areas of tissue regulation and cancer development. The mathematical modeling of cancer stem cells and cell compartments has lead to significant biological insights (see e.g. [15, 41, 54, 58]). In particular numerous mathematical models explore hematopoiesis and different types of blood cancers [1, 5, 12]. Negative feedback regulation through control loops has been explored in various tissues including the olfactory epithelium, hematopoietic system, and intestinal crypts [7, 23, 26].

Evidence suggests that tumors retain basic architectural components characteristic of healthy tissue, containing so called ‘cancer stem cells’ or ‘cancer initiating cells’ that maintain the disease, which leads to the concept of stem-cell-driven tumors [11]. Carcinogenesis is a complex process, in which different aspects such as angiogenesis, nutrient availability, metabolic processes, interactions with the microenvironment, and immune responses all influence how the tumor grows and evolves [57]. Despite this great complexity and heterogeneity in the mechanism of tumor formation, it is reasonable to postulate that escape from feedback regulation must be a key ingredient in the formation of any stem-cell-driven tumor.

In this chapter we discuss a computational evolutionary model which suggests that full escape from feedback inhibition can only proceed through a unique sequence of phenotypic transitions. Furthermore, we propose that these dynamics are a common feature amongst the majority of stem-cell-driven tumors, even if

the nature and number of the mutational events required to achieve an escape from feedback regulation are certainly tissue specific. We find that the specific pathways that lead to uncontrolled proliferation, together with the composition of the tissue (solid or non-solid), determine the tumor growth pattern that will take place. According to our models these patterns can be classified into five different categories, which is supported by data fitting and an extensive search of the tumor growth data reported in the literature.

2 Model of Feedback Regulated Tissue Homeostasis

In order to examine the evolutionary dynamics of feedback loss, we will first discuss a computational model that describes feedback-regulated tissue homeostasis, and then add mutational processes to this model. We consider two types of cells: stem cells that are characterized by their ability to differentiate and self renew through cell division, and differentiated cells that do not divide (this includes all cells that do not have a full capacity to self-renew, for example transit amplifying cells). When a stem cell divides it may produce either two stem cells with probability p, or two differentiated daughter cells with probability $1 - p$ (including asymmetric stem cell divisions leads to an equivalent mathematical formulation and does not alter any of the results). In accordance with experimental data, we assume that differentiated cells produce two regulatory factors: one reduces the probability of stem cell self renewal and promotes differentiation; the other reduces the rate of cell division. Thus, a high number of differentiated cells reduces proliferation and increases the rate of differentiation, which eventually leads to a reduction of the overall cell population through terminal differentiation. If we call the division rate of stem cells v and the death rate of differentiated cells d the model is represented schematically by Fig. 1a.

The system of ordinary differential equations (1) describes the model's behavior, where S is the number of stem cells and D the number of differentiated cells. The self renewal probability of stem cells $p(D)$ and the division rate $v(D)$ are treated as general functions that depend on the number of differentiated cells D. This ensures that results are not dependent on the particular mathematical expressions used to describe feedback inhibition. The functions obey the following constraints. First we require that the self renewal probability as well as the division rate of stem cells are differentiable decreasing functions of the number of differentiated cells D. Also, it is assumed that $0.5 < p(0) \leq 1$, i.e., the maximum probability of self renewal, $p(0)$, has to be greater than 0.5 (otherwise the stem cell population will go extinct). Finally, we require that the feedback functions go to zero as the number of differentiated cells grow without bound.

$$\begin{aligned} \dot{S} &= (2p(D) - 1)\, v(D)\, S \\ \dot{D} &= 2(1 - p(D))\, v(D)\, S - d\, D \end{aligned} \tag{1}$$

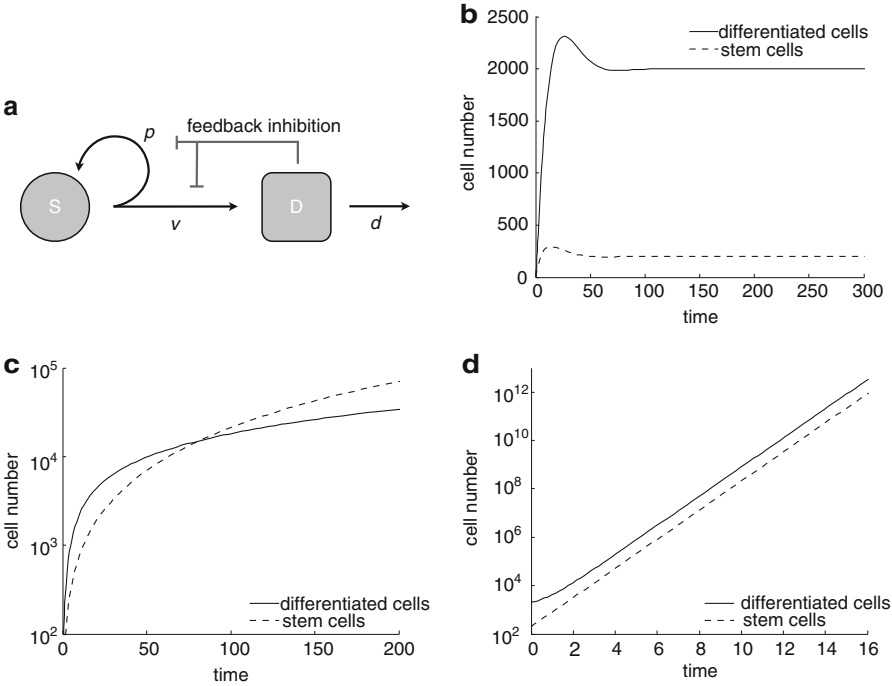

Fig. 1 Feedback-regulated tissue homeostasis and cell growth properties. (**a**) Stem cells divide at a rate v producing either two stem cells with probability p or two differentiated cells with probability $(1-p)$. Differentiated cells die at a rate d and produce factors that promote cell differentiation and inhibit division in stem cells. (**b**) If the feedback loops satisfy specific conditions (discussed in the text) the system has a unique equilibrium point that is independent of the initial conditions and is asymptotically stable. (**c**) *Inhibited growth*. If only differentiation feedback is lost, the population of stem cells and differentiated cells grows without bound at a slower than exponential rate. (**d**) *Uninhibited growth*. If both feedbacks are lost stem cells and differentiated cells grow at a rate dominated by the same exponential. Time is expressed in units of $\ln 2/v(\hat{D})$, the expect duration of one cell cycle at equilibrium. Functional forms used to produce the figure: $p(D) = p_0/(1+gD)$ and $v(D) = v_0/(1+hD)$; $p_0 = 0.6, v_0 = 6.93, d = 6.93 \times 10^{-2}, h = 4.5 \times 10^{-3}, g = 10^{-4}$

System (1) has exactly one nonzero equilibrium point $(\hat{S}, \hat{D})$, defined by the conditions $p(\hat{D}) = 0.5$ and $\hat{S} = d\,\hat{D}/v(\hat{D})$. We proved in [38] that this equilibrium point is asymptotically stable if and onlyif $-p'(\hat{D}) < 1/(2\hat{D})$ (Fig. 1b). Two examples of families of functions that satisfy this condition are given by (2). There are no additional requirements imposed on the function $v(D)$.

$$\begin{aligned} p(D) &= p_0/(1 + g\log(1+D)) \;, 0 < g < 1 \\ p(D) &= p_0/(1 + gD^m) \qquad\quad , 0 < g,\ 0 < m \ (\text{for } m > 1,\ p_0 < \tfrac{m}{2(m-1)}) \end{aligned} \tag{2}$$

3 Feedback Loss and Cell Growth Properties

In this section we will use the model of tissue homeostasis to study the evolutionary dynamics of feedback escape and the consequent emergence of uncontrolled cellular growth. In the model abnormal cell growth occurs when the feedback mechanisms that control the size of the cell population fail. Failures in each of the two feedback mechanisms produce different results. If feedback on the division rate is completely lost, the system remains stable, the steady state number of differentiated cells does not change, and the steady number of stem cells decreases from $d\hat{D}/v(\hat{D})$ to $d\hat{D}/v(0)$. If on the other hand the differentiation feedback is completely lost, we find that the division rate feedback by itself is incapable of controlling cell growth: both the number of stem cells and differentiated cells grow without bound (Fig. 1c). These observations point to the differentiation feedback as the more fundamental of the two control mechanisms. However, even though feedback on the division rate is by itself incapable of stopping abnormal growth, it does play a critical role by significantly slowing down the rate of cell proliferation. If feedback inhibition on stem cell self-renewal is lost, but the feedback on the division rate is still intact, then the population dynamics are characterized by a relatively slow sub-exponential increase of the numbers that we called "inhibited growth" (Fig. 1c). When both feedbacks are lost the growth of the cell population occurs at a faster exponential rate, which we call "uninhibited growth" (Fig. 1d).

There is another distinctive difference between inhibited and uninhibited growth. When uninhibited growth takes place, the ratio of stem cells to differentiated cells in the population converges to a fixed number $((2p_0 - 1)v_0 + d)/(2(1 - p_0)v_0)$. With inhibited growth, we find that this ratio cannot converge. More precisely, the ratio of stem cells to differentiated cells goes to infinity (Fig. 1c). Thus, inhibited tumor growth is relatively slow and characterized by a predominance of stem cells in the cell population at late stages of its development; while uninhibited tumor growth is faster and is characterized by a constant ratio of stem cells to differentiated cells.

4 Mutations and the Evolutionary Dynamics of Feedback Loss

Here we investigate the evolutionary dynamics of cells that carry mutations responsible for corrupted feedback mechanisms. Such cells must emerge from healthy cells and have a growth advantage in order to initiate tumor growth. Mutations can corrupt either the division feedback or the differentiation feedback. In each case, mutations can lead to failures in the production of feedback signals by differentiated cells, or to failures in the response to these signals by stem cells. Hereafter we will call the wild type stem and differentiated cells S and D, and the mutant stem cells and differentiated cells S_m and D_m. We assume that a mutation occurs in one or a small group of stem cells, and that the daughters of the mutant stem cells carry

the same mutations as their parent. We will denote mutations that cause a failure in production of feedback signals by differentiated cells with the prefix D; and those that lead to a failure of response by stem cells to these signals with the prefix S. Mutations that affect cell differentiation will carry the suffix diff- and those that affect the division rate the suffix div-. Note that when we refer to a mutation event that inactivates certain feedback processes, we do not imply that a single mutation is sufficient to achieve this. Indeed, an accumulation of mutations is likely necessary. In the computational model, what we study are the transitions from one phenotype to another; we do not explicitly take into account the number of genetic steps required to attain a particular phenotype, which are certainly specific to the tissue in question.

We consider four types of mutations:

- Stem cells with mutation Ddiff- generate differentiated cells that do not produce the differentiation-promoting factor (described by system (3)).
- Stem cells with mutation Sdiff- do not respond to the differentiation-promoting factor (described by system (4)).
- Stem cells with mutation Ddiv- generate differentiated cells that do not produce the division-inhibiting factor (described by system (5)).
- Stem cells with mutation Sdiv- do not respond to the division-inhibiting factor (described by system (6)).

$$\begin{aligned}
\dot{S} &= (2p(D)-1)\,v(D+D_m)\,S \\
\dot{D} &= 2(1-p(D))\,v(D+D_m)\,S - dD \\
\dot{S}_m &= (2p(D)-1)\,v(D+D_m)\,S_m \\
\dot{D}_m &= 2(1-p(D))\,v(D+D_m)\,S_m - dD_m
\end{aligned} \tag{3}$$

$$\begin{aligned}
\dot{S} &= (2p(D)-1)\,v(D)\,S \\
\dot{D} &= 2(1-p(D))\,v(D)\,S + (2p_0-1)\,v(D)\,S_m - dD \\
\dot{S}_m &= (2p_0-1)\,v(D)\,S_m
\end{aligned} \tag{4}$$

$$\begin{aligned}
\dot{S} &= (2p(D+D_m)-1)\,v(D)\,S \\
\dot{D} &= 2(1-p(D+D_m))\,v(D)\,S - dD \\
\dot{S}_m &= (2p(D+D_m)-1)\,v(D)\,S_m \\
\dot{D}_m &= 2(1-p(D+D_m))\,v(D)\,S_m - dD_m
\end{aligned} \tag{5}$$

$$\begin{aligned}
\dot{S} &= (2p(D)-1)\,v(D)\,S \\
\dot{D} &= 2(1-p(D))\,v(D)\,S + (2p(D)-1)\,v_0\,S_m - dD \\
\dot{S}_m &= (2p(D)-1)\,v_0\,S_m
\end{aligned} \tag{6}$$

We now summarize the main findings in [38]. Mutations that induce a lack of production by differentiated cells of signals that control cell division and differentiation (Ddiv- and Ddiff-, respectively) do not confer a competitive advantage to cells that carry them. This absence of competitive advantage is intuitively explained

by the fact that at any time t the feedback signals are the same for the wild type and mutant stem cells (Eqs. (3) and (5)). If these mutations arise in a very small number of cells, as one should expect from a random mutation, the steady state number of mutant stem cells would remain at a negligible level (Fig. 2a). Moreover, in a stochastic formulation the probability that this species goes extinct is very high. A similar result applies to the mutation inducing a lack of response by stem cells to the division feedback signals Sdiv-. If the system is near equilibrium when the mutation emerges in one cell, the steady state percentage of mutant stem cells will be very small. In practice this means that these three mutations would, in all likelihood, disappear from the cell population. An entirely different scenario occurs if cells acquire a mutation that leads to a loss of response by stem cells to signals that control differentiation Sdiff-. This mutation does confer a competitive advantage to cells that carry it: eventually the mutant stem cells will take over the entire stem cell population and the total number of cells grows without bound (Fig. 2b,d).

Another possibility is that a mutation confers only a partial loss of response to signals that control cell differentiation (denoted by Sdiff-/partial). This scenario is modeled by system (7) where $\tilde{p}(D) \geq p(D)$. In this case the mutation leads to a finite increase in the number of both mutant stem cells and differentiated cells, which results in a sigmoidal growth pattern (Fig. 2c). The size of this increase depends on how diminished the response to the differentiation-promoting factors is. The wild type stem cells go extinct and the ratio of stem cells to differentiated cells does not change.

$$\begin{aligned} \dot{S} &= (2p(D) - 1)\, v(D)\, S \\ \dot{D} &= 2(\,1 - p(D)\,)\, v(D)\, S + 2(1 - \tilde{p}(D))v(D)\, S_m - d\, D \\ \dot{S}_m &= (2\tilde{p}(D) - 1)\, v(D)\, S_m \end{aligned} \tag{7}$$

According to our analysis, the first step towards uncontrolled proliferation must be the loss of stem cell response to the differentiation feedback. We now want to investigate what happens to the cell population if a subsequent mutation occurs in a cell that carries mutation Sdiff-. We find that two types of double mutants, Sdiff-/Ddiff- and Sdiff-/Ddiv-, do not have a competitive advantage to single mutants Sdiff-. If the additional mutation occurs in a single cell, the number of stem cells with a double mutation grows (like the rest of the cell population), but it remains as a very small percentage of the stem cell population. As a result the growth dynamics of the entire cell population do not change in any significant way. A different scenario occurs if the second mutation is Sdiv-. In this case the number of double mutants Sdiff-/Sdiv- grows at an exponential rate while single mutants would continue to growth at a much slower sub-exponential pace. As a result the number of single mutants would eventually become a negligible percentage of the total number of cells and the entire cell population would appear to grow at an exponential rate.

Finally, there is the possibility that a mutation produces only a partial loss in the ability to respond to feedback factors that control the rate of cell division (denoted

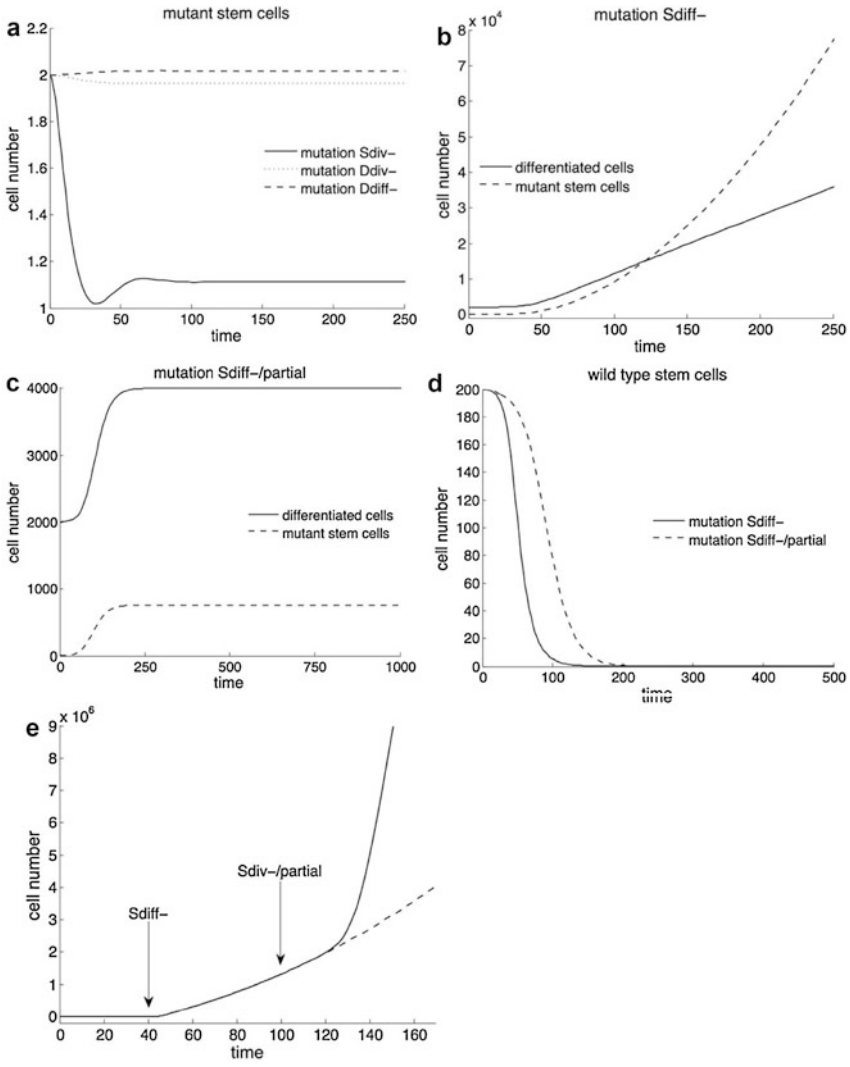

Fig. 2 Evolutionary dynamics of feedback loss. The simulations begin at equilibrium with two stem cells carrying the specified mutation. (**a**) For populations near equilibrium, mutations Sdiv-, Ddiv- and Ddiff- do not confer any competitive advantages over their wild type counterparts. If the mutation arises in a small number of cells, the steady state number of mutant stem cells will be negligible. (**b**) Mutation Sdiff- results in unlimited growth in the number of mutant stem cells and differentiated cells. (**c**) Mutation Sdiff-/partial produces a finite increase in both the number of mutant stem cells and differentiated cells. (**d**) Mutations Sdiff- and Sdiff-/partial result in the extinction of the wild type stem cell population. (**e**) In a cell population that carries mutation Sdiff- (*dashed line*) the appearance of mutation Sdiv-/partial produces an acceleration in the growth rate of the tumor size (*solid line*). (**f**) Tumor progression towards uninhibited growth follows a unique sequence of feedback inactivations: first mutation Sdiff- must occur, followed by mutation Sdiv-. Simulations use the functional forms and parameters of Fig. 1. In panel 2C, $\tilde{p}(D) = 0.1p(D)$; in 2E, $\tilde{v}(D) = 0.05p(D)$

by Sdiv-/partial). If this type of mutation emerges in a population of wild type cells the steady state number of mutants will be negligible and invasion is not possible. However, if the mutation appears in a population of cells that has completely lost feedback on differentiation (mutation Sdiff-), this diminished response to the division rate factors will accelerates the rate of tumor growth (Fig. 2e).

This analysis suggests that full escape from feedback-regulated tissue homeostasis can only occur via a unique sequence of phenotypic transitions that we propose to be common among stem-cell-driven tumors, even if the nature and number of mutational events required to achieve this are certainly tissue specific. First, a mutation must occur that inactivates the ability of stem cells to respond to differentiation feedback factors. In a second step, a mutation has to inactivate the ability of stem cells to respond to division feedback factors. Note that the order in which these mutation types occur is crucial. In terms of growth dynamics, this would lead to an initial slow (inhibited) growth, followed by a fast (uninhibited) growth phase. However, it is important to mention that by the time a tumor is detected, both sets of mutations might have already occurred and thus the transition between both growth phases might not be clinically observed.

5 Evolutionary Dynamics in a Spatial Model

The analysis performed so far uses ordinary differential equations that assume perfect mixing of cells (i.e., no spatial structure) and does not take into account any stochastic effects. This can be a good description for non-solid tumor growth, which allows us to gain a thorough analytical understanding of the system. Many tumors, however, exhibit three-dimensional spatial structure. In this section, we investigate the evolutionary dynamics of feedback loss in a spatial stochastic model.

To construct the spatial model we assume that cells are restricted to a three-dimensional rectangular lattice, such that a lattice point can host at most one cell at any time. As before, stem cells divide producing either two stem cells or two differentiated cells. A cell is capable of cell division only if there is a free lattice point adjacent to it. If a cell division takes place, then one offspring remains in the position occupied by the parent cell and the other occupies a position next to it, which is chosen randomly from the free adjacent lattice points. The simulations are based on the stochastic simulation algorithm [20], where the probabilities of cell division, differentiation, and death correspond to our previous non-spatial mass action model. More precisely let S and D be the number of differentiated cells at a given time t. Let $F \leq S$ be the number of stem cells that are able to divide and α, β and γ be defined by: $\alpha = dD$, $\beta = Fv(D)$, and $\gamma = \alpha + \beta$. To implement the algorithm, set the time of the next reaction to $t' = t - 1/\gamma \log(r)$, where r is a random number uniformly distributed in $[0, 1)$. Then choose the type of reaction that occurs. The next reaction will be either cell death with a probability α/γ, or cell division with a probability β/γ. If the next reaction is cell death, every differentiated cell has the same probability of being chosen; if it is cell division; every stem cell

that is able to divide has the same probability of being selected. Finally, if cell division occurs, the probability that the cell divides into two stem cells is $p(D)$, and the probability that it divides into two differentiated cells is $1 - p(D)$; the place where one of the offspring will reside is chosen at random, with each available adjacent position having an equal probability of hosting one of the daughter cells.

In the spatial stochastic model we find the same basic dynamics of feedback escape (Fig. 3). Again, we observe uninhibited tumor growth if both feedback loops are broken, and inhibited growth when only the differentiation feedback loop is lost. In agreement with the non-spatial model, the percentage of stem cells in the cell population increases progressively with inhibited growth (Fig. 3b), while it converges to a fixed percentage for uninhibited growth. However, in contrast to the non-spatial situation, the tumor growth rates are slower. Uninhibited growth is now

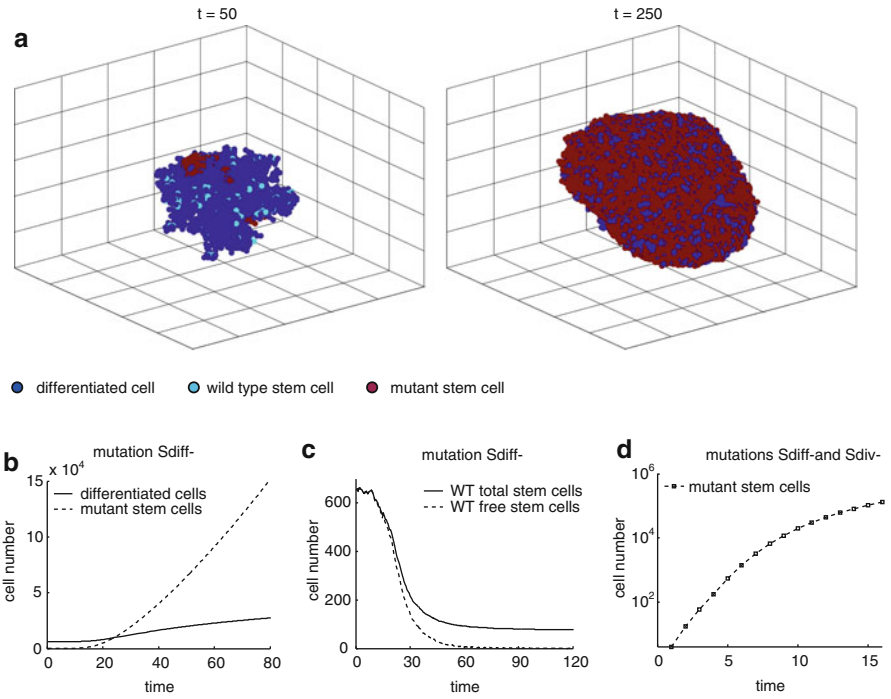

Fig. 3 Spatial model. (**a**) Spatial arrangement of the cell population at two different times. The simulation begins with a tissue at near equilibrium with two stem cells randomly selected to carry mutation Sdiff- at time $t = 0$. (**b**) The appearance of mutation Sdiff- results in the unlimited growth of the mutant stem cell and differentiated cell populations. (**c**) The number of wild type stem cells decreases. Note that a small number of stem cells that are trapped—and thus unable do divide—lingers in the population for a long time. The number of wild type stem cells, however, becomes a negligible percentage of the entire cell population (see text for discussion). (**d**) Cell population with stem cells carrying mutations Sdiff- and Sdiv-. Cell growth is much faster than if only mutation Sdiff- is present; but, unlike the non-spatial model, the growth is not exponential

cubic (not exponential) and inhibited growth sub-cubic (Fig. 3d). This is explained by the fact that in the 3D model the number of stem cells that are able to divide (free cells) is smaller than the total number of stem cells. We also find that full feedback escape can only occur through the same unique sequence of phenotypic transitions. The only mutation that by itself confers a fitness advantage is *S*diff-. The transition from inhibited to uninhibited growth occurs when an *S*diff- mutant acquires the additional mutation *S*div-.

Finally, we note that in the spatial model, when the number mutant stem cells increases the number of wild type stem cells goes down, but a small number of wild type stem cells might persist in the population for a long period of time (Fig. 3c). Indeed, as the overall cell population grows a number of wild type stem cells might get spatially trapped by surrounding cells leaving them no space available to divide. (Fig. 3a). As the cell population grows, however, the number of wild type stem cells becomes a negligible part of the cell population.

Table 1 Fitting parameters in Fig. 5. The functional forms used are $p(D) = p_0/(1 + g\sqrt{D})$ and $v(D) = v_0/(1 + h\sqrt{D})$. For details about the fitting procedure see the methods section in [38]

Figure	p_0	v_0	d	h	g
5A	0.71	0.31 Hours^{-1}	0.736 Hour^{-1}	2.22×10^{-3}	0
5B	0.55	295 Hours^{-1}	126 Hours^{-1}	3.67×10^{-3}	0
5C	0.62	6.29 Days^{-1}	0.251 Days^{-1}	0	0
5D	0.68	1.46 Days^{-1}	0.146 Days^{-1}	0	0
5E	0.67	2.91 Days^{-1}	5.93 Days^{-1}	0	1.74×10^{-4}

6 Predicted Versus Experimentally Observed Growth Patterns

The models analyzed here predict the occurrence of five basic growth patterns, which can be categorized as: exponential, surface, atypical, sigmoidal and multi-step [40]. The first two patterns correspond to uninhibited growth: exponential growth in non-spatial tumors and surface (cubic) growth in spatial tumors. In this categorization both types of inhibited growth (sub-cubic in spatial tumors and sub-exponential in non-spatial tumors) are grouped together under the name of atypical tumor growth. Multi-step growth occurs when a sequence of mutations of type *S*diff-/partial progressively erode the stem cells' ability to respond to feedback signals that promote differentiation. Figure 4 summarizes the different types of mutations and the evolutionary pathways that produce each of these growth patterns.

In the next subsection we will provide references of published tumor growth data for each of the growth patterns discussed. We will also provide data fits for our models. Our modeling approach assumes general functions describing the feedbacks $p(D)$ and $v(D)$; however, data fitting algorithms require us to choose specific functional forms. To produce these fits we use Hill functions to model feedback inhibition (8). Hill functions are widely used to describe ligand–receptor interactions, which make them natural choices to model the actions of secreted feedback factors [2]. Moreover, they have been used extensively to model the specific phenomena of tissue regulation in cell lineage models [7, 10, 26, 30, 42, 62]. The precise data fitting procedures can be found in [38].

$$p(D) = p_0/(1 + gD^n), \quad v(D) = v_0/(1 + hD^m) \tag{8}$$

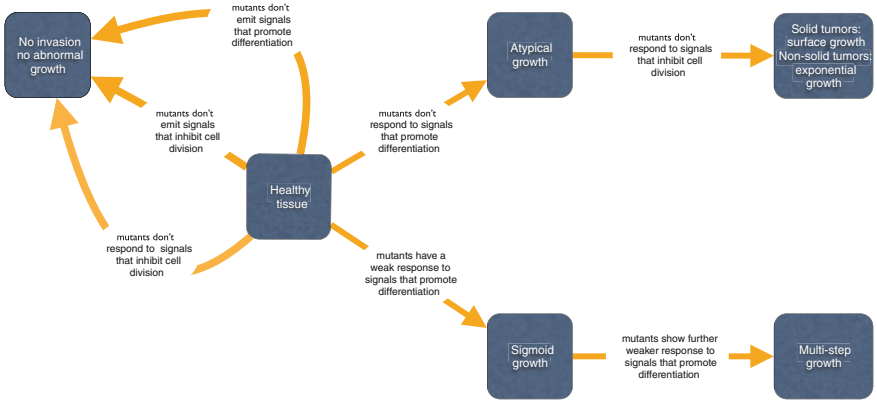

Fig. 4 Schematic representation of the possible phenotypic mutations and their effects on the cell population. According to the model of feedback regulation different evolutionary pathways produce the various tumor growth patterns observed in the literature (See text for discussion)

6.1 Exponential Growth

In our framework this type of growth takes place when feedback on differentiation and feedback on cell division is lost in non-spatial tissues. The growth pattern is produced by the emergence of double mutants Sdiff-/Sdiv-.

Experimentally evidence for exponential tumor growth has been reported in various types of human and murine leukemias [46, 50, 52]. Figure 5c presents In vivo

growth data of L1210 cells [46], a mouse lymphocytic leukemia, which exhibits exponential dynamics representative of an uninhibited growth pattern in a non-spatial setting. The best fit resulted in a value of $g = 0$ and $h = 0$, the case when both feedbacks are lost.

6.2 Surface Growth

In our framework this type of growth takes place when feedback on differentiation and feedback on cell division is lost in spatial tissues. The growth pattern is produced by the emergence of double mutants Sdiff-/Sdiv-. Intuitively this growth pattern takes place when the active growth of a solid tumor is limited to a thin surface layer of cells located near the tumor's boundary.

Experimental evidence for surface tumor growth has been reported in rat sarcomas [24], multicellular tumor spheroids [18, 19], in vitro colonies of various immortalized cancer cell lines [8], and glioblastomas [29]. In Fig. 5d we plot in vitro data from multicellular tumor spheroids of EMT6/Ro cells [19], a mouse mammary tumor. The data shows approximately cubic surface growth (as seen by plotting the cube root of the cell numbers). The best fit of the model occurred when both feedbacks were lost ($g = 0, h = 0$).

6.3 Atypical Growth

In our framework this type of growth takes place when feedback on differentiation is lost, but feedback on the division rate is still operating. The growth pattern is produced by the emergence of single mutants Sdiff-.

Experimental evidence for atypical tumor growth has been reported in breast cancer [22], ovarian carcinoma [48], Ehrlich's ascites tumor [25] and murine leukemia [49]. In Fig. 5a we plot data from Ehrlich's ascites tumor [25] growing in vivo. This tumor, which originated spontaneously as a breast carcinoma in a mouse, grows in ascitic form, i.e., cells mix well. The data shows sub-exponential growth with no saturation, suggesting an inhibited growth pattern. The best fit resulted in a value of $g = 0$ and $h > 0$, a scenario where there is a complete loss of differentiation feedback, but feedback on the division rate is still present. In Fig. 5b we fitted the spatial model to data from A2780 human ovarian carcinoma [48] (a solid tumor) growing in mice. The data shows sub-cubic behavior with a power law of 2.17 and no saturation, consistent with a description of inhibited growth in a spatial setting. With this behavior in mind we fitted the data assuming that feedback on the division rate was still present, but feedback on differentiation had been lost. The main frame shows a projection of the model using the function $y = ax^b$; in the inset the results from the model are plotted together with this function. Simulations were not carried further due to computational constraints.

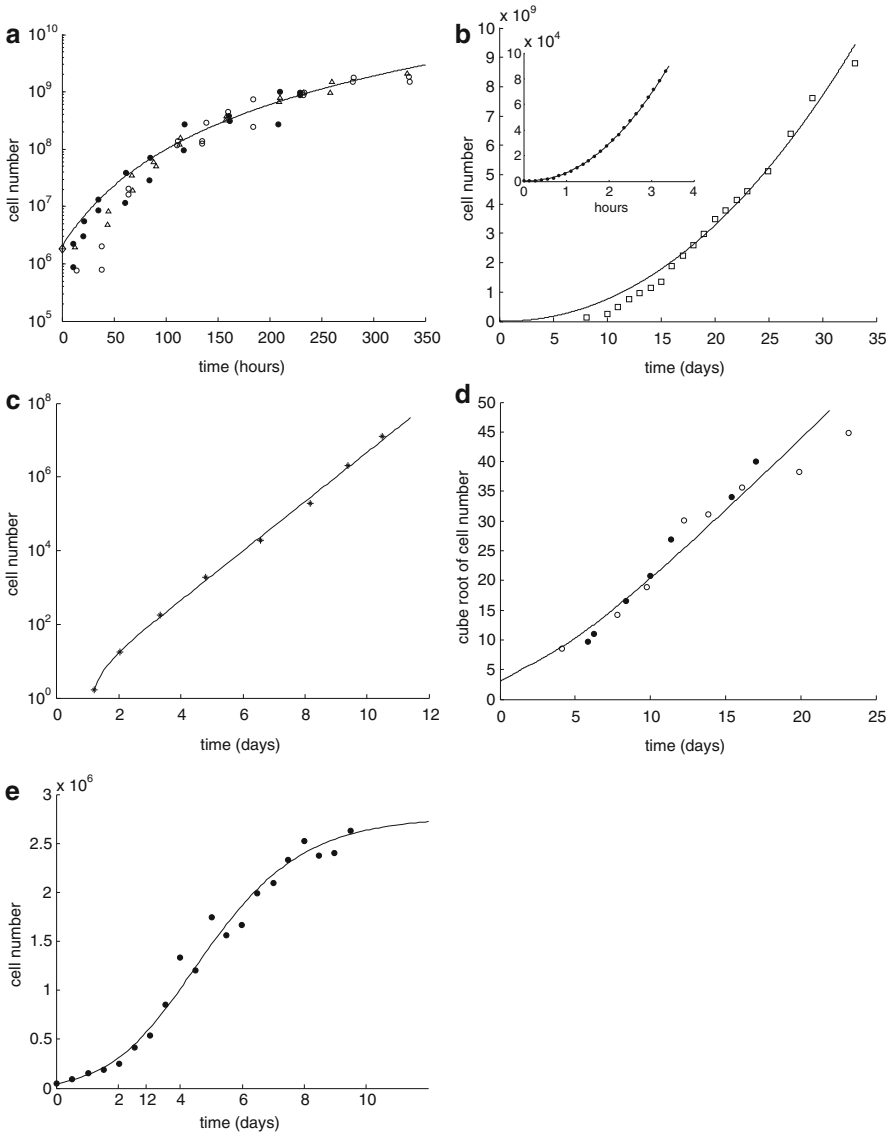

Fig. 5 Experimentally observed growth patterns. (**a**) Atypical pattern. *Inhibited* growth in the non-spatial model. Ehrlich ascites tumor [25] (three experiments shown: •, △, ∘). (**b**) Atypical pattern. *Inhibited* growth in the spatial model. Main frame: (□) A2780 human ovarian carcinoma [48] and projection of the model (*solid line*). *Inset*: Simulation results (•) and projection using the functional form $y = ax^b$. (**c**) Exponential pattern. *Uninhibited* growth in the non-spatial model. (∗) L1210 a mouse lymphocytic leukemia [46]. (**d**) Surface pattern. *Uninhibited* growth in the spatial model. Multicellular tumor spheroids of EMT6/Ro cells [19], a mouse mammary tumor (two experiments shown: ∘, •). (**e**) Sigmoidal pattern. Example in non-spatial tumor. (•) Jurkat T cell human leukemia [37]. In all the plots the simulations are shown in *solid lines*; those corresponding to the spatial model represent the average of 24 runs. For parameters see Table 1

6.4 Sigmoidal Growth

In our framework this type of growth takes place when feedback on differentiation is only partially lost. The growth pattern is produced by the emergence of single mutants of type Sdiff-/partial.

Experimental evidence for sigmoidal tumor growth has been reported for a large number of tumors (see e.g. [21]), which include breast cancer [51, 56], multiple types of rodent tumors [9, 25], and human leukemia [37]. Figure 5e plots data of Jurkat cells [37], originating from a T cell human leukemia. The best fit resulted in a value of $g > 0$, a case where the differentiation feedback mechanism is only partially broken.

6.5 Multi-Step Growth

In our framework this type of growth takes place when a sequence of mutations progressively erode the stem cells' ability to respond to feedback signals that promote differentiation. The growth pattern is produced by sequential acquisitions of the mutations of the type Sdiff-/partial.

This type of growth pattern is at least partially backed by the theory of multistage carcinogenesis. According to this theory, cancer is primarily a genetic disease that requires cells to accumulate sequentially several random mutations and epigenetic changes [34, 35]. Experimental evidence for multi-step tumor growth has been reported in multiple mouse mammary tumors [53] and several types of human sarcomas and carcinomas [36].

7 Dynamics of Tissue Regulation

As we saw in the previous sections tumor initiation requires an escape from the control mechanisms that maintain tissue homeostasis. It is fundamental then to understand the regulatory mechanisms themselves and how their dynamics are shaped by two objectives: promoting the rapid regeneration after an injury and maintaining tissue homeostasis under normal conditions.

Let us again focus our attention on the regulation of the rates of stem cell division and self-renewal by negative feedback factors and go back to the analysis of system (1). First, as we recall that the equilibrium number of stem cells $\hat{S}$ and differentiated cells $\hat{D}$ is characterized by the conditions $p(\hat{D}) = 1/2$ and $\hat{S} = d\,\hat{D}/v(\hat{D})$. Hence, the equilibrium number of differentiated cells $\hat{D}$ depends only on the self-renewal probability $p(D)$, and the equilibrium fraction of stem cells $\hat{S}/(\hat{S} + \hat{D})$ on the ratio $d/v(\hat{D})$. To understand the recovery of the system after a

perturbation we look at the eigenvalues of the Jacobian matrix evaluated at $(\hat{S}, \hat{D})$. If we write $b = (2p'(\hat{D})\hat{D} + 1)$ and $\hat{v} = v(\hat{D})$, the eigenvalues are:

$$\lambda_1, \lambda_2 = \frac{-db \pm \sqrt{d^2b^2 + 4d(b-1)\hat{v}}}{2} \tag{9}$$

From this last equation it follows that the equilibrium values are asymptotically stable if and only if $b > 0$. Conversely if $b < 0$, the equilibrium is unstable. If $b = 0$ a Hopf bifurcation might be possible, but this would depend on the specific choice of the regulation functions $v(D)$ and $p(D)$.

In most tissues the number of stem cells makes up only a small fraction of the entire cell population [57]. It is important then to understand how this requirement affects the cell dynamics of the regulatory system. In particular we will find that the equilibrium fraction of stem cells is related to the possibility of oscillatory behavior after an injury.

To avoid oscillation near the equilibrium point we need the discriminant Δ in (9) to be non-negative. As we mention earlier the fraction of stem cells is completely determined by the ratio $\varepsilon = d/\hat{v}$: the smaller ε the smaller the fraction of stem cells. We prove in [39] that if $\Delta \geq 0$, then:

$$\lim_{\varepsilon \to 0} \lambda_1, \lambda_2 = -d, 0 \tag{10}$$

Now, if the absolute value of one of the eigenvalues is very small, then the dynamics of the system are characterized by rapid approach to a slow manifold, followed by a very slow approach toward equilibrium. Hence, we find a trade-off between requiring a small equilibrium fraction of stem cells (ε small) while avoiding oscillations and the speed at which the system is able to recover from a perturbation (influenced by the magnitude of the eigenvalues).

We find then that the existence of a stable nontrivial steady state is independent of feedback inhibition on the division rate. Moreover, for a fixed equilibrium division rate $\hat{v}$ the steady state population sizes are independent on the actual function $v(D)$. The role of feedback on the division rate in the system lies instead in increasing the speed at which the system recovers from a perturbation and reducing the amplitude of oscillations if they happen to occur.

To illustrate these dynamics we perform simulations using Hill equations (8) to model the feedback functions $p(D)$ and $v(D)$. Figure 6a,b track the trajectory of a cell population that only has feedback on stem cell differentiation ($v(D)$ constant). In Fig. 6b the fraction of stem cells is less than 10 % and the maximum self-renewal probability is kept small ($p_0 = 0.51$). For the special case of Hill functions it is shown in [39] that by keeping the maximum self-renewal probability p_0 very small it is possible to avoid oscillations while keeping the fraction of stem cells low. However, in agreement with the previous results this comes at the price of having a slow speed of regeneration indicated by the small value of p_0.

Figure 6c,d plot the trajectories for systems with feedback inhibition in both the self-renewal probability and the division rate of stem cells. Call $\beta(D) = 1 + hD^m$,

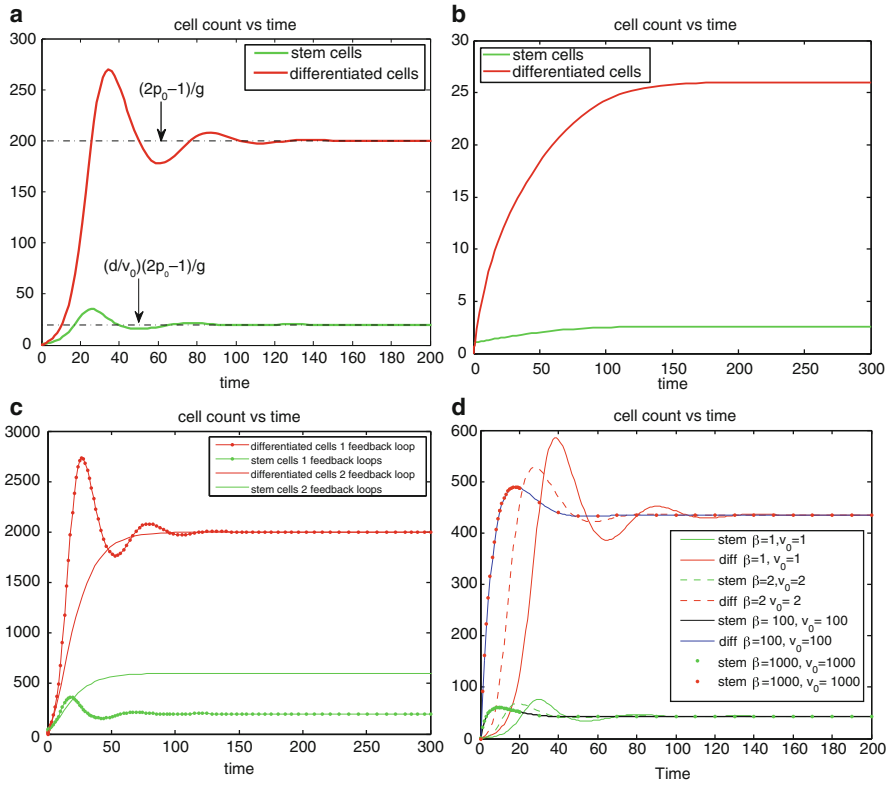

Fig. 6 (**a**) and (**b**) Cell population with one feedback loop. (**a**) The trajectories oscillate towards steady state values (*dotted line*). Parameters, $p_0 = 0.6$, $d = 0.1$, $g = 0.001$, $S(0) = 1$, $D(0) = 0$. (**b**) If there is only one feedback loop the maximum self-renewal probability must be very close to 0.5 to ensure that the trajectories approach the steady states monotonically. In this subfigure d and g are the same as in (**a**) but $p_0 = 0.513$. (**c**) and (**d**) cell population with two feedback loops. (**c**) The steady state number of differentiated cells depends only p_0 and g and is independent of feedback on the division rates. The steady state number of stem cells increases when the number of feedback loops increase from one to two. The addition of feedback in the division rate dampens or altogether eliminates the oscillations. (**d**) Fitting fixed steady state values of stem cells and differentiated cells values with different levels of feedback inhibition in the division rate. The stronger the feedback signal in the division rate the smoother the transition the equilibrium transition to equilibrium

then $v(D) = v_0/\beta(D)$ and $\beta(D)$ controls the strength of the inhibition signal. We can get a specific target division rate at equilibrium $\hat{v}$ with different combinations of the pair $(v_0, \beta(\hat{D}))$; the larger themagnitude of these quantities, the stronger the feedback in the division rate will be. Figure 6d plots the trajectories for the same target number of cells with different combinations of the pair $(v_0, \beta(\hat{D}))$. Note how the addition of feedback on the division rate provides for smoother and faster recoveries after a perturbation.

8 Tissue Regulation in a Spatial-Stochastic Model

We now want to assess the dynamics of tissue regulation in the spatial-stochastic model that was introduced earlier. In general we find that the addition of a spatial structure results in smoother transitions from perturbed states to equilibrium. When there are oscillations in the spatial model the amplitudes are smaller than those found in the corresponding mass action formulation (Fig. 7a,b). Moreover, as we discuss in [39] oscillation in the mass action model after extreme perturbation could result in the stochastic extinction of the stem cell pool. The number of these extinctions is greatly reduced by the addition of the spatial structure. For example, with the set of parameters ($p_0 = 0.7, v_0 = 0.2, g = 2 \times 10^{-5}, \beta = 1, d = 0.0025$), a perturbation of the initial conditions $(S(0), D(0)) = 0.1(\hat{S}, \hat{D})$ resulted in the stochastic extinction of the cell population in all of 100 independent simulations using the a stochastic version of the mass action model. By comparison extinction never took place in 30 simulations using the spatial-stochastic model with the same set of parameters and initial conditions.

In the spatial model we can divide stem cells into two categories: free stem cells, which have adjacent free lattice points and are thus capable of cell division; and trapped stem cells, which are completely surrounded by cells and are thus unable to divide. The equilibrium fraction of stem cells in the mass action model is the same as the equilibrium number of free stem cells in the spatial model. Hence, for the same set of parameters the equilibrium number of stem cells will be greater in the spatial model than in the non-spatial model (Fig. 7b,c).

Suppose that we start with a perturbation in which the number of differentiated cells is less than $\hat{D}$. Then the probability of differentiation is small and most cell divisions result in the production of two stem cells. Once the number of differentiated cells is above $\hat{D}$, differentiation becomes the more likely event and in the ODE model one sees a steep reduction in the number of stem cells. In the spatial model, however, the rapid growth phase means that the fraction of free stem cells is reduced as most stem cells become trapped by other stem cells. Only these free stem cells are able to divide, slowing down the speed at which they are depleted and thus reducing the severity of the oscillations. This behavior is exemplified by Fig. 7b.

9 Discussion

A wealth of data indicates that feedback loops play a central role in the regulation of healthy tissue. Recent data also supports the notion that tumors retain some of the architectural aspects of the underlying healthy tissue. It is thought that tumors are maintained and driven by so-called tumor stem cells or tumor initiating cells, and that the bulk of the tumor is made up of more differentiated cells that have a reduced ability to divide and therefore cannot maintain or initiate a cancer. In the light of

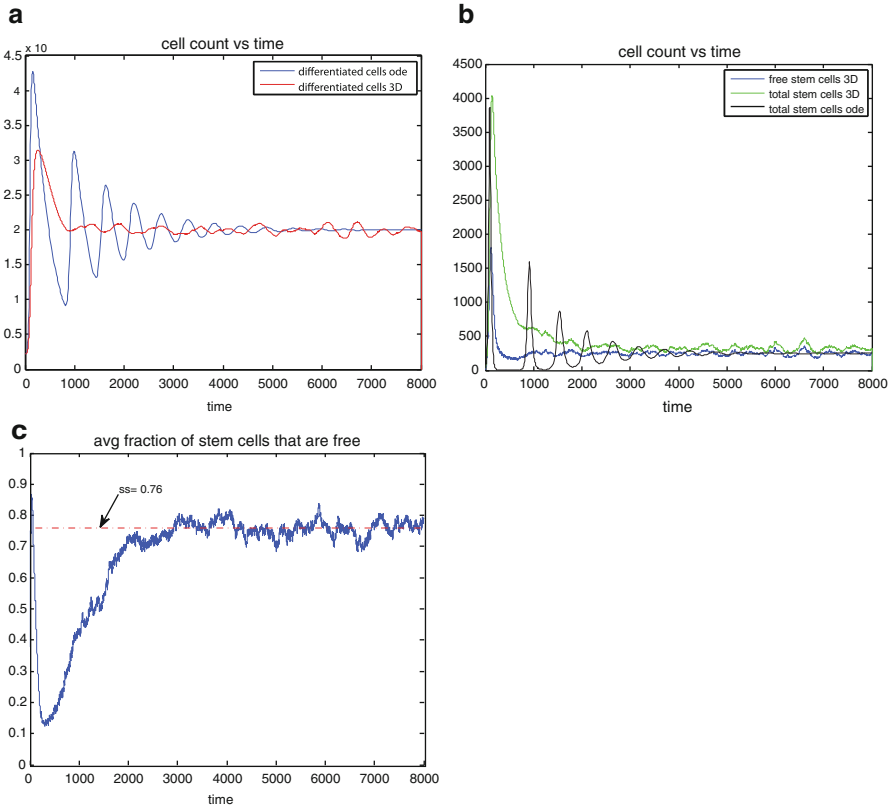

Fig. 7 (**a**) Cell count of differentiated cells vs time. The *blue line* was computed using the ODE model. The *red line* is the expected cell count in the spatial-stochastic model. (**b**) Cell count of stem cells. Results from the ODE (*black*) and expected cell count in spatial model (*green*). The expected number of cells in the spatial model is shown in *blue*. (**c**) Expected fraction of stem cells that are free in the three-dimensional model. Parameters in all figures are: $p_0 = 0.7$, $v_0 = 0.2$, $g = 2 \times 10^{-5}$, $\beta = 1$ and $d = 0.0025$

this, it is reasonable to assume that tumor initiation requires the loss of some of these feedback loops. In particular, two types of feedback mechanisms appear to be a common theme across different tissues: negative feedback on the rate of stem cell division, and negative feedback on the probability that a stem cell division results in self-renewal rather than in differentiation. Mutations can occur that lead to the loss of feedback signals produced by cells or that lead to a loss of response to the feedback signals by stem cells. Using an evolutionary dynamics model, it is found that only one sequence of events can lead to full escape from feedback control: The first step is loss of the cells' ability to respond to the differentiation feedback. While this leads to unbounded cell growth, the cell population grows relatively slowly because the emerging tumor is still regulated in part by remnants of the feedback system (inhibited growth). To escape this remaining regulation, cells also have to

lose the ability to respond to the division feedback control factors, leading to fast, uninhibited growth. We note that the order of events is crucial here. In a healthy cell population, mutant cells that do not respond to the division feedback will not enjoy a selective advantage and are therefore unlikely to emerge. Such mutants are only selected for and can only emerge in a background population that has already lost the ability to respond to the differentiation feedback factors.

Our analysis is supported by key mutations in carcinogenesis that disrupt negative feedback regulation of cell division patterns. For example, the protein transforming growth factor beta (TGF-β) plays a key role in tissue homeostasis by inhibiting mitosis and promoting cell differentiation [57]. Mutations that affect TGF-β receptors occur in gastric, biliary, pulmonary, ovarian, esophageal, and head and neck carcinomas [32]. Moreover, half of all pancreatic carcinomas and more than a quarter of colon cancers carry mutations that make cells irresponsive to TGF-β signals that inhibit cell division and promote differentiation [43, 59]. Another example comes from the epigenetic silencing of BMP4 receptors in glioblastomas [27]. BMP4 induces glia stem cells to differentiate, inhibiting cell proliferation [28].

Another line of evidence that supports the importance of the Sdiff- phenotype comes from the manipulation of the MYC gene. A mouse model of human hepatocellular carcinoma was developed, in which it is possible to regulate the expression of the human MYC oncogene in murine liver cells, suppressing it through doxycycline treatment [16,44,45]. Mice treated with doxycycline remained disease free, while those with active MYC developed malignant tumors that were locally invasive and able to metastasize. When MYC was subsequently inactivated, rapid tumor regression was observed that was associated with terminal differentiation into normal liver cells. MYC expression influences self-renewal and differentiation of cells, and thus influences the function $p(D)$ in our model. Activation of MYC corresponds to a corrupted differentiation feedback (i.e., to the Sdiff- phenotype in the model), whereas inhibition of MYC reverses this phenotype. The model predicts Sdiff- to be the initial event leading to uncontrolled growth. Even if cells have acquired other mutations that can also contribute to tumor progression, these mutations are predicted to promote growth only in cells that already have corrupted differentiation feedback. Hence, the model predicts that the restoration of the differentiation feedback loop, even in cells with further alterations, results in tumor regression. This same behavior is observed in the experiments where the macroscopic and malignant nature of the tumors indicate the presence of additional mutations, which are incapable of promoting growth in the absence of MYC [16, 44, 45].

Overall, these processes can give rise to five different categories of tumor growth laws, which we call “exponential,” “surface,” “sigmoidal,” “atypical,” and “multi-step.” Following an extensive literature search for different tumor growth patterns, we suggest that most can be assigned to one of these categories. Fitting our model to experimental data on in vitro and in vivo tumor cell growth, we demonstrated that the predicted growth patterns describe biological data well. The finding of inhibited tumor growth patterns in the literature is of particular interest. Such a growth pattern can only come about if the growing tumor is still partially subject to regulation

that has remained from the underlying tissue. This gives support to the notion that tumors are organized and structured according to similar principles as healthy tissue, at least early in the disease process. The finding of sub-cubic growth laws among data is particularly notable in this respect because it has not been possible to ascribe such slow growth to factors other than feedback. While we have shown that our model can describe a range of tumor growth data well, a crucial experimental test would be to document the presence of negative feedback loops in early tumors that are characterized by an inhibited growth pattern, and to further demonstrate that elimination of this feedback loop leads to accelerated tumor growth.

The findings discussed here have implications for elucidating carcinogenesis pathways in specific cancers. While we have identified the sequence of two key phenotypic events in the emergence of stem-cell-driven tumors, this does not mean that each event corresponds to a single mutation. The inactivation of feedback responses can involve a multi-step accumulation of mutations, the nature of which are most likely tissue specific. Hence, it will be important to identify the relevant feedback loops in the tissues under consideration, and to study the nature of the mutations that are required for the sequential escape documented here. This could lead to the discovery of new targets for therapeutic intervention.

We also discussed how the two feedback mechanisms affect the dynamics of tissue regulation. Feedback on the rate of stem cell differentiation uniquely determines the equilibrium number of differentiated cells and is by itself capable of maintaining tissue homeostasis. Feedback on rate of stem cell division controls the fraction of stem cells in the population and promotes faster recoveries from perturbations.

It was also found that when the system is recovering from a perturbation oscillations in the number of cells might take place, a behavior that may be dangerous and of no obvious biological value. Near equilibrium oscillations are more likely to occur when the steady state fraction of stem cells is small. Adding feedback inhibition on the division rate significantly dampens the magnitude of the oscillations and increases the speed at which the trajectories reach the steady states; the stronger the feedback signal the stronger the effect. Thus, even if feedback on the division rate is unnecessary to establish control, it promotes faster and more stable recoveries after an injury. The addition of spatial structure to the tissue also adds to the robustness of the systems, by eliminating oscillations or significantly reducing their amplitude.

Understanding the population dynamics that take place during tissue regeneration has important applications and has led to significants insights (see, e.g., [26]). In particular the study of oscillatory behavior is relevant to the dynamics of blood cells. Damped oscillations have been observed in healthy hematopoiesis [31]. Amongst pathologies periodic oscillations are a characteristic feature of cyclical neutropenia [6]. Furthermore, oscillatory behavior has also been identified in chronic and acute myeloid leukemia [1, 3, 12].

Two principal aims of regulatory mechanisms in hierarchical tissues are the maintenance of homeostasis, which prevents the onset of cancer, and the promotion of fast and reliable recovery from injuries. In this chapter we discussed several

mathematical models that identify key features of the regulatory mechanisms that promote tissue regeneration and stability. Furthermore, we discussed the phenotypical pathways by which cancer can escape tissue regulation and how this might leas to different types of tumor growth patterns. These insights could help the search for mutations that drive specific cancers and could lead to novel ideas for treatment.

Acknowledgements This work was funded by NIH grant R01 CA129286.

References

1. Adimy, M., Crauste, F., Ruan, S.: Modelling hematopoiesis mediated by growth factors with applications to periodic hematological diseases. Bull. Math. Biol. **68**, 2321–2351 (2006)
2. Alon, U.: An introduction to systems biology: design principles of biological circuits. Chapman and Hall/CRC mathematical and computational biology series, vol. 10. Chapman and Hall/CRC, Boca Raton (2007)
3. Andersen, L.K., Mackey, M.C.: Resonance in periodic chemotherapy: a case study of acute myelogenous leukemia. J. Theor. Biol. **209**, 113–130 (2001)
4. Arino, O., Kimmel, M.: Stability analysis of models of cell production systems. Math. Model. **7**(9), 1269–1300 (1986)
5. Ashkenazi, R., Gentry, S.N., Jackson, T.L.: Pathways to tumorigenesis–modeling mutation acquisition in stem cells and their progeny. Neoplasia **10**, 1170–1182 (2008)
6. Bernard, S., Bélair, J., Mackey, M.C.: Oscillations in cyclical neutropenia: new evidence based on mathematical modeling. J. Theor. Biol. **223**, 283–298 (2003)
7. Bocharov, G., Quiel, J., Luzyanina, T., Alon, H., Chiglintsev, E., Chereshnev, V., Meier-Schellersheim, M., Paul, W.E., Grossman, Z.: Feedback regulation of proliferation vs. differentiation rates explains the dependence of cd4 t-cell expansion on precursor number. Proc. Natl. Acad. Sci. USA **108**, 3318–3323 (2011)
8. Bru, A., Albertos, S., Subiza, J. Garcia-Asenjo, J., Bru, I.: The universal dynamics of tumor growth. Biophys. J. **85**, 2948–2961 (2003)
9. Choe, S.C., Zhao, G., Zhao, Z., Rosenblatt, J.D., Cho, H.-M., Shin, S.-U., Johnson, N.F.: Model for in vivo progression of tumors based on co-evolving cell population and vasculature. Sci. Rep. **1**, 31 (2011)
10. Chou, C.-S., Lo, W.-C., Gokoffski, K.K., Zhang, Y.-T., Wan, F.Y.M., Lander, A.D., Calof, A.L., Nie, Q.: Spatial dynamics of multistage cell lineages in tissue stratification. Biophys J. **99**, 3145–3154 (2010)
11. Clevers, H.: The cancer stem cell: premises, promises and challenges. Nat. Med. **17**, 313–319 (2011)
12. Colijn, C., Mackey, M.C.: A mathematical model of hematopoiesis–i. periodic chronic myelogenous leukemia. J. Theor. Biol. **237**, 117–132 (2005)
13. Daluiski, A., Engstrand, T., Bahamonde, M.E., Gamer, L.W., Agius, E., Stevenson, S.L., Cox, K., Rosen, V., Lyons, K.M.: Bone morphogenetic protein-3 is a negative regulator of bone density. Nat. Genet. **27**, 84–88 (2001)
14. Elgjo, K., Reichelt, K.L.: Chalones: from aqueous extracts to oligopeptides. Cell Cycle **3**, 1208–1211 (2004)
15. Enderling, H., Anderson, A.R.A., Chaplain, M.A.J., Beheshti, A., Hlatky, L., Hahnfeldt, P.: Paradoxical dependencies of tumor dormancy and progression on basic cell kinetics. Cancer Res. **69** 8814–8821 (2009)

16. Felsher, D.W.: Cancer revoked: oncogenes as therapeutic targets. Nat. Rev. Cancer **3**, 375–380 (2003)
17. Frank, S.A., Dynamics of Cancer: Incidence, Inheritance, and Evolution. Princeton University Press, Princeton (2007)
18. Freyer, J.P., Sutherland, R.M.: A reduction in the in situ rates of oxygen and glucose consumption of cells in emt6/ro spheroids during growth. J. Cell Physiol. **124**, 516–524 (1985)
19. Freyer, J.P., Sutherland, R.M.: Regulation of growth saturation and development of necrosis in emt6/ro multicellular spheroids by the glucose and oxygen supply. Cancer Res. **46**, 3504–3512 (1986)
20. Gillespie, D.T.: Exact stochastic simulation of coupled chemical reactions. J. Phys. Chem. **81**(25), 2340–2361 (1977)
21. Guiot, C., Degiorgis, P.G., Delsanto, P.P., Gabriele, P., Deisboeck, T.S.: Does tumor growth follow a universal law? J. Theor. Biol. **225**, 147–151 (2003)
22. Hart, D., Shochat, E., Agur, Z.: The growth law of primary breast cancer as inferred from mammography screening trials data. Br. J. Cancer **78**, 382–387 (1998)
23. Johnston, M.D., Edwards, C.M., Bodmer, W.F., Maini, P.K., Chapman, S.J.: Mathematical modeling of cell population dynamics in the colonic crypt and in colorectal cancer. Proc. Natl. Acad. Sci. USA **104**, 4008–4013 (2007)
24. Knighton, D., Ausprunk, D., Tapper, D., Folkman, J.: Avascular and vascular phases of tumour growth in the chick embryo. Br. J. Cancer **35**, 347–356 (1977)
25. Laird, A.K.: Dynamics of tumor growth. Br. J. Cancer **13**, 490–502 (1964)
26. Lander, A.D., Gokoffski, K.K., Wan, F.Y.M., Nie, Q., Calof, A.L.: Cell lineages and the logic of proliferative control. PLoS Biol. **7**, e15 (2009)
27. Lee, J., Son, M.J., Woolard, K., Donin, N.M., Li, A., Cheng, C.H., Kotliarova, S., Kotliarov, Walling, Y.J., Ahn, S., Kim, M., Totonchy, M., Cusack, T., Ene, C., Ma, H., Su, Q., Zenklusen, J.C., Zhang, W., Maric, D., Fine, H.A.: Epigenetic-mediated dysfunction of the bone morphogenetic protein pathway inhibits differentiation of glioblastoma-initiating cells. Cancer Cell **13**, 69–80 (2008)
28. Lim, D.A., Tramontin, A.D., Trevejo, J.M., Herrera, D.G., García-Verdugo, J.M., Alvarez-Buylla, A.: Noggin antagonizes bmp signaling to create a niche for adult neurogenesis. Neuron **28**, 713–726 (2000)
29. Mandonnet, E., Delattre, J.-Y., Tanguy, M.-L., Swanson, K.R., Carpentier, A.F., Duffau, H., Cornu, P., Van Effenterre, R., Alvord, Jr. E.C., Capelle, L.: Continuous growth of mean tumor diameter in a subset of grade ii gliomas. Ann. Neurol. **53**, 524–528 (2003)
30. Marciniak-Czochra, A., Stiehl, T., Ho, A.D., Jäger, W., Wagner, W.: Modeling of asymmetric cell division in hematopoietic stem cells–regulation of self-renewal is essential for efficient repopulation. Stem Cells Dev. **18**, 377–385 (2009)
31. Marciniak-Czochra, A., Stiehl, T.: Model based parameter estimation: theory and applications. Contributions in mathematical and computational sciences. Mathematical Models of Hematopoietic Reconstitution after Stem Cell Transplantation, vol. 4, pp. 191–207. Springer, New York (2013)
32. Massagué, J.: Tgf? in cancer. Cell **103**, 295–309 (2000)
33. McPherron, A.C., Lawler, A.M., Lee, S.J.: Regulation of skeletal muscle mass in mice by a new tgf-beta superfamily member. Nature **387**, 83–90 (1997)
34. Meza, R., Jeon, J., Moolgavkar, S.H., Luebeck, E.G.: Age-specific incidence of cancer: Phases, transitions, and biological implications. Proc. Natl. Acad. Sci. USA **105**, 16284–16289 (2008)
35. Moolgavkar, S.H., Knudson, Jr. A.G.: Mutation and cancer: a model for human carcinogenesis. J. Natl. Cancer Inst. **66**, 1037–1052 (1981)
36. Retsky, M.W., Swartzendruber, D.E., Wardwell, R.H., Bame, P.D.: Is gompertzian or exponential kinetics a valid description of individual human cancer growth? Med. Hypotheses **33**, 95–106 (1990)

37. Reuss, R., Ludwig, J., Shirakashi, R., Ehrhart, F., Zimmermann, H., Schneider, S., Weber, M.M., Zimmermann, U., Schneider, H., Sukhorukov, V.L.: Intracellular delivery of carbohydrates into mammalian cells through swelling-activated pathways. J. Membr. Biol. **200**, 67–81 (2004)
38. Rodriguez-Brenes, I.A., Komarova, N.L., Wodarz, D.: Evolutionary dynamics of feedback escape and the development of stem-cell-driven cancers. Proc. Natl. Acad. Sci. USA **108**, 18983–18988 (2011)
39. Rodriguez-Brenes, I.A., Wodarz, D., Komarova, N.L.: Stem cell control, oscillations, and tissue regeneration in spatial and non-spatial models. Front Oncol. **3**, 82 (2013)
40. Rodriguez-Brenes, I.A., Komarova, N.L., Wodarz, D.: Tumor growth dynamics: insights into evolutionary processes. Trends Ecol. Evol. **28**, 597–604 (2013)
41. Rodriguez-Brenes, I.A., Wodarz, D., Komarova, N.L.: Minimizing the risk of cancer: tissue architecture and cellular replication limits. J. R. Soc. Interface **10**, 20130410 (2013)
42. Rodriguez-Brenes, I.A., Komarova, N.L., Wodarz, D.: Cancer-associated mutations in healthy individuals: assessing the risk of carcinogenesis. Cancer Res. **74**(6), 1661–1669 (2014)
43. Rozenblum, E., Schutte, M., Goggins, M., Hahn, S.A., Panzer, S., Zahurak, M., Goodman, S.N., Sohn, T.A., Hruban, R.H., Yeo, C.J., Kern, S.E.: Tumor-suppressive pathways in pancreatic carcinoma. Cancer Res. **57**, 1731–1734 (1997)
44. Shachaf, C.M., Kopelman, A.M., Arvanitis, C., Karlsson, A., Beer, S., Mandl, S., Bachmann, M.H., Borowsky, A.D., Ruebner, B., Cardiff, R.D., Yang, Q., Bishop, J.M., Contag, C.H., Felsher, D.W.: Myc inactivation uncovers pluripotent differentiation and tumour dormancy in hepatocellular cancer. Nature **431**, 1112–1117 (2004)
45. Shachaf, C.M., Felsher, D.W.: Tumor dormancy and myc inactivation: pushing cancer to the brink of normalcy. Cancer Res. **65**, 4471–4474 (2005)
46. Shackney, S.E.: A computer model for tumor growth and chemotherapy, and its application to l1210 leukemia treated with cytosine arabinoside (nsc-63878). Cancer Chemother. Rep. **54**, 399–429 (1970)
47. Shizuru, J.A., Negrin, R.S., Weissman, I.L.: Hematopoietic stem and progenitor cells: clinical and preclinical regeneration of the hematolymphoid system. Annu. Rev. Med. **56**, 509–538 (2005)
48. Simeoni, M., Magni, P., Cammia, C., De Nicolao, G., Croci, V., Pesenti, E., Germani, M., Poggesi, I., Rocchetti, M.: Predictive pharmacokinetic-pharmacodynamic modeling of tumor growth kinetics in xenograft models after administration of anticancer agents. Cancer Res. **64**, 1094–1101 (2004)
49. Simpson-Herren, L., Lloyd, H.H.: Kinetic parameters and growth curves for experimental tumor systems. Cancer Chemother. Rep. **54**,143–174 (1970)
50. Skipper, H.E., Schabel, Jr. F.M., Wilcox, W.S.: Experimental evaluation of potential anticancer agents. xiii. on the criteria and kinetics associated with curability of experimental leukemia. Cancer Chemother. Rep. **35**, 1–111 (1964)
51. Spratt, J.A., von Fournier, D., Spratt, J.S., Weber, E.E.: Decelerating growth and human breast cancer. Cancer **71**, 2013–2019 (1993)
52. Steel, G.G.: Growth Kinetics of Tumours: Cell Population Kinetics in Relation to the Growth and Treatment of Cancer. Clanesdon press, Oxford (1977)
53. Squartini, F.: Strain differences in growth on mouse mammary tumors. J. Nat. Cancer Inst. **26**, 81 (1961)
54. Tomlinson, I.P., Bodmer, W.F.: Failure of programmed cell death and differentiation as causes of tumors: some simple mathematical models. Proc. Natl. Acad. Sci. USA **92**, 11130–11134 (1995)
55. Tzeng, Y.-S., Li, H., Kang, Y.-L., Chen, W.-C., Cheng, W.-C., Lai, D.-M.: Loss of cxcl12/sdf-1 in adult mice decreases the quiescent state of hematopoietic stem/progenitor cells and alters the pattern of hematopoietic regeneration after myelosuppression. Blood **117**, 429–439 (2011)

56. Weedon-Fekjaer, H., Lindqvist, B.H., Vatten, L.J., Aalen, O.O., Tretli, S.: Breast cancer tumor growth estimated through mammography screening data. Breast Cancer Res. **10**(3), R41 (2008)
57. Weinberg, R.A.: The Biology of Cancer. Garland Science, New York (2007)
58. Werner, B., Dingli, D., Lenaerts, T., Pacheco, J.M., Traulsen, A.: Dynamics of mutant cells in hierarchical organized tissues. PLoS Comput. Biol. **7**, e1002290 (2011)
59. Woodford-Richens, K.L., Rowan, A.J., Gorman, P., Halford, S., Bicknell, D.C., Wasan, H.S., Roylance, R.R., Bodmer, W.F., Tomlinson, I.P.: Smad4 mutations in colorectal cancer probably occur before chromosomal instability, but after divergence of the microsatellite instability pathway. Proc. Natl. Acad. Sci. USA **98**, 9719–9723 (2001)
60. Wu, H.-H., Ivkovic, S., Murray, R.C., Jaramillo, S., Lyons, K.M., Johnson, J.E., Calof, A.L.: Autoregulation of neurogenesis by gdf11. Neuron **37**, 197–207 (2003)
61. Yamasaki, K., Toriu, N., Hanakawa, Y., Shirakata, Y., Sayama, K., Takayanagi, A., Ohtsubo, M., Gamou, S., Shimizu, N., Fujii, M., Miyazono, K., Hashimoto, K.: Keratinocyte growth inhibition by high-dose epidermal growth factor is mediated by transforming growth factor beta autoinduction: a negative feedback mechanism for keratinocyte growth. J. Invest. Dermatol. **120**, 1030–1037 (2003)
62. Zhang, L., Lander, A.D., Nie, Q.: A reaction-diffusion mechanism influences cell lineage progression as a basis for formation, regeneration, and stability of intestinal crypts. BMC Syst. Biol. **6**, 93 (2012)

A Cellular Automata Model to Investigate Immune Cell–Tumor Cell Interactions in Growing Tumors in Two Spatial Dimensions

Trisilowati, Scott W. McCue, and Dann G. Mallet

Abstract We develop a hybrid cellular automata model to describe the effect of the immune system and chemokines on a growing tumor. The hybrid cellular automata model consists of partial differential equations to model chemokine concentrations, and discrete cellular automata to model cell–cell interactions and changes. The computational implementation overlays these two components on the same spatial region. We present representative simulations of the model and show that increasing the number of immature dendritic cells (DCs) in the domain causes a decrease in the number of tumor cells. This result strongly supports the hypothesis that DCs can be used as a cancer treatment. Furthermore, we also use the hybrid cellular automata model to investigate the growth of a tumor in a number of computational "cancer patients." Using these virtual patients, the model can explain that increasing the number of DCs in the domain causes longer "survival." Not surprisingly, the model also reflects the fact that the parameter related to tumor division rate plays an important role in tumor metastasis.

1 Introduction

In this chapter, we present a mathematical model of a growing tumor and the interaction between the tumor cells and the host immune system using a cellular automata model. This model can describe the system in much more detail than models based on ordinary differential equations because it allows for spatial variations and cell–cell interactions of every single cell in the system.

Strong evidence exists in the literature supporting the hypothesis that tumor growth is directly influenced by the cellular immune system of the host. We stress this point further and note some specific interactions that, with the cellular automata

Trisilowati
Department of Mathematics, Brawijaya University, Jalan Veteran Malang 65145, Indonesia

S.W. McCue • D.G. Mallet (✉)
Mathematical Sciences School, Queensland University of Technology,
GPO Box 2434, Brisbane 4001, Australia
e-mail: dg.mallet@qut.edu.au

A. Eladdadi et al. (eds.), *Mathematical Models of Tumor-Immune System Dynamics*, Springer Proceedings in Mathematics & Statistics 107,
DOI 10.1007/978-1-4939-1793-8_9

(CA) modeling strategy, can now be incorporated directly into our mathematical model. Hart [21] states that dendritic cells (DCs), found in many types of tumors, are the dominant antigen-presenting cells for initiating and maintaining the host immune response. They are critical in activating, stimulating, and recruiting T lymphocytes which have the ability to lyse tumor cells. Also, Sandel et al. [42] discuss the influence of DCs in controlling prostate cancer. Furthermore, tumor-infiltrating DCs are a key factor at the interface between the innate and adaptive immune responses in malignant diseases. Beside their primary role in the induction and regulation of the adaptive anti-tumoral immune response, more recent studies have shown that DCs have a capacity to directly kill cancer cells [27]. Natural killer (NK) cells and cytotoxic T lymphocyte cells also play important roles in the response of the immune system against the tumor as described in Kindt et al. [25].

In the tumor microenvironment, the tumor produces chemokines that can attract components of the immune system including DCs, NK cells, and T cells to the neighborhood. Chemokines are a family of small cytokines, or proteins secreted by many different cell types, including tumor cells. These chemokines also function to activate DCs which, in turn, can stimulate and activate other parts of the immune system [46]. They can affect cell–cell interactions and play a fundamental role in the recruiting or attracting of cells of the immune system to sites of infection or, of interest in the present research, tumor growth.

The dynamics of tumor growth has been studied intensively using mathematical models over the past four decades (see also Araujo and McElwain for a review to the early 2000s [4]) with the interaction of growing tumors with the host immune system rising to prominence in around the last 15 years. Many of these models are presented using ordinary differential equations (ODEs) or partial differential equations (PDEs). Such methodologies impose restrictions on the modeled system's time-scales, as described in Ribba et al. [39].

Unlike ODE and PDE models, CA models can describe more complex mechanisms in the biological system without such restrictions by way of detailing phenomena at the individual cell or particle level. In this chapter we employ a *hybrid* cellular automata (HCA) modeling strategy, allowing us to extend the CA to incorporate other effects by coupling a CA with PDEs.

The interactions of a tumor and the host immune system using the CA framework have been modeled previously by, for example, Mallet and de Pillis [31] and de Pillis et al. [12], where they presented the first multidimensional, hybrid cellular automata model of the process that incorporated important signalling molecules. However, these models and others neglected to describe DCs and chemokines and their roles in tumor growth and control. Kim and Lee also modeled cancer and immunity via a hybrid model, however the approach they took was to use an agent-based model coupled with a system of delay differential equations [24]. In this chapter, we offer an alternative to Kim and Lee's model and improve on the work of Mallet and de Pillis by explicitly describing more of the host immune system.

The purpose of the model developed in the present research is to investigate the growth of a small solid tumor when that growth is affected by the immune system.

To this end, we present a hybrid cellular automata model of the interaction between a growing tumor and cells of the innate and specific immune system, including the role of DCs and chemokines.

To include the effect of a chemokine in this model, we recognize the significantly smaller size of such molecules compared with biological cells and introduce a PDE to describe the concentration of chemokine secreted by the tumor. We combine the numerical solution of the PDE with a number of biologically motivated automata rules to govern the evolution of various cell populations from the HCA model. We use the hybrid cellular automata model to simulate the growth of a tumor in a number of computational "cancer patients." Each simulated patient is distinguished from others by way of patient-specific characteristics reflected through particular parameter choices. We define "death" of a patient as the situation where the cells of the tumor reach the boundary of our model domain; effectively this represents tumor metastasis.

In the sections to follow, we present a discussion of the role of DCs and chemokines related to cell–cell interactions in tumor growth. Furthermore, the development of the HCA model is considered before analyzing numerical simulations. We conclude with a discussion of the results.

2 The Role of Dendritic Cells and Chemokines

Here we present a more detailed discussion of the role of the immune system (especially DCs) and chemokines as related to cell–cell interactions in tumor growth. This discussion provides us the basis for making rules in HCA model.

The immune system plays an important role in defending the body against pathogens by identifying and killing non-self or foreign matter such as viral particles, parasites and importantly here, tumor cells [41]. The immune system consists of two components: namely the innate and adaptive systems. The innate immune system, including DCs, NK cells, and macrophages, can recognize antigen without the requirement for previous priming by specific non-self antigens [41]. However, the adaptive immune system, including cytotoxic T cells, helper T cells and B cells, need the antigen to be processed and presented in a histocompatibility complex through antigen presenting cells (APCs) [5, 41]. DCs are known to be the most efficient APC and express high levels of MHC class I and II molecules [20].

Current evidence suggests that there is a large number of functional states for DCs and their immunogenic capacity depends on the microenvironment [29]. The tumor microenvironment is a complex system that consists of the extracellular matrix [38] and stromal cells including fibroblasts, endothelial cells, lymphocytes, macrophages, DCs, and neutrophils, and it supports and regulates tumor growth [38, 46].

In the tumor microenvironment, DCs play a crucial role in activating, stimulating and recruiting the immune system. DCs can be activated by chemokines secreted by tumor cells or after direct interactions with the tumor itself [38, 46]. These activated DCs can stimulate and regulate components of the immune system including CTL

cells [44] and NK cells, which after activation can directly kill tumor cells [7, 20]. Furthermore, helper T cells that are activated by DCs [44] can produce chemokines which, in turn, lead to CTL cell stimulation [46].

Dendritic cells found in various types of solid tumors are antigen presenting cells that initiate and regulate immunity as well as shape the host response to tumors [13, 21]. They play an important role in activating, stimulating, recruiting, and developing the immune response. Therefore, it can be concluded that tumor-infiltrating DCs play a key role in a cellular anti-tumor immune response by infiltrating, capturing, and processing tumor antigens, recruiting and activating the immune system [13, 42].

Dendritic cells play a vital role as the major regulator in CTL cell and NK cell activation [10, 15, 27], they also can control the activation of B cells [5]. As well, DCs have a unique function depending on their stage of maturation. Immature DCs (iDC) are very efficient in antigen uptake and are capable of presenting captured antigens through their surface receptors. After antigen uptake, DCs migrate from peripheral tissues to the lymph nodes, where antigen presentation to the immune system occurs [5, 45]. In the secondary lymphoid tissues, DCs are mature and able to attract, interact, and activate the immune system including T lymphocytes and helper T cells to initiate a primary immune response [1].

Cytotoxic T cells are activated by DCs through antigens presented to MHC class I molecules. Also, DCs activate CD4 helper T cells which then secrete chemokines that can enhance immunoglobulin production. CD4 helper T cells are activated by binding via their T cell receptor (TCR) to MHC class II molecules. Then they can be recognized by specific CD4 helper T cells in the cell membrane, where MHC peptide complex is presented to the CD4 helper T cells by DCs. CD4 cells can be categorized according to the type of signalling that they receive, Th1 CD4 helper T cells and Th2 CD4 helper T cells. Th1 CD4 helper T cells secrete chemokines such as IL-2, thereby stimulating cell-mediated immunity by activating CTL cells. Th2 CD4 helper T cells mediate an antibody response by releasing chemokines such as IL-4 and IL-10 [20].

On the other hand, active CTL cells can kill mature DCs [9] by presenting antigen on their surface. In a recent study, cytokine-induced killer T cells (CIK), expanded T cells from *ex vivo* have been shown to selectively eliminate iDC by direct cytotoxicity [23]. Furthermore, Moretta [34] notes that NK cells can downregulate the function of DCs by killing iDCs in peripheral tissues, and also states that NK cells might have a role in killing mature DCs.

Dendritic cells are considered as the most potent component of the immune system because they facilitate transport of antigen-presenting cells to the lymphoid tissue and provide efficient stimulation of T cells [30]. From experimental studies in mice, DCs have been shown to be very efficient in stimulating CTL cells [30]. Because of their unique role in initiating and regulating the immune response, currently DCs are exploited in the hope of becoming a novel tool for cancer therapy. It has been shown that DCs are feasible, safe [8, 32, 43], and efficient for treatment of some cancer patients, especially if DCs are matured and activated [1]. The first study related to DC vaccination was carried out by Hsu et al. in 1996 [22].

They investigated the ability of DCs pulsed *ex vivo* to stimulate host anti-tumor immunity in patients with B cell lymphoma. Other research, for example, Schuler et al. [43], Fong et al. [19], and Burgdorf et al. [8], also discussed the use of DCs in cancer immunotherapy.

Chemokines and chemokine receptors, important in immune homeostatis and surveillance, also play an important role in the tumor environment. In the tumor microenvironment, chemokines are produced both by stromal cells (fibroblasts, endothelial cells, and infiltrating leukocytes) and by the tumor itself [3, 46]. Tumors, such as glioblastoma, melanoma, and neuroblastoma, secrete high levels of chemokines that can promote tumor growth and progression. These chemokines also can induce stromal cells to produce cytokines or chemokines which, in turn, can regulate angiogenesis, tumor growth, and metastasis in the tumor microenvironment [46]. Stromal cells within the tumor, including DCs, lymphocytes, fibroblasts, macrophages, and neutrophils, may be activated by tumor cells through cell–cell interactions or cytokines or chemokines produced by tumor cells [46].

Chemokines secreted by tumor or stromal cells can also attract a large number of leukocytes such as DCs, NK cells, and T cells (helper T and cytotoxic T lymphocytes) to the tumor site which may result in tumor regression and elimination [46]. Although chemokines secreted by tumor cells can stimulate or inhibit tumor growth, modulation of chemokine activity in a selective manner at the site of the tumor can lead to tumor cell apoptosis. These kinds of chemokines can be chosen for their potential to attract immune cells to the tumor site that may result in successful tumor treatment. From experiments involving mouse tumors, chemokines such as CCL5 and CCL21 are promising avenues for cancer therapy investigations [37, 47].

3 Mathematical Model

We consider the early growth of a solid tumor and its interaction with the immune system and a tumor-secreted chemokine. The model is comprised of a system of partial differential equations to describe the chemokines secreted by the tumor and $CD4^+$ T cells, coupled with a discrete, stochastic cellular automata that describes the various cell types comprising the host-tumor environment.

Following Ferreira et al. [16,17] and de Pillis et al. [12,31] the tumor environment is modeled as a square-shaped computational domain of side length L (see Fig. 1). Each square element in the grid represents a location that may contain a healthy cell, tumor cell, or immune cell. The domain is partitioned into a regular square grid with each element of the grid representing a space approximately corresponding with the size of a tumor cell (around 10–20μm; [2, 28]). These elements are the discrete locations considered in the cellular automata component of the model, while the midpoint of each element will be used as a mesh-point in the numerical scheme used to solve the partial differential equation component.

Initially, non-cancerous healthy cells cover the whole of the model domain, then the tumor mass is allowed to grow from one cancer cell placed at the center

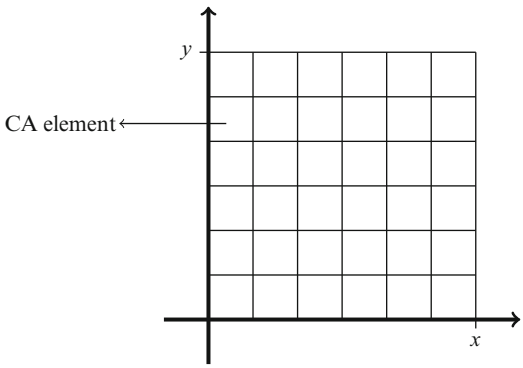

Fig. 1 Schematic showing the partitioning of the problem domain into cellular automata elements (*squares*) and mesh-points for numerical solution of the partial differential equation

of the grid. Cells of the host immune system are initially spread randomly over the domain throughout the other healthy cells. Four separate immune cell populations are considered here—the NK cells and DCs of the innate immune system and cells of the specific immune response, represented by the CTL cells and helper T cells. Each of these four cell types may exist in either an active or inactive state.

Computationally, the CA grid is stored as a two-dimensional data structure (matrix) with CA elements directly corresponding with elements of the data structure. The number stored in the matrix corresponds with the type of cell occupying that element in the domain, according to the definitions given in Table 1.

Simulations of the model progress via discrete time steps, at which each spatial location is investigated to determine its contents and ascertain whether or not any change will occur. This is summarized in Algorithm 1.

The rules for the cellular automata component as well as the form of the diffusion equation for chemokines are presented below.

3.1 Diffusion Equation for Chemokine Concentration

Chemokines are small (8–14 kDa, in size [38]), cell-secreted protein molecules that can affect cell–cell interactions. In this model we consider two different chemokine molecules. Given that such molecules are very small compared with the size of tumor and host cells, we treat them essentially as a continuum and use a partial differential equation to model changes in their concentration in space and time. Denoting the concentration of the chemokines as $C_1(x, y, t)$ and $C_2(x, y, t)$ we have,

$$\frac{\partial C_1}{\partial t} = D_{C_1}\left(\frac{\partial^2 C_1}{\partial x^2} + \frac{\partial^2 C_1}{\partial y^2}\right) + \sigma T, \tag{1}$$

$$\frac{\partial C_2}{\partial t} = D_{C_2}\left(\frac{\partial^2 C_2}{\partial x^2} + \frac{\partial^2 C_2}{\partial y^2}\right) - \lambda C_2 + \gamma + \alpha D^A H^I - \beta C_2 I^I, \tag{2}$$

Table 1 The different cell species tracked in the cellular automata and the numerical value denoting each species in the computational implementation

Number	Description
0	Healthy cell
1	Tumor cell
2	Necrotic debris
3	Inactive $CD8^+$ cytotoxic T cell
4	Active $CD8^+$ cytotoxic T cell
5	Inactive dendritic cell
6	Active dendritic cell
7	Inactive $CD4^+$ helper T cell
8	Active $CD4^+$ helper T cell
9	Active natural killer cell
10	Inactive natural killer cell

Algorithm 1 Pseudocode overview for the full model algorithm

```
Set parameters for current computational patient
Initialize CA domain contents
Solve PDEs
for each time step do
    for each CA element do
        Determine cell type in element
        Characterize neighborhood of element
        Update PDE solutions (chemokine concentration)
        Test whether event will occur and update state
    end for
end for
Export data
```

where D_{C_1} and D_{C_2} are the diffusion coefficients for the chemokines. The parameter σ is the rate of secretion of chemokine by tumor cells. The rate of chemokine secretion by $CD4^+$ helper T cells is represented by λ as a natural degradation rate and γ as a natural production rate. The constant α represents the rate of secretion of chemokine resulting from interactions between activated DCs and helper T cells, while β represents the rate at which chemokine is used up in activating $CD8^+$ cytotoxic T cells. The description of model variables can be seen in Table 2.

Initially and on the boundaries, we assume that there are no chemokines. However, these partial differential equations must be solved at each time step of the HCA model. Given that chemokines are secreted by the tumor cells and when $CD4^+$ T helper cells and DCs come in contact (in the cellular automata component of the model), at later times the initial condition used in a HCA time step becomes nonzero and is in fact provided by the outcomes of the cell-level interactions.

Table 2 The variables used in the hybrid cellular automata model. Here x and y are the spatial variables for the PDE component, t denotes the time variable, and i and j represent spatial locations in the cellular automata component

Variable	Description
$C_1(x, y, t)$	Concentration of chemokine secreted by tumor cells
$C_2(x, y, t)$	Concentration of chemokine secreted by $CD4^+$ T cells
$N_{i,j}$	Healthy host cell
$T_{i,j}$	Tumor cell
$D^I_{i,j}$	Inactive dendritic cell
$D^A_{i,j}$	Active dendritic cell
$I^I_{i,j}$	Inactive $CD8^+$ cytotoxic T cell
$I^A_{i,j}$	Active $CD8^+$ cytotoxic T cell
$H^I_{i,j}$	Inactive $CD4^+$ helper T cell
$H^A_{i,j}$	Active $CD4^+$ helper T cell
$K^I_{i,j}$	Inactive natural killer cell
$K^A_{i,j}$	Active natural killer cell

3.2 Cellular Automata Rules

In this model, we consider a number of biological cell types including normal healthy cells, tumor cells (necrotic, dividing and migrating), DCs, NK cells, CTL cells, and helper T cells. To build the CA model, we define "rules" that draw upon the biological literature to describe cell–cell interactions, cell effects on the environment, and effects of the environment on cells.

The evolution of the cell species involved in the tumor-host interactions considered here is governed by a set of discrete, stochastic rules which are presented below. Each particular cell-level action or interaction has associated with it, a probability of success. Generally speaking, we calculate the number

$$P^{\text{cell}}_{\text{event}} = f(.),$$

where f depends on relevant cell types and conditions in the neighborhood. We compare $P^{\text{cell}}_{\text{event}}$ with a pseudo-random number, r, drawn from the uniform distribution on the interval [0,1]. If $r < P^{\text{cell}}_{\text{event}}$, then the event is carried out, otherwise the event is deemed to have failed to occur. To describe the evolution of the cell population, we introduce the general algorithm for our cellular automata rules, as presented in Algorithm 2.

We now consider each cell type in turn and introduce the specific forms of the CA rules utilized in the model.

Algorithm 2 Pseudocode for testing occurrence of individual events.

```
Draw r ~ U[0, 1]
Calculate P_event^cell using current state of CA
if r < P_event^cell then
    update state (the event occurs)
end if
```

3.2.1 Host Cells

Following from the work of Ferreira et al. [16] and of Mallet and de Pillis [31], we assume that the healthy host cells are effectively passive bystanders in the interaction. They do not hinder the growth of the tumor cells or the movement of any cell type.

3.2.2 Tumor Cells

In this model, we consider tumor growth to be influenced by the immune system via NK cells, CTL cells, and DCs. The tumor cells undergo the processes of division, migration, and lysis resulting from interactions with components of the immune system such as NK cells, $CD8^+$ cytotoxic T cells, and DCs. We assume lysis is dependent upon the local strength of the immune system and model division to be influenced by crowding due to the presence of other tumor cells, respectively.

At each time step, the neighborhood of each tumor cell is surveyed to determine whether the cells of the active immune system are present or not. If immune cells are present, the tumor cell is marked for potential lysis whereas if there are no active immune system cells in the neighborhood, then the tumor cell is marked for potential division or migration. A stochastic rule is then implemented to determine whether or not the action (division, migration or lysis) will be carried out. While the time-scales of these processes can vary (between or within cell types), for generality we consider equal time-scales and tie to this the time step of the numerical solution method. With this in mind, we impose the following cellular automata rules for tumor cells.

Cell division: When a tumor cell is marked for division, that action is carried out with a probability that depends upon the density of tumor cells in the neighborhood of the dividing cell. In particular, we have

$$P_{\text{div}}^{\text{T}} = 1 - \frac{\sum_{i,j\in\eta} T_{i,j}}{8},$$

where $\sum_{i,j\in\eta} T_{i,j}$ is the number of tumor cells in a one-cell radius of the cell of interest.

When division occurs, the resulting daughter cell is placed in an element of the neighborhood of the dividing cell in the following order: filling an empty element,

replacing (killing and consuming/removing) a healthy host cell, adding to the tumor burden of the least filled neighboring element. From Fig. 2a, it can be seen that tumor cell division is more likely when there is space in the neighborhood for the resulting daughter cell.

Lysis by CD8$^+$ cytotoxic T cells: Active CD8$^+$ T cells are able to directly lyse tumor cells when they share a local neighborhood. We assume that the intensity of the immune system effect is proportional to the number of active CD8$^+$ T cells in the neighborhood of the tumor cell. The probability of tumor lysis depends on the strength of the active immune system in the neighborhood of the tumor cell (see Fig. 2b), and is given by

$$P^{\mathrm{T}}_{\mathrm{lysis}} = 1 - \exp\left(-\left(\theta_{\mathrm{lysis}} \sum_{i,j\in\eta} \left(I^A_{i,j} + K^A_{i,j} + D^A_{i,j}\right)\right)^2\right),$$

where again θ_{lysis} controls the shape of the curve allowing it to capture qualitative understanding of the biology and

$$\sum_{i,j\in\eta} \left(I^A_{i,j} + K^A_{i,j} + D^A_{i,j}\right)$$

is the number of active immune cells in a one-cell radius of the tumor cell of interest.

Cell migration: At each time step the tumor cells marked for migration do so with a constant probability, k_1 as given below

$$P^{\mathrm{T}}_{\mathrm{mig}} = k_1.$$

These rules are presented in pseudocode form in Algorithm 3.

3.2.3 CD4$^+$ Helper T Cells

Inactive CD4$^+$ helper T cells are subject to change as a result of natural replenishment and activation due to direct interaction between DCs and existing inactive CD4$^+$ helper T cells. At each time step, the neighborhood of each inactive CD4$^+$ helper T cell is surveyed to determine whether DCs are present. If any DCs are present, then the CD4$^+$ helper T cell is marked for potential activation, otherwise the CD4$^+$ helper T cell is marked for random migration. A stochastic rule is then implemented to determine whether or not the action (migration or activation) will be carried out. A normal background level of inactive CD4$^+$ helper T cells is also maintained at each time step. To this end, we impose the following cellular automata rules.

Algorithm 3 Pseudocode for tumor cell related events.

```
if (location holds tumor cell) then
    Calculate the number of tumor cells in the neighborhood
    Calculate the number of immune cells in the neighborhood
    Find new location at random in the neighborhood
    Draw r ~ U[0, 1]
    Calculate P_div^T using current state of CA
    Calculate P_lysis^T using current state of CA
    if r < P_div^T and (new location holds healthy cell) then
        fill new location with tumor cell
    else if r < P_lysis^T then
        current surface become necrotic debris
    else if r < P_mig^T then
        cell move
    end if
end if
```

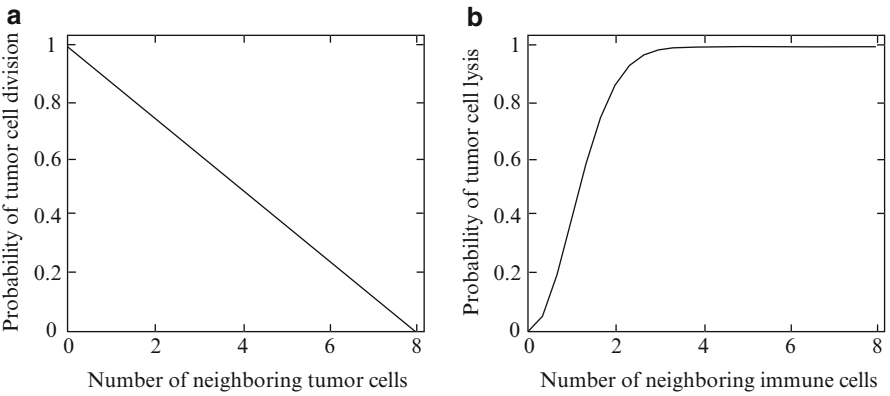

Fig. 2 The form of the *curves* used to determine the probability of (**a**) tumor cell division and (**b**) tumor cell lysis, given different neighborhood conditions

Activation following DC and inactive CD4$^+$ helper T cell contact: When inactive helper T cells come in contact with DCs, they have probability

$$P_{\text{act}}^{\text{CD4}} = 1 - \exp\left(-\sum_{i,j\in\eta}\left(D_{i,j}^{I} + D_{i,j}^{A}\right)^2\right)$$

of becoming active CD4$^+$ T cells which are then able to secrete chemokines to activate cytotoxic T cells (see Eq. (2)). Here

$$\sum_{i,j\in\eta}\left(D_{i,j}^{I} + D_{i,j}^{A}\right)$$

is the number of inactive and active DCs in a one-cell radius of the cell of interest.

CD4$^+$ T cell migration: If any DCs are present, then the CD4$^+$ helper T cell is marked for potential activation, otherwise the CD4$^+$ helper T cell is marked for random migration with probability of migration given by

$$P_{\text{mig}}^{\text{CD4}} = k_2.$$

Natural replenishment to background level: A near-constant minimum background level of inactive and active helper T cells is ensured at each time step by replacing some healthy cells on the boundary with inactive helper T cells. This mimics replenishment of the CD4$^+$ population from external sources (such as the lymph nodes). At each time step we determine the proportion of all locations in the domain occupied by inactive and active helper T cells. Whenever this is less than the minimum background level, H_0, each healthy cell on the boundary of the domain has probability

$$P_{\text{rep}}^{\text{CD4}} = H_0 - \frac{1}{n^2} \sum_{i,j \in \eta} \left(H_{i,j}^I + H_{i,j}^A \right)$$

of being replaced with an inactive CD4$^+$ T cell from outside of the problem domain, where H_0 is the 'normal' density of inactive CD4$^+$T helper cells and n^2 is the total number of CA elements.

These rules are presented in pseudocode form in Algorithm 4.

Algorithm 4 Pseudocode for CD4$^+$ helper T cell related events.

```
if (location holds inactive CD4+ helper T cell ) then
    Calculate the number of tumor cells in the neighborhood
    Find inactive DCs in the neighborhood
    Calculate the number of inactive and active DCs in the neighborhood
    Draw r ~ U[0, 1]
    Calculate P_act^CD4 using current state of CA
    if The number of tumor cells in the neighborhood >= 1 then
        current surface replace with healthy cell
    else if r < P_act^CD4 then
        current surface replace with active CD4+ helper T
    else if r < constant then
        inactive CD4+ helper T cell moves towards the higher chemokine concentration
    end if
end if
```

3.2.4 CD8$^+$ Cytotoxic T Cells

Inactive CD8$^+$ cytotoxic T cells are subject to change as a result of natural replenishment and activation as a result of direct interaction between existing

inactive $CD8^+$ cytotoxic T cells and either active DCs, tumor cells, or cytokines produced by active $CD4^+$ helper T cells. At each time step, the neighborhood of each inactive $CD8^+$ cytotoxic T cell is surveyed to determine whether active DCs or tumor cells are present. If any DCs or tumor cells or cytokines are present, then the inactive $CD8^+$ cytotoxic T cell is marked for potential activation, otherwise the $CD8^+$ cytotoxic T cell is marked for random migration or movement towards regions of higher chemokine concentration. If the chemokine level secreted by active $CD4^+$ T cells is greater than some threshold concentration, C_{2_0}, then the inactive $CD8^+$ cytotoxic T cell is marked for activation. A stochastic rule is then implemented to determine whether or not the action (migration or activation) will be carried out. A normal background level of inactive $CD8^+$ T cells is also maintained at each time step. As a result, we impose the following cellular automata rules.

Activation following DC and/or tumor cell and inactive $CD8^+$ T cell contact: When inactive cytotoxic T cells come in contact with DCs and/or activated T cells they have probability

$$P_{\text{act}}^{\text{CD8}} = 1 - \exp\left(-\left(\sum_{i,j\in\eta} D_{i,j}^{I} + I_{i,j}^{A}\right)^2\right),$$

of becoming active $CD8^+$ T cells, which are then able to lyse tumor cells. Here

$$\sum_{i,j\in\eta}\left(D_{i,j}^{I} + I_{i,j}^{A}\right),$$

is the number of active DCs and active $CD8^+$ T cells in a one-cell radius of the cell of interest. We assume that active $CD8^+$ cytotoxic T cells can lyse tumor cells more than once. $CD8^+$ cytotoxic T cells are neutralized if there are no more tumor cells in the neighborhood. $CD8^+$ cytotoxic T cells can also kill active DCs. At each time step, the neighborhood of each active $CD8^+$ cytotoxic T cell is surveyed to determine whether active DCs are present. If any DCs are present, then the $CD8^+$ cytotoxic T cells lyse the DCs.

$CD8^+$ T cell migration: At each time step the inactive $CD8^+$ T cells marked for migration do so with a constant probability given by,

$$P_{\text{mig}}^{\text{CD8}} = k_3.$$

Natural replenishment to background level: Similar to the helper T cells, a near-constant minimum background level of inactive and active cytotoxic T cells is maintained at each time step by replacing some healthy cells on the boundary with inactive cytotoxic T cells. At each time step we determine the proportion of all locations in the domain occupied by inactive and active cytotoxic T cells.

Whenever this is less than the minimum background level, I_0, each healthy cell on the boundary of the domain has probability

$$P_{\text{rep}}^{\text{CD8}} = I_0 - \frac{1}{n^2} \sum_{i,j \in \eta} \left(I_{i,j}^{I} + I_{i,j}^{A} \right)$$

of being replaced with an inactive $CD8^+$ T cell from outside of the problem domain, where I_0 is the 'normal' density of inactive $CD8^+$ T cells and n^2 is the total number of CA elements.

These rules are presented in pseudocode form in Algorithm 5.

Algorithm 5 Pseudocode for inactive $CD8^+$ T cell related events.

```
if (location holds CD8+ T cell) then
    Calculate the number of tumor cells in the neighborhood
    Find active DCs in the neighborhood
    Find active CD4+ helper T cells in the neighborhood
    Calculate chemokine concentration in the neighborhood
    Find new location at random in the neighborhood
    Draw r ~ U[0, 1]
    Calculate P_act^CD8 using current state of CA
    if the number of tumor cells in the neighborhood >= 1 then
        current surface replace with active CD8+ T cell
    else if r < P_act^CD8 then
        current surface replace with active CD8+ T cell
    else if chemokine concentration > threshold chemokine concentration then
        current surface replace with active CD8+ T cell
    else if r < k_3 then
        inactive CD8+ T cells move to the new location
    end if
end if
```

3.2.5 Dendritic Cells

Inactive DCs are activated when they come in contact with either chemokines secreted by tumor cells or with the tumor itself. DCs process the tumor-associated antigens and present the antigen on their cell surface. Active DCs play an important role in the activation of T cells and can also be lysed by activated $CD8^+$ cytotoxic T cells as a result of presenting antigen on their surface. At each time step, the neighborhood of each inactive DC is surveyed to determine whether tumor cells or chemokines are present nearby. If either are present, the DCs are marked for potential activation. The neighborhood of each active dendritic cell is surveyed for the presence of active $CD8^+$ T cells. If the chemokine concentration level secreted by tumor cells is greater than some threshold concentration, C_{1_0}, then the inactive

DC is marked for activation. When active cytotoxic T cells reside nearby, the DC is marked for potential lysis. A stochastic rule is then implemented to determine whether or not the action (migration, lysis, or activation) will be carried out. A normal background level of inactive DCs is also maintained at each time step. As a result, we impose the following cellular automata rules.

Activation by interaction with chemokines and/or tumor cells: Inactive DCs process and present tumor associated antigen upon interaction with tumor cells. That is, active DCs are activated with a probability given by

$$P_{\text{act}}^{\text{DC}} = 1 - \exp\left(-\left(\theta_{\text{act}} \sum_{i,j \in \eta} T_{i,j}\right)^2\right),$$

where θ_{act} controls the shape of the curve allowing it to capture qualitative understanding of the biology and $\sum_{i,j \in \eta} T_{i,j}$ is the number of tumor cells in a one-cell radius of the cell of interest.

Lysis by active CD8$^+$ T cells: CD8$^+$ T cells kill DCs presenting antigen with probability

$$P_{\text{lysis}}^{\text{DC}} = k_4.$$

Dendritic cell migration: At each time step the inactive DCs marked for migration do so with a constant probability

$$P_{\text{mig}}^{\text{DC}} = k_5.$$

Natural replenishment to background level: Similarly, a near-constant minimum background level of inactive and active DCs is maintained at each time step by replacing some healthy cells on the boundary with inactive DCs. At each time step we determine the proportion of all locations in the domain occupied by inactive and active DCs. Whenever this is less than the minimum background level, D_0, each healthy cell on the boundary of the domain has probability

$$P_{\text{rep}}^{\text{inactDC}} = D_0 - \frac{1}{n^2} \sum_{i,j \in \eta} \left(D_{i,j}^I + D_{i,j}^A\right) \tag{3}$$

of being replaced with an inactive DC from outside of the problem domain, where D_0 is the "normal" density of inactive DCs and n^2 is the total number of CA elements.

These rules are presented in pseudocode form in Algorithm 6.

3.2.6 Natural Killer Cells

Inactive NK cells are subject to change as a result of natural replenishment and activation as a result of direct interaction between existing inactive NK cells and either active DCs, tumor cells, or cytokines produced by tumor cells. At each time step, the neighborhood of each inactive NK cell is surveyed to determine whether active DCs or tumor cells are present. If any DCs or tumor cells or cytokines are present, then the inactive NK cell is marked for potential activation, otherwise the NK cell is marked for random migration. If the chemokine level secreted by tumor cellsis greater than some threshold concentration, C_{1_0}, then the inactive NK cell is

Algorithm 6 Pseudocode for DCs related events.

```
if (location holds inactive DCs) then
    Calculate the number of tumor cells in the neighborhood
    Calculate chemokines concentration in the neighborhood
    Find new location at random in the neighborhood
    Draw r ~ U[0, 1]
    Calculate P_act^DC using current state of CA
    if number of tumor cells in the neighborhood >= 1 then
        if r < P_act^DC then
            current surface replace with active DCs
        end if
    else if chemokine concentration > threshold chemokine concentration then
        current surface replace with active DCs
    else if r < k5 then
        inactive DCs move to the new location
    end if
end if
```

marked for activation. Active NK cells will survey their neighborhood to determine whether tumor cells are present. If any tumor cells are present, then the active NK cell is marked as having potential to lyse tumor cells. A stochastic rule is then implemented to determine whether or not the action will be carried out. A normal background level of inactive NK cells is also maintained at each time step. To this end, we impose the following cellular automata rules.

Activation by interaction with DCs: When inactive NK cells come in contact with DCs, they have probability

$$P_{\text{act}}^{\text{NK}} = 1 - \exp\left(-\left(\sum_{i,j\in\eta} D_{i,j}^{A}\right)^{2}\right)$$

of becoming activated, which are then able to lyse tumor cells. Here

$$\sum_{i,j\in\eta} D^A_{i,j}$$

is the number of active DCs in a one-cell radius of the cell of interest.

NK cells migration: At each time step the inactive NK cells marked for migration do so with a constant probability given by

$$P^{\mathrm{NK}}_{\mathrm{mig}} = k_6,$$

where k_6 is a constant.

Natural replenishment to background level: Similarly, a near-constant minimum background level of inactive and active NK cells are maintained at each time step by replacing some healthy cells on the boundary with inactive NK cells. At each time step we determine the proportion of all locations in the domain occupied by inactive and active NK cells. Whenever this is less than the minimum background level, K_0, each healthy cell on the boundary of the domain has probability

$$P^{\mathrm{inactNK}}_{\mathrm{rep}} = K_0 - \frac{1}{n^2}\sum_{i,j\in\eta}\left(K^I_{i,j} + K^A_{i,j}\right)$$

of being replaced with an inactive NK cell from outside of the problem domain, where K_0 is the 'normal' density of inactive NK cells and n^2 is the total number of CA elements.

These rules are presented in pseudocode form in Algorithm 7.

Algorithm 7 Pseudocode of NK cell related events.

```
if (location holds inactive NK cell) then
    Calculate the number of tumor cells in the neighborhood
    Find active DCs in the neighborhood
    Calculate chemokine concentration in the neighborhood
    Find new location at random in the neighborhood
    Draw r ~ U[0, 1]
    Calculate P_act^NK using current state of CA
    if the number of tumor cells in the neighborhood >= 1 then
        current surface replace with active NK cell
    else if r < P_act^NK then
        current surface replace with active NK cell
    else if chemokine concentration > threshold chemokine concentration then
        current surface replace with active NK cell
    else if r < k_6 then
        inactive NK cells move to the new location
    end if
end if
```

4 Simulation and Results

The numerical simulation of the model involves two main steps. Spatial changes for the chemokine species are determined by solving the partial differential equation. Then the cell-level phenomena (such as cell–cell interactions, cell death, division, and migration) are carried out, dependent on the updated chemokine levels, by updating the cellular automata component of the model. We tie the time step of this iteration process to the approximate period of tumor cell division (approximately 0.5–10 days; see for example, [26, 40]).

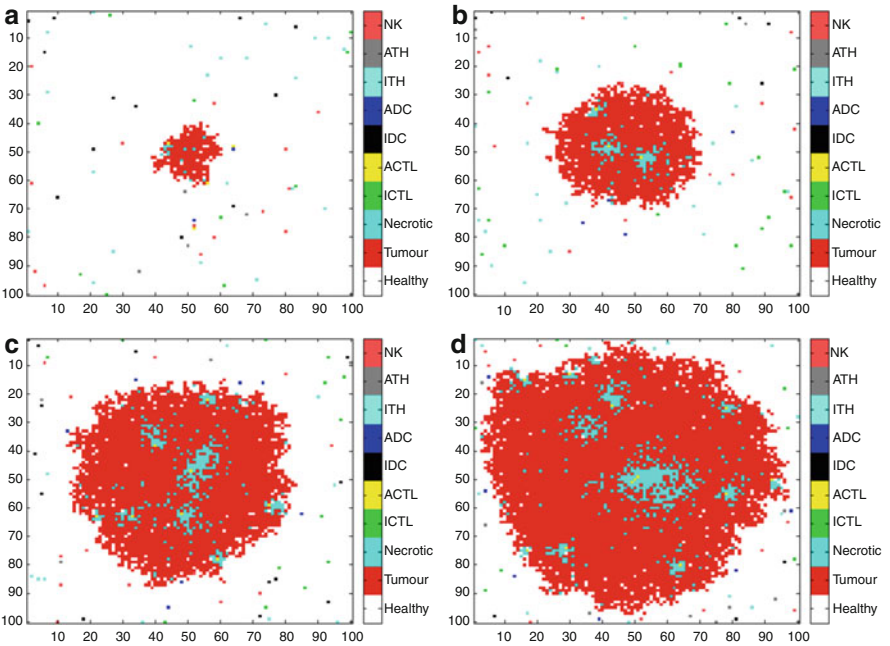

Fig. 3 The growing tumor and host immune system. After 25 cell cycles (**a**). After 50 cell cycles (**b**). After 75 cell cycles (**c**). After 100 cell cycles (**d**)

We combine the solution of the PDE with the CA as described in Sect. 3.2 to simulate the evolution of the growing tumor. Here, a two-dimensional regular 100×100 square domain is used with 100 cell cycles and a Moore neighborhood is considered for the cellular automata rules. In this simulation, we solve the PDE model using the finite difference method and an estimated value of diffusion coefficient for chemokine, D_{C_1} and D_{C_2}, is $10^{-4}\,\mu\text{m}^2\text{s}^{-1}$. The distribution of the growing tumor after 25, 50, 75, and 100 cell cycles is shown in Fig. 3, with results qualitatively matching those of Mallet and de Pillis [31] and those commonly found in tumor modeling literature.

Figure 4 shows the evolution of the tumor cell and necrotic cell densities over 100 cell cycles. This plot shows the characteristic exponential and linear growth phases of solid, avascular tumors (see, for example, Folkman and Hochberg [18]), as well as a slower growing population of necrotic cells. Figure 5 shows the number of tumor cells for 100 simulations (thin lines) and the median simulation (thick line) of the CA model over 100 cell cycles. In addition, increasing the number of immature DCs in the domain causes a decrease in the number of tumor cells (this result is run by 100 simulations), as shown in Fig. 6. This result strongly supports the hypothesis that DCs can be used as a cancer treatment.

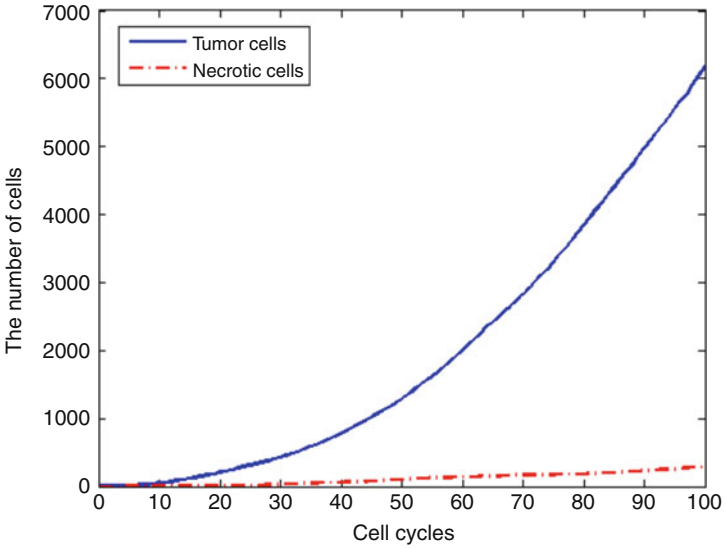

Fig. 4 Total cell counts of tumor and necrotic cells after 100 cell cycles. This plot shows the familiar exponential growth of tumor cells and a slower (approximately linear) growth of a population of necrotic cells

In Fig. 7b we see that initially, the number of mature DCs is zero until immature DCs come in contact with tumor cells, at which point the matured DCs commence killing the tumor cells. Also, immature DCs are activated by chemokines secreted by the tumor cells. As expected, due to the nature of Eq. (3), the populations of immature and mature DCs remain approximately steady over the extent of the tumor growth. Similarly, the same behavior occurs in the populations of CTL cells and helper T cells, see Figs. 7 and 8.

Figure 9 represents the evolution of cytotoxic T cells, DCs, T helper cells, NK cells, healthy cells, tumor cells, and necrotic cells for five simulations over 300 cell cycles. Parameters used are: $I_0 = 0.005, D_0 = 0.002, H_0 = 0.002, K_0 = 0.001, P_{div} = 0.5, P_{mig} = 0.2$. The initial number of $CD8^+$ T cells is approximately 50 cells or 0.005 % of the total cells in the domain (see Fig. 9a). In this case,

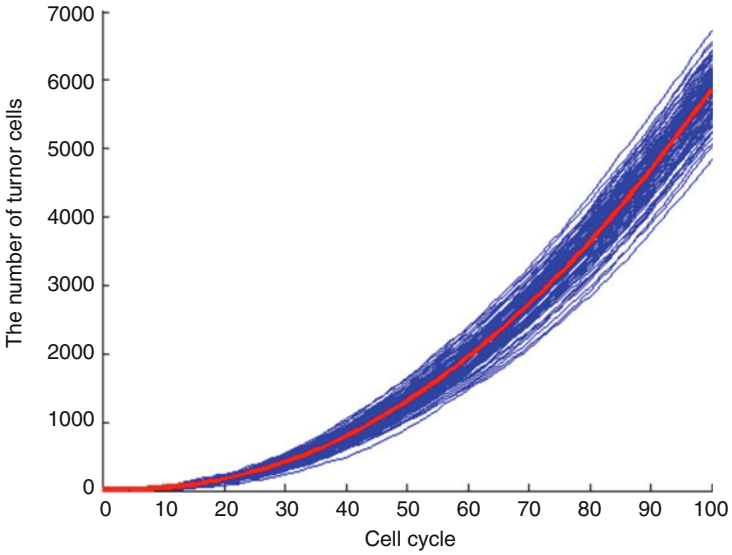

Fig. 5 Total tumor cell counts for 100 simulations (*thin*) and the median simulation (*thick*) of the CA model over 100 cell cycles. We see that the model successfully predicts the familiar exponential growth stage for a growing tumor

the tumor cells reach the boundary after approximately 140 cell cycles (see Fig. 9e). However, increasingthe probability of tumor cell division to $P_{div} = 0.9$, results in the tumor cells reaching the boundary after only approximately 100 cell cycles (see Fig. 10e). It means that the probability of tumor cell division is more dominant to affect the growing of tumor than increasing the immune cells.

We also use the hybrid cellular automata model to investigate the growth of a tumor in a number of computational "cancer patients." Each computational patient is distinguished from others by altering model parameters. We define "death" of a patient as occurring when the tumor is able to metastasize. Effectively, this is when the cells of the tumor reach the boundary of our model domain. We define Kaplan–Meier "survival" estimates as

$$S(t) = \frac{\text{number of individuals 'surviving' longer than } t}{\text{total number of individuals studied}},$$

where t is a time from initial diagnosis to "death." We present the results of these simulations using a simulated Kaplan–Meier survival curve, shown in Figs. 11 and 12.

Figure 11 describes that metastasis sets in for the first patients after approximately 80 cell cycles. In addition, at 300 cell cycles after one tumor cell is allowed to grow, the metastasis of the simulated tumors occurred in approximately 70 % of patients with lowest iDC in the domain, but approximately 40 % of the patients

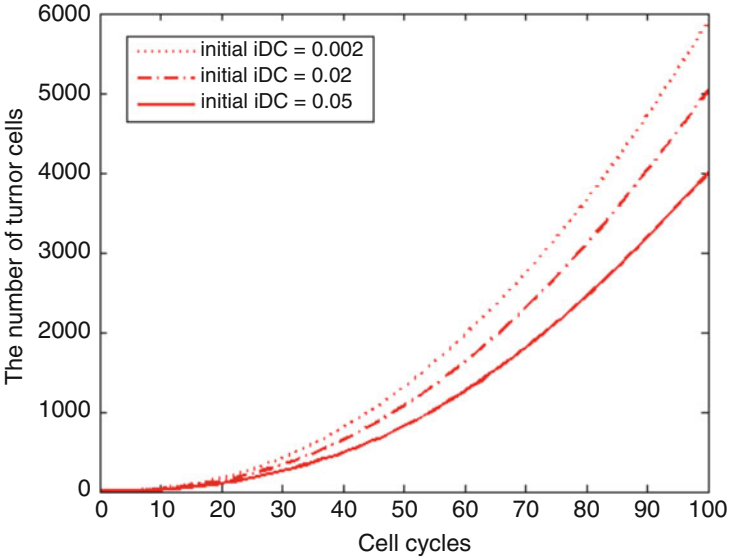

Fig. 6 Total cell counts of tumor cells for 100 simulations showing the effect of varying the DCs as indicated on the graph over 100 cell cycles. This plot shows that increasing the population of DCs decreases the number of tumor cells

with the highest iDC in the domain. This means that increasing the number of immature DC in the domain results in significantly longer "survival." These results qualitatively agree with experimental data, see for example, Becker et al., Daud et al., and Nagorsen et al. [6, 11, 35].

Similarly, as shown in Fig. 12, the patients showed better survival as the number of inactive CTLs within the domain increases. These results also agree with experimental data as explained by Naito et al. [36].

5 Discussion

In this chapter, we have developed a hybrid cellular automata model to describe the interaction between a growing tumor and the immune system of the host, including chemokines. The model is able to describe the effect of the immune system and chemokines on a growing tumor. Increasing the number of immature DCs in the domain causes a decrease in the number of tumor cells. This result strongly supports the hypothesis that DCs can be used as a cancer treatment. Furthermore, we also use the hybrid cellular automata model to investigate the growth of a tumor in a number of computational "cancer patients." Using these virtual patients, the model can explain that increasing the number of DCs in the domain causes longer "survival."

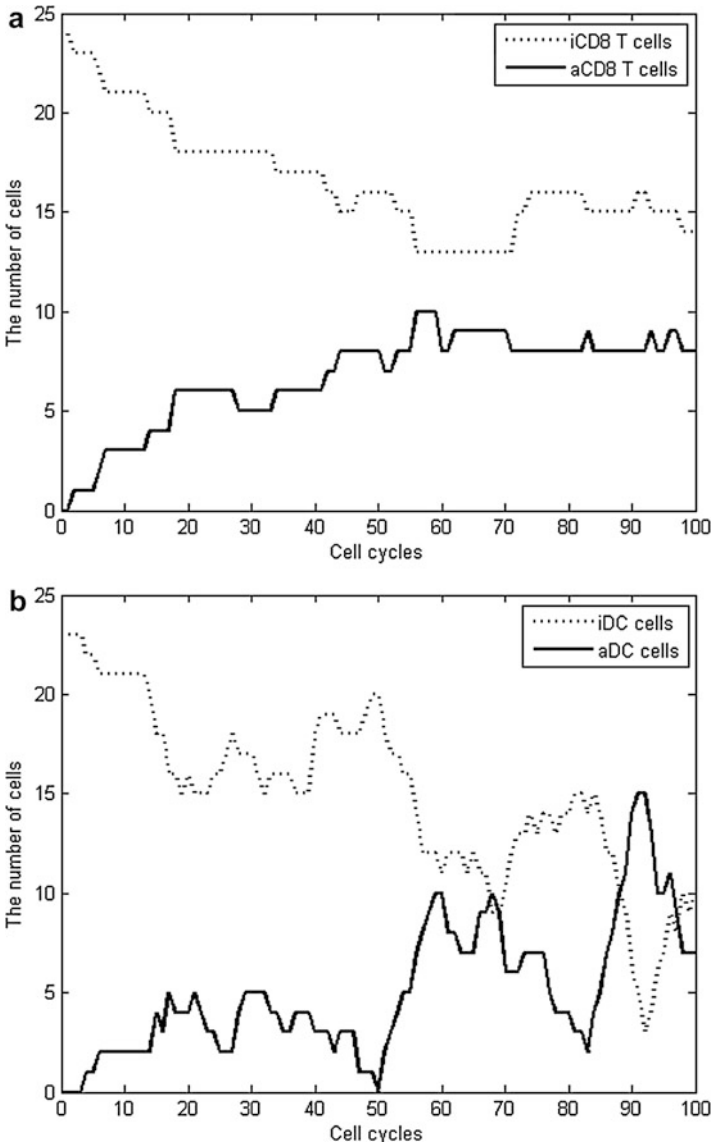

Fig. 7 Total cell counts of $CD8^+$ T cells (**a**) and DCs (**b**) after 100 cell cycles

Not surprisingly, the model also reflects the fact that the parameter related to tumor division rate plays an important role in tumor metastasis.

In previous work, Duchting and Vogelsaenger [14] pioneered the use of discrete cellular automata for modeling cancer, in an investigation of the effects of radiotherapy. Ferreira et al. [16] modeled avascular cancer growth with a CA model based on

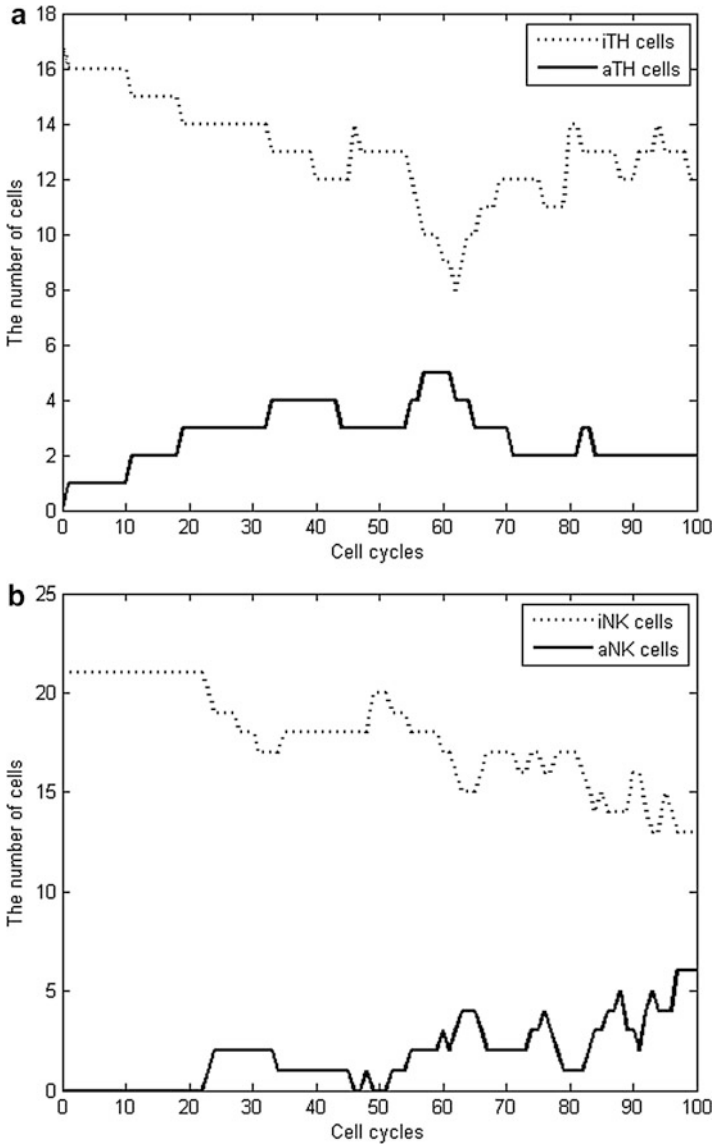

Fig. 8 Total cell counts of $CD4^+$ helper T cells (**a**) and NK cells (**b**) after 100 cell cycles

the fundamental biological processes of proliferation, motility, and death, including competition for diffusing nutrients among normal and cancer cells. Mallet and de Pillis [31] constructed a hybrid cellular automata cancer model that built on the work of Ferreira et al. to include NK cells as the innate immune system and CTL cells as the specific immune system. The Mallet and de Pillis model was lacking in its detail

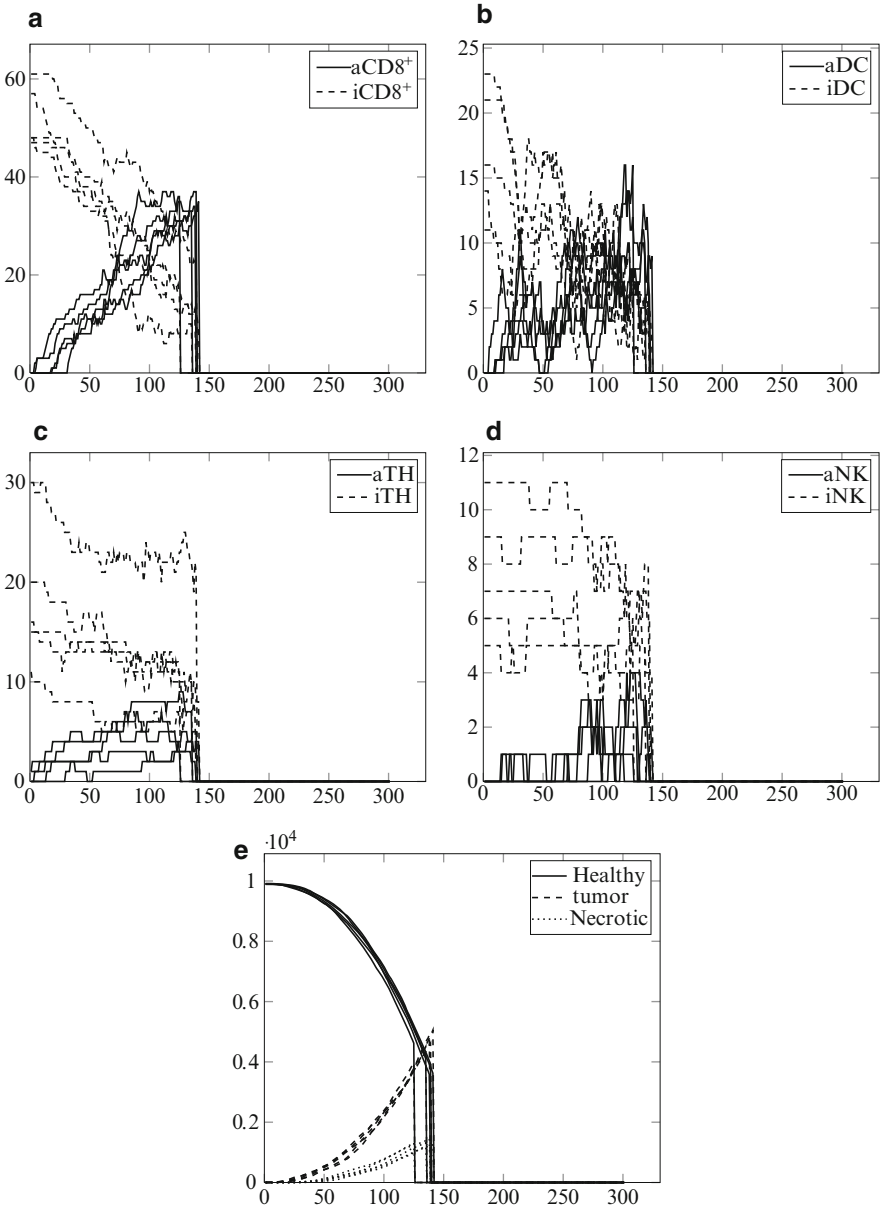

Fig. 9 The evolution of CD8$^+$ T cells, DCs, T Helper cells, NK cells, healthy cells, tumor cells and necrotic cells for 5 simulations over 300 cell cycles. Parameters used are: $I_0 = 0.005$, $D_0 = 0.002$, $H_0 = 0.002$, $K_0 = 0.001$, $P_{div} = 0.5$, $P_{mig} = 0.2$. All tumors metastasize at or before around 150 cell cycles

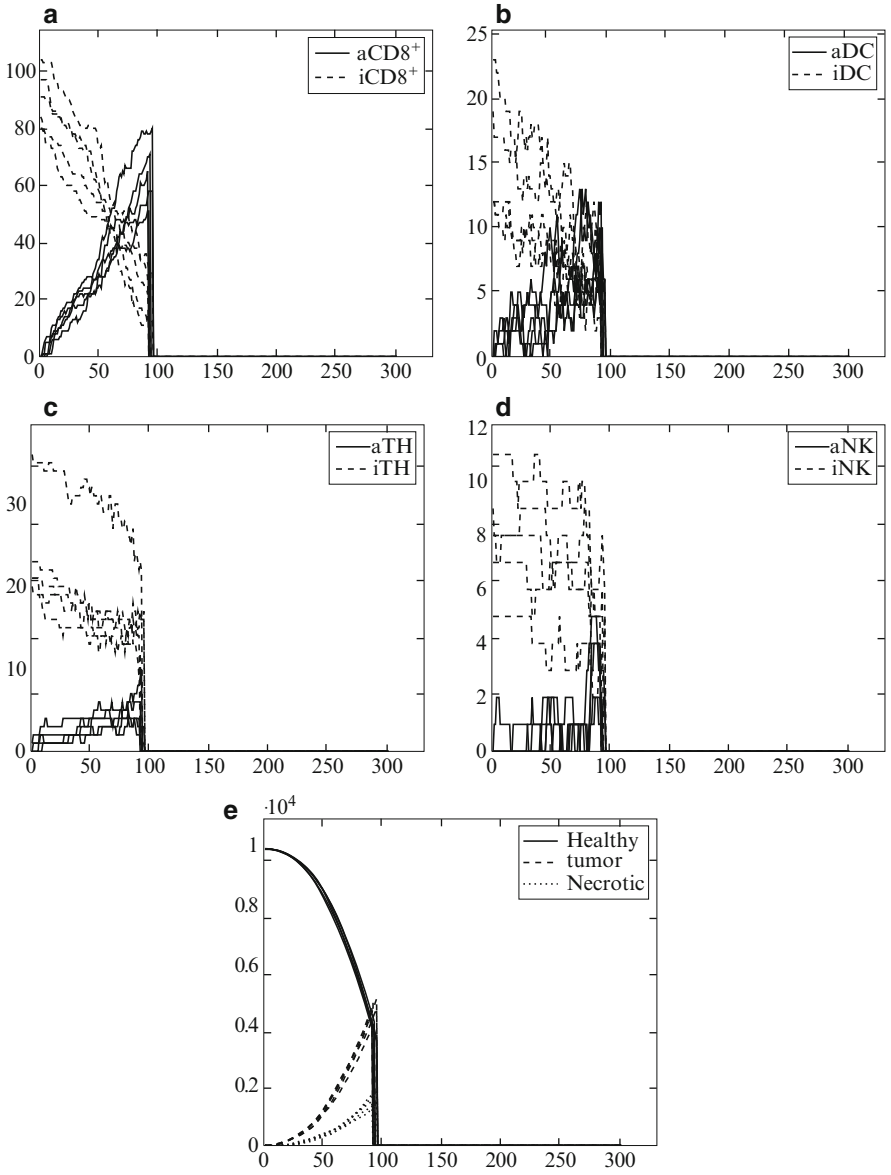

Fig. 10 The evolution of $CD8^+$ T cells, Dendritic cells, T Helper cells, NK cells, healthy cells, tumor cells, and necrotic cells for 5 simulations over 300 cell cycles. Parameters used are: $I_0 = 0.009$, $D_0 = 0.002$, $H_0 = 0.002$, $K_0 = 0.001$, $P_{div} = 0.9$, $P_{mig} = 0.2$. All tumors metastasize at or before around 100 cell cycles

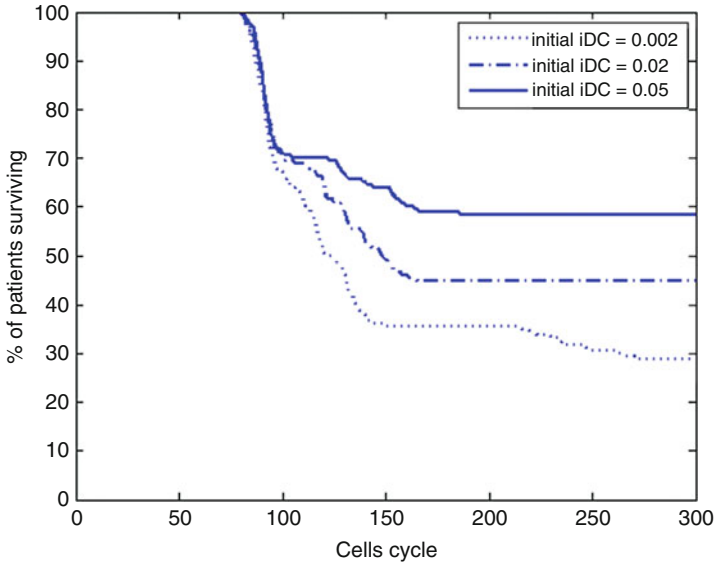

Fig. 11 Simulated Kaplan–Meier curve with different initial values of immature DCs as indicated on the graph. This plot shows that increasing the population percentage of DCs in patients will increase survival rate

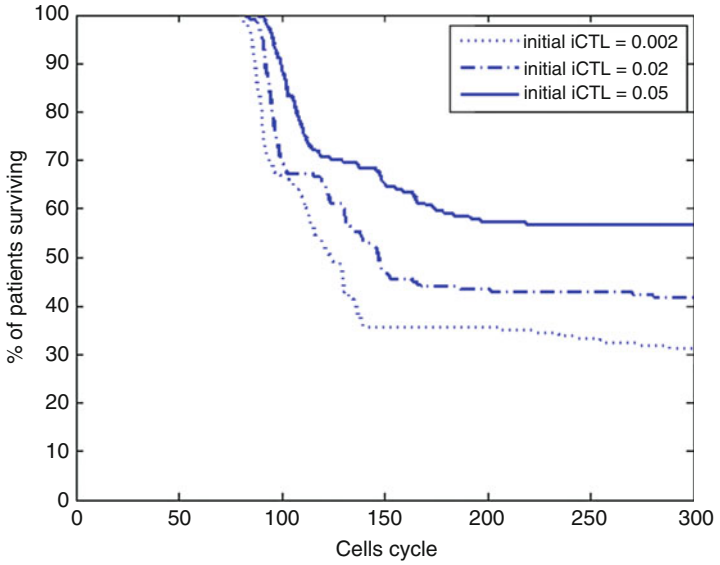

Fig. 12 Simulated Kaplan–Meier curve with different initial values of immature CTL as indicated on the graph. This plot shows that increasing the population percentage of CTL cells in patients will increase survival rate

of the immune system and in this present research we have improved on their work by explicitly describing more of the host immune system. While direct comparison of the models is difficult, the results as presented in this chapter qualitatively reflect the findings of Mallet and de Pillis and of Ferreira et al. while extending them to incorporate greater realism in the description of the immune system.

While models based on differential equations allow for analytical investigations such as stability and parameter sensitivity analyses, and ease of fitting the model to experimental data, these types of models cannot capture the detailed cellular and sub-cellular level complexity of the biological system. On the other hand, HCA models can describe, in far greater detail, the intricacies of the biological process such as the interaction between individual cells. In current work complementary to the present research of this chapter, we have included greater realism in the modeling of tumor-secreted chemokines by allowing secretion due to cell–cell interaction. Currently, chemokines and their receptors in the tumor microenvironment are being extensively investigated to produce therapeutic interventions to combat cancer (see for example, Allavena et al. [3] and Murooka et al. [33]). Future developments based upon this model will allow for simulation-based and theoretical investigations of such interventions.

In this chapter, we have developed a model that can be employed as a preliminary investigative tool for experimentalists who conduct expensive in vitro and in vivo experiments to test and refine hypotheses prior to entering the lab. With further cross-disciplinary collaboration, this type of model can be refined to provide a more accurate description of the underlying cancer biology and hence yield more relevant predictions and tests of hypotheses.

References

1. Aarntzen, E.H.J.G., Figdor, C.G., Adema, G.J.: Dendritic cell vaccination and immune monitoring. Cancer Immunol. Immunother. **57**, 1559–1568 (2008)
2. Alarcon, T., Byrne, H.M., Maini, P.K.: A cellular automata model for tumour growth in inhomogeneous environment. J. Theor. Biol. **225**, 257–274 (2003)
3. Allavena, P., Marchesi, F., Mantovani, A.: The role of chemokines and their receptors in tumor progression and invasion: potential new target of biological therapy. Curr. Cancer Ther. Rev. **1**, 81–92 (2005)
4. Araujo, R.P., McElwain, D.L.S.: A history of the study of solid tumour growth: the contribution of mathematical modelling. Bull. Math. Biol. **66**, 1039–1091 (2004)
5. Banchereau, J., Steinman, R.M.: Dendritic cells and the control of immunity. Nature **392**, 245–252 (1998)
6. Becker, Y.: Dendritic cell activity against primary tumours: an overview. In Vivo **7**, 187–191 (1993)
7. Bhat, R., Dempe, S., Dinsart, C., Rommelaere, J.: Enhancement of NK cell antitumor responses using an oncolytic parvovirus. Int. J. Cancer **128**(4), 908–919 (2011). doi:10.1002/ijc.25415
8. Burgdorf, S.K., Fischer, A., Myschetzky, P.S., et al.: Clinical responses in patients with advanced colorectal cancer to a dendritic cell based vaccine. Oncol. Rep. **20**, 1305–1311 (2008)
9. Castiglione, F., Piccoli, B.: Optimal control in a model of dendritic cell transfection cancer immunotherapy. Bull. Math. Biol. **68**, 255–274 (2006)

10. Cooper, M.A., Fehniger, T.A., Fuchs, A., et al.: NK cell and DC interactions. Trends Immunol. **25**, 47–52 (2004)
11. Daud, A.I., Mirza, N., Lenox, B., et al.: Phenotypic and functional analysis of dendritic cells and clinical outcome in patients with high-risk melanoma treated with adjuvant granulocyte macrophage colony-stimulating factor. J. Clin. Oncol. **26**, 3235–3241 (2008)
12. de Pillis, L.G., Mallet, D.G., Radunskaya, A.E.: Spatial tumor-immune modeling. Comput. Math. Methods Med. **7**(2–3):159–176, 2006.
13. Dhodapkar, M.V., Dhodapkar, K.M., Palucka, A.K.: Interactions of tumor cells with dendritic cells: balancing immunity and tolerance. Cell Death Differ. **15**, 39–50 (2008)
14. Duchting, W., Vogelsaenger, T.: Analysis, forecasting and control of three-dimensional tumor growth and treatment. J. Med. Syst. **8**, 461–475 (1984)
15. Ferlazzo, G., Tsang, M.L., Moretta, L., et al.: Human dendritic cells activate resting natural killer (NK) cells and are recognized via the NKp30 receptor by activated NK cells. J. Exp. Med. **195**, 343–351 (2002)
16. Ferreira, Jr.S.C., Martins, M.L., Vilela, M.J.: Reaction diffusion model for the growth of avascular tumor. Phys. Rev. E **65**, 021907 (2002)
17. Ferreira, Jr.S.C., Martins, M.L., Vilela, M.J.: Morphology transitions induced by chemotherapy in carcinomas *in situ*. Phys. Rev. E **67**, 051914 (2003)
18. Folkman, J., Hochberg, M.: Self regulation of growth in three dimensions. J. Exp. Med. **138**, 745–753 (1973)
19. Fong, L., Engleman, E.G.: Dendritic cells in cancer immunotherapy. Annu. Rev. Immunol. **18**, 245–273 (2000)
20. Foon, K.A., Yannelli, J., Bhattacharya-Chatterjee, M.: Colorectal cancer as a model for immunotherapy. Clin. Cancer Res. **5**, 225–236 (1999)
21. Hart, D.N.: Dendritic cells: unique leukocyte populations which control the primary immune response. Blood **90**, 3245–3287 (1997)
22. Hsu, F.J., Benike, C., Fagnoni, F., et al.: Vaccination of patients with B-cell lymphoma using autologous antigen-pulsed dendritic cells. Nat. Med. **2**, 52–58, (1996)
23. Joshi, P.S., Liu, J.Q., Wang, Y., et al.: Cytokine-induced killer T cells kill immature dendritic cells by TCR-independent and perporin-dependent mechanisms. J. Leukoc. Biol. **80**, 1345–1353 (2006)
24. Kim, P.S., Lee, P.P.: Modeling protective immunity via preventative cancer vaccines using a hybrid agent-based and delay differential equation approach. PLoS Comput. Biol. **8**(10), e1002742 (2012)
25. Kindt, T.J., Goldsby, R.A., Osborne, B.A.: Kuby Immunology. Freeman and Company, New York (2007)
26. Kirschner, D., Panetta, J.C.: Modeling immunotherapy of the tumor-immune interaction. J. Math. Biol. **37**, 235–252 (1998)
27. Larmonier, N., Fraszack, J., Lakomy, D., et al.: Killer dendritic cells and their potential for cancer immunotherapy. Cancer Immunol. Immunother. **59**, 1–11 (2010)
28. Lin, A.: A model of tumour and lymphocyte interactions. Discrete Contin. Dynam. Syst. Ser. B **4**(1), 241–266 (2004)
29. Lin, A., Schildknecht, A., Nguyen, L.T., et al.: Dendritic cells integrate signals from the tumor microenvironment to modulate immunity and tumor growth. Immunol. Lett. **127**, 77–84 (2010)
30. Ludewig, B., Krebs, P., Junt, T., et al.: Determining control parameters for dendritic cell-cytotoxic T lymphocyte interaction. Eur. J. Immunol **34**, 2407–2418 (2004)
31. Mallet, D.G., de Pillis, L.G.: A cellular automata model of tumour-immune system interactions. J. Theor. Biol. **239**, 334–350 (2006)
32. Mazzolini, G., Murillo, O., Atorrasagasti, C., et al.: Immunotherapy and immunoescape in colorectal cancer. World J. Gastroenterol. **13**(14), 5822–5831 (2007)
33. Murooka, T.T., Ward, S.E., Fish, E.N.: Chemokines and Cancer, in: Cytokines and Cancer. Springer, New York (2005)
34. Moretta, A.: Natural killers and dendritic cells: rendezvous in abused tissues. Nat. Rev. Immunol. **2**(12), 957–964 (2002)

35. Nagorsen, D., Voigt, S., Berg, E., et al.: Tumor-infiltrating macrophages and dendritic cells in human colorectal cancer: relation to local regulatory T cells, systemic T-cell response against tumor-associated antigens and survival. J. Transl. Med. **5**(62) (2007)
36. Naito, Y., Saito, K., Shiiba, K., et al.: $CD8^+$ T cells infiltrated within cancer cell nests as a prognostic factor in human colorectal cancer. Cancer Res. **58**, 3491–3494 (1998)
37. Negus, R.P., Stamp, G.W., Hadley, J., et al.: Quantitative assessment of leukocyte infiltrate in ovarium cancer and its relationship to the expression of C-C chemokines. Am. J. Pathol. **150**, 1723–1734 (1997)
38. Raman, D., Baugher, P.J., Thu, Y.M., et al.: Role of chemokines in tumour growth. Cancer Lett. **256**, 137–165 (2007)
39. Ribba, B., Alarkon, T., Marron, K., et al.: The use of hybrid cellular automata models for improving cancer therapy. ACRI 2004, LNCS 3305, 444–453 (2004)
40. Riedel, H.: Models for tumour growth and differentiations. In: Alison, M.R. (ed.) The Cancer Handbook. Wiley, New York (2004)
41. Ruddon, R.W.: Cancer Biology. Oxford University Press, New York (2007)
42. Sandel, M.H., et al.: Prognostic value of tumor-infiltrating dendritic cells in colorectal cancer: role of maturation status and intra-tumoral localization. Clin. Cancer Res. **11**(7), 2576–2582 (2005)
43. Schuler, G., Schuler-Thurner, B., Steiman, R.M.: The use of dendritic cells in cancer immunotherapy. Curr. Opin. Immunol. **15**, 138–147 (2003)
44. Smith, C.L., Dylphy, N., Salio., M., Cerundolo,V.: Immunotherapy of colorectal cancer. Br. Med. Bull. **64**, 181–200 (2002)
45. Steinman, R.M.: The dendritic cell system and its role in immunogenicity. Ann. Rev. Immunol. **9**, 271–296 (1991)
46. Somasundaram, R., Herlyn, D.: Chemokines and the microenvironment in neuroectodermal tumor-host interaction. Semin. Cancer Biol. **19**, 92–96 (2009)
47. Vicari, A.P., Ait-Yahia, S., Chemin, K., et al.: Antitumor effects of the mouse chemokine 6Ckine/SLC through angiostatic and immunological mechanisms. J. Immunol. **165**, 1992–2000 (2000)

Differential Equation Techniques for Modeling a Cycle-Specific Oncolytic Virotherapeutic

Joanna R. Wares, Joseph J. Crivelli, and Peter S. Kim

Abstract The development of a mathematical model of oncolytic virotherapeutic vesicular stomatitis virus (VSV) is presented in stages. Standard mathematical tools are discussed along with the development and analysis of the model. A defining property of VSV is that it only affects tumor cells when they are in the active phases of the cell cycle. To model this characteristic, we first model tumor growth and separate cells into active and resting, which takes the form of a linear system of differential equations. We then take into account the minimum time needed for cells to travel through the active phases of the cell cycle, first using delay-differential equations and then later age-structured partial differential equations. Our basic tumor growth model allows us to investigate linear systems analysis (eigenvalue analysis). We then study similar techniques for delay differential equations, after adding the minimum time necessary to travel through the active phases of the cell cycle to the model. After tumor growth alone has been modeled, we include viral dynamics, which takes the form of a nonlinear system of ordinary differential equations. We investigate how linearization helps us understand how to properly develop the model. Finally we add the minimum biological time to the viral model. With the model fully developed, we arrive at a system of differential equations, one of which is an age-structured partial differential equation, which provides a nice example for discussing the method of characteristics. Finally, we show how our model can be used to investigate the dynamics of the tumor-virus system. As we travel through the development of our model, we discuss various techniques to analyze ordinary, delay, and partial differential equations.

J.R. Wares (✉)
University of Richmond, Richmond, VA 23173, USA
e-mail: jwares@richmond.edu

J.J. Crivelli
Weill Cornell Medical College, New York, NY 10065, USA
e-mail: jjc2004@med.cornell.edu

P.S. Kim
University of Sydney, Camperdown, NSW 2006, Australia
e-mail: pkim@maths.usyd.edu.au

A. Eladdadi et al. (eds.), *Mathematical Models of Tumor-Immune System Dynamics*, Springer Proceedings in Mathematics & Statistics 107,
DOI 10.1007/978-1-4939-1793-8_10

1 Introduction

In this chapter, we provide a review of the mathematical techniques used to develop and analyze a model of oncolytic virotherapeutic vesicular stomatitis virus, VSV [9]. The model provides a platform for understanding the dynamics of systems of ordinary differential equations (ODE), delay differential equations (DDE), as well as a starting point for understanding partial differential equations (PDE).

Oncolytic virotherapeutics (OV), specially engineered cancer-killing viruses, differ based on the mechanisms of the underlying virus used. Examples of oncolytic viruses that have demonstrated anti-tumor efficacy include adenoviruses [12], Coxsackieviruses [1], herpes simplex viruses [21], measles viruses [10], Newcastle disease virus [18], reoviruses [8], Seneca Valley virus [20], vaccinia viruses [17], and vesicular stomatitis virus [5]. Various models have been proposed as representations for treatment of cancer with oncolytic virotherapeutics, and frequently the models are novel specifically because of the differences in the underlying virus.

Early OV modeling efforts by Wodarz et al. [23] explored the different oncolytic mechanisms at play, death from replication of the virus, from an immune response mounted against the virus, or from an immune response due to molecules secreted by the tumor cells in response to the virus invasion. Wu et al. [25] looked at the race between the tumor, the OV, and the immune system (which attacks both the tumor and the OV) in a partial differential equations model which included spatial dynamics. More specific models followed, Friedman et al. looked at Glioma virotherapy in combination with an immunosuppressant, cyclophosphamide [11]. Bajzer et al. and Biesecker et al. [2, 6] look at optimal dosing and timing of doses using recombinant measles virus. Wodarz and Komarova followed up in 2009 with a more general study of virus therapy, looking at which models were consistent with various experimentally validated tumor dynamics [13, 24].

In a previous work, we developed a model of the oncolytic virotherapeutic, VSV [9]. VSV is an RNA virus that has demonstrated anti-tumor efficacy in a large range of human tumor cell lines, including prostate, breast, cervical, and hematologic cancers [4]. VSV also has the distinguishing characteristic that it is only transmissible when the tumor cells are in the active phases of the cell cycle [16]. We therefore developed the model to differentiate between tumor cells in active phases and the quiescent phase of the cell cycle. To do so, the tumor population was separated into two compartments, one compartment for the cells in the active phases and one compartment for cells in the quiescent phase. In the first part of this chapter, we describe the movement of cells between these two compartments, including cell division and natural cell death. The differential equations system that was developed is simple being linear with constant coefficients. To begin our discussion, we describe how linear systems analysis was used to analyze the dynamics of the tumor growth system alone.

Next, we include the idea that there is a minimum time necessary for cells to travel through the active phases of the cell cycle. To force cells to remain in the active phases for a minimum time, the model is converted into a system of

differential equations, one of which includes a delay. Basic theory of analyzing delay differential equations is then presented, along with some results particular to the VSV model, as an example of how to utilize the analysis methods.

Next we incorporate virotherapy into the base model, while at first excluding the delay. To build the model properly, an investigation of the transmission term was necessary. We explain the basics of local nonlinear systems analysis and reveal how it was helpful in developing our model. Upon completion of this stage, the model became a four-dimensional model, with cycling cells separated into infected and susceptible, with an additional compartment for the virions [2].

Finally, we bring all of the components together, transmission and delay, and arrive at a system of five equations, one of which is an age-structured partial differential equation, which captures the minimum time necessary to travel through the active phases of the cell cycle. We review the method of characteristics and show how this method was utilized twice in the paper, in one case to solve an equation and later in a proof that shows that solutions of the PDE system remain nonnegative.

The development of the model and underlying mathematical theory are interesting alone, but mathematical biology is at its best when we can say something about the underlying biological system using the mathematical model. Therefore, at the end of this chapter, we review the biological results in the original paper, obtained through numerical simulations and stability analysis, which elucidate the factors that promote complete remission, controlled tumor growth, or uncontrolled tumor growth.

2 Linear System Techniques

First, tumor growth alone is modeled. The model comprises two compartments, $Q(t)$ and $S(t)$, representing the volume of tumor cells in the quiescent phases and the active phases of the cell cycle at time t, respectively. Later in the chapter, the minimum biological time needed to travel through the active phases of the cell cycle and the viral dynamics will be added to the model. But for now, the model will simply track tumor growth, accounting for the transition to resting and back to the active phases of the cell cycle. The equations of the model are

$$Q'(t) = 2a_2 S - a_1 Q - d_1 Q, \tag{1}$$

$$S'(t) = a_1 Q - a_2 S - d_2 S. \tag{2}$$

The parameters a_1 and a_2 are the rates that cells move from Q to S and S to Q, respectively, with cells dividing into two when they leave the active phase, hence the $2a_2$ in the first term of the $Q'(t)$ equation. Cells die naturally at rates d_1 and d_2 for Q and S, respectively.

The system is linear with constant coefficients and provides a nice example of how linear analysis is used to qualitatively understand a system of differential

equations. The system is also solvable but the solution is in terms of parameters, and understanding how the parameters affect the dynamics of the system is easier if we analyze the stability of the equilibria, rather than looking at the analytical forms of the solutions. To fully appreciate this, we will look at both methods.

The solutions can be found using the eigenvalue method. If the eigenvalues of the coefficient matrix are real, the general solution of the system has the form

$$\begin{bmatrix} Q(t) \\ S(t) \end{bmatrix} = c_1 e^{\lambda_1 t} \begin{bmatrix} v_1 \\ v_2 \end{bmatrix} + c_2 e^{\lambda_2 t} \begin{bmatrix} v_3 \\ v_4 \end{bmatrix}, \tag{3}$$

where, λ_1 and λ_2 are the eigenvalues of the coefficient matrix. The corresponding eigenvectors are $[v_1\ v_2]^T$ and $[v_3\ v_4]^T$, respectively, and c_1 and c_2 are constants that can be found once initial values, $Q(0)$ and $S(0)$ are given.

The coefficient matrix of our model system is

$$A = \begin{bmatrix} -(a_1 + d_1) & 2a_2 \\ a_1 & -(a_2 + d_2) \end{bmatrix}, \tag{4}$$

so the eigenvalues of A are

$$\lambda_1 = \frac{-(a_1 + a_2 + d_1 + d_2) - \sqrt{\Delta}}{2}, \tag{5}$$

$$\lambda_2 = \frac{-(a_1 + a_2 + d_1 + d_2) + \sqrt{\Delta}}{2}, \tag{6}$$

where

$$\Delta = (a_1 + a_2 + d_1 + d_2)^2 - 4\left(a_1(d_2 - a_2) + d_1(a_2 + d_2)\right),$$

with corresponding eigenvectors

$$\begin{bmatrix} v_1 \\ v_2 \end{bmatrix} = \begin{bmatrix} 3a_2 + d_2 - \sqrt{\Delta} \\ 2a_1 \end{bmatrix}, \tag{7}$$

$$\begin{bmatrix} v_3 \\ v_4 \end{bmatrix} = \begin{bmatrix} 3a_2 + d_2 + \sqrt{\Delta} \\ 2a_1 \end{bmatrix}. \tag{8}$$

As you can imagine, trying to divine anything from (3) with these eigenvalues and eigenvectors inserted would be quite difficult. Instead, qualitative analysis is employed to study the long term behavior of the tumor. With qualitative analysis, we can ask, based solely on the growth and death parameters, will the tumor prosper or decline? Unless A is singular, which is highly improbable, the only equilibrium of the system is the tumor free equilibrium ($Q(t)$, $S(t)$) = (0,0), so another way to ask our question is, will nonzero solutions of the system approach (0,0) or move away from it?

To determine our answer, we look at the eigenvalues of the matrix A. Linear systems analysis allows us to determine the stability of the equilibrium (0,0) solely from the sign of the real parts of the eigenvalues of the coefficient matrix. If the real parts of the eigenvalues of A are less than zero, then (0,0) is asymptotically stable, and solutions move toward (0,0) as $t \to \infty$. Therefore, the tumor will be extinguished naturally. On the other hand, if the eigenvalues of A have positive real parts, then (0,0) is unstable and the tumor will grow indefinitely. If one eigenvalue has positive real part and the other has negative real part, then (0,0) is a saddle and is unstable (with only two trajectories moving toward the equilibrium). If the eigenvalues have real part equal to zero, then the situation is more complicated. Also note that the eigenvectors are not used in understanding the stability of (0,0). Using qualitative analysis, we can more easily discuss the long term behavior of the solutions of the system than if we only had the analytical form of the solution alone.

Using the information in the preceding paragraph and the equations for the eigenvalues, we can come up with conditions, based on the parameters of the model, that determine when (0,0) will be stable. We only need to determine when the real parts of the eigenvalues are both negative [9].

From (5) and (6), we know both eigenvalues are always real when all parameters are nonnegative, since

$$\begin{aligned}
&(a_1 + a_2 + d_1 + d_2)^2 - 4(a_1(d_2 - a_2) + d_1(a_2 + d_2)) \\
&= d_1^2 + (a_1 + a_2 + d_2)^2 - 2d_1(a_1 + a_2 + d_2) + 4a_1a_2 \\
&= (d_1 - (a_1 + a_2 + d_2))^2 + 4a_1a_2 \geq 0.
\end{aligned}$$

Hence, if $a_1(d_2 - a_2) + d_1(a_2 + d_2) > 0$, both eigenvalues are negative and the cancer-free equilibrium is asymptotically stable, implying that the tumor would disappear naturally. On the contrary, if $a_1(d_2 - a_2) + d_1(a_2 + d_2) < 0$, then one eigenvalue is positive, the cancer-free equilibrium is unstable, implying that the tumor will grow without bounds. Notice that if either $d_1 > a_1$ or $d_2 > a_2$ (i.e., either compartment has a death rate which dominates the corresponding rate of transfer within the system), then the cancer-free equilibrium is stable [9]. We note that these results are analogous to those of Crivelli et al. [9] and Villasana and Radunskaya [22].

3 Delay Differential Equations

If we model cell transitions as above, there is a possibility that the cell will move into the active phases of the cell cycle and immediately split and transition to quiescence. In reality, cells take some amount of time to transit through the active phases of the cell cycle, due to various biological process in mitosis. The amount of time it takes to travel through the cell cycle is not pre-determined, but is stochastic in nature.

We think of the total amount of time needed to travel through the cell cycle as some minimum time τ plus some additional time that is Poisson in nature. The minimum time is deterministic and is modeled with a delay. The additional time is modeled through the exponential rate that cells transition back to resting.

To model the minimum time necessary to complete the active phases of the cell cycle, we add a delay to the model. Cells transition from quiescence to the active phases of the cell cycle at a rate of a_1 and remain there for a minimum time τ, representing the duration of mitosis. The way we model this mathematically, is to transition cells through a holding compartment, $\bar{S}$, representing mitosis, for τ days. Cells move from S to $\bar{S}$ at a rate of a_2, but cannot move back to Q until the minimum time is over. After the requisite time τ, cells move from $\bar{S}$ into Q. If this were the whole story, we could account for the transition through $\bar{S}$ by moving cells out of $\bar{S}$ at rate $a_2 S(t-\tau)$, so that the rate of cells leaving at time t would be precisely equal to the rate that cells entered τ days ago at time $t-\tau$. However, cells still die at a rate of d_3 while traveling through $\bar{S}$. Therefore, the model equations are

$$Q'(t) = 2a_2 e^{-d_3\tau} S(t-\tau) - a_1 Q - d_1 Q, \tag{9}$$

$$S'(t) = a_1 Q - a_2 S - d_2 S, \tag{10}$$

$$\bar{S}'(t) = a_2 S - d_3 \bar{S} - a_2 e^{-d_3\tau} S(t-\tau), \tag{11}$$

where the term $e^{-d_3\tau}$ accounts for the proportion of cells that have died over the τ days in the holding compartment, $\bar{S}$. To have a well-defined model, we also include history functions given by $Q(t) = \phi_q(t)$, $S(t) = \phi_s(t)$ and $\bar{S}(t) = \phi_{\bar{s}}(t)$, for $-\tau \le t \le 0$.

Notice that the first two equations in the system are not coupled with the holding compartment, so we can analyze the behavior of the system by only considering the first two equations and solving the equation for $\bar{S}$ in terms of $S(t)$.

Even though our system is still linear, the delay makes the system much more difficult to analyze. In general, systems of DDEs lead to characteristic quasipolynomials that include terms of the form $e^{-\lambda\tau}$, where τ is a time delay in the system.

To obtain the characteristic equation for our DDE system, we guess a solution of the form $e^{\lambda t}\mathbf{v}$ for some constant vector $\mathbf{v}$. Substituting this solution into (9) and (10) and simplifying, we obtain

$$\left(\begin{bmatrix} -(a_1+d_1) & 2a_2 e^{-d_3\tau} e^{-\lambda\tau} \\ a_1 & -(a_2+d_2) \end{bmatrix} - \lambda I_2 \right) \mathbf{v} = 0$$

where I_2 is the 2×2 identity matrix. Hence, it follows that

$$\det \begin{bmatrix} -(a_1+d_1)-\lambda & 2a_2 e^{-d_3\tau} e^{-\lambda\tau} \\ a_1 & -(a_2+d_2)-\lambda \end{bmatrix} = 0.$$

Calculating this determinant, we obtain the characteristic equation

$$P(\lambda) = 2a_1a_2e^{-d_3\tau}e^{-\lambda\tau} - (a_1 + d_1 + \lambda)(a_2 + d_2 + \lambda) = 0. \tag{12}$$

As is the case with transcendental equations of this form, in general, there are infinitely many roots. As in the ODE case, we use the eigenvalues to prove something about the tumor-free-equilibrium instead of finding the actual solutions to the delay equations.

Given below, a result from the original work [9] which is proved using the eigenvalues from the characteristic equation, describes a condition on τ, which, if achieved, results in a stable cancer-free equilibrium.

Theorem 1. *For any a_1, a_2, d_1, d_2, $d_3 > 0$, $(Q, S) = (0, 0)$ is stable when*

$$\tau > \frac{1}{d_3}\log\left(\frac{2a_1a_2}{(a_1 + d_1)(a_2 + d_2)}\right) > 0$$

and unstable when

$$0 < \tau < \frac{1}{d_3}\log\left(\frac{2a_1a_2}{(a_1 + d_1)(a_2 + d_2)}\right).$$

Theorem 1 shows that for any growth and death rates, there is a τ, given by the condition in the theorem, for which the tumor would be naturally eliminated. To prove this theorem, we first proved the following lemma [9]. See the original work for the proof.

Lemma 1. *For any a_1, a_2, d_1, d_2, $d_3 > 0$, the rightmost eigenvalue derived from the characteristic equation (12) is real.*

Having proven the previous lemma, we proved the following proposition [9]. The theorem directly follows.

Proposition 1. *For any parameters a_1, a_2, d_1, d_2, $d_3 > 0$, the cancer-free equilibrium $(Q, S) = (0, 0)$ of the system (9)–(10) is globally asymptotically stable if*

$$2a_1a_2e^{-d_3\tau} - (a_1 + d_1)(a_2 + d_2) < 0,$$

and unstable if

$$2a_1a_2e^{-d_3\tau} - (a_1 + d_1)(a_2 + d_2) > 0.$$

Using our result, it is also possible to determine a threshold delay value of τ, about which stability switches occur. We see that lengthening the time spent in the active phases of the cell cycle can cause the doubling time of the tumor population to

increase and thereby cause the tumor to be eliminated. Many therapeutics work in this way to lengthen the time that cells stay in the cell cycle so that they reproduce more slowly.

4 Virus System

So far, we have been investigating a system that describes tumor growth, including the minimum time necessary for the cell to travel through the active phases of the cell cycle. But the main goal of the work was to understand the dynamics of the oncolytic virus, VSV. At this point, the virus is introduced into the system. To add the virus, we must add compartments for the virus, V, and for cells that are infected by the virus, I.

Mathematically, the most interesting question here is how to model transmission of the virus to cells that are in the active phases of the cell cycle. As not to confound the situation, we first look at transmission, ignoring the minimum time spent in the active phases of the cell cycle.

As previously considered in (1) and (2), the model without virus is

$$Q'(t) = 2a_2S - a_1Q - d_1Q, \tag{13}$$

$$S'(t) = a_1Q - a_2S - d_2S. \tag{14}$$

After adding the virus and infected cell populations, we arrive at

$$Q'(t) = 2a_2S - a_1Q - d_1Q, \tag{15}$$

$$S'(t) = a_1Q - a_2S - d_2S - \kappa\frac{VS}{N}, \tag{16}$$

$$I'(t) = \kappa\frac{VS}{N} - \delta I, \tag{17}$$

$$V'(t) = \alpha I - \kappa\frac{VS}{N} - \omega V. \tag{18}$$

Let us examine how the system changes when the virus and infected cells are added. The top equation is the same because the virus cannot act when cells are in the Q state. The next equation, which describes how the size of the population of active cells changes, has a new term, $-\kappa\frac{VS}{N}$, which describes the rate that cells become infected. This term then appears again in the next equation, as cells move from S to I when they become infected. Here, N, is the total volume of tumor cells and virions in the system ($N = S + I + V$). Modelers frequently use a mass-action term for transmission (here that would be $-\kappa VS$). On the other hand, the term we used is called a ratio- or frequency-dependent term.

If we use a mass-action term to describe the dynamics of the virus, then the virus has no effect on the local stability of the tumor-free equilibrium ($(Q, S, I, V) = (0, 0, 0, 0)$). To understand this, we extend our linear analysis from Sect. 3 to nonlinear systems. To do so, we must call on the Hartman–Grobman Theorem.

Formally, the Hartman–Grobman Theorem is a topological result. Informally, it is likely the most used tool for understanding the long term behavior of nonlinear differential equations systems. A formal statement is given in Perko [19]:

Theorem 2 (Hartman–Grobman Theorem). *Let E be an open subset of $\mathbb{R}^n$ containing the origin, let $\mathbf{f} \in C^1(E)$, and let ϕ_t be the flow of the nonlinear system $\dot{\mathbf{x}} = \mathbf{f}(\mathbf{x})$. Suppose that $\mathbf{f}(\mathbf{0}) = \mathbf{0}$ and that the matrix $A = D\mathbf{f}(\mathbf{0})$ has no eigenvalue with zero real part. Then there exists a homeomorphism H of an open set U containing the origin onto an open set V containing the origin such that for each $\mathbf{x_0} \in U$, there is an open interval $I_0 \subset \mathbb{R}$ containing zero such that for all $\mathbf{x_0} \in U$ and $t \in I_0$*

$$H \circ \phi_t(\mathbf{x_0}) = e^{At} H(\mathbf{x_0}). \tag{19}$$

A friendlier (but less technical) version of this theorem can be found in Cain and Reynolds [7] and is helpful in this discussion:

Theorem 3 (Hartman–Grobman Theorem, Friendly Version). *Suppose $\mathbf{x_0}$ is an isolated equilibrium of a nonlinear system $\dot{\mathbf{x}} = \mathbf{f}(\mathbf{x})$. Then in the vicinity of $\mathbf{x_0}$, the linearization $\mathbf{x_0} = J\mathbf{f}(\mathbf{x_0})(\mathbf{x} - \mathbf{x_0})$ about that equilibrium has the same qualitative behavior as the original nonlinear system.*

In the virus system, the vectors $\mathbf{x} = (Q, S, I, V)^T$ and $\mathbf{f}$ is the vector formulated right hand side of our system of differential equations.

The Hartman–Grobman Theorem tells us that solutions of a nonlinear system act like solutions of their corresponding linearized system near hyperbolic equilibria. Assuming that the tumor-free equilibrium is hyperbolic (no eigenvalues with zero real part), we can linearize the system and see how the virus affects the stability of the tumor-free equilibrium.

But what is this term $J\mathbf{f}(\mathbf{x_0})(\mathbf{x} - \mathbf{x_0})$, and what does it have to do with linearization? Linearizing a nonlinear system means that we take the multivariate functions on the right hand side of each differential equation in the system and Taylor expand each one around each equilibrium ($\mathbf{x_0}$), so that

$$\frac{d\mathbf{x}}{dt} = \mathbf{f}(\mathbf{x_0}) + J\mathbf{f}(\mathbf{x_0})(\mathbf{x} - \mathbf{x_0}) + \text{higher order terms}, \tag{20}$$

where J is the Jacobian, the matrix of all first derivatives of the vector valued function, $\mathbf{f}$. We then drop the higher order terms, since we want to know about the local stability of the equilibria. We can drop the higher order terms because we are interested in the local behavior of the system and the higher order terms are small when we are near the equilibrium.

Since $\mathbf{x_0}$ is an equilibrium of the system, we know that $\mathbf{f}(\mathbf{x_0}) = 0$ so that

$$\frac{d\mathbf{x}}{dt} = J\mathbf{f}(\mathbf{x_0})(\mathbf{x} - \mathbf{x_0}). \tag{21}$$

Next, we want to change the main vector of variables to be the distance from the equilibrium instead of the total distance. We do so by substituting $\bar{x} = (\mathbf{x} - \mathbf{x_0})$ and noting that $\frac{d\mathbf{x}}{dt} = \frac{d\bar{\mathbf{x}}}{dt}$ since $\frac{d\mathbf{x_0}}{dt} = 0$. We then have

$$\frac{d\bar{\mathbf{x}}}{dt} = J\mathbf{f}(\mathbf{x_0})(\bar{\mathbf{x}}). \tag{22}$$

This is the linearized version of the system around the equilibrium $\mathbf{x_0}$. From the Hartman–Grobman Theorem, we know we can determine the stability of any hyperbolic equilibrium by eigenvalue analysis of the Jacobian evaluated at the equilibrium of interest.

Now going back to virus system, we want to know how the stability of the tumor-free equilibrium ($(Q, S, I, V) = (0, 0, 0, 0)$) is affected by the introduction of the virus. The real question is, by introducing the virus, can we eliminate the tumor over time, or in mathematical terms, can introduction of the virus change the sign of the real part of the eigenvalues of the Jacobian so that they go from at least one being positive to all negative?

In the original paper, we make the argument that the virus cannot affect local stability of the tumor-free equilibrium if transmission is modeled using a mass-action term κVS instead of the ratio-dependent term $\frac{\kappa VS}{N}$, where $N = Q + S + I + V$. Now that we understand what it means to linearize a system and talk about stability of the tumor-free equilibrium under linearization, let us look at what happens when we linearize the system which includes mass-action transmission:

$$Q'(t) = 2a_2 S - a_1 Q - d_1 Q, \tag{23}$$

$$S'(t) = a_1 Q - a_2 S - d_2 S - \kappa VS, \tag{24}$$

$$I'(t) = \kappa VS - \delta I, \tag{25}$$

$$V'(t) = \alpha I - \kappa VS - \omega V. \tag{26}$$

The Jacobian, J, of the right-hand side of this system is

$$J(Q, S, I, V) = \begin{bmatrix} -a_1 - d_1 & 2a_2 & 0 & 0 \\ a_1 & -a_2 - d_2 - \kappa V & 0 & -\kappa S \\ 0 & \kappa V & -\delta & \kappa S \\ 0 & -\kappa V & \alpha & -\omega \end{bmatrix}.$$

So far, it looks like the parameters of the virus are coming into play repeatedly in the Jacobian matrix and will have an important role to play in determining the sign

of the eigenvalues. But we must remember that before we find the eigenvalues, we evaluate the Jacobian at the tumor-free equilibrium $(Q, S, I, V) = (0, 0, 0, 0)$), so anywhere we see a V or an S, that term will be zero. These are all of the transmission terms. At the tumor-free equilibrium, the Jacobian is

$$J(0,0,0,0) = \begin{bmatrix} -a_1 - d_1 & 2a_2 & 0 & 0 \\ a_1 & -a_2 - d_2 & 0 & 0 \\ 0 & 0 & -\delta & 0 \\ 0 & 0 & \alpha & -\omega \end{bmatrix}.$$

This is a block matrix and the eigenvalues from the top-left block only depend on the parameters a_1, a_2, d_1, and d_2, which is the coefficient matrix of the linear submodel describing tumor growth alone without virus (see (13) and (14)). The two eigenvalues of the lower-right block are $-\delta$ and $-\omega$, which are always negative, because δ and ω are always positive. So we see that if we use mass-action transmission, the virus is not able to affect the stability of the tumor-free equilibrium because the terms related to the virus do not alter the signs of the eigenvalues associated with tumor growth. The eigenvalues due to the virus-associated parameters are always negative and the others are unaffected by the virus.

However, if we use ratio-dependent transmission, as is in (15) and (18), it has been shown that the virus can affect the stability of the tumor-free equilibrium [15]. Ratio dependence also makes sense biologically because it allows for the spatial size of the tumor to change, whereas mass action makes the assumption that the spatial dimension is staying constant, while the density changes, which is not usually the case for tumors.

It is noted that the biological relevance of these results is not certain. In the mass-action type model, oscillations are frequently seen that drive the tumor size to near zero [9, 13, 24]. In the true biological system, when the tumor is near zero, it can be removed completely due to the stochasticity of the underlying dynamics. Additionally, the formulation of the ratio-dependent term is sensitive to perturbations, causing the model to not be entirely robust.

5 PDE Virus System

First, a model of tumor growth was developed. We then investigated how incorporating the time needed to travel through the cell cycle affected the stability of the tumor-free equilibrium of the model by developing a system of equations that included a delay. Next, we created a model of tumor growth and viral dynamics without the delay. In this section, we finally put all of the components together into one model.

We can no longer use delay differential equations, because the transmission term is nonlinear and we can no longer solve directly for the loss of cells in the holding

state $\bar{S}$, as we did in the simpler growth-only model. After developing the model, we want to make sure that the solutions match those of the simpler model, if the viral parameters are set to zero. To do so, we must first complete our analysis of (11) by solving for $\bar{S}$ in terms of S, which we think of as a known function of t.

Begin with the differential equation

$$\bar{S}'(t) = a_2 S - d_3 \bar{S} - a_2 e^{-d_3 \tau} S(t-\tau), \tag{27}$$

which is *linear* in $\bar{S}$.

The integrating factor is $e^{d_3 t}$. After multiplying by the integrating factor on both sides and integrating between 0 and t, we find that

$$\bar{S}(t) = \bar{S}(0) e^{-d_3 t} + a_2 e^{-d_3 t} \int_{t-\tau}^{t} e^{d_3 u} S(u) du - a_2 e^{-d_3 t} \int_{-\tau}^{0} e^{d_3 u} \phi_s(u) du. \tag{28}$$

We also assume that cells that are in the holding state before $t = -\tau$, leave before $t = 0$. Mathematically we can do this by setting $\bar{S}(0) = a_2 \int_{-\tau}^{0} e^{d_3 u} \phi_s(u) du$. Therefore, the solution is

$$\bar{S}(t) = a_2 e^{-d_3 t} \int_{t-\tau}^{t} e^{d_3 u} S(u) du. \tag{29}$$

After developing the full model, we will check that it is consistent with this solution.

Now to the full model. Our full PDE model, including the minimum biological time needed to complete the active phases of the cell cycle, as well as the viral transmission, is

$$\frac{dQ}{dt} = 2\hat{S}(\tau, t) - a_1 Q - d_1 Q, \tag{30}$$

$$\frac{dS}{dt} = a_1 Q - a_2 S - d_2 S - \kappa \frac{VS}{N}, \tag{31}$$

$$\frac{\partial \hat{S}}{\partial t} + \frac{\partial \hat{S}}{\partial x} = -d_3 \hat{S} - \kappa \frac{V\hat{S}}{N}, \tag{32}$$

$$\frac{dI}{dt} = -\delta I + \kappa \frac{VS + V\bar{S}}{N}, \tag{33}$$

$$\frac{dV}{dt} = \alpha I - \omega V - \kappa \frac{VS + V\bar{S}}{N}. \tag{34}$$

where $\bar{S}(t) = \int_0^\tau \hat{S}(x,t) dx$, $N(t) = Q(t) + S(t) + \bar{S}(t) + I(t) + V(t)$, and the boundary condition is given by

$$\hat{S}(0,t) = a_2 S(t).$$

$\hat{S}$ is a function of two variables: t–time, and x–the length of time already spent in the cell cycle. A diagram of the full PDE model is given in Fig. 1.

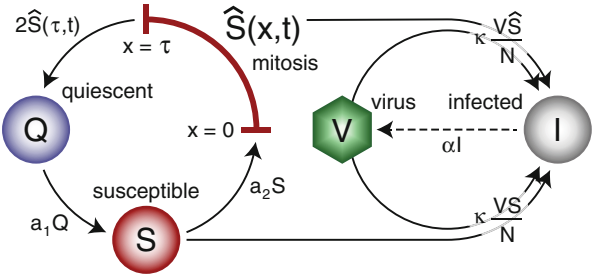

Fig. 1 Compartmental diagram for the full model of virotherapy, given by (30)–(34). Transfer occurs from the quiescent to the non-quiescent, or susceptible, cell population at rate a_1, and susceptible cells begin mitosis at rate a_2. Cells undergoing mitosis remain in a holding state for τ units of time. After completing mitosis, two daughter cells enter the quiescent population. Susceptible cells are infected through contact with the free virus population at rate $\kappa V/N$ and enter the infected state. Viral reproduction in infected cells, combined with lysis, leads to production of free virions at a rate α. Although not shown in the diagram, all cell and virus populations, Q, S, $\hat{S}$, I, and V die or decay at rates d_1, d_2, d_3, δ, and ω, respectively

Note that the PDE now accounts for the loss of susceptible cells in the delay period. For biological relevance, the initial conditions, $Q(0)$, $S(0)$, $\hat{S}(x,0)$, $I(0)$, and $V(0)$, are all assumed to be nonnegative. To extend the model to the origin, when $N = 0$, we let the right-hand sides of (30)–(34) equal zero. Note that the system (30)–(34) also reduces to (15)–(18) when $\tau = 0$.

Remember, we want to show that if we remove virotherapy, the solution we obtain is the same as (29). To do so, we will use the method of characteristics, a technique that can be used to solve certain partial differential equations (PDE). We use it here to find the solution of the full system when virotherapy is turned off, and then afterward, to prove that solutions of the full system with virotherapy do not become negative.

The main idea behind the method of characteristics is that you divide the domain into characteristic curves. Along these characteristic curves, the PDE becomes an ODE that you can solve, given suitable initial value data. After you find solutions on the characteristic curves, you convert the solutions into one concise surface solution for the PDE.

A standard example involves the advection equation

$$a\frac{\partial u}{\partial t} + b\frac{\partial u}{\partial x} = 0, \tag{35}$$

where a and b are not zero. We are looking for solutions $u(t,x)$ that satisfy this PDE.

The characteristic curves are found by realizing that the normal to the surface $(t, x, u(t, x))$ is given by $(u_t, u_x, -1)$. Our PDE tell us that $(a, b, 0)\cdot(u_t, u_x, -1) = 0$, so we look for $(a, b, 0)$ which lies in the tangent plane to $(t, x, u(t, x))$. To do so, we let

$$\frac{dt}{ds} = a \tag{36}$$

$$\frac{dx}{ds} = b \tag{37}$$

$$\frac{du}{ds} = 0, \tag{38}$$

where we are parameterizing the characteristic curve in the tangent plane by s. Solving the system of ordinary differential equations in terms of s we find

$$\begin{aligned} t(s) &= as + c_1 \\ x(s) &= bs + c_2 \\ u(s) &= c_3. \end{aligned}$$

We can get rid of the parameter s, noting that the characteristic curves are $ax - bt$ and that the solution u is constant along these characteristic curves. Therefore, the solution is an arbitrary differentiable function $u(t, x) = f(ax - bt)$. The particular function needed when modeling is determined from auxiliary conditions. To see why the solution makes sense, notice from the chain rule that

$$a\frac{\partial u}{\partial t} + b\frac{\partial u}{\partial x} = abf'(ax - bt) - baf'(ax - bt) = 0.$$

Now, let us examine how we used the method of characteristics in a couple different ways in the paper. Going back to the model, if we remove virotherapy, and assume that, for $0 \leq x \leq \tau$, $\hat{S}(x, 0) = a_2\phi_s(-x)e^{-d_3 x}$, then this system acts like (9)–(11). We want to show that is the PDE model really is equivalent to (9)–(11) by showing that $\bar{S}$ is the same as (29).

Similar to the preceding example, if we use the method of characteristics, we let

$$\begin{aligned} \frac{dt}{ds} &= 1 \\ \frac{dx}{ds} &= 1 \\ \frac{d\hat{S}}{ds} &= -d_3\hat{S}, \end{aligned}$$

Solving the system of ODEs, we find

$$\begin{aligned} t(s) &= s + c_1 \\ x(s) &= s + c_2 \\ \hat{S}(s) &= \hat{S}(s=0)e^{-d_3 s}, \end{aligned}$$

which implies

$$\hat{S}(s + c_2, s + c_1) = \hat{S}(c_2, c_1)e^{-d_3 s}.$$

Letting $s = \tilde{x}$, $c_1 = \tilde{t} - \tilde{x}$, and $c_2 = 0$ for $\tilde{t} \geq \tilde{x}$ and removing the tildes, we obtain

$$\hat{S}(x, t) = \hat{S}(0, t - x)e^{-d_3 x}.$$

We can then find $\bar{S}(t)$ by noting that $\hat{S}(0, t - x) = a_2 S(t - x)$:

$$\bar{S}(t) = \int_0^\tau \hat{S}(x, t)dx = \int_0^\tau \hat{S}(0, t - x)e^{-d_3 x}dx \tag{39}$$

$$= \int_0^\tau a_2 S(t - x)e^{-d_3 x}dx \tag{40}$$

$$= \int_{t-\tau}^t a_2 S(u)e^{-d_3(t-u)}du \tag{41}$$

$$= a_2 e^{-d_3 t} \int_{t-\tau}^t e^{d_3(u)} S(u)du. \tag{42}$$

And so we have achieved our goal, showing that $\bar{S}$ is the same as for the virus free system, see (29).

We also used the method of characteristics and integrating factor techniques to prove that solutions that begin nonnegative remain nonnegative for all time. We include the theorem and proof here as a more complicated example of using the method of characteristics [9].

Theorem 4. *Assume that $Q(0)$, $S(0)$, $\hat{S}(x, 0)$, $I(0)$, and $V(0)$ are nonnegative. Then, solutions of the system (30)–(34) are nonnegative for $t \geq 0$.*

Proof. If $Q(0) = S(0) = \hat{S}(x, 0) = \hat{S}(0, t) = I(0) = V(0) = 0$, then $Q(t) = S(t) = \hat{S}(x, t) = I(t) = V(t) = 0$ for all t, and we are at equilibrium.

Otherwise by assumption, at $t = 0$, all compartments are greater than or equal to zero and the total population $N(0) > 0$. In this case, we assume

$$t_0 = \inf_{t>0}\{t \mid Q(t) < 0, S(t) < 0, \bar{S}(t) < 0, I(t) < 0 \text{ or } V(t) < 0\},$$

with $t_0 < \infty$ and proceed to arrive at a contradiction.

Let $W = I + V$. We first assume that $\omega \geq \delta$, so

$$W' = -\omega W + (\alpha - \delta + \omega)I.$$

If $f(t) = (\alpha - \delta + \omega)I$, then $f(t) \geq 0$ for $t \in [0, t_0]$. Second, we assume that $\omega < \delta$, so

$$W' = -\delta W + \alpha I + (\delta - \omega)V.$$

If $f(t) = \alpha I + (\delta - \omega)V$, then $f(t) \geq 0$ for $t \in [0, t_0]$, so in general,

$$W' = -c_1 W + f(t), \tag{43}$$

for some $c_1 > 0 \in \mathbb{R}$ and $f(t) \geq 0$ for $t \in [0, t_0]$.

The solution of (43) is

$$W(t) = W(0)e^{-c_1 t} + e^{-c_1 t} \int_0^t e^{c_1 \xi} f(\xi) d\xi.$$

If $W(0) = 0$, the system reduces to the model with no treatment. Otherwise, because $W(0) > 0$ and $f(t) \geq 0$, it follows that $W(t) > 0$ for $t \in [0, t_0]$. Then, since $W(t_0) > 0$, the total population $N(t_0) > 0$. Now, with $N(t_0) > 0$, we can show that all compartments will stay nonnegative past t_0.

We begin with the age-structured PDE (32) and show that $\hat{S}(\tau, t) \geq 0$ for $t \in [0, t_0 + \eta)$ where $\eta = \min\{\epsilon, \tau\}$ for some $\epsilon > 0$. For each $\zeta \in \mathbb{R}$, we define

$$S_\zeta^*(T) = \hat{S}(\zeta + T, T).$$

and find solutions along the characteristic lines $x = \zeta + T$ with $t = T$. Then,

$$\frac{dS_\zeta^*}{dT} = \frac{\partial \hat{S}}{\partial x} + \frac{\partial \hat{S}}{\partial t}$$

and

$$(S_\zeta^*)' = -d_3 S_\zeta^* - \kappa \frac{V S_\zeta^*}{N}.$$

Hence, for each ζ, we have converted (32) into an ODE.

Since $t = T$,

$$S_\zeta^{*'}(t) = -d_3 S_\zeta^*(t) - \kappa \frac{V(t) S_\zeta^*(t)}{N(t)}.$$

Letting $g(t) = d_3 + \frac{\kappa V(t)}{N(t)}$, we rewrite the equation above as

$$S_\zeta^{*'}(t) = -g(t)S_\zeta^*(t). \tag{44}$$

Replacing Eq. (32) with (44), we obtain a system of ODEs for each characteristic line. From the form of the system of equations and the nonnegativity of initial conditions, it follows that $t_0 > 0$.

Since $N(t_0) > 0$, the ODE system is well-posed and a solution exists on an interval $(t_0 - \epsilon, t_0 + \epsilon)$. Moreover, by continuity, we may assume $N(t) > 0$ for $t \in (t_0 - \epsilon, t_0 + \epsilon)$.

Then solutions of Eq. (44) along the characteristic lines $x = \zeta + t$ are

$$S_\zeta^*(t) = S_\zeta^*(0)e^{-\int_0^t g(u)du}.$$

Each characteristic line in the (x, t) plane intersects either the nonnegative x-axis or the positive t-axis. If $\zeta \geq 0$, then the characteristic line intersects the nonnegative x-axis and $S_\zeta^*(0) = \hat{S}(\zeta, 0)$, which is nonnegative by assumption. Otherwise, if $\zeta < 0$, the characteristic line intersects the positive t-axis at $-\zeta$, and $S_\zeta^*(0) = \hat{S}(0, -\zeta) = a_2 S(-\zeta)$. By definition of t_0, we know that $S(-\zeta)$ is nonnegative when $-\zeta \in [0, t_0]$. Thus, $S_\zeta^*(0) \geq 0$ for each characteristic line that intersects the positive t-axis at or below t_0, $(\zeta \geq -t_0)$.

Since $g(t)$ is bounded $(0 \leq g(t) \leq d_3 + \kappa)$ and $S_\zeta^*(0) \geq 0$ for $\zeta \geq -t_0$, on the corresponding characteristic lines, $S_\zeta^*(t)$ will remain nonnegative for as long as the solution exists. Therefore, $\hat{S}(\tau, t)$ will also remain nonnegative for $t \in (t_0 - \eta, t_0 + \eta)$ where $\eta = \min\{\epsilon, \tau\}$. The constant η is defined in this way to ensure that solutions lie on the proper characteristic lines and that solutions exist.

Next, we evaluate (30)–(34), excluding the PDE. Each of the four equations is of the form $B'(t) = A(t) - r(t)B(t)$, and each equation has a solution of the form

$$B(t) = B(0)e^{-\int_0^t r(s)ds} + \int_0^t e^{-\int_\xi^t r(s)ds} A(\xi)d\xi,$$

where B is Q, S, I or V. For (30), the variable $A(t) = 2\hat{S}(\tau, t)$, and we know that $\hat{S}(\tau, t)$ is greater than or equal to zero for $t \in [0, t_0 + \eta)$ from the earlier argument using the method of characteristics. By assumption, the initial condition $Q(0) \geq 0$, so we obtain $Q(t) \geq 0$ for $t \in (t_0 - \eta, t_0 + \eta)$. For (31), the variable $A(t) = a_1 Q(t)$, so by similar reasoning, it follows that $S(t) \geq 0$ for $t \in (t_0 - \eta, t_0 + \eta)$. Since $S(t) \geq 0$ for $t \in (t_0 - \eta, t_0 + \eta)$, it follows that $S_\zeta^*(0) \geq 0$ for characteristic lines intersecting the t-axis up to $t_0 + \eta$. So, $\hat{S}(x, t) \geq 0$ for $t \in (t_0 - \eta, t_0 + \eta)$, and therefore the same holds for $\bar{S}(t)$. Finally, since $Q, S, \hat{S} \geq 0$, it follows from (33) and (34) that solutions cannot leave the positive quadrant of the $I - V$ plane and I and V will remain nonnegative for $t \in (t_0 - \eta, t_0 + \eta)$.

We have shown that all compartments remain nonnegative for $t \in (t_0 - \eta, t_0 + \eta)$. This contradicts the definition of t_0. We conclude that solutions remain nonnegative for all time.

6 Numerical Simulations

Models of biological systems are interesting from a mathematical point of view, but more importantly, for what they say about the biology. We used the models we developed above to understand the dynamics of the tumor-virus system in terms of biological parameters. In our paper [9], we numerically studied the dynamics from two perspectives: trajectories over time and stability regions using parameters from the literature (Table 1). By investigating trajectories over time, we showed that increasing the delay or adding virus can change the stability of the tumor free equilibrium. We also showed, using stability regions, that the specific parameters of the tumor or the virus affect the stability of the tumor-free equilibrium.

6.1 Non-Delay Case

We numerically simulated the various models using solvers, such as dde23, in MATLAB (Mathworks, MA), first without delay, then with the delay. Figure 2 plots solutions under three different conditions. The leftmost plot displays exponential tumor growth resulting from the system (13) and (14). The middle plot shows solutions of the system when a mass-action transmission term is used, whereas the plot on the right shows solutions for ratio-dependent transmission, using system (15)–(18) for the case of ratio-dependent transmission and system (23)–(26) for the case of mass-action transmission. Note that the untreated tumor grows exponentially (Fig. 2, left), whereas the treated tumor is eliminated (Fig. 2, right). Mass-action solutions are presented to show how solutions oscillate under such dynamics (Fig. 2, middle).

Two parameters, α and κ, are strongly correlated with the effectiveness of VSV treatment in system (15)–(18). Increase in viral replication is modeled by increasing α. Increasing viral replication increases virus-cell contact and results in a better treatment. As κ increases, likelihood of infection increases, also increasing the efficacy of the treatment. Figure 3 shows the effects of changing α and κ on the stability or instability of the cancer-free equilibrium.

6.2 Delay Case

Next, we looked at the models including the minimum time biologically necessary to complete division and compared to the non-delay system. In the left panel of Fig. 4, we plot solutions of the system, including the delay, but without VSV treatment.

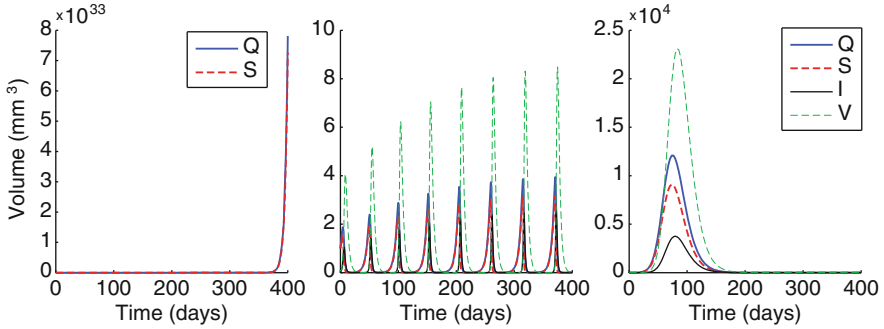

Fig. 2 Numerical solutions of VSV, excluding delay. *Left*: exponential tumor growth in the absence of therapy, (13) and (14). *Middle*: growing oscillatory behavior of solutions when virus-cell contact is modeled using mass action, (23)–(26). *Right*: complete tumor elimination; virus-cell contact is modeled using ratio dependence, (15)–(18). Parameter values: $a_1 = 0.9$, $a_2 = 0.6$, $d_1 = 0.00001$, $\delta = 1.119$, $\omega = 0.3$, $\alpha = 3$, $\kappa = 1$ in the case of mass-action transmission (*middle*), and $\kappa = 1$, in the case of ratio-dependent transmission (*right*)

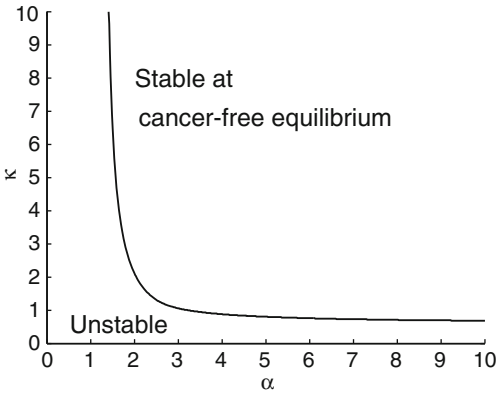

Fig. 3 Stability diagram for viral reproduction (α) and contact (κ). Other parameter values are as in Fig. 2, i.e. $a_1 = 0.9$, $a_2 = 0.6$, $d_1 = 0.00001$, $\delta = 1.119$, $\omega = 0.3$, and $\alpha = 3$

Parameters were chosen so that the solutions grow exponentially. In the middle panel, using the same parameters for tumor growth, we look at the VSV model that excludes the delay. We once again see exponential growth of the tumor (middle panel). The right most panel shows how interaction of the treatment and the delay causes successful elimination of the tumor. When the time delay is included, VSV successfully eliminates the tumor (right panel), demonstrating how the delay and the treatment interact, leading to successful eradication of the tumor.

Finally, we study stability diagrams of the VSV treatment parameters, α, κ, and τ. Figure 5 shows how the parameters interact, two at a time, to change the stability of the tumor free equilibrium.

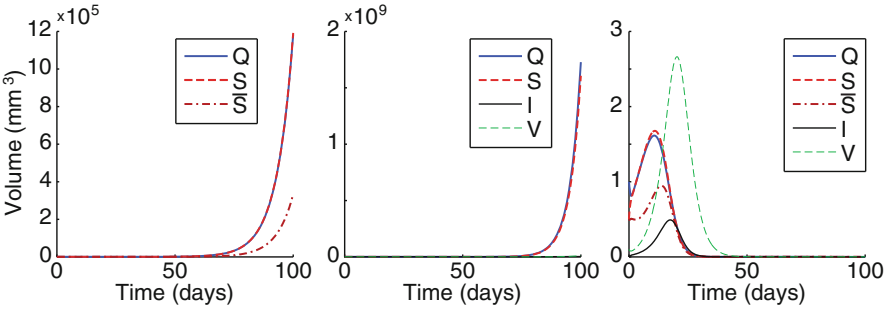

Fig. 4 *Left*: uncontrolled tumor growth (in the absence of virotherapy) under prolonged cell cycle progression ($\tau = 0.5$). *Middle*: when $\kappa = 0.8$, virotherapy treatment fails; minimum cell cycle time is not accounted ($\tau = 0$). *Right*: when $\kappa = 0.8$, virotherapy with a minimum cycling time ($\tau = 0.5$) results in a stable cancer-free state. All other parameter values are the same as in Fig. 2, i.e. $a_1 = 0.9$, $a_2 = 0.6$, $d_1 = 0.00001$, $\delta = 1.119$, $\omega = 0.3$, and $\alpha = 3$

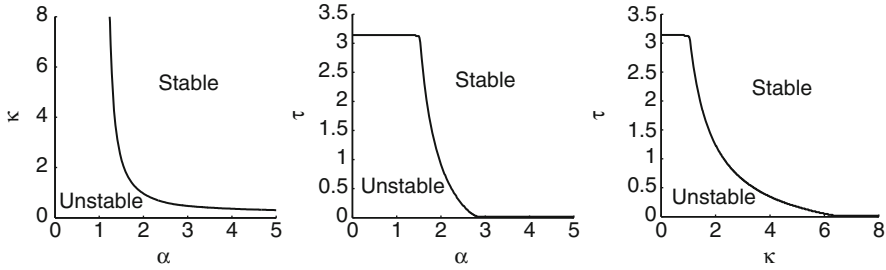

Fig. 5 Stability maps when α, κ, and τ are varied, two at a time. For small α and κ, a delay value (τ) beyond a certain threshold will ensure stability of the origin. Parameter values, if not varied, are $a_1 = 0.9$, $a_2 = 0.6$, $d_1 = 0.00001$, $\delta = 1.119$, $\omega = 0.3$,$\alpha = 1.5$, $\kappa = 1$, and $\tau = 1$

7 Discussion

In this chapter, we have developed a model of vesicular stomatitus virus (VSV), a candidate oncolytic virus, which has the defining feature that it can only infect tumor cells when they are in the active phases of the cell cycle.

We began with a simple tumor growth model containing compartments for resting and proliferating cells. This model took the form of a linear system of differential equations. We used the model to discuss basic techniques for linear systems analysis, the eigenvalue method. We presented results from the original work [9], giving conditions, in terms of parameters, for which the tumor would grow indefinitely or decay based solely on parameters related to the tumor.

Next, we extended the model to account for the minimum biological time course of the active phases of the cell cycle. In doing so, we arrived at a three-dimensional system of linear delay differential equations. Eigenvalue analysis for delay differential equations was discussed and a basic example given. We also

Table 1 Table of parameters given by (30)–(34). Parameters were obtained from the references cited in the fourth column. For all simulations, it was assumed that $d_3 = d_2$

Parameter	Description	Estimate	Reference
a_1	Quiescent cell entrance into active phases (day^{-1})	0.9	[14]
a_2	Active cell entrance into quiescence (day^{-1})	0.6	[14]
d_1	Quiescent cell death (day^{-1})	1×10^{-5}	[14]
d_2	Active cell death (day^{-1})	0.15	[14]
α	Virion production (day^{-1})	3	Variable
δ	Infected cell elimination (day^{-1})	1.119	[3]
ω	Free virion decay (day^{-1})	0.3	[3]
τ	Minimum duration of active phases (day)	[0, 3]	Variable
κ	Kinetic coefficient (day^{-1})	[0, 5]	Variable

reviewed the main result for that model: for a given set of model parameters, there exists a minimum value of the delay τ that will drive the system towards a globally stable cancer-free state, which can be calculated in terms of the growth and death rates of tumor populations.

Our next extension involved introducing virotherapy treatment by including two additional compartments: infected cells and free virions, creating a nonlinear system of differential equations. We discussed linearization techniques and methods of analysis. These methods helped us understand why transmission kinetics should be modeled through ratio-dependent contact between free virions and tumor cells. Our model complements experimental results that suggest that initiation of virotherapy treatment can drive the system towards the cancer-free equilibrium.

Finally, we developed our full model using an age-structured PDE model. We introduced the method of characteristics, a method commonly used to solve basic hyperbolic PDEs. We then showed how we used this method to obtain results in our original work. We first showed that the PDE without virotherapy is identical to the DDE model. The method of characteristics was used in a more complicated example to show that the solutions of our full model remain nonnegative. As a last note, we showed how numerical simulations could further the discussion by allowing us to examine time trajectories and stability regions.

This work reveals how techniques and tools from differential equations can be used to develop and analyze models of oncolytic viruses. Each virus is unique and therefore different models will be needed to study the characteristics of each one. Here, we progressively developed a model of VSV using ordinary, delay, and partial differential equations and presented the necessary tools to build and analyze that particular model.

References

1. Au, G.G., Lindberg, A.M., Barry, R.D., Shafren, D.R.: Oncolysis of vascular malignant human melanoma tumors by Coxsackievirus A21. Int. J. Oncol. **26**(6), 1471–1476 (2005)
2. Bajzer, Z., Carr, T., Dingli, D., Josic, K.: Optimization of tumor virotherapy with recombinant measles virus. In: Lim, G.J., Lee, E.K. (eds.) Optimization in Medicine and Biology. Auerbach Publications, New York (2008)
3. Bajzer, Z., Carr, T., Josic, K., Russell, S.J., Dingli, D.: Modeling of cancer virotherapy with recombinant measles viruses. J. Theor. Biol. **252**(1), 109–122 (2008)
4. Balachandran, S., Barber, G.N.: Vesicular stomatitis virus (VSV) therapy of tumors. IUBMB Life **50**(2), 135–138 (2000)
5. Bell, J., Parato, K., Atkins, H.: Vesicular stomatitis virus. In: Harrington, K.J., Vile, R.G., Pandha, H.S. (eds.) Viral Therapy of Cancer. Wiley, Hoboken (2008)
6. Biesecker, M., Kimn, J.H., Lu, H., Dingli, D., Bajzer, Z.: Optimization of virotherapy for cancer. Bull. Math. Biol. **72**(2), 469–489 (2010)
7. Cain, J.W., Reynolds, A.M.: Ordinary and Partial Differential Equations. An Introduction to Dynamical Systems. Creative Commons. Virginia Commonwealth University, Richmond (2010)
8. Comins, C., Spicer, J., Protheroe, A., Roulstone, V., Twigger, K., White, C.M., Vile, R., Melcher, A., Coffey, M.C., Mettinger, K.L., Nuovo, G., Cohn, D.E., Phelps, M., Harrington, K.J., Pandha, H.S.: REO-10: a phase I study of intravenous reovirus and docetaxel in patients with advanced cancer. Clin. Cancer Res. **16**(22), 5564–5572 (2010)
9. Crivelli, J.J., Foldes, J., Kim, P.S., Wares, J.R.: A mathematical model for cell cycle-specific cancer virotherapy. J. Biol. Dyn. **6**(Suppl 1), 104–120 (2012)
10. Dingli, D., Peng, K.W., Harvey, M.E., Greipp, P.R., O'Connor, M.K., Cattaneo, R., Morris, J.C., Russell, S.J.: Image-guided radiovirotherapy for multiple myeloma using a recombinant measles virus expressing the thyroidal sodium iodide symporter. Blood **103**(5), 1641–1646 (2004)
11. Friedman, A., Tian, J.P., Fulci, G., Chiocca, E.A., Wang, J.: Glioma virotherapy: effects of innate immune suppression and increased viral replication capacity. Cancer Res. **66**(4), 2314–2319 (2006)
12. Heise, C., Sampson-Johannes, A., Williams, A., McCormick, F., Von Hoff, D.D., Kirn, D.H.: ONYX-015, an E1B gene-attenuated adenovirus, causes tumor-specific cytolysis and antitumoral efficacy that can be augmented by standard chemotherapeutic agents. Nat. Med. **3**(6), 639–645 (1997)
13. Komarova, N.L., Wodarz, D.: ODE models for oncolytic virus dynamics. J. Theor. Biol. **263**(4), 530–543 (2010)
14. Liu, W., Hillen, T., Freedman, H.I.: A mathematical model for M-phase specific chemotherapy including the G0-phase and immunoresponse. Math. Biosci. Eng. **4**(2), 239–259 (2007)
15. Novozhilov, A.S., Berezovskaya, F.S., Koonin, E.V., Karev, G.P.: Mathematical modeling of tumor therapy with oncolytic viruses: regimes with complete tumor elimination within the framework of deterministic models. Biol. Direct **1**, 6 (2006)
16. Oliere, S., Arguello, M., Mesplede, T., Tumilasci, V., Nakhaei, P., Stojdl, D., Sonenberg, N., Bell, J., Hiscott, J.: Vesicular stomatitis virus oncolysis of T lymphocytes requires cell cycle entry and translation initiation. J. Virol. **82**(12), 5735–5749 (2008)
17. Park, B.H., Hwang, T., Liu, T.C., Sze, D.Y., Kim, J.S., Kwon, H.C., Oh, S.Y., Han, S.Y., Yoon, J.H., Hong, S.H., Moon, A., Speth, K., Park, C., Ahn, Y.J., Daneshmand, M., Rhee, B.G., Pinedo, H.M., Bell, J.C., Kirn, D.H.: Use of a targeted oncolytic poxvirus, JX-594, in patients with refractory primary or metastatic liver cancer: a phase I trial. Lancet Oncol. **9**(6), 533–542 (2008)
18. Pecora, A.L., Rizvi, N., Cohen, G.I., Meropol, N.J., Sterman, D., Marshall, J.L., Goldberg, S., Gross, P., O'Neil, J.D., Groene, W.S., Roberts, M.S., Rabin, H., Bamat, M.K., Lorence, R.M.: Phase I trial of intravenous administration of PV701, an oncolytic virus, in patients with advanced solid cancers. J. Clin. Oncol. **20**(9), 2251–2266 (2002)

19. Perko, L.: Differential Equations and Dynamical Systems, 3rd edn. Springer, New York (2001)
20. Reddy, P.S., Burroughs, K.D., Hales, L.M., Ganesh, S., Jones, B.H., Idamakanti, N., Hay, C., Li, S.S., Skele, K.L., Vasko, A.J., Yang, J., Watkins, D.N., Rudin, C.M., Hallenbeck, P.L.: Seneca Valley virus, a systemically deliverable oncolytic picornavirus, and the treatment of neuroendocrine cancers. J. Natl. Cancer Inst. **99**(21), 1623–1633 (2007)
21. Todo, T., Martuza, R.L., Rabkin, S.D., Johnson, P.A.: Oncolytic herpes simplex virus vector with enhanced MHC class I presentation and tumor cell killing. Proc. Natl. Acad. Sci. USA **98**(11), 6396–6401 (2001)
22. Villasana, M., Radunskaya, A.: A delay differential equation model for tumor growth. J. Math. Biol. **47**(3), 270–294 (2003)
23. Wodarz, D.: Computational approaches to study oncolytic virus therapy: insights and challenges. Gene Ther. Mol. Biol. **8**, 137–146 (2004)
24. Wodarz, D., Komarova, N.: Towards predictive computational models of oncolytic virus therapy: basis for experimental validation and model selection. PLoS ONE **4**(1), e4271 (2009)
25. Wu, J.T., Byrne, H.M., Kirn, D.H., Wein, L.M.: Modeling and analysis of a virus that replicates selectively in tumor cells. Bull. Math. Biol. **63**(4), 731–768 (2001)